University of Southampton

Faculty of Social Sciences
School of Mathematical Sciences

Quasinormal modes, Strong Cosmic Censorship and Instabilities

Alex Davey
ORCiD: 0000-0002-2271-4501

Supervisors: Óscar J.C. Dias,
Kostas Skenderis

A thesis for the degree of
Doctor of Philosophy

November 2023

University of Southampton

Abstract

Faculty of Social Sciences
School of Mathematical Sciences

Doctor of Philosophy

Quasinormal modes, Strong Cosmic Censorship and Instabilities

Alex Davey

Quasinormal modes (QNMs) are the damped vibrations of black hole (BH) spacetimes, characterising much of the response of a black hole to perturbations. In Chapter 1, we introduce quasinormal modes, their applications, and ways to compute them numerically using pseudospectral methods.

In Chapter 2 we study the scalar QNM spectrum of Kerr-Newman. Starting from the Reissner-Nordström limit, we understand how the spectrum changes as we vary the ratio of charge to angular momentum, all the way until the Kerr limit. This clarifies the relationship between the QNM spectra of Reissner-Nordström and Kerr, and highlights an intricate form of interaction called *eigenvalue repulsion*.

In asymptotically de Sitter (dS) spacetimes, an important application of quasinormal modes is the strong cosmic censorship (SCC) conjecture. In four dimensions, Christodoulou's formulation of SCC is violated by charged BHs (Reissner-Nordström-dS), but holds for rotating BHs (Kerr-dS). In Chapter 3, we study a higher-dimensional analogue of Kerr-dS, equal angular momentum Myers-Perry-dS, and show that SCC is respected in odd $d \geqslant 5$ dimensions. This suggests that the preservation of SCC in uncharged rotating black hole backgrounds might be a universal property of Einstein gravity and not limited to the $d = 4$ Kerr-dS background.

Finally, in Chapter 4, we construct the static hairy black holes of Einstein-Maxwell-Scalar theory in a cavity that confines the scalar field. These hairy black holes are asymptotically flat, with a scalar condensate floating above the horizon. When they coexist with Reissner-Nordström BHs, the hairy BHs are thermodynamically preferred, and hence they are natural candidates for the endpoint of the superradiant and near-horizon instabilities of the charged black hole bomb system.

Contents

Declaration of Authorship

I declare that this thesis and the work presented in it is my own and has been generated by me as the result of my own original research.

I confirm that:

1. This work was done wholly or mainly while in candidature for a research degree at this University;
2. Where any part of this thesis has previously been submitted for a degree or any other qualification at this University or any other institution, this has been clearly stated;
3. Where I have consulted the published work of others, this is always clearly attributed;
4. Where I have quoted from the work of others, the source is always given. With the exception of such quotations, this thesis is entirely my own work;
5. I have acknowledged all main sources of help;
6. Where the thesis is based on work done by myself jointly with others, I have made clear exactly what was done by others and what I have contributed myself;
7. Parts of this work have been published as:
    - A. Davey, O. J. C. Dias and P. Rodgers, *Phase diagram of the charged black hole bomb system*, *Journal of High Energy Physics* **2021** (May, 2021) 189, [2103.12752]
    - A. Davey, O. J. C. Dias, P. Rodgers and J. E. Santos, *Strong Cosmic Censorship and Eigenvalue Repulsions for rotating de Sitter black holes in higher-dimensions*, *Journal of High Energy Physics* **2022** (July, 2022) 86, [2203.13830]
    - A. Davey, O. J. C. Dias and J. E. Santos, *Scalar QNM spectra of Kerr and Reissner-Nordström revealed by eigenvalue repulsions in Kerr-Newman*, *(submitted to JHEP)* (May, 2023) , [2305.11216]

Signed:..... Date:.....

Chapter 1

Introduction

Stationary and axisymmetric black holes paint a remarkably simple picture of General Relativity (GR). This is due to the uniqueness theorems, which state that Kerr-Newman (KN) [4, 5] is the most general stationary, axisymmetric and asymptotically-flat electro-vacuum black hole solution of four-dimensional Einstein-Maxwell theory [6–8] [1]. Black holes, being the most extreme objects in the universe, offer a way to understand the limits of GR as an effective field theory, by theoretically probing the nature of the black hole interior.

In contrast to the relative simplicity of the Kerr-Newman solution, astrophysical black holes form as a consequence of gravitational collapse, with a wide range of possible matter fields, not to mention the presence of other gravitating bodies. This dynamical perspective forces us to consider phenomena that might be otherwise overlooked, such as deviations from perfect axisymmetry or dynamical instabilities which may render a stationary solution physically irrelevant.

The groundbreaking observation of gravitational waves by the LIGO-Virgo collaboration in 2015 opened the door to a new era of gravitational physics [11–13]. This first observation was of the inspiral, merger and ringdown of a pair of black holes. During the ringdown phase, the newly-merged black hole rapidly settles down to a spacetime well-approximated by a stationary vacuum state, *i.e.* with the exterior described by the Kerr solution [14]. The dynamics of the ringdown phase are dominated by the *quasinormal modes* (QNMs). These are damped oscillations that characterise much of how a black hole responds to a generic perturbation. Because the QNMs are completely determined by the black hole parameters, they

[1] Alternatively, one can drop the axisymmetry condition, and instead consider black hole spacetimes which are real analytic [9, 10].

can be thought of as a fingerprint of a black hole. Black holes are therefore not just a mathematical curiosity. Observational evidence can be used, for example, to constrain potential classical modifications to General Relativity, with wide-ranging cosmological implications [15].

The computation of quasinormal modes is an important ingredient in the analysis of gravitational wave signals. For example, gravitational wave templates have recently been constructed to constrain the remnant charge of binary black hole mergers, using the QNM spectrum of Kerr-Newman [16–18]. It is widely expected that astrophysical black holes have negligible charge [19–21], but this could allow a direct verification of the charge neutrality of black holes. Improvements to detectors, including future detectors such as LISA [22, 23] will enable increasingly precise measurements of the parameters of a black hole binary system and, by extension, of General Relativity.

Kerr-Newman is an asymptotically-flat spacetime. However, the accelerating expansion of the universe [24, 25] suggests that asymptotically de Sitter spacetimes may be more astrophysically relevant. While the experimentally measured value of the cosmological constant is very small [26], even the presence of a small cosmological constant can drastically change the physics. For example, in asymptotically flat spacetimes, the decay rate of perturbations outside a black hole obeys a power law at late times [27, 28], while in asymptotically de Sitter spacetimes the decay is exponential [29, 30]. These asymptotic behaviours have important implications for the strong cosmic censorship conjecture, which is concerned with the existence of Cauchy horizons deep inside a black hole, as we will discuss in Chapter 3.

A final motivation for the study of black holes is the AdS/CFT correspondence [31–33], which provides a correspondence between string theory on an asymptotically Anti-de Sitter (AdS) spacetime and a dual quantum field theory living on the boundary of that spacetime. It is a strong/weak coupling duality, in that weakly-coupled gravitational theories are dual to strongly-coupled quantum field theories. In particular, this means that the low-energy limit of string theory, supergravity, is dual to a gauge theory with large 't Hooft coupling. From this correspondence, the quasinormal modes of asymptotically AdS spacetimes can be identified with the poles of the Green's function of the dual field theory [34]. One can therefore study strongly-coupled gauge theories by constructing AdS black holes. Some of the most well-known examples are models of the quark-gluon plasma [35] and high-temperature superconductors [36–38]. While we do not study asymptotically AdS

spacetimes explicitly, we will see in Chapter 4 that asymptotically AdS spacetimes share many common features with other forms of confining potential.

The overarching theme of this thesis is the study of linear perturbations, in particular *quasinormal mode* (QNM) perturbations. We study the quasinormal mode spectrum numerically, whose classification is intrinsically interesting (Chapter 2), but also has implications for the strong cosmic censorship conjecture (Chapter 3). QNM perturbations can also tell us about potential instabilities of black hole spacetimes, which can then evolve to new solutions with scalar hair, which we find in Chapter 4.

For concreteness, consider the four-dimensional Einstein-Maxwell-Scalar action, with a minimally coupled massless scalar field Φ and cosmological constant Λ:

$$S = \frac{1}{16\pi G_N}\int\left(R - 2\Lambda - \frac{1}{2}F_{ab}F^{ab} - \nabla_a\Phi\nabla^a\Phi\right)\sqrt{-g}\,d^4x, \tag{1.1}$$

where R is the Ricci scalar and $F = dA$ is the Maxwell field strength tensor. We use units where $G_N = c = 1$. We will be primarily interested in asymptotically-flat ($\Lambda = 0$) and de Sitter ($\Lambda > 0$) spacetimes, so we take $\Lambda \geqslant 0$. Variation of the action gives with respect to the metric g_{ab} and Maxwell potential A yields the usual Einstein-Maxwell equations

$$R_{ab} - \frac{1}{2}(R - 2\Lambda)g_{ab} = T_{ab}, \qquad \nabla^a F_{ab} = 0, \qquad dF = 0, \tag{1.2}$$

with the Maxwell-Scalar stress-energy tensor

$$T_{ab} \equiv \nabla_a\Phi\nabla_b\Phi - \frac{1}{2}g_{ab}\nabla_c\Phi\nabla^c\Phi + F_a{}^cF_{bc} - \frac{1}{4}g_{ab}F^{cd}F_{cd}. \tag{1.3}$$

Variation with respect to the scalar field Φ gives the (massless) Klein-Gordon equation,

$$\nabla_a\nabla^a\Phi = 0. \tag{1.4}$$

The scalar field Φ appears quadratically in the stress-energy tensor (1.3). Therefore, starting with a solution of the Einstein-Maxwell system (with vanishing scalar field), we can study linear scalar field perturbations by finding solutions of the Klein-Gordon equation (1.4) on that fixed background spacetime, as the backreaction induced by scalar field perturbations is second-order. In the asymptotically-flat limit $\Lambda = 0$, the most general stationary and axisymmetric black hole solution is Kerr-Newman, most commonly expressed in standard Boyer-Lindquist coordinates (t, r, θ, ϕ), *i.e.* time, radial, polar and azimuthal coordinates [4], in which the metric

and Maxwell potential take the form

$$\begin{aligned} \mathrm{d}s^2 &= -\frac{\Delta}{\Sigma}\left(\mathrm{d}t - a\sin^2\theta\mathrm{d}\phi\right)^2 + \frac{\Sigma}{\Delta}\mathrm{d}r^2 + \Sigma\,\mathrm{d}\theta^2 + \frac{\sin^2\theta}{\Sigma}\left[\left(r^2+a^2\right)\mathrm{d}\phi - a\mathrm{d}t\right]^2, \\ A &= \frac{Q\,r}{\Sigma}\left(\mathrm{d}t - a\sin^2\theta\mathrm{d}\phi\right), \end{aligned} \tag{1.5}$$

with $\Delta = r^2 - 2Mr + a^2 + Q^2$ and $\Sigma = r^2 + a^2\cos^2\theta$. The Kerr-Newman solution has three parameters: mass M, charge Q and angular momentum $J \equiv Ma$. It encompasses the Schwarzschild ($a = Q = 0$) [39], Kerr ($Q = 0$) [14] and Reissner-Nordström ($a = 0$) [40, 41] black holes as limiting cases. The event and Cauchy horizons occur at the positive roots of $\Delta(r)$, with $r = r_+$ at the event horizon and $r = r_-$ at the Cauchy horizon, where $r_- \leqslant r_+$. Extremality occurs when the horizons coincide $r_- = r_+$.

It's worthwhile reviewing some basic facts about the analytic continuation of the Kerr-Newman metric (1.5), for later. In Boyer-Lindquist coordinates, the metric (1.5) is analytic in the exterior region $r > r_+$, but it has a coordinate singularity at the event horizon $r = r_+$. However, the metric can be analytically extended beyond the (future) event horizon and into the interior region $r_- < r < r_+$, by transforming to *ingoing Eddington-Finkelstein* (EF) coordinates (v, r, x, ϕ'), defined by

$$t = v - r_\star \qquad \phi = \phi' - \Omega_\star, \tag{1.6}$$

$$r_\star \equiv \int \frac{r^2+a^2}{\Delta}\,\mathrm{d}r, \qquad \Omega_\star \equiv \int \frac{a}{\Delta}\,\mathrm{d}r, \tag{1.7}$$

where $r_\star$ is a *tortoise coordinate* such that $r_\star \to -\infty$ at the event horizon and $r_\star \to \infty$ as $r \to \infty$. Similarly, one can define *outgoing Eddington-Finklestein* coordinates (u, r, θ, ϕ'') by $t = u + r_*$ and $\phi = \phi'' + \Omega_\star$. However, if we were to use outgoing EF coordinates the extend beyond the event horizon $r = r_+$ we would find a new region $r_- < r < r_+$, the *white hole region*, which is not the same as the black hole region found using ingoing EF coordinates. We therefore distinguish between the future event horizon (defined in ingoing EF coordinates) and the past event horizon (defined in outgoing EF coordinates). This distinction will be important, because perturbations which are regular at the future event horizon are not regular at the past event horizon.

We now want to find solutions of the Klein-Gordon equation (1.4) on the Kerr-Newman background. Stationarity and axisymmetry of the background allows us

to decompose the scalar field Φ into Fourier modes in the t and ϕ directions

$$\Phi = e^{-i\omega t + im\phi} R_{\omega\ell m}(r) S_{\omega\ell m}(\theta) \tag{1.8}$$

with frequency ω and angular quantum numbers m and ℓ. The Klein-Gordon equation separates into a pair of coupled ODEs. The radial component can be expressed as a Schrödinger-type equation

$$\left[-\frac{d}{dr_*^2} + V_{\omega\ell m}(r) \right] R_{\omega\ell m}(r) = 0 \tag{1.9}$$

while the angular equation is the spheroidal harmonic equation, such that $S_{\omega\ell m}(\theta)$ are the oblate spheroidal harmonics, with m and ℓ must be integers satisfying the constraint $0 \leqslant |m| \leqslant \ell$. The full explicit details will be discussed in Chapter 2.

In order to have a well-posed boundary value problem, we must impose appropriate boundary conditions on the radial component $R_{\omega\ell m}(r)$. In particular, we will impose *quasinormal mode* boundary conditions. To motivate quasinormal modes, we first review normal modes. As a toy example, consider the Klein-Gordon equation (1.4) on 1+1 dimensional Minkowski space $(-\partial_t^2 + \partial_r^2)\chi = 0$. After a Fourier decomposition $\Phi = e^{-i\omega t}\chi(r)$, we get the wave equation

$$\chi'' + \omega^2 \chi = 0. \tag{1.10}$$

After imposing, say, Dirichlet boundary conditions on a finite domain $\chi(0) = \chi(L) = 0$ we find the normal modes; the eigenfunctions

$$\chi_n = C_n \sin(\omega_n\, r), \qquad \omega_n = \frac{n\pi}{L}, \qquad n = 1, 2, \ldots \tag{1.11}$$

Here ω_n is a discrete set of real eigenvalues. The eigenfunctions χ_n form a complete basis, *i.e.* we can express any smooth solution as a sum over normal modes $\chi = \sum_{n=1}^{\infty} e^{-i\omega_n t}\chi_n$. Due to our choice of boundary conditions this system is closed, *i.e.* the energy is conserved.

In contrast, quasinormal mode boundary conditions are dissipative. Classically, the event horizon acts as a one-way membrane, such that only ingoing waves are allowed. Similarly, one expects that there are no waves coming in from spatial infinity (or the future cosmological horizon), only outgoing waves. These are the physical motivations for QNM boundary conditions: Φ must be a purely ingoing wave at the future event horizon and a purely outgoing wave at spatial infinity (or the future cosmological horizon) [42–45]. The resulting QNM frequencies ω

describe damped oscillations, with a negative imaginary part representing the decay rate, while the real part characterises the oscillation frequency.

A more precise definition for the QNM boundary conditions in asymptotically flat or de Sitter spacetimes can be given in term of regularity: $R_{\omega\ell m}(r)$ must be regular at the future event horizon in ingoing Eddington-Finklestein coordinates (1.6), and regular at the future cosmological horizon (or spatial infinity) in outgoing Eddington-Finklestein coordinates. To see this, we use the fact that Δ can be factorised in terms of the horizon radii $\Delta = (r - r_+)(r - r_-)$ to explicitly integrate the tortoise coordinate (1.12)-(1.13):

$$r_\star = r + \frac{\log(r - r_+)}{2\kappa_+} - \frac{\log(r - r_-)}{2\kappa_-}, \tag{1.12}$$

$$\Omega_\star = \frac{\Omega(r_+)\log(r - r_+)}{2\kappa_+} - \frac{\Omega(r_-)\log(r - r_-)}{2\kappa_-}, \tag{1.13}$$

where we have neglected the constants of integration, and identified the surface gravities $\kappa_\pm$ and angular velocities $\Omega(r_\pm)$ of the event horizon ($r = r_+$) and Cauchy horizon $r = r_-$. Starting with a Fourier mode in ingoing EF coordinates (1.6) with radial dependence $R_{\rm EF}(r)$, and transforming to Boyer-Lindquist coordinates, we find

$$e^{-i\omega v + im\phi'} R_{\rm EF}(r) = e^{-i\omega t + im\phi} e^{-i(\omega r_\star - m\Omega_\star)} R_{\rm EF}(r) \tag{1.14}$$

$$= e^{-i\omega t + im\phi} (r - r_+)^{-i\frac{\omega - m\Omega(r_+)}{2\kappa_+}} R_+(r) \tag{1.15}$$

where $R_+(r)$ includes both $R_{\rm EF}$ and the terms in the tortoise coordinates (1.12)-(1.13) which are regular at $r = r_+$. By comparison to the original Fourier decomposition (1.8) in Boyer-Lindquist coordinates, we see that if $R_+(r)$ is any function that is regular at the event horizon $r = r_+$, then this corresponds to a mode which is regular in ingoing EF coordinates at the event horizon. In the limit $r \to \infty$, the tortoise coordinate reduces to $r_\star \to r + 2M \log r$ (and $\Omega_\star$ vanishes), dependent on only the BH mass. Therefore, QNM boundary conditions for Kerr-Newman are given by

$$R_{\omega\ell m}(r) \sim \begin{cases} (r - r_+)^{-i\frac{\omega - m\Omega(r_+)}{2\kappa_+}} R_+(r) & \text{as} \quad r \to r_+, \\ e^{i\omega r} r^{2i\omega M} R_\infty(r) & \text{as} \quad r \to \infty, \end{cases} \tag{1.16}$$

where $R_+(r)$ is regular at the event horizon $r = r_+$ and $R_\infty(r)$ is regular for large

$r \to \infty$ [2]. For asymptotically de Sitter spacetimes (*e.g.* Kerr-Newman-de Sitter [46] or cohomogeneity-one Myers-Perry de Sitter) QNM boundary conditions are given by

$$R_{\omega\ell m}(r) \sim \begin{cases} (r-r_+)^{-i\frac{\omega-m\Omega(r_+)}{2\kappa_+}} R_+(r) & \text{as} \quad r \to r_+, \\ (r_c-r)^{-i\frac{\omega-m\Omega(r_c)}{2\kappa_c}} R_c(r) & \text{as} \quad r \to r_c, \end{cases} \tag{1.17}$$

where $R_+(r)$ is regular at the event horizon $r = r_+$ and $R_c(r)$ is regular at the cosmological horizon $r = r_c$, and κ_c is the surface gravity there. The above boundary conditions are only valid in the case of non-degenerate horizons, *i.e.* a sub-extremal BH. In the extremal limit $r_- \to r_+$ both logarithms in the tortoise coordinate $r_\star$ (and $\Omega_\star$) contribute and the QNM boundary conditions need to be modified accordingly. Quasinormal mode boundary conditions in asymptotically-AdS black holes are somewhat different, due to the reflective nature of the timelike boundary, and are typically motivated via the AdS/CFT correspondence. We do not discuss these here, but refer the reader to [47, 42].

After imposing QNM boundary conditions, the radial and angular ODEs for the Klein-Gordon equation constitute a coupled eigenvalue problem for the QNM frequency ω and angular separation constant λ. In black hole spacetimes with the reflection symmetry ($t \to -t, \phi \to -\phi$), the quasinormal mode frequencies form complex conjugate pairs [48, 49]. For example, in Kerr-Newman, if $\{\omega_m, \lambda_m\}$ are a quasinormal mode frequency and angular separation constant (for a given azimuthal quantum number m), there exists another solution pair $\{-\omega^*_{-m}, \lambda^*_{-m}\}$. This symmetry allows us to consider $m \geqslant 0$ only, provided we study both signs of $\mathrm{Re}\,\omega$. In the static limit (*e.g.* Schwarzschild or Reissner-Nordström), QNMs are symmetric about the imaginary axis, forming pairs $(\omega_m, -\omega^*_m)$.

An alternative way to define QNMs is by identifying them as the poles of the Green's function [50]. To compute the response to a generic perturbation in the frequency domain, we can consider the Klein-Gordon equation (1.4) with an additional inhomogeneous source term representing the perturbation. Formally, one can solve this by constructing the Green's function for the Klein-Gordon operator in the frequency domain, and then taking an inverse Laplace transform to get the time-response [50–52]. In general, there are three contributions to the contour integral: the residues, a semi-circular contour in the lower half plane, and a branch cut along the negative imaginary axis. The semi-circle contour corresponds to the *prompt response*, the early-time contribution of waves propagating directly from the

[2] It is common to pull out an additional regular factor r^{-1} from R_∞. It is not required, but an explicit analysis in Kerr-Newman (Chapter 2) shows that the linearly-independent asymptotic solution which obeys QNM boundary conditions has that additional factor.

source, which can be shown by taking the limit of vanishing black hole mass. The sum over the residues is the QNM contribution. These residues are at the simple poles where the Wronskian between the two linearly independent functions used to construct the Green's function vanishes, and the Green's function becomes singular. If we ignore the contribution from the prompt response, we simply have the sum over residues. In the Schwarzschild limit, one can show that, after separating out the angular dependence, the sum over residues can be written [53, 52]:

$$\Phi \sim \mathrm{Re}\left[\sum_{n=0}^{\infty} C_n e^{-i\omega_n (t-r_\star)}\right], \tag{1.18}$$

where the coefficients C_n are defined by the residue at each pole. (The real part comes from the fact that we are actually summing over pairs of QNMs $\{\omega, -\omega^*\}$). In this way, we can see that, at least at intermediate times, much of the spacetime dynamics is characterised by a sum over quasinormal modes, like the normal modes of a closed system. However, we have ignored the other contributions to the Green's function. Unlike normal modes, quasinormal modes do not form a complete set (hence *quasi*-normal). We can also see this from the fact that, in order for QNMs to be decaying exponentially in time, they must blow up as we go to earlier times. More formally, we can see this from the fact that QNMs are not regular at the past event horizon or past null infinity (or the past cosmological horizon). This follows from the definition of QNMs. For example, since they regular at the future event horizon they cannot be regular at the past event horizon. One consequence of this is that, if we want to include the past event horizon and past null infinity in our Cauchy surface Σ, we cannot express regular initial data on Σ in terms of QNMs.

Finally, in asymptotically-flat spacetimes the very late-time behaviour is governed by an inverse-power decay rate, arising as the branch cut contribution to the contour integral. These are known as *late-time tails* or *Price's law*, as it was first observed by Price when studying linearised perturbations of Schwarzschild [27, 28, 54, 55] (see also [56]). In general, the field decays at very late times as $\Phi \sim t^{-(2\ell+3)}$. Physically, the late-time tails can be associated to the backscattering of waves off of the background geometry [50, 27]. Therefore, the late-time behaviour of perturbations is strongly dependent on the spacetime asymptotics. We will see another manifestation of this in Section 1.2.

1.1 Three families of quasinormal mode

Asymptotically flat, four-dimensional black holes which admit a Cauchy horizon (including Kerr-Newman black holes and its Kerr and Reissner-Nordström limits) have two distinct families of QNMs, namely the *photon sphere* modes (also known as damped modes), and the *near-horizon* modes, (also known as *near-extremal* or *zero-damped* modes). In Chapter 2, we will show that this classification is only unique in the Reissner-Nordström limit ($a = 0$) and Kerr-Newman BHs when the ratio of angular momentum to mass a/Q is small. For general Kerr-Newman black holes, or in asymptotically de Sitter black holes, this classification breaks down, and the QNMs become entangled, via a phenomenon called *eigenvalue repulsion*. In that case, the modes are often described by more than one family simultaneously.

The photon sphere (PS) modes (also denoted as *damped modes* in [57–59]) are typically described by the well-known eikonal approximation of the quasinormal mode spectrum, where the angular momentum quantum numbers m and ℓ are taken to be large and we thus have a null particle limit [60–69, 59, 18]. The eikonal approximation also provides a geometric interpretation, first presented by Goebel [60] and Ferrari and Mashhoon [61, 63], in terms of the dynamics of circular null geodesics in the equatorial plane:

$$\omega_{\rm PS} \simeq m\,\Omega_0 - i\left(n+\frac{1}{2}\right)|\lambda_{\rm L}|, \qquad n = 0, 1, 2, \ldots \tag{1.19}$$

where $\Omega_0 \equiv \frac{d\phi}{dt}$ is the Keplerian velocity of the photon orbit, $\lambda_{\rm L}$ is the principal Lyapunov exponent, and n is the overtone number. The principal Lyapunov exponent $\lambda_{\rm L}$ characterises the instability timescale of the geodesic, *i.e.* the rate at which a null geodesic congruence increases its area under infinitesimal radial deformations. This result coincides with a leading order WKB analysis of the QNM problem, as first discussed by Schutz and Will [64] and completed for Schwarzschild(-Tangherlini), RN and Kerr in [70–74]. The PS modes form pairs, called *co-rotating* and *counter-rotating* (also sometimes called prograde and retrograde), in accordance with the t-ϕ symmetry of QNMs. One mode co-rotates with the horizon ($\Omega_0 > 0$) while the other orbits in the opposite direction (assuming it does not lie in an ergoregion). Typically, the co-rotating mode which is dominant, decaying more slowly (*i.e.* with smaller $|\operatorname{Im}\omega|$).

An important property of the leading-order eikonal approximation (1.19) is that it is *isospectral*, independent of the spin of the perturbation, so it is valid for

not just scalar perturbations, but also *e.g.* gravitational and electromagnetic perturbations [42, 43] (although higher-order corrections are spin-dependent [74, 75]). Furthermore, while the correspondence (1.19) is only valid for equatorial modes $m = \ell$, it can be generalised to arbitrary $m \neq \ell$, corresponding to non-equatorial spherical orbits in the photon sphere [75, 76].

In spacetimes that admit a Cauchy horizon, there is also a second QNM family – the *near-horizon* (NH) modes (a.k.a *near-extremal* or *zero-damped* modes) [77–82, 57, 58, 83, 59, 84, 16, 18, 55, 85]. The NH modes are generally suppressed except very near extremality, and are characterised by a frequency with a vanishing imaginary part in the extremal limit, with the real part saturating the superradiant bound $\omega \to m\Omega(r_+)$ at extremality [86–89]. Near the Reissner-Nordström limit, the wavefunction is very localised near the event horizon. The NH modes can typically be captured by a *matched asymptotic expansion*. That is, we find the ingoing wavefunction near the event horizon and also find the outgoing wavefunction far from the horizon, before matching the two in an overlap region where the regimes of validity of both regions hold [77, 78, 57–59]. Through this calculation one can highlight the link between the NH modes and the near-horizon geometry of the extremal spacetime, as we will do in later chapters.

In asymptotically de Sitter spacetimes, a third family of QNMs is present: the *de Sitter* (dS) family. In the limit where the mass, charge and angular momentum of the black hole vanish, the frequency of these modes approaches the QNM frequency of pure de Sitter space[3], *i.e.*

$$\omega_{\rm dS} = \begin{cases} -i\,\ell\,\kappa_c & n = 0, \\ -i(\ell + n + 1)\kappa_c & n \neq 0. \end{cases} \tag{1.20}$$

for $n = 0, 1, 2, \ldots$, where κ_c is the surface gravity at the cosmological horizon. In $d = 4$, the dS modes have a weak dependence on the black hole parameters [86]. We will show that this is no longer true in higher dimensions.

The three families of QNM described here are by no means an attempt to exhaustively describe the QNMs of all possible black hole spacetimes. For example, accelerating spacetimes such as the C-metric [90–92], which feature an acceleration horizon, appear to have a family of *acceleration modes* much like the de Sitter

[3]Pure de Sitter space does not have an event horizon. Instead, we impose regularity at the origin.

modes of RNdS [93], despite being asymptotically-flat[4]. However, to the best of our knowledge, all of the QNMs in Kerr-Newman-de Sitter and its subfamilies can be understood as belonging to one (or more) of the three families [86, 94, 46, 77–82, 57, 58, 83, 59, 84, 16, 18, 55, 85, 57–59].

Given a QNM in any part of the parameter space of a black hole spacetime, we can try to classify it as *uniquely* belonging to a photon sphere, near-horizon or de Sitter mode, by tracing it to a suitable corner of the parameter space, where it agrees with one of the analytic approximations. In particular, we could try to define the photon sphere modes as QNMs whose eigenvalues are continuously connected to the QNMs of the eikonal limit, the near-horizon modes are those which tend to the matched asymptotic expansion in the near-extremal limit, and the de Sitter modes as QNMs continuously connected to the pure dS QNMs in the de Sitter limit. As we will see in later chapters, such a unique classification is not possible in general except near the Reissner-Nordström limit, where the modes disentangle.

1.2 Strong cosmic censorship

Predictability is an important requirement of any physical theory. In this section we review the strong cosmic censorship (SCC) conjecture, which calls into question the predictability of any spacetime hidden behind a Cauchy horizon. The issue is best understood in the context of the initial value formulation of General Relativity [95, 96], where we specify initial data on some partial Cauchy hypersurface Σ, for example a constant time slice or a pair of null hypersurfaces, and evolve it according to the Einstein equations. The resulting spacetime $(\mathcal{M}, g)$, the *maximal Cauchy development*, is unique and by definition globally-hyperbolic. This is the shaded region in Fig. 1.1.

Sometimes, it is possible to find a non-trivial extension $(\mathcal{M}', g')$ of the maximal Cauchy development. In that case, the boundaries of the maximal Cauchy development are known as *Cauchy horizons*. The Kerr solution provides example of such an extendible spacetime [97]. Using the ingoing and outgoing Eddington-Finklestein coordinates defined in (1.6), which are also valid for Kerr in the limit $Q \to 0$, one can extend $(\mathcal{M}, g)$ beyond the Cauchy horizons, for example beyond the right

[4]This is because the acceleration generated by the string or strut in these spacetimes effectively mimics the de Sitter cosmological expansion (for example, the causal structure of the C-metric has similarities with the one for the Schwarzschild-de Sitter solution, with the cosmological horizon replaced by the acceleration horizon).

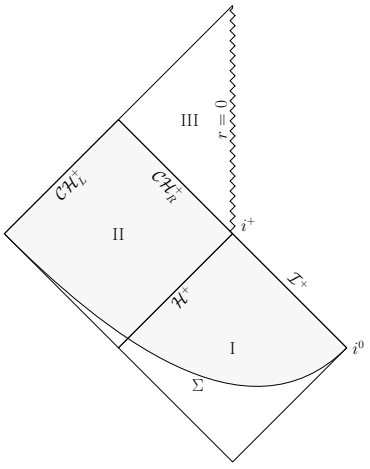

Fig. 1.1: Causal structure of the exterior region I and interior region II of (subextremal) Kerr (and Kerr-Newman), as well as the extension beyond the right future Cauchy horizon $\mathcal{CH}^+_R$ into region III. The maximal future Cauchy development of initial data on Σ is shaded.

future Cauchy horizon $\mathcal{CH}^+_{\mathrm{R}}$, into a new region III shown in Fig. 1.1 [5]. However, this extension is not unique, nor is it globally-hyperbolic — region III does not depend causally on the initial data on Σ. There is in general no physical reason to assume the extension must be analytic, and if we drop this assumption there are typically an infinite number of possible smooth extensions beyond $\mathcal{CH}^+_R$ [89]. In other words, physics is predicted by General Relativity only up to the Cauchy horizons. This lack of predictability calls into question the physical relevance of region III, or indeed any extension beyond a Cauchy horizon.

A hint at the resolution to this problem, known as the *infinite blueshift instability*, was first noted by Penrose [98]. Consider two observers A and B in region I. A falls into the black hole and then approaches the Cauchy horizon $\mathcal{CH}^+_R$, while B stays outside, emitting light signals at regular intervals. It takes B an infinite amount of proper time to "reach" timelike infinity, so they will have emitted an infinite number of signals, but A will receive all of those signals in the finite amount of proper time that it takes to reach the Cauchy horizon[6]. This infinite blueshift effect suggests that any small perturbation of the spacetime will back-react on the background fields and cause them to blow up rendering the Cauchy horizon a singular boundary, such that one could not extend beyond the Cauchy horizon. The strong cosmic

[5] Typically, we do not need to consider the left Cauchy horizon $\mathcal{CH}^+_{\mathrm{L}}$ as it will be occluded, at least partially, by matter in the process of gravitational collapse [98].

[6] Much recent work has been done in the mathematical community formalising the blueshift instability, see [99] for an overview.

censorship conjecture[7] posits that, for generic initial data, the maximal Cauchy development is inextendible beyond the Cauchy horizon as a suitably regular manifold [101]. A violation of SCC indicates a failure of predictability, since if one *can* extend beyond a Cauchy horizon then this new region would not depend causally on only the initial data specified on Σ.

What is the appropriate notion of regularity that we should require? At least historically, the research programme of strong cosmic censorship has been as much about precisely formulating Penrose's conjecture as actually proving it. One might hope that the maximal Cauchy development is inextendible as a continuous C^0 manifold. Physically, this requirement corresponds to the divergence of tidal forces at the Cauchy horizon [102]. This is true for extensions beyond the singularity in Schwarzschild [103]. However, this has been proven false in both Kerr[8] [102] and Reissner-Nordström [105, 56]. We could instead require that the maximal Cauchy development is inextendible as a C^2 manifold, corresponding to a curvature singularity, as the Ricci tensor includes second derivatives of the metric. This C^2 formulation has been shown to hold for Kerr and Reissner-Nordström [106]. However, a curvature singularity does not necessarily imply that macroscopic observers are destroyed at the Cauchy horizon [107]. The modern formulation of strong cosmic censorship, due to Christodoulou, is that the maximal Cauchy development is inextendible as a *weak solution* of the Einstein Equations, or gravitational equations with matter fields [108]. This is the formulation of strong cosmic censorship that we will be considering.

By allowing extensions which are *weak solutions* of the Einstein equations, we will see a sense in that the Einstein equations can be satisfied even if the extension is not in C^2. To motivate this, we return to the example of the wave equation in 1+1 dimensional Minkowski space, with the addition of an inhomogeneous source term $I(t, r)$,

$$\left(-\partial_t^2 + \partial_r^2\right)\, \Phi = I(t, r). \tag{1.21}$$

If the source term is zero, the most general solution, d'Alembert's solution [109], is a sum of arbitrary left-moving and right-moving functions:

$$\Phi(t, r) = f(t + r) + g(t - r). \tag{1.22}$$

[7] This is not related to the weak cosmic censorship conjecture, which roughly speaking asserts that the maximal Cauchy development of generic asymptotically-flat initial data has a complete future null infinity (*i.e.* does not contain naked singularities). Despite the nomenclature, the modern formulations of weak and strong cosmic censorship are in fact independent [100].

[8] This assumes the stability of the exterior of Kerr, which has been proven in the slowly-rotating case [104].

Strictly speaking, f and g must be in C^2 for Φ to be a solution, however it certainly seems reasonable to enlarge the class of functions which we consider solutions to include discontinuous solutions such as square waves — one propagating to the right and the other to the left. This kind of discontinuous solution does in fact occur in nature. The most well-known example of this are shocks in fluids, which can form dynamically, i.e., from smooth initial data [110]. Gravitational shocks are expected to exist, however shock solutions Einstein equations do not form dynamically, except possibly at the boundary of the domain of dependence [89].

To formalise this idea, we multiply the wave equation by an arbitrary test function $\psi(t, r)$ (*i.e.* smooth, with compact support), and integrate by parts:

$$0 = \int \psi(-\partial_t^2\Phi + \partial_r^2\Phi - I)\, dr\, dt \tag{1.23}$$

$$= \int \left[(\partial_t\psi)(\partial_t\Phi) - (\partial_r\psi)(\partial_t\Phi) - I\psi\right] dr\, dt. \tag{1.24}$$

Then, we define *weak solution* of the wave equation (1.21) to be a function that satisfies our integral expression (1.24) for all test functions ψ. While we no longer require Φ to be twice-differentiable, we now have a new requirement: the source term $I(t, r)$ must be *locally integrable*, in the sense that $I(t, r)\psi$ is integrable for any test function ψ.

When applied to the Einstein equations (possibly coupled to matter fields), an extension beyond the Cauchy horizon is a weak solution if the Christoffel symbols are locally square-integrable in some gauge [108]. Meanwhile, for scalar field initial data, Φ is a weak solution if it is locally square-integrable at the Cauchy horizon, *i.e.* in the Sobolev space H^1_{loc} [111, 112].

1.3 The status of strong cosmic censorship

There is growing evidence that the Christodoulou formulation of strong cosmic censorship is respected[9] for asymptotically flat initial data close to Reissner-Nordström [113–116] and Kerr [117, 118]. Ultimately, this is due to the infinite blueshift effect described above [119, 27].

[9]This may not be true for spacetimes which feature an acceleration horizon, such as the C-metric [93].

However, for positive cosmological constant ($\Lambda > 0$) there is a competing redshift associated with the gravitational potential well of asymptotically de Sitter spacetimes [120]. As a result of the delicate competition between these two effects, the decay of generic linear perturbations depends instead on the imaginary part of the slowest-decaying quasinormal mode [111, 112]:

$$|\Phi - \Phi_0| \leqslant Ce^{-\alpha t} \tag{1.25}$$

where Φ_0 and C are constants, and α is the *spectral gap*, the magnitude of the imaginary part of the slowest-decaying quasinormal mode. Starting from smooth initial data on Σ in RNdS or (slowly-rotating) Kerr-de Sitter [121], the regularity of Φ at the Cauchy horizon $r = r_-$ is in the Sobolev space $H^{1/2+\min(\beta)-\epsilon}_{\text{loc}}$ (for any $\epsilon > 0$), where we have defined

$$\beta \equiv -\frac{\text{Im}(\omega)}{\kappa_-} \tag{1.26}$$

and κ_- is the surface gravity at the Cauchy horizon. Also note [94], which argue that this condition is also valid for Kerr-dS with arbitrary rotation (if we only consider QNM initial data). To summarize, the Christodoulou formulation of SCC is respected if there exists a QNM perturbation with $\beta \leqslant \frac{1}{2}$. In order to prove that SCC is respected in a specific spacetime (for some fixed mass, charge, etc.), we just need to find a single QNM with $\beta \leqslant \frac{1}{2}$. On the other hand, to show that it is violated, we need to show that *every* QNM has $\beta > \frac{1}{2}$.

In recent years, an exhaustive search of the scalar field and gravito-electric QNM spectra has established that for initial data close to Reissner-Nordström−de Sitter (RNdS) there does not always exist a QNM with $\beta \leqslant \frac{1}{2}$, and therefore SCC is violated. This occurs in particular for RNdS black holes with large charge to mass ratio Q/M, *i.e.* those close to extremality (RNdS) [86, 89, 122]. Meanwhile, Kerr-dS respects SCC [94]. In particular, it is the photon sphere modes with large $m = \ell$ that enforce SCC throughout the parameter space.

The violation of SCC for initial data close to RNdS is worrying. Charged matter fields are required in a theory that allows the formation of RNdS black holes through gravitational collapse, which motivated several studies of a charged scalar field on RNdS [122–124]. While the addition of charge pushes the region which violates SCC closer to extremality, SCC is ultimately still violated in sufficiently

extremal RNdS black holes[10]. These analyses were accomplished within linear theory, and it remains an open problem to show that they extend to the full non-linear theory. Existing non-linear studies are inconclusive, due to difficulties pushing the evolution to sufficiently late times [125, 126]. However, one would not expect non-linear effects to rescue SCC in RNdS, since the linear analysis has shown that every single perturbation remains sufficiently regular at the Cauchy horizon.

Equally important is an understanding of *why* Kerr-dS respects SCC. A better understanding of what feature of the Kerr-dS data may provide insights as to the kind of initial data that is required for SCC, or which reformulation of SCC is appropriate. Is this a universal feature of (uncharged) rotating spacetimes, or is Kerr-dS an isolated exception? As a step towards answering this question, we study the scalar field QNMs of the higher-dimensional generalisation of Kerr-dS, Myers-Perry-dS, in Chapter 3, and compare it to higher-dimensional Reissner-Nordström-de Sitter.

In four-dimensional asymptotically AdS spacetimes, perturbations decay slowly due to the stable trapping of null geodesics [127], so one would not expect AdS black holes to violate strong cosmic censorship. However, the 2+1 dimensional BTZ black hole does not exhibit stable trapping, and severely violates strong cosmic censorship, not just the Christodoulou formulation but also the C^k formulations for all k [47]. At the level of QNMs, this violation is due to a remarkable coincidence between the co-rotating quasinormal mode frequencies and the "interior quasinormal mode" frequencies, which obey QNM-like boundary conditions, but in the interior region. As a result, only the counter-rotating modes contribute to SCC. This is expected to be a very special property of the BTZ black hole, related to the fact that linear perturbations are governed by Hypergeometric equations (*i.e.* with three regular singular points) rather than Heun equations. Indeed, it has been shown explicitly that such a coincidence does not occur in RNdS [128]. It was later shown that this violation remains even in a fully non-linear gravitational collapse [129]. In the conclusion, we will discuss ways in which strong cosmic censorship may be saved in RNdS and BTZ.

[10]Refs. [123, 124] arrived at the opposite conclusion because these studies did not extend the analysis sufficiently close to extremality where the violation is finally observed (see associated discussion in [122]).

1.4 Instabilities and near-horizon geometries

To discuss the physical relevance of a spacetime, we should ensure that it is free of dynamical instabilities, or if instabilities are present, we should evaluate their timescale to see if they are relevant. By an instability, we mean initial data that is bounded and with compact support that grows exponentially in time. A simpler problem than studying the full non-linear stability is the *linear mode stability*, *i.e.* determining whether there exist quasinormal mode solutions with frequencies in the upper half plane $\mathrm{Im}\,\omega > 0$, which will therefore blow up exponentially in time, indicating instability. In this section we will describe two specific types of instability that rotating (and charged) black holes can be susceptible to: superradiant and near-horizon instabilities.

Superradiant scattering is a mechanism by which waves incident on a black hole are reflected with amplified energy, extracting energy from the black hole. This occurs in black holes which posses an ergoregion (such as Kerr-Newman), provided that the wave frequency ω is within the range

$$0 < \omega < m\Omega_H + q\mu \tag{1.27}$$

where Ω_H is the angular velocity of the event horizon and μ is the chemical potential. This is the wave analogue of the Penrose-Christodoulou process [130, 131]. Superradiance can be seen as a consequence of the laws of black hole mechanics, in particular the area theorem [9], as first shown by Bekenstein [132]. The ratio of energy δM, angular momentum δJ and charge δQ imparted by a scalar wave of Fourier form (1.8) is given by [133, 134]

$$\frac{\delta J}{\delta M} = \frac{m}{\omega}, \qquad \frac{\delta Q}{\delta M} = \frac{q}{\omega}. \tag{1.28}$$

The first law of black hole mechanics states that, to first order, a small variation in energy, angular momentum, and charge induces a variation of the horizon area δA_H by $\frac{\kappa_+}{8\pi}\delta A_H = \delta M - \Omega_{\mathrm{H}}\delta J - \mu\delta Q$ [135, 136]. Inserting (1.28) into the first law and solving for δM yields

$$\delta M = \frac{\kappa_+}{8\pi}\frac{\omega\,\delta A_H}{\omega - m\Omega_H - q\mu}. \tag{1.29}$$

Now, the second law tells us that, for matter which satisfies the weak energy condition, the horizon area never decreases, $\delta A_H \geqslant 0$ [9]. As a consequence, waves with a frequency ω within the range (1.27) reduce the black hole mass δM,

extracting energy by superradiant amplification. The fraction of energy amplified by superradiance is usually much less than one percent [137], but by confining the scalar field near the horizon in a reflective cavity, for example, the repeated process of reflections and superradiant amplifications can cause an instability to develop. In uncharged black holes where the chemical potential vanishes $\mu = 0$, such as Kerr, this is the *rotating black hole bomb* setup, designed by Zel'dovich [138] and Press and Teukolsky [137]. At the other extreme, in the charged non-rotating case $\Omega_H = 0$, we have the *charged black hole bomb*, provided the scalar field charge q is within the bound $0 < \omega < q\mu$ [132, 139]. Note that in both of these cases we do not need a literal cavity. The gravitational potential of AdS or a massive bosonic field can also give rise to an analogous black hole bomb system [140–143].

It turns out that this system is not just susceptible to superradiant instabilities, but also a second type of instability, which is known as a *near-horizon instability* due to the relationship with the near-horizon geometry of black holes. In planar AdS black holes, this instability (also known as a *scalar condensation instability*) initiated the holographic superconductor programme [36–38]. It was later found that this instability is not limited to asymptotically AdS black holes, or even systems with confining potentials, but is really a feature of the near-horizon geometry of the extremal black holes [144–146].

In the near-horizon limit, the geometry of many extremal black holes can be expressed locally as a product of AdS_2 times a compact space [144]. This is true even if the original spacetime is asymptotically flat or de Sitter. In this limit, the Klein-Gordon equation on the near-horizon geometry reduces to an effective scalar field equation on pure AdS_2 with a certain effective mass μ_{AdS} and charge q_{AdS}. It is well known that in AdS_2 (with radius L_{AdS}), a scalar field perturbation is normalisable even if its squared mass μ^2_{AdS} is negative, provided that it obeys the 2-dimensional Breitenlohner-Freedman (BF) bound $\mu^2_{\text{AdS}} L^2_{\text{AdS}} \geqslant -\frac{1}{4}$ [147, 148]. On the other hand, the scalar field on AdS_2 is not stable if its mass is below the 2-dimensional BF bound.

However, a violation of the effective AdS_2 BF bound of the near-horizon geometry does not *necessarily* imply an instability of the scalar field on the full (extremal) black hole geometry. For asymptotically flat or AdS black holes, a conjecture by Durkee and Reall [144], later proven by Hollands and Ishibashi [149], gives a sufficient (but not necessary) condition for this near-horizon AdS_2 BF bound violation to develop into an instability of the extremal black hole. If an instability is present, one expects that it also extends away from extremality, by continuity.

Details of the condition for an instability, and the potential to extend the theorem to include asymptotically de Sitter spacetimes, are given in Chapter 3.

Given a system susceptible to these instabilities, it is natural to wonder what the endpoint of a time evolution would be. One possibility is that it evolves to a nakedly singular solution in a finite time, violating the weak cosmic censorship conjecture (see footnote 7), as occurs for the Gregory-Laflamme instability [150–152]. Another possibility is that modes with increasingly high energies are excited, moving into the regime of quantum gravity. However, is often the case that following the time evolution to its endpoint will reveal a new black hole solution, one that is stable to the original instability.

The discovery of Hawking radiation cemented the idea that the laws of black hole mechanics are not just analogous to the laws of thermodynamics [133], but that black holes are really thermodynamic objects [133, 153, 154], with a temperature $T = \kappa_+/2\pi$ and an entropy proportional to the area of the event horizon $S = A_H/4$. Therefore, one can use thermodynamic arguments to try to determine the endpoint of a black hole instability. We can find candidates for the endpoint of the instability by constructing solutions (with the same fields and boundary conditions) that are stable to the original instability, but with a higher entropy for a given energy (and eventually for a given angular momentum and/or charge).

In Chapter 4, we do exactly this for the charged black hole bomb system. We find the phase diagram of static solutions of the Einstein-Maxwell-Scalar system with boundary conditions that confine the scalar field inside the box, including those with a scalar condensate floating above the horizon, to understand which phase is thermodynamically preferred.

1.5 Pseudospectral methods

Fundamentally, the numerical computation of quasinormal modes boils down to the computation of the eigenvalues of a coupled system of differential equations. As a result there are as many ways to find QNMs as there are ways to find eigenvalues. We refer the reader to [43, 42] for comprehensive reviews of the numerical methods traditionally used to compute QNMs. In this thesis we will use *pseudospectral collocation methods*, a highly accurate general-purpose method for solving differential equations, in combination with two complementary ways to reduce non-linear ODEs/eigenvalue problems to a linear problem. While pseudospectral methods

have been a mainstay of domains such as fluid dynamics since the 1970s [155], they have only much more recently been applied to gravitational problems. We will briefly review these techniques in this section. For further details and examples, see the review [156] or [157–165].

1.5.1 Pseudospectral collocation

Here, we will give a brief review of pseudospectral collocation methods and a comparison to finite differences. An excellent introduction to the subject is the book by Trefethen [155]. Recall that in a (symmetric) finite difference scheme of order N, we approximate the derivative at each point by the average of the Nth order Taylor expansion to the left and to the right. For example, for a second-order method we first expand $f(x)$ as

$$f(x_{i+1}) = f(x_i) + \Delta x f'(x_i) + (\Delta x)^2 f''(x_i) + \mathcal{O}(\Delta x^3), \tag{1.30}$$
$$f(x_{i-1}) = f(x_i) - \Delta x f'(x_i) + (\Delta x)^2 f''(x_i) + \mathcal{O}(\Delta x^3), \tag{1.31}$$

where Δx is the grid spacing. Solving each equation for $f'(x_i)$, and then taking the average yields the central finite difference formula

$$f'(x_i) = \frac{f(x_{i+1}) - f(x_{i-1})}{2\Delta x} + \mathcal{O}\left(\Delta x^2\right). \tag{1.32}$$

To express this as a matrix operator, note that each row i of the derivative matrix corresponds to $f'(x = x_i)$. We evaluate $f(x)$ in the right hand side of (1.32) by substituting in the Kronecker delta $f(x_i) = \delta_{ij}$ and evaluating the resulting expression for all i, j. The resulting derivative matrix is

$$D^{\mathrm{FD}}_{ij} = \frac{1}{2\Delta x} \begin{bmatrix} & & & & & & & \\ \ddots & \ddots & \ddots & & & & & \\ & -1 & 0 & 1 & & & & \\ & & -1 & 0 & 1 & & & \\ & & & -1 & 0 & 1 & & \\ & & & & \ddots & \ddots & \ddots & \\ & & & & & & & \end{bmatrix}_{ij}. \tag{1.33}$$

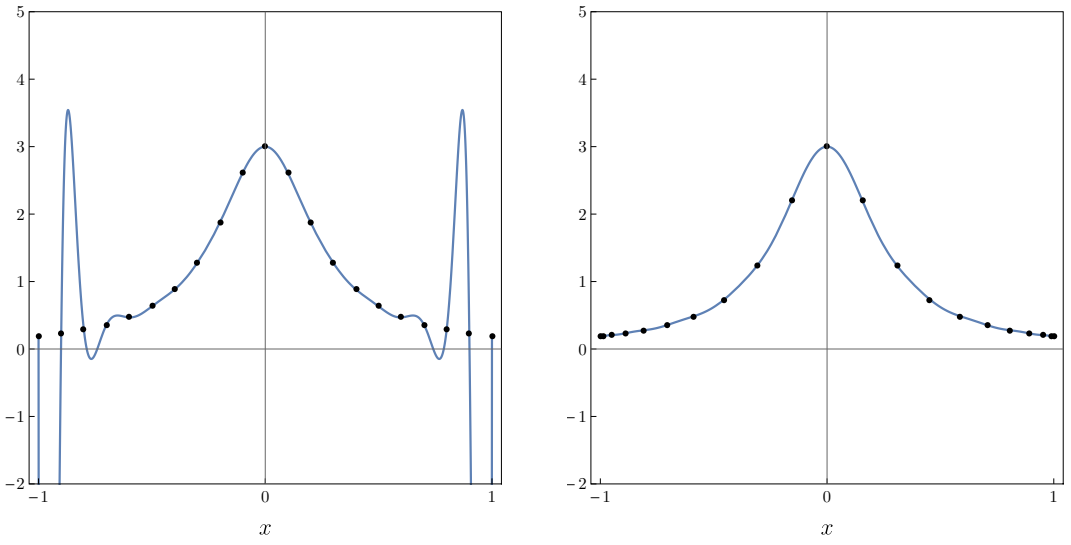

Fig. 1.2: The Runge function $\frac{3}{1+15x^2}$ evaluated at uniformly spaced points (left) and Chebyshev points (right). The blue curve is a polynomial interpolation. Note the clustering of the Chebyshev points near the boundaries in the right plot.

Strictly speaking, this derivative matrix is only valid for periodic domains, otherwise we would have to use one-sided derivatives at the boundaries. However the Chebyshev derivatives later will be specialised to non-periodic domains, hence the nomenclature *pseudospectral*, rather than simply *spectral*. The fact that the finite difference matrix D^{FD} is sparse is characteristic of the local nature of finite differences — we are only using information about the neighbouring grid points. One could use a finite difference method of extremely high order to get a dense matrix, but we will see that pseudospectral methods are a more sophisticated and practical way to achieve a dense matrix that uses information about the whole grid.

Suppose that $f(x)$ has been evaluated at n grid points x_j. In pseudospectral methods, we fit an $(n-1)$-th order polynomial $p(x)$, such that $p(x_j) = f(x_j)$ for all $j = 1, \ldots, n$. Then, we use the analytically computed derivatives $p'(x)$ to estimate $f'(x)$. As one would expect, this gives us *numerically exact* results when $f(x)$ is a polynomial (with enough grid points). For analytic functions we get exponential convergence in the number of grid points. This rapid convergence for analytic functions is what makes (pseudo-)spectral methods so useful.

Let's see how this works in practice. Polynomial interpolation on a uniformly spaced grid suffers from the *Runge phenomenon*, where even a smooth function can have very large and oscillatory interpolation errors at the boundaries, increasing as the number of grid resolution increases, see Fig. 1.2. Instead, we use points which cluster at the boundaries and minimise this error, in particular the Chebyshev

points

$$x_j = \cos\left(\frac{j\pi}{N}\right), \qquad j = 0, 1, \ldots, N \tag{1.34}$$

which have the range $[-1, 1]$ but can be scaled linearly as necessary. The Chebyshev points also have the incidental advantage of sampling $f(x)$ more near the boundaries, which is typically where interesting phenomena occur. For more details about why these specific points are optimal, see [155]. A set of n points uniquely specifies an interpolating polynomial $p(x)$ of order $n - 1$.

In Lagrange form, the unique interpolating polynomial for $f(x)$ evaluated at each point $x = x_j$ is

$$P(x) = \sum_{j=1}^{n} f(x_j)\, p_j(x), \qquad p_j(x) \equiv \prod_{\substack{k=1 \\ k\neq j}}^{n} \frac{x - x_k}{x_j - x_k}. \tag{1.35}$$

Taking the log derivative of each $p_j(x)$ and evaluating at $x = x_i$, the derivative of the interpolating polynomial is

$$P'(x_i) = \sum_{j=1}^{n} f(x_j)\, p_j'(x_i), \qquad p_j'(x_i) = p_j(x_i) \sum_{\substack{k=1 \\ k\neq j}}^{n} \frac{1}{x_i - x_k}. \tag{1.36}$$

As with finite differences, the entries of the derivative matrix can be found by substituting in the Kronecker delta $f(x_i) = \delta_{i\,j}$ for all i, j. This kills the first sum in $P'(x_i)$. The entries of the Chebyshev derivative matrix are therefore

$$D_{ij} \equiv P'(x_i) = p_j(x_i) \sum_{\substack{k=1 \\ k\neq j}}^{n} \frac{1}{x_i - x_k}. \tag{1.37}$$

Note that, for practical computation, one can simplify this further to get an explicit form for the diagonal and non-diagonal entries of D_{ij} that is more numerically stable, see [155]. The Chebyshev derivative matrix D is dense. We are using information about all of the points on the grid to compute each D_{ij} and so we expect this to be much more accurate than a finite difference derivative of low order. Provided that the function is analytic, we achieve exponential convergence in the number of grid points. On top of this rather theoretical asymptotic convergence rate, the practical performance is excellent, see [155, 166] for many examples of this.

To solve a single homogenous ODE of the form $\mathcal{L}y = 0$ numerically, we discretise y on a grid of Chebyshev points (1.34), replacing derivatives in $\mathcal{L}$ with the appropriate

derivative matrix, with entries given by (1.37). We have then converted the ODE into a linear system of equations. It is straightforward to generalise this method to a system of linear homogeneous ODEs. Consider a pair of linear ODEs with operators $\mathcal{L}$ and $\mathcal{S}$ acting on x and y. Without loss of generality, we can split the operators into terms which act on x and y, and then write it as a block matrix equation

$$\begin{aligned} \mathcal{L}_1 x + \mathcal{L}_2 y &= 0 \\ \mathcal{S}_1 x + \mathcal{S}_2 y &= 0 \end{aligned} \qquad \Longrightarrow \qquad \begin{bmatrix} \mathcal{L}_1 & \mathcal{L}_2 \\ \mathcal{S}_1 & \mathcal{S}_2 \end{bmatrix} \begin{bmatrix} x \\ y \end{bmatrix} = 0. \tag{1.38}$$

Discretising each of the operators blockwise, we have reduced a coupled system of ODEs to a single matrix equation for $[x\ y]^{\mathrm{T}}$.

However, to ensure that a solution exists, *i.e.* the matrix is invertible, we must impose boundary conditions. To impose Dirichlet or Neumann boundary conditions, one can simply follow the same discretisation procedure as above, except only applying it to the relevant row of the matrix operator. For example, to apply Neumann boundary conditions at $x = 1$ we replace the first row of the discretisation of $\mathcal{L}y = 0$ with the first row of the discretisation of $y'(x) = 0$.

If we simply need to solve a system of linear ODEs with Dirichlet of Newmann boundary conditions, we can just solve the resulting matrix equation using *e.g.* Mathematica's *LinearSolve*, and we are done. Unfortunately, none of the problems we are interested in here are so simple. We need to solve either coupled systems of non-linear ODEs, or quadratic eigenvalue problems subject to QNM boundary conditions. For both of these we need to use some numerical methods to convert them into a suitable form for pseudospectral discretisation.

We will focus on QNM problems, *i.e.* quadratic eigenvalue problems, and then return to non-linear ODEs at the end. To impose QNM boundary conditions numerically, we take a different approach to that of Dirichlet or Neumann boundary conditions. We redefine the radial function by factoring out the desired asymptotic behaviours (1.16) at the two boundaries. In Kerr-Newman, we make the redefinition

$$R(r) = e^{i\,\omega\, r} \left(\frac{r_+}{r}\right)^{1-2i\omega M} \left(1 - \frac{r_+}{r}\right)^{-i\,\frac{\omega - m\Omega(r_+)}{2\kappa_+}} \chi(r). \tag{1.39}$$

Because pseudospectral collocation methods are only able to converge to smooth functions, any $\chi(r)$ that is convergent must correspond to an $R(r)$ that satisfies QNM boundary conditions. A similar procedure can be applied to the angular equation, where we typically impose regularity at the north and south poles. For

simplicity we will ignore the angular equation, and focus on the radial part. The explicit details will be given in the relevant chapter.

After this redefinition, we have to solve an eigenvalue problem, with eigenvalue ω and eigenfunction $\chi(r)$. In particular, we have a quadratic eigenvalue problem, since ω appears up to second order. Let us represent it as the abstract linear homogeneous ODE $\mathcal{L}y(x) = 0$. For a quadratic eigenvalue problem, we can group the terms in $\mathcal{L}$ according their power of ω,

$$\mathcal{L} \equiv \omega^2 D_{(2)} - \omega D_{(1)} + D_{(0)}, \tag{1.40}$$

for some linear differential operators $D_{(i)}$. We now describe two ways to solve this numerically.

1.5.2 Direct eigenvalue approach

The direct eigenvalue approach is simply the trick of rewriting $\mathcal{L}y = 0$ as a system of equations [166]:

$$\underbrace{\begin{bmatrix} D_{(0)} & \omega D_{(2)} \\ 0 & D_{(1)} \end{bmatrix}}_{\tilde{D}} \underbrace{\begin{bmatrix} y \\ \omega y \end{bmatrix}}_{\tilde{y}} = \omega D_{(1)} \begin{bmatrix} y \\ \omega y \end{bmatrix}. \tag{1.41}$$

The first row is the original equation and the second is identically true. This matrix equation is now a standard generalised eigenvalue problem $\tilde{D}\tilde{y} = \omega D_{(1)}\tilde{y}$. After discretising the differential operators using pseudospectral method, we can solve this using any standard eigenvalue solver. We will use Mathematica's *Eigensystem*.

One issue with this approach is that discretisation errors result in *spurious eigenvalues*, which are unphysical and must be removed. As the precision or grid resolution is increased they do not converge to a fixed value, but instead vary rapidly. The simplest way to filter them out is by solving the eigenvalue problem multiple times, at different resolutions or precisions, removing any eigenvalues that have not converged to within some tolerance. For our purposes it is typically sufficient to use two grid resolutions, one 20 grid points larger than the other, both at the same numerical precision.

1.5.3 Newton-Raphson approach

An alternative to the direct eigenvalue method described above is to start with a nearby seed eigenvalue and eigenvector and use an analogue of Newton-Raphson iteration to converge on the correct solution. Recall that in a single iteration of Newton-Raphson, we take a possibly non-linear function $f(x)$ and linearise it

$$f(x_{i+1}) - f(x_i) = f'(x_i)\,\Delta x + \dots \tag{1.42}$$

where $\Delta x = x_{i+1} - x_i$. Assuming that x_{i+1} is sufficiently close to a root $f(x_{i+1}) \simeq 0$, we can rearrange this to get the Newton-Raphson formula

$$x_{i+1} = x_i - \frac{f(x_i)}{f'(x_i)}. \tag{1.43}$$

We can generalise this to solve differential equations $\mathcal{L}[y] = 0$ by instead taking the functional derivative[11] of $\mathcal{L}$ and assuming that $\mathcal{L}[y^{(i+1)}] \simeq 0$,

$$-\mathcal{L}[y^{(i)}] = \frac{\delta \mathcal{L}}{\delta y}[y^{(i)}]\,\delta y + \dots \tag{1.44}$$

where $\delta y = y^{(i+1)} - y^{(i)}$. Now consider the quadratic eigenvalue form of $\mathcal{L}$ given in (1.40). To find the eigenvalue, we view ω as an independent variable with its associated variation. Due to the linearity of $\mathcal{L}$ in y its variation with respect to y is trivial to compute. The linearisation of quadratic eigenvalue problem (1.40) is

$$-\mathcal{L}[\omega^{(i)}, y^{(i)}] = \mathcal{L}[\omega^{(i)}, y^{(i)}]\,\delta y + \frac{\partial \mathcal{L}}{\partial \omega}[\omega^{(i)}, y^{(i)}]\delta\omega. \tag{1.45}$$

The addition of the variable ω means that we need to impose another boundary condition to get a unique solution, consistent with the fact that the eigenvectors are unique up to an overall scale factor. To fix the normalisation we impose an additional boundary condition on the eigenvector. If one can guarantee that the eigenvector should not vanish at some point $x = x_0$, the simplest normalisation to impose is that $y(x_0) = 1$, which is an additional equation that we linearise by the same approach as $\mathcal{L}$. Other more flexible normalisations are possible, such as fixing the normalisation of $y(x)$ using an integral condition, see [166] for a further

[11] When we say functional derivative, we are referring to the discrete analogue $\frac{\delta y(x_i)}{\delta y(x_j)} = \delta_{ij}$ since we will eventually discretise $y(x)$ on a grid.

discussion. The resulting system of equations is

$$\begin{bmatrix} \mathcal{L}[\omega^{(i)}, y^{(i)}] & \frac{\partial \mathcal{L}}{\partial \omega}[\omega^{(i)}, y^{(i)}] \\ -\delta_{0i} & 0 \end{bmatrix} \begin{bmatrix} \delta y \\ \delta \omega \end{bmatrix} = - \begin{bmatrix} \mathcal{L}[\omega^{(i)}, y^{(i)}] \\ y^{(i)}(x_0) \end{bmatrix} \tag{1.46}$$

Starting with a seed $(y^{(i)}, \omega^{(i)})$, we iteratively solve the linear set of equations (1.46), updating the eigenvalue $\omega^{(i)}$ and eigenvector $y^{(i)}$

$$y^{(i+1)} = y^{(i)} + \delta y, \qquad \omega^{(i+1)} = \omega^{(i)} + \delta \omega, \tag{1.47}$$

until the eigenvalue corrections $|\delta\omega^{(i)}|$ are sufficiently small. Note that we solve (1.46) directly, as a linear system, rather than inverting the left hand side, since this is faster and more accurate in practice [166].

This functional form of Newton-Raphson has the advantage of being much faster than the direct eigenvalue method at finding a single eigenvalue. The obvious disadvantage is that it requires a sufficiently close seed to converge. The seed will typically be eigendata from a nearby point in the parameter space, or from an analytic approximation. In this case, provided the step size is sufficiently small, the Newton-Raphson approach guarantees that the new eigenvalue found is continuously connected to the seed. As we will see, this is particularly useful for tracking modes from one end of the parameter space to the other in order to identify them with their limiting behaviour.

While we have described the Newton-Raphson method as a way to solve non-linear eigenvalue problems, it is also a very powerful way to solve coupled systems of non-linear ODEs (or PDEs), such as those which arise when trying to find stationary solutions of the Einstein equations coupled to some form of matter. In fact, we will use this method in Chapter 4 to solve a system of ODEs that describes static solutions of the Einstein-Maxwell-Scalar system with a non-vanishing scalar field. In the next chapter, we use these numerical methods to study the scalar QNM spectra of Kerr-Newman black holes, which are described by a coupled quadratic eigenvalue problem.

Chapter 2

Eigenvalue repulsions in Kerr-Newman

In this chapter we study the quasinormal (QNM) spectrum of the Kerr-Newman (KN) black hole [4, 5]. As discussed in the introduction, Kerr-Newman is the most general stationary, axisymmetric and asymptotically flat electro-vacuum black hole solution of the Einstein-Maxwell equations [6–8]. In the limiting cases of Schwarzschild ($a = Q = 0$) [39], Kerr ($Q = 0$) [14] and Reissner-Nordström ($a = 0$) [40, 41], the quasinormal mode spectrum has been known for a long time [167–175, 78, 176, 48, 177–181, 57], since the perturbation equations reduce to a system of two coupled ordinary differential equations [167–169, 175]. However, while the theoretical basis for a computation of the QNM spectrum of Kerr-Newman was set out in the 1980s, when Chandrasekhar reduced the equations governing gravito-electromagnetic perturbations to a system of two coupled partial differential equations [176] (see also [182, 18] for a gauge invariant derivation of this system), a numerical computation of the QNMs remained an open problem for several decades, due to a lack of further separability.

The gravito-electromagnetic QNM spectrum of Kerr-Newman was finally computed in [182], but it focused attention on the near-extremal part of the parameter space most relevant to search for linear mode instabilities (which are not present [182])[1]. Recently, efficiency improvements have made a full KN parameter space search feasible, and these results have been used to construct templates that model existing gravitational wave data, to constrain the range of remnant charge in a binary merger [16–18]. In these later studies of KN [16, 18], a surprising phenomenon

[1]Recent advances towards a proof of stability of the full linear problem, with the assumption of linear mode stability, have been made in [183].

– called *eigenvalue repulsion* – was observed. This phenomenon is common in some eigenvalue problems of quantum mechanical systems where it is also known as *level repulsion*, *avoided crossing* or *Wigner-Teller effect* [184, 185]. Typically, two different QNM families of a black hole can have eigenfrequencies that may simply cross in the real or imaginary plane (but not in both), but they do not interact in any way. However, in KN an intricate interaction between the gravito-electromagnetic $\ell = m = 2$ modes was observed, where in certain parts of the parameter space the frequencies of two QNM families approach in the complex plane very closely, without crossing (i.e. without matching in frequency), before repelling violently and moving apart again. These repulsions are very strongly dependent on the black hole parameters (M, a, Q) – a relatively minor change of the black hole parameters can cause the repulsion to be absent – and hence are crucial to understanding the structure of the QNM spectrum in KN and how the latter bridges the Reissner-Nordstöm and Kerr cases to solve some puzzling properties of the QNM spectra of the latter two. This full understanding will be completed only after the present study since scalar modes behave qualitatively similarly to the gravito-electromagnetic modes but are much easier to explore.

Eigenvalue repulsions have also recently been observed in several black hole spacetimes, including charged and rotating de Sitter black holes in higher dimensions, as we discuss in the next chapter [145, 186]. However, they have not been observed in studies of (four-dimensional) Schwarzschild, RN or Kerr [167–175, 78, 176, 48, 177, 178, 180, 181, 57]. In section 2.3.1, we review a first-principles argument that explains why eigenvalue repulsions are more likely to occur in black hole families with two or more dimensionless parameters [18].

Despite recent technical advancements, the computation of gravito-electromagnetic perturbations remains numerically costly. Although gravito-electromagnetic perturbations on KN do not separate, scalar (and Dirac) perturbations are separable, and reduce to a pair of ODEs for the radial and angular components. Thus, in this chapter, we study the scalar QNM spectra for the full parameter space of KN in fine detail to better understand the phenomena of eigenvalue repulsions. Typically, it is the dominant (*i.e.* slowest decaying) quasinormal mode that is of interest, however we take advantage of the reduced numerical complexity to also compute several sub-dominant radial overtones (often denoted by integer $n \geqslant 0$). This is necessary for a complete understanding of the QNM spectra, as one consequence of eigenvalue repulsions is that modes trade dominance in a highly non-trivial way as we move around the parameter space near extremality. We focus our study on scalar QNMs with harmonic numbers $m = \ell = 2$ because these are the dominant

modes in the gravito-electromagnetic sector and we want to use the scalar field as a proxy for the latter case, but we also study the ground state scalar QNMs with $m = \ell = 0$ because they are the dominant scalar modes, and provide an example where eigenvalue repulsions are *not* present (here ℓ is the wave quantum number that is related to the number of nodes in the angular eigenfunction along the polar direction and m is the azimuthal quantum number).

As discussed in section 1.1, there are two families of QNMs present in Reissner-Nordström, namely the *photon sphere* (PS) modes (also denoted as *damped modes* in [57–59]) and *near-horizon* (NH) modes (a.k.a *near-extremal* or *zero-damped* modes) [77–82, 57, 58, 83, 59, 84, 16, 18, 55, 85].

The photon sphere modes can be captured in the eikonal limit, *i.e.* the leading-order WKB approximation where $|m| = \ell \to \infty$. As can be seen from the PS mode formula (1.19), the real part is $\mathcal{O}(|m|)$ and the imaginary part is $\mathcal{O}(1)$. In section 2.2 we perform a WKB expansion, beyond the eikonal result, by a further three orders in $\mathcal{O}(|m|)$, significantly improving the accuracy for the small values of $|m|$ and ℓ that one typically considers. To the best of our knowledge, this extension has never been done for the QNMs of KN although it is a standard higher-order WKB analysis first discussed in the context of QNMs by Will and Guinn [187] and reduces to the higher-order WKB results of [70–73] in the Schwarzschild, RN and Kerr limits.

We capture the NH modes by performing a matched asymptotic expansion (MAE) that is similar to the one performed in [77, 78, 57–59]. We first solve for the eigenfunction near the horizon, then for the eigenfunction far from the horizon, before matching the two in the overlap region where both eigenfunctions overlap. As pointed out in [59], the RN PS modes (a.k.a. damped modes in [59]) are very well known in the literature, starting with the WKB analysis of [72]. However, the existence of the RN NH modes (a.k.a. zero-damped modes in [59]) seem to have been missed till the work of [59] in spite of the seminal work of Teukolsky and Press [77] already suggesting that such a family might or should be present in any black hole with an extremal configuration. To the best of our knowledge, the scalar field NH QNMs of RN are first computed exactly (within numerical accuracy) here (see Fig. 2.6); the gravito-electromagnetic NH QNMs of RN were computed in [59].

Given a QNM in any part of the parameter space of RN, we *can* uniquely classify it (but would not need to) as either a photon sphere mode or a near-horizon mode by tracing it to the extremal limit, where it agrees with either the WKB or MAE approximation of the PS or NH modes of RN. As we add angular momentum to the

system (while simultaneously decreasing the charge, so that the black hole remains subextremal) and move along the KN space to approach the Kerr configuration, the situation is more complicated. Depending on the harmonic wave numbers m and ℓ, the two QNM families may interact in some part of the parameter space. Namely, the curves describing the imaginary part of the two frequencies can merge and bifurcate again (but in a different way) to form QNM families that can no longer be clearly identified as PS or NH modes, since they are often well approximated by both the WKB and the near-horizon matched asymptotic expansion (possibly with a higher radial overtone). Whether this is the case or not depends on the angular momentum quantum numbers m and ℓ of the perturbation. The precise set of values of m and ℓ for which the NH modes are an independent family of the PS modes have been partially studied previously in [58, 69, 57]. To complement this analysis and get a deeper understanding of this transition, we will do a first-principles analysis (later explored in more detail in Chapter 3) that finds that the boundary between the two behaviours can be approximately determined by finding the case where modes start violating the effective AdS_2 Breitenlöhner-Freedman mass bound that characterizes scalar perturbations of the near-horizon geometry of extremal Kerr-Newman.

We then focus our detailed discussion on two important representatives cases: $m = \ell = 2$, for which the PS and NH modes get entangled and lose their original independence (that they had in the RN limit), and $m = \ell = 0$ for which both families remain independent and clearly distinguishable as we span the KN parameter space. The $m = \ell = 2$ case (as a representative element of its class) is particularly interesting since the two families of QNM that exist in the RN limit, unlike in the $\ell = m = 0$ case, become a *single* one in the Kerr limit (that we can denote as a combined PS-NH family, with its radial overtones); see Fig. 2.15. Thus the KN spectra and its eigenvalue repulsions will help us understand a long puzzling fact. Namely, for example when $\ell = m = 2$, how can it be that we start with *two distinct* QNM families of damped and zero-damped modes (and their tower of overtones) in RN (Fig. 2.6) and end up with a single QNM family of zero damped modes (and its tower of overtones) in Kerr (Fig. 2.15)? (This is to be contrasted, e.g. with the $m = \ell = 0$ case where we start with two QNM families in RN and end up with the same two QNM families in Kerr; see Fig. 2.19.)

In more detail, the aim of this chapter is to connect the RN and Kerr QNM spectra explicitly, while navigating through the eigenvalue repulsions that settle in the way. Starting with the two QNM families in RN, we track how they change as we increase the rotation and/or vary the charge, until we reach either the Kerr

limit or the extremal limit of Kerr-Newman. While the PS and NH modes are unambiguously discernible in the RN limit, as stated above, these distinctions are often blurred by eigenvalue repulsions as we turn on angular momentum. We will study the KN QNM spectra with a focus on the $m = \ell = 2$ modes which are most closely analogous to the gravito-electromagnetic modes in [16, 18] (most likely because $m = \ell = 2$ then equals the spin of gravitational perturbations) but also the $m = \ell = 0$ modes since these are the dominant spin-0 modes. Overall, our study is complementary to [57–59, 55, 85] and it offers a fresh perspective of the RN/KN/Kerr QNM spectra, identifies and studies the features of eigenvalue repulsions and helps understanding the Kerr QNM spectra when coming from the RN QNM spectra.

The plan of this chapter is as follows. In the next section we introduce a novel "polar parameterisation" of the Kerr-Newman parameter space, which has the advantage of allowing us to smoothly transition between the RN and Kerr limits while always keeping at the same 'distance' from extremality. We also formulate the scalar QNM eigenvalue problem including its boundary conditions. In section 2.2, we first review the well-known eikonal limit of the QNM problem in Kerr-Newman (section 2.2.1.1), which is universal to any perturbation spin and defines the photon sphere family of modes. We then proceed beyond this leading WKB order and derive a high-order WKB expansion of the scalar field QNM spectrum (section 2.2.1.2), which is novel and necessarily more accurate for finite m (in a wide neighbourhood about the Reissner-Nordström and Kerr solutions) than the eikonal approximation. We also perform a near-horizon matched asymptotic expansion that identifies the near-horizon family of modes (section 2.2.2). In section 2.3, after reviewing a first-principles analysis of the phenomenon of eigenvalue repulsion (section 2.3.1), we compute the exact $m = \ell = 2$ spectra of KN QNMs (using numerical methods), focusing on the near-extremal region where eigenvalue repulsions often blur the distinction between the photon sphere and near-horizon QNM families (section 2.3.2). We then discuss the full KN spectrum, for both $m = \ell = 2$ and $m = \ell = 0$ modes, in section 2.4.

2.1 Klein-Gordon equation in the Kerr-Newman background

2.1.1 KN black hole and its polar parameterization

The Kerr-Newman black hole was briefly reviewed in the introduction. Here we provide the explicit details necessary for a study of the QNM spectra. Recall that, as was given in (1.5), the metric and Maxwell potential in Boyer-Lindquist coordinates (t, r, θ, ϕ) take the form

$$\begin{aligned} \mathrm{d}s^2 &= -\frac{\Delta}{\Sigma}\left(\mathrm{d}t - a\sin^2\theta \mathrm{d}\phi\right)^2 + \frac{\Sigma}{\Delta}\mathrm{d}r^2 + \Sigma\,\mathrm{d}\theta^2 + \frac{\sin^2\theta}{\Sigma}\left[\left(r^2+a^2\right)\mathrm{d}\phi - a\mathrm{d}t\right]^2, \\ A &= \frac{Q\,r}{\Sigma}\left(\mathrm{d}t - a\sin^2\theta\mathrm{d}\phi\right), \end{aligned} \tag{2.1}$$

with $\Delta = r^2 - 2Mr + a^2 + Q^2$ and $\Sigma = r^2 + a^2\cos^2\theta$. We will find it convenient to work with the angular coordinate $x = \cos\theta$ with range $x \in [-1, 1]$.

The roots of the function $\Delta(r)$ correspond to the inner (r_-) and outer (r_+) horizons, $r_- \leqslant r_+$. We can solve $\Delta(r_+) = 0$ with respect to M to find that

$$M = \frac{r_+^2 + a^2 + Q^2}{2r_+}. \tag{2.2}$$

Moreover, the system has a scaling symmetry that allows one to write all physical quantities in units of r_+ (or M).[2] Thus the KN black hole is effectively a 2-parameter family of solutions that we can parametrize by the dimensionless quantities

$$\alpha = \frac{a}{r_+}, \qquad \tilde{Q} = \frac{Q}{r_+}. \tag{2.3}$$

The outer event horizon $(r = r_+)$ is a Killing horizon generated by the Killing vector $K = \partial_t + \Omega_H\partial_\phi$, with angular velocity Ω_H and temperature T_H given by

$$\tilde{\Omega}_H \equiv \Omega_H r_+ = \frac{\alpha}{1+\alpha^2}, \qquad \tilde{T}_H \equiv T_H r_+ = \frac{1}{4\pi}\frac{1-\alpha^2-\tilde{Q}^2}{1+\alpha^2}. \tag{2.4}$$

[2]The scaling symmetry is $\{t, r, \theta, \phi\} \to \{\lambda t, \lambda r, \theta, \phi\}$ and $\{r_+, a, Q\} \to \{\lambda\, r_+, \lambda\, a, \lambda Q\}$ which rescales the metric and Maxwell potential as $g_{ab} \to \lambda^2\, g_{ab}$ and $A_a \to \lambda\, A_a$ but leaves the equations of motion invariant (since the affine connection $\Gamma^c{}_{ab}$, and the Riemann $(R^a{}_{bcd})$, Ricci (R_{ab}) and energy-momentum (T_{ab}) tensors are left invariant).

If $r_- = r_+$, *i.e.* $\alpha = \alpha_{\rm ext} = \sqrt{1-\tilde{Q}^2}$, the KN BH has a regular extremal ("ext") configuration with $T_H^{\rm ext} = 0$, and maximum angular velocity $\tilde{\Omega}_H^{\rm ext} = \alpha_{\rm ext}/(1+\alpha_{\rm ext}^2)$.

Finally, for our purposes, we will find it very enlightening to parametrize the KN black hole by "polar" parameters. For that, we first define the parameter $\mathcal{R}(\sigma)$ as:

$$\sigma = 1 - \frac{r_-}{r_+} = 1 - \alpha^2 - \tilde{Q}^2\,, \qquad \mathcal{R} = \sqrt{1-\sigma}\,, \tag{2.5}$$

and we then introduce the polar parameterisation

$$\alpha = \mathcal{R}\,\sin\Theta\,, \qquad \tilde{Q} = \mathcal{R}\,\cos\Theta\,. \tag{2.6}$$

This parameterisation $(\mathcal{R},\Theta)$ has the property that $\mathcal{R}$ is an off-extremality radial measure (since it vanishes in the Schwarzschild limit and attains its maximum value of $\mathcal{R}=1$ at extremality), while the polar parameter Θ ranges between the Reissner-Nordström solution (where $\Theta = 0$ and thus $\alpha = 0$) and the Kerr solution (where $\Theta = \pi/2$ and thus $\tilde{Q} = 0$). So, with this parameterisation we will be able to follow a family of KN black holes that starts at the Reissner-Nordström solution ($\Theta = 0$) and evolves in Θ towards the Kerr solution ($\Theta = \pi/2$) while staying always at fixed distance from extremality (*i.e.* at fixed $\mathcal{R}$).

2.1.2 Klein-Gordon equation and boundary conditions of the problem

We are interested in studying massless scalar field perturbations in the KN background which are described by the Klein-Gordon equation $\Box\,\Phi = 0$. Since ∂_t and ∂_ϕ are Killing vectors of the KN background we can perform a Fourier decomposition of the modes along these directions, which introduces the frequency ω and azimuthal quantum number $m \in \mathbb{Z}$. We make the same separability ansatz as before (1.8), except using $x = \cos\theta$ for the polar variable,

$$\Phi = e^{-i\omega t} e^{im\phi} R(r) S(x)\,. \tag{2.7}$$

In this case the Klein-Gordon equation separates into a set of radial and angular ODEs:

$$\frac{d}{dr}\left(\Delta\,\frac{dR}{dr}\right) + \left[\frac{\left[(r^2+a^2)\,\omega - m\,a\right]^2}{\Delta} + 2ma\omega - a^2\omega^2 - \lambda\right] R = 0, \tag{2.8a}$$

$$\frac{d}{dx}\left((1-x^2)\,\frac{dS}{dx}\right)+\left(-a^2\omega^2(1-x^2)-\frac{m^2}{1-x^2}+a^2\omega^2+\lambda\right)S=0, \qquad (2.8b)$$

where λ is the separation constant of the problem.

The angular equation (2.8b) is a standard oblate spheroidal harmonic equation, namely $[(1-x^2)\,S']'+\left[\gamma^2\,(1-x^2)-\frac{m^2}{1-x^2}+\Lambda\right]S=0$ with $\gamma\equiv i\,a\,\omega$ and $\Lambda\equiv\lambda+a^2\omega^2$, whose regular solutions are given by the oblate spheroidal harmonics $S=S^m_\ell(\gamma;x)$. Here, ℓ is a non-negative integer that essentially gives the number of zeros of the eigenfunction along the polar angle and regularity at the north and south poles ($x=\pm1$) requires that m is an integer that obeys the constraint $|m|\leqslant\ell$.

To solve the coupled ODEs (2.8a)-(2.8b), we need to impose the QNM boundary conditions for an asymptotically-flat spacetime (1.16). A Frobenius analysis of (2.8a) yields the two independent asymptotic solutions for large r:

$$R\big|_\infty\simeq A_{out}e^{i\,\omega\,r}\left(\frac{r_+}{r}\right)^{1-i\,\frac{\omega}{r_+}\left(r_+^2+a^2+Q^2\right)}(1+\cdots)+A_{in}e^{-i\,\omega\,r}\left(\frac{r_+}{r}\right)^{1+i\,\frac{\omega}{r_+}\left(r_+^2+a^2+Q^2\right)}(1+\cdots)\,, \qquad (2.9)$$

where A_{out} and A_{in} are two arbitrary amplitudes. QNM boundary conditions require that only outgoing waves are permitted. By comparison to (1.16) we see that we must set $A_{in}\equiv0$.

At the event horizon, a Frobenius analysis yields the expansion

$$R\big|_H\simeq B_{in}\,(r-r_+)^{-i\,\frac{\omega-m\Omega_H}{4\pi T_H}}\,(1+\cdots)+B_{out}\,(r-r_+)^{i\,\frac{\omega-m\Omega_H}{4\pi T_H}}\,(1+\cdots)\,,$$

where B_{in} and B_{out} are two arbitrary amplitudes, and Ω_H,T_H are defined in (2.4). We want to keep only the solution that is regular in ingoing Eddington-Finkelstein coordinates (1.6), *i.e.* that excludes outgoing waves across the future event horizon, and by comparison to (1.16) this requires that we set $B_{out}\equiv0$. These two boundary conditions can be automatically imposed if we redefine the radial function as

$$R=e^{i\,\omega\,r}\left(\frac{r_+}{r}\right)^{1-i\,\frac{\omega}{r_+}\left(r_+^2+a^2+Q^2\right)}\left(1-\frac{r_+}{r}\right)^{-i\,\frac{\omega-m\Omega_H}{4\pi T_H}}\chi(r) \qquad (2.10)$$

and search for eigenfunctions $\chi(r)$ that are smooth everywhere in the outer domain of communications.

Similarly, we impose regularity on the angular eigenfunction solutions to (2.8b) at the North and South poles ($x = \pm 1$) by the redefinition

$$S = (1 - x^2)^{\frac{|m|}{2}} Y(x) \tag{2.11}$$

and then solve for smooth eigenfunctions $Y(x)$. After inserting the field redefinitions (2.10) and (2.11) into (2.8a)-(2.8b), we have a coupled eigenvalue problem that is quadratic in ω and linear in λ. To solve this numerically, we first discretise the system using pseudospectral collocation methods and then use the Newton-Raphson method, as described in section 1.5, to march an appropriate seed from one part of the parameter space to another. The numerical results in this chapter are accurate to at least the eighth decimal place.

2.2 Two families of QNM: photon sphere and near-horizon modes

In subsection 2.2.1.1, we review the well-known eikonal limit of the QNM problem in Kerr-Newman, which is independent of the perturbation spin and defines the photon sphere family of modes. Then, in subsection 2.2.1.2 we go beyond this leading WKB order and derive a high-order WKB expansion of the scalar field QNM spectrum, which is novel and necessarily more accurate for finite m (in a wide neighbourhood about the RN and Kerr solutions) than the eikonal approximation. Finally, in subsection 2.2.2, we introduce a near-horizon matched asymptotic expansion that identifies the near-horizon family of modes.

2.2.1 WKB expansion of photon sphere modes

2.2.1.1 Photon sphere modes in the eikonal limit (the leading WKB result)

We will study the eikonal limit of modes with $\ell = m$ or $\ell = -m$ and denote the associated frequency by $\omega_{\rm PS}^{\rm eikn}$. The final analytical formula for these frequencies is strictly valid in the WKB limit $\ell = |m| \to \infty$. That is, it only captures the leading behaviour of a WKB expansion in $1/m$ with $\ell = |m| \to \infty$. This analysis is independent of the spin of the perturbation and was already performed previously in several references in the literature, either for the KN background or

its limiting solutions (Kerr, Reissner-Nordström or Schwarzschild), see *e.g.* [60–63, 65–69, 59, 18]. We review it here because we want to compare our numerical results with the eikonal limit (to identify the nature of some of the modes), and more importantly, in the next subsection we will extend this WKB expansion to higher-orders in a $1/m$ expansion, so it is good to have a self-contained analysis of the leading term at hand.

The geodesic equation that describes the motion of pointlike particles around a KN BH leads to a set of quadratures. This may be an unexpected result given that KN only possesses two Killing fields $K = \partial/\partial_t$ and $\xi = \partial/\partial_\phi$, seemingly one short of leading to an integrable system. There is however another conserved quantity − the Carter constant − associated to a Killing tensor K_{ab}, which rescues the day [176].

The Hamilton-Jacobi equation [176] provides a quick way to identify the integrable structure of the system:

$$\frac{\partial S}{\partial x^\mu}\frac{\partial S}{\partial x^\nu}g^{\mu\nu} = 0\,, \tag{2.12}$$

with S being denoted as the principal function. The motion of null particles is obtained noting that, according to Hamilton-Jacobi's theory, the particle momenta can be obtained from the principal function as

$$\frac{\partial S}{\partial x^\mu} \equiv p_\mu \quad \text{and} \quad p^\mu = \frac{\mathrm{d}x^\mu}{\mathrm{d}\tau}\,, \tag{2.13}$$

where τ is an affine parameter. To proceed, we take a separation *ansatz* of the form (using $x = \cos\theta$ where θ is the polar angle)

$$S = -e\,t + j\,\phi + R(r) + X(x)\,, \tag{2.14}$$

with the constants e and j being the conserved charges associated with the Killing fields K and ξ [3] through

$$e \equiv -K_\mu \dot{x}^\mu \qquad \text{and} \qquad j \equiv \xi_\mu \dot{x}^\mu\,, \tag{2.15}$$

where the dot ($\dot{}$) describes the derivative w.r.t. the affine parameter τ. With (2.14), the Hamilton-Jacobi equation (2.12) for null geodesics yields coupled ODEs for $R(r)$ and $X(x)$ (the prime ($'$) describes a derivative w.r.t. the argument, r or

[3] For massive particles, these coincide with the energy and angular momentum of the particle, but for massless particles e and j have no physical meaning since they can be rescaled. The ratio j/e, however, is invariant under such rescalings.

x, respectively)

$$\Delta^2 R'^2 - \left[e\left(r^2+a^2\right) - aj\right]^2 + \Delta\left[\mathcal{Q} + (j-ae)^2\right] = 0\,, \tag{2.16}$$

$$X'^2 - \frac{(j-ae)^2 + \mathcal{Q}}{1-x^2} + \frac{\left[ae\left(1-x^2\right) - j\right]^2}{\left(1-x^2\right)^2} = 0\,, \tag{2.17}$$

where $\mathcal{Q}$ is Carter's separation constant. Additionally, from (2.13), *i.e.* $\dot{x}^\mu = g^{\mu\nu}\frac{\partial S}{\partial x^\mu}$, one has

$$\begin{aligned}\dot{t} &= \frac{\left(r^2+a^2\right)\left[e\left(r^2+a^2\right) - aj\right] + a\Delta\left[j - ae\left(1-x^2\right)\right]}{\Delta\left(r^2+a^2x^2\right)}\,,\\ \dot{\phi} &= \frac{\left(1-x^2\right)a\left[e\left(r^2+a^2\right) - aj\right] + \Delta\left[j - ae\left(1-x^2\right)\right]}{\Delta\left(1-x^2\right)\left(r^2+a^2x^2\right)}\,.\end{aligned} \tag{2.18}$$

We want null geodesics whose behaviour matches that of large $\ell = |m|$ QNMs, *i.e.* geodesics confined to the equatorial plane $x = 0$. It follows from (2.17) that such geodesics exist only if at $\tau = 0$ one has $X(0) = \dot{X}(0) = 0$ and $\mathcal{Q} = 0$. Introducing the geodesic impact parameter

$$b \equiv \frac{j}{e}, \tag{2.19}$$

the equation (2.16) governing the radial motion can be rewritten as

$$\dot{r}^2 = V(r;b)\,, \tag{2.20}$$

where the potential is

$$V(r;b) = \frac{j^2}{b^2}\left(1 + \frac{a^2-b^2}{r^2} + \frac{2M(b-a)^2}{r^3} - \frac{Q^2(b-a)^2}{r^4}\right). \tag{2.21}$$

We now want to find the photon sphere (the region where null particles are trapped on unstable circular orbits), *i.e.* the values of $r = r_s$ and $b = b_s$, such that

$$V(r_s;b_s) = 0 \quad \text{and} \quad \partial_r V(r;b)\big|_{r=r_s,b=b_s} = 0. \tag{2.22}$$

The first equation allows to find

$$b_s(r_s) = \frac{r_s^2\sqrt{\Delta(r_s)} + a\left(Q^2 - 2Mr_s\right)}{r_s^2 - 2Mr_s + Q^2}\,, \tag{2.23}$$

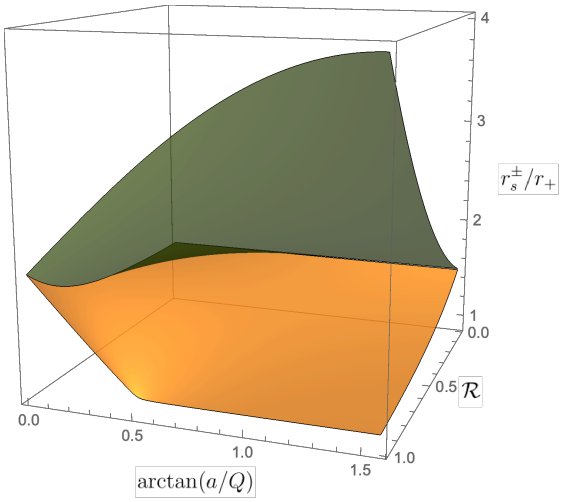

Fig. 2.1: The radii $r_s^{\pm}$ (with $r_s^+ \geqslant r_s^- \geqslant r_+$) of the two unstable circular orbits in the equatorial plane of the KN black hole that ultimately yield the co-rotating $m = \ell$ (in the r_s^- case) and the counter-rotating $m = -\ell$ (in the r_s^+ case) PS QNM frequencies in the eikonal limit.

which is then inserted in the second equation of (2.22) to get (after algebraic manipulations) a fourth order polynomial equation for r_s:

$$4\left[r_s^2 + 2a\left(\sqrt{\Delta(r_s)} + a\right)\right]^2 - \left(3Mr_s + \sqrt{9M^2r_s^2 - 8Q^2\left[r_s^2 + 2a\left(\sqrt{\Delta(r_s)} + a\right)\right]}\right)^2 = 0\,, \tag{2.24}$$

where $\Delta(r)$ is defined below (2.1) and we are interested in solutions with $r_s > r_+$. Alternatively, (2.22) can be solved to get the black hole parameters M and Q that have circular orbits with radius r_s and impact parameter b_s, namely

$$M = \frac{r_s\left(b_s^2 - a^2 - 2r_s^2\right)}{\left(b_s - a\right)^2}\,, \qquad Q = \frac{r_s\sqrt{b_s^2 - a^2 - 3r_s^2}}{\sqrt{\left(b_s - a\right)^2}}\,. \tag{2.25}$$

This system has two real roots r_s larger than r_+, in correspondence with the two PS modes: the *co-rotating* one (with $m = \ell$) which is in correspondence with the eikonal orbit with radius $r_s = r_s^-$ and $b_s > 0$ (and that has the lowest $|\mathrm{Im}\,\tilde{\omega}|$, as we will see) and the *counter-rotating* mode with $m = -\ell$ that maps to the orbit with radius $r_s = r_s^+$ and $b_s < 0$, with $r_s^+ \geqslant r_s^- \geqslant r_+$. The two real roots $r_s^{\pm}$ larger than r_+ are displayed in Fig. 2.1. In the RN $\Theta = \arctan\left(a/Q\right) = 0$ or Schwarzschild $\mathcal{R} = 0$ (*i.e.* $a = 0 = Q$) limits, one has $r_s^+ = r_s^-$, and at extremality ($\mathcal{R} = 1$, *i.e.* $\alpha = \alpha_{\rm ext} = \sqrt{1 - \tilde{Q}^2}$) the co-rotating orbit radius equals the event horizon radius, $r_s^- = r_+$, when $\Theta \geqslant \pi/6 \simeq 0.52$.

Finally, we can compute the orbital angular velocity (a.k.a. Kepler frequency) of the null circular photon orbit, which is simply given by

$$\Omega_0 \equiv \frac{\dot{\phi}}{\dot{t}} = \frac{1}{b_s}\,, \tag{2.26}$$

where we used (2.18) evaluated at $r = r_s$ and $b = b_s$. Moreover, we can also compute the largest Lyapunov exponent λ_L, measured in units of t, associated with infinitesimal fluctuations around photon orbits with $r(\tau) = r_s$. This can be obtained by perturbing the geodesic equation (2.20) with the potential (2.21) evaluated on an orbit with impact parameter $b = b_s$ and setting $r(\tau) = r_s + \delta r(\tau)$. We find that small deviations from the orbit decay exponentially in time as $\delta r \sim e^{-\lambda_L t}$ with Lyapunov exponent given by

$$\begin{aligned}\lambda_L &= \sqrt{\frac{1}{2}\frac{V''(r;b)}{\dot{t}(\tau)^2}}\bigg|_{r=r_s,b=b_s} \\ &= \frac{1}{b_s r_s^2}\sqrt{\frac{\left(r_s^2+a^2-ab_s\right)^2\left(6r_s^2+a^2-b_s^2\right)}{\left(b_s-a\right)^2}}\,.\end{aligned} \tag{2.27}$$

where a prime ($'$) denotes a derivative with respect to r. We finally obtain the approximate spectrum of the photon sphere family of QNMs in the leading WKB limit $\ell = |m| \to \infty$ using the PS mode correspondence (1.19):

$$\begin{aligned}\omega_{\rm PS}^{\rm eikn} &\simeq m\,\Omega_0 - i\left(n+\frac{1}{2}\right)\lambda_L \\ &\simeq \frac{m}{b_s} - i\,\frac{n+1/2}{b_s r_s^2}\frac{|r_s^2+a^2-ab_s|}{|b_s-a|}\sqrt{6r_s^2+a^2-b_s^2}\,,\end{aligned} \tag{2.28}$$

where $n = 0, 1, 2, \ldots$ is the radial overtone. The frequency $\omega_{\rm PS}^{\rm eikn}$ describes the eikonal approximation for the PS modes. This expression is blind to the spin of the perturbation, *i.e.* it is the same for scalar and gravito-electromagnetic perturbations (at higher order in the $1/m$ expansion, the result does depend on the spin; see the next subsection for the scalar field case in KN and the WKB spin dependence for Kerr in [73]).

Strictly speaking, (2.28) is valid only in the geometric optics limit $\ell = |m| \to \infty$, with corrections to $\mathrm{Im}\,\tilde{\omega}$ and $\mathrm{Re}\,\tilde{\omega}$ being of order $\mathcal{O}(|m|)$ and $\mathcal{O}(1)$, respectively. However, in practice we find that it is already a good approximation for $\ell = m = 2$ in a wide window of the KN parameter space centred around the Kerr and Reissner-Nordström limiting solutions. In the next subsection we do a higher-order WKB expansion that finds the corrections to the leading eikonal result (2.28).

2.2.1.2 Photon sphere modes in a WKB expansion: beyond the eikonal limit

The eikonal limit of the previous subsection was first studied by Goebel [60] and Ferrari and Mashhoon [61–63]. Naturally, this eikonal limit is the leading order result of a WKB expansion in $1/m$ in the limit $m \gg 1$ initiated by Schutz and Will [64] and completed for Schwarzschild, RN and Kerr in [70–73]. In this subsection, we extend the WKB expansion of KN QNMs (which is also valid for the sub-families of this black hole) to higher orders to capture the next-to-leading order WKB contributions to the photon sphere QNM frequencies. We will only consider modes with large $\ell = m > 0$. To the best of our knowledge, this extension has never been done for the QNMs of KN although it is a standard higher-order WKB analysis first discussed in the context of QNMs by Will and Guinn [187], and reduces to the higher-order WKB results of [70–73] in the Schwarzschild, RN and Kerr limits. Unlike the leading eikonal WKB result, the next-to-leading order WKB corrections depend on the spin of the perturbation. Our analysis is valid for spin-0 perturbations.

Consider first the angular equation (2.8b) for the oblate spheroidal harmonics $S(x)$. To leading order in $1/m$ (and for modes with $\ell = m$) the leading WKB solution that is regular at $x = \pm 1$ is given by $S(x) = (1-x^2)^{m/2}$ with eigenvalue $\lambda = \ell(\ell+1)$. At higher WKB order, the angular eigenfunction and the angular eigenvalue receive $(1/m)^k$ corrections (with integer $k > 0$). To find them we assume the WKB ansatz for these quantities,

$$S(x) = (1-x^2)^{\frac{m}{2}} \left(1 + \frac{\mathcal{S}_1(x)}{m} + \frac{\mathcal{S}_2(x)}{m^2} + \frac{\mathcal{S}_3(x)}{m^3}\right) + \mathcal{O}\left(1/m^4\right), \tag{2.29a}$$

$$\lambda = \ell(\ell+1) + \frac{\lambda_1}{m} + \frac{\lambda_2}{m^2} + \mathcal{O}\left(1/m^3\right), \tag{2.29b}$$

and we solve the angular equation (2.8b) order by order in a small $1/m$ series expansion to find the WKB coefficients:

$$\mathcal{S}_1(x) = \frac{1}{4}a^2\omega^2x^2, \quad \mathcal{S}_2(x) = \frac{1}{32}a^2\omega^2x^2\left(a^2\omega^2x^2 - 12\right),$$
$$\mathcal{S}_3(x) = \frac{1}{384}a^2\omega^2x^2\left(a^4\omega^4x^4 + 24a^2\omega^2\left(1-2x^2\right) + 216\right); \tag{2.30a}$$

$$\lambda_1 = -\frac{1}{2}a^2\omega^2, \quad \lambda_2 = \frac{3}{4}a^2\omega^2; \tag{2.30b}$$

where the coefficients λ_1 and λ_2 were chosen to be such that $\mathcal{S}_2(x)$ and $\mathcal{S}_3(x)$ are everywhere regular (*i.e.* the choices made eliminate $\ln(x)$ divergences at $x = 0$ at

each order).

Next, we want to solve the radial equation (2.8a) also in a $1/m$ expansion to obtain the higher-order corrections to the leading order solution obtained in the previous subsection. For that, we insert (2.25) and the expansion for λ of (2.29b) and (2.30b) into (2.8a) and we assume the WKB ansatzë for the radial eigenfunction and eigenfrequency

$$\begin{aligned} R(r) &= e^{-m\chi(r)}\left(Q_0(r)+\frac{Q_1(r)}{m}+\frac{Q_2(r)}{m^2}+\mathcal{O}\left(1/m^3\right)\right), \\ \omega &= \frac{m}{b_s}+\omega_0+\frac{\omega_1}{m}+\frac{\omega_2}{m^2}+\mathcal{O}\left(1/m^3\right), \end{aligned} \tag{2.31}$$

where the leading order contribution (m/b_s) to the frequency is the one we already determined in the eikonal limit (2.28). Inserting these WKB ansatzë into the radial equation (2.8a) we can solve the latter order by order in a small $1/m$ series expansion. At each order, the requirement that the radial equation must be valid, in particular at $r = r_s$, yields a condition that allows one to determine the eigenfrequency correction $\omega_{0,1,2}$. Then, before proceeding to the next order, we just need to find the equation of motion for the eigenfunction's correction χ and $Q_{0,1,2}$ (but not the solution itself) to use it at next order. At the end of the day, the WKB frequency coefficients of (2.31) are given as a function of (a, r_s, b_s) by:

$$\omega_0 = -\frac{r_s^2+a^2-ab_s}{4b_s^2r_s^2(b_s-a)}\left(a^2-2b_s^2+2ib_s\sqrt{6r_s^2+a^2-b_s^2}\right), \tag{2.32a}$$

$$\begin{aligned} \omega_1 = {} & \frac{r_s^2+a^2-ab_s}{32b_s^3r_s^4(a-b_s)^3\left(6r_s^2+a^2-b_s^2\right)^2}\Bigg[2a^{11}-10a^{10}b_s+a^9\left(8b_s^2+26r_s^2\right) \\ & +3a^8\left(20b_s^3-37b_sr_s^2\right)+a^7\left(92b_s^2r_s^2-110b_s^4+96r_s^4\right)+a^6\left(486b_s^3r_s^2-50b_s^5-396b_sr_s^4\right) \\ & +2a^5\left(-443b_s^4r_s^2+204b_s^2r_s^4+98b_s^6+36r_s^6\right)-3a^4\left(29b_s^5r_s^2-356b_s^3r_s^4+16b_s^7+180b_sr_s^6\right) \\ & +a^3\left(864b_s^6r_s^2-1976b_s^4r_s^4+864b_s^2r_s^6-96b_s^8\right)+4a^2\left(-84b_s^7r_s^2+112b_s^5r_s^4+77b_s^3r_s^6+12b_s^9\right) \\ & -8a\left(6b_s^8r_s^2-41b_s^6r_s^4+74b_s^4r_s^6\right)+4\left(50b_s^3r_s^8-37b_s^5r_s^6+6b_s^7r_s^4\right) \\ & +4iab_s\sqrt{6r_s^2+a^2-b_s^2}\Bigg(a^8-8a^7b_s+a^6\left(12b_s^2+13r_s^2\right)+a^5\left(14b_s^3-61b_sr_s^2\right) \\ & +a^4\left(77b_s^2r_s^2-37b_s^4+48r_s^4\right)+a^3\left(49b_s^3r_s^2+6b_s^5-150b_sr_s^4\right)+6a^2\Big(-23b_s^4r_s^2+29b_s^2r_s^4+4b_s^6 \\ & +6r_s^6\Big)-12a\left(-4b_s^5r_s^2+b_s^3r_s^4+b_s^7+6b_sr_s^6\right)+12b_s^2r_s^2\left(-5b_s^2r_s^2+b_s^4+6r_s^4\right)\Bigg)\Bigg], \end{aligned} \tag{2.32b}$$

$$\begin{aligned} \omega_2 = {} & \frac{r_s^2+a^2-ab_s}{128b_s^4r_s^6(a-b_s)^5\left(6r_s^2+a^2-b_s^2\right)^5}\Bigg[2a^{22}-20b_sa^{21}+\left(74b_s^2+64r_s^2\right)a^{20} \\ & -2\left(32b_s^3+301r_s^2b_s\right)a^{19}+\left(-670b_s^4+2128r_s^2b_s^2+842r_s^4\right)a^{18} \end{aligned}$$

$$
\begin{aligned}
&+\left(2428b_s^5-2028r_s^2b_s^3-7530r_s^4b_s\right)a^{17}+\left(-654b_s^6-15920r_s^2b_s^4+25383r_s^4b_s^2+5820r_s^6\right)a^{16}\\
&-2\left(4616b_s^7-30185r_s^2b_s^5+12927r_s^4b_s^3+25290r_s^6b_s\right)a^{15}\\
&+\left(11710b_s^8-31432r_s^2b_s^6-147595r_s^4b_s^4+164382r_s^6b_s^2+22320r_s^8\right)a^{14}\\
&+4\left(2857b_s^9-44084r_s^2b_s^7+146495r_s^4b_s^5-44532r_s^6b_s^3-49140r_s^8b_s\right)a^{13}\\
&+\left(-28802b_s^{10}+266496r_s^2b_s^8-443136r_s^4b_s^6-680476r_s^6b_s^4+631512r_s^8b_s^2+45792r_s^{10}\right)a^{12}\\
&+2\left(736b_s^{11}+58709r_s^2b_s^9-599046r_s^4b_s^7+1440568r_s^6b_s^5-368712r_s^8b_s^3-220320r_s^{10}b_s\right)a^{11}\\
&+2\big(15131b_s^{12}-233552r_s^2b_s^{10}+1092082r_s^4b_s^8-1409730r_s^6b_s^6-799010r_s^8b_s^4+719064r_s^{10}b_s^2\\
&+22032r_s^{12}\big)a^{10}-2\big(7590b_s^{13}-73778r_s^2b_s^{11}-30543r_s^4b_s^9+1715704r_s^6b_s^7-3849468r_s^8b_s^5\\
&+907200r_s^{10}b_s^3+260496r_s^{12}b_s\big)a^9+\big(-13338b_s^{14}+307472r_s^2b_s^{12}-2463177r_s^4b_s^{10}\\
&+8094764r_s^6b_s^8-9116984r_s^8b_s^6-1532896r_s^{10}b_s^4+1714608r_s^{12}b_s^2+15552r_s^{14}\big)a^8\\
&+2\big(6216b_s^{15}-114257r_s^2b_s^{13}+673253r_s^4b_s^{11}-1173570r_s^6b_s^9-1560404r_s^8b_s^7+5369000r_s^{10}b_s^5\\
&-1108080r_s^{12}b_s^3-116640r_s^{14}b_s\big)a^7+b_s^2\big(552b_s^{14}-42248r_s^2b_s^{12}+713245r_s^4b_s^{10}-4681810r_s^6b_s^8\\
&+13463880r_s^8b_s^6-14621120r_s^{10}b_s^4+208752r_s^{12}b_s^2+692064r_s^{14}\big)a^6-8b_s^3\big(408b_s^{14}-10395r_s^2b_s^{12}\\
&+99510r_s^4b_s^{10}-438984r_s^6b_s^8+844913r_s^8b_s^6-278048r_s^{10}b_s^4-823092r_s^{12}b_s^2+93312r_s^{14}\big)a^5\\
&+2b_s^4\big(432b_s^{14}-9776r_s^2b_s^{12}+66617r_s^4b_s^{10}-64822r_s^6b_s^8-985532r_s^8b_s^6+4000144r_s^{10}b_s^4\\
&-4892832r_s^{12}b_s^2+362016r_s^{14}\big)a^4-8b_s^5r_s^2\big(128b_s^{12}-4260r_s^2b_s^{10}+45727r_s^4b_s^8-217699r_s^6b_s^6\\
&+473398r_s^8b_s^4-318564r_s^{10}b_s^2-203688r_s^{12}\big)a^3+4b_s^4r_s^2\big(24b_s^{14}-740r_s^2b_s^{12}+5834r_s^4b_s^{10}\\
&-5685r_s^6b_s^8-107628r_s^8b_s^6+462432r_s^{10}b_s^4-612144r_s^{12}b_s^2+82512r_s^{14}\big)a^2\\
&-32b_s^5r_s^4\big(3b_s^{12}-97r_s^2b_s^{10}+1068r_s^4b_s^8-5289r_s^6b_s^6+11814r_s^8b_s^4-7884r_s^{10}b_s^2-5400r_s^{12}\big)a\\
&+8b_s^6r_s^6\left(b_s^2-6r_s^2\right)^3\left(6b_s^4-37r_s^2b_s^2+50r_s^4\right)\\
&+2ib_s\sqrt{6r_s^2+a^2-b_s^2}\Big(2a^{20}-26b_sa^{19}+\left(153b_s^2+64r_s^2\right)a^{18}-\left(362b_s^3+727r_s^2b_s\right)a^{17}\\
&-\left(271b_s^4-3772r_s^2b_s^2-842r_s^4\right)a^{16}+\left(2556b_s^5-8769r_s^2b_s^3-8399r_s^4b_s\right)a^{15}-\big(2426b_s^6\\
&+3010r_s^2b_s^4-37394r_s^4b_s^2-5820r_s^6\big)a^{14}-2\left(2366b_s^7-24551r_s^2b_s^5+41584r_s^4b_s^3+25845r_s^6b_s\right)a^{13}\\
&+2\big(4566b_s^8-28560r_s^2b_s^6+1424r_s^4b_s^4+98757r_s^6b_s^2+11160r_s^8\big)a^{12}\\
&+2\big(619b_s^9-28977r_s^2b_s^7+171002r_s^4b_s^5-207154r_s^6b_s^3-90900r_s^8b_s\big)a^{11}\\
&-\left(12035b_s^{10}-147852r_s^2b_s^8+472290r_s^4b_s^6-157566r_s^6b_s^4-616644r_s^8b_s^2-45792r_s^{10}\right)a^{10}\\
&+\left(5094b_s^{11}-28091r_s^2b_s^9-173950r_s^4b_s^7+1099064r_s^6b_s^5-1224580r_s^8b_s^3-362016r_s^{10}b_s\right)a^9\\
&+\left(6369b_s^{12}-123188r_s^2b_s^{10}+773952r_s^4b_s^8-1781082r_s^6b_s^6+819180r_s^8b_s^4+1149336r_s^{10}b_s^2\right.\\
&\left.+44064r_s^{12}\right)a^8+\left(-5400b_s^{13}+82355r_s^2b_s^{11}-350365r_s^4b_s^9+158096r_s^6b_s^7+1637020r_s^8b_s^5\right.\\
&\left.-2178848r_s^{10}b_s^3-371952r_s^{12}b_s\right)a^7-2\big(246b_s^{14}-11611r_s^2b_s^{12}+150842r_s^4b_s^{10}-760087r_s^6b_s^8\\
&+1586638r_s^8b_s^6-921032r_s^{10}b_s^4-581256r_s^{12}b_s^2-7776r_s^{14}\big)a^6+2\big(816b_s^{15}-18214r_s^2b_s^{13}\\
&+144727r_s^4b_s^{11}-492003r_s^6b_s^9+583154r_s^8b_s^7+416552r_s^{10}b_s^5-1057824r_s^{12}b_s^3-73872r_s^{14}b_s\big)a^5
\end{aligned}
$$

$$
\begin{aligned}
&- \big(432 b_s^{16} - 8456 r_s^2 b_s^{14} + 42434 r_s^4 b_s^{12} + 38464 r_s^6 b_s^{10} - 855632 r_s^8 b_s^8 + 2340904 r_s^{10} b_s^6 \\
&- 1895226 r_s^{12} b_s^4 - 435456 r_s^{14} b_s^2\big) a^4 + 4 b_s^3 r_s^2 \big(128 b_s^{12} - 3906 r_s^2 b_s^{10} + 35243 r_s^4 b_s^8 - 136975 r_s^6 b_s^6 \\
&+ 224308 r_s^8 b_s^4 - 44484 r_s^{10} b_s^2 - 188352 r_s^{12}\big) a^3 - 4 b_s^4 r_s^2 \big(12 b_s^{12} - 343 r_s^2 b_s^{10} + 1990 r_s^4 b_s^8 \\
&+ 1678 r_s^6 b_s^6 - 48290 r_s^8 b_s^4 + 153429 r_s^{10} b_s^2 - 159738 r_s^{12}\big) a^2 \\
&+ 8 b_s^3 r_s^4 \big(6 b_s^{12} - 212 r_s^2 b_s^{10} + 2109 r_s^4 b_s^8 - 9354 r_s^6 b_s^6 + 19398 r_s^8 b_s^4 - 13632 r_s^{10} b_s^2 - 5400 r_s^{12}\big) a \\
&+ 2 b_s^4 r_s^8 \big(146 b_s^8 - 2044 r_s^2 b_s^6 + 11133 r_s^4 b_s^4 - 28212 r_s^6 b_s^2 + 28212 r_s^8\big)\Big)\Big]. \qquad (2.32c)
\end{aligned}
$$

We can immediately compare the WKB result (2.31)-(2.32), which is obtained by directly solving the radial Klein-Gordon equation and is valid for the first radial overtone $n = 0$, with the eikonal result (2.28), which is obtained solving the geodesic equation for a point particle. We see that the leading WKB frequency (which is $\mathcal{O}(m)/\mathcal{O}(1)$ for the real/imaginary part of the frequency) indeed agrees with the eikonal frequency, thus confirming the validity of the latter. On the other hand, the WKB result (2.31)-(2.32) now finds the next-to-leading order corrections in the frequency up to $\mathcal{O}(1/m^2)$.

The WKB result (2.31)-(2.32) describes the first radial overtone, $n = 0$. In the simplest scenario, one expects that the overtone dependence (2.28) of the eikonal result [64] extends to the higher-order WKB corrections. This expectation is supported by the comparison with our numerical data: we find that the WKB frequencies of higher overtones are well approximated by

$$
\omega_{\rm WKB} = \frac{m}{b_s} + \mathrm{Re}(\omega_0) + (2n+1)\left(i\,\mathrm{Im}(\omega_0) + \frac{\omega_1}{m} + \frac{\omega_2}{m^2} + \mathcal{O}\left(1/m^3\right)\right), \qquad (2.33)
$$

with $\omega_{0,1,2}$ given by (2.32), and radial overtone $n = 0, 1, 2, \ldots$. We have split the ω_0 correction into real and imaginary parts, which is consistent with the eikonal result (2.28), since the real part $\mathrm{Re}(\omega_0)$ is a sub-leading correction not present in (2.28). To use this formula, recall that given a KN black hole with parameters (M, Q, a) we can find r_s solving (2.24) and then b_s is given by (2.23). Further recall that we can use the polar parameterisation (2.6) to express the rotation and charge of the KN black hole in terms of $(\mathcal{R}, \Theta)$.

Naturally, the WKB result $\omega_{\rm WKB}$ in (2.31)-(2.32) with corrections up to $\mathcal{O}(1/m^2)$ represents a considerable improvement over the (leading order WKB) eikonal approximation $\omega_{\rm PS}^{\rm eikn}$ in (2.28). This is best illustrated in Figs. 2.2 and 2.3. Here we plot the numerical PS frequency (orange points) for a KN family with $\mathcal{R} = 0.5$ (Fig. 2.2) and $\mathcal{R} = 0.99$ (Fig. 2.3) as $\Theta = \arctan\frac{a}{Q}$ ranges from the Reissner-Nordström black hole ($\Theta = 0$) to the Kerr solution ($\Theta = \pi/2$). We compare this

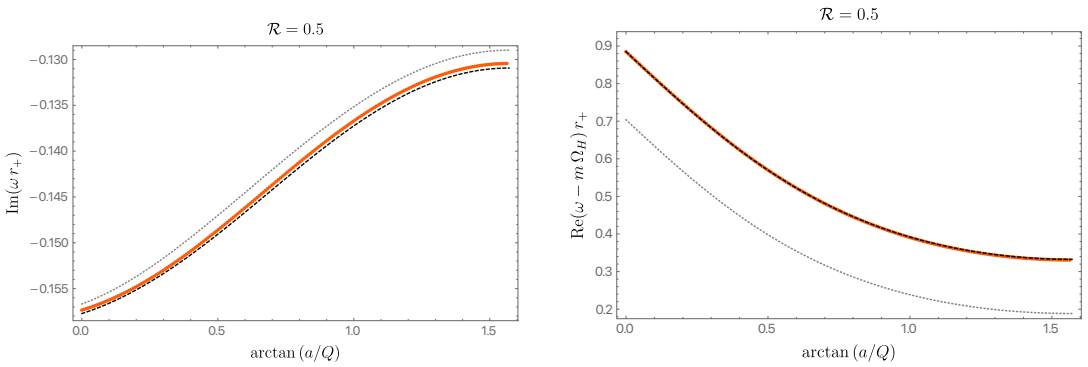

Fig. 2.2: Comparing the eikonal prediction $\omega_{\mathrm{PS}}^{\mathrm{eikn}}$ (dotted gray line) with the WKB result ω_{WKB} (dashed black line) and with the actual numerical frequencies (orange points) for co-rotating PS modes with $m = \ell = 2, n = 0$ in a KN black hole family with fixed $\mathcal{R} = 0.5$. **Left panel:** Imaginary part of the frequency as a function of Θ. **Right panel:** Real part of the frequency measured with respect to the superradiant bound $m\Omega_H$ as a function of Θ.

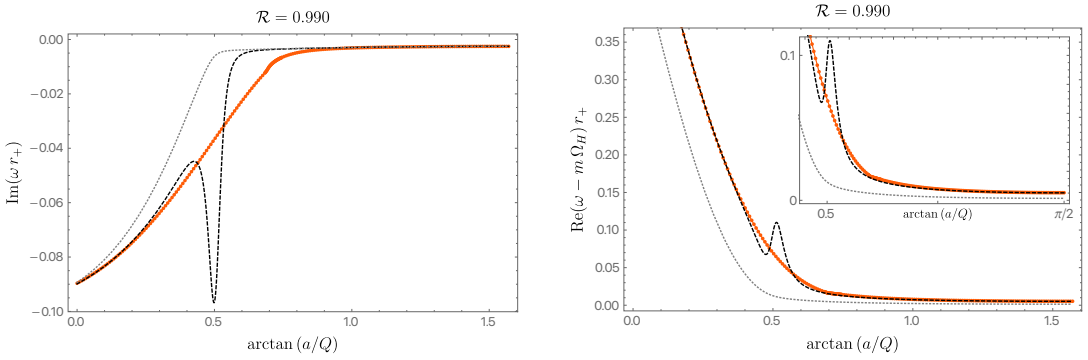

Fig. 2.3: Comparing the eikonal prediction $\omega_{\mathrm{PS}}^{\mathrm{eikn}}$ (dotted gray line) with the WKB result ω_{WKB} (dashed black line) and with the actual numerical frequencies (orange points) for co-rotating PS modes with $m = \ell = 2, n = 0$ in a KN black hole family with fixed $\mathcal{R} = 0.99$. **Left panel:** Imaginary part of the frequency as a function of Θ. **Right panel:** Real part of the frequency measured with respect to the superradiant bound $m\Omega_H$ as a function of Θ.

exact numerical result with the WKB result ω_{WKB} in (2.31)-(2.32) (dashed black line) and with the eikonal approximation $\omega_{\mathrm{PS}}^{\mathrm{eikn}}$ in (2.28) (dotted gray line). We see that the WKB prediction is an excellent approximation for any Θ for values of $\mathcal{R}$ that are not too close to extremality (Fig. 2.2). Moreover, even for values of $\mathcal{R}$ close to extremality (Fig. 2.3), the WKB prediction is still an excellent approximation in a wide neighbourhood around $\Theta = 0$ and again in a large vicinity around $\Theta = \pi/2$. On the other hand, in both plots, one sees that the eikonal approximation is a less good approximation (as expected, since it is strictly valid only in the limit $\ell = m \to \infty$).

In the extremal limit $\mathcal{R} \to 1$, the imaginary part of the (co-rotating) eikonal

approximation $\omega_{\rm PS}^{\rm eikn}$ vanishes when $\Theta \geqslant \Theta_\star^{\rm eik}$ with $\Theta_\star^{\rm eik} \equiv \pi/6 \simeq 0.52$, since the orbit radius reaches the event horizon $r_s^- \to r_+$ (see Fig. 2.1). This occurs because the peak of the eikonal effective Schrödinger potential reaches the event horizon $r_s = r_+$, as previously mentioned in [59]. However, going beyond the eikonal approximation, this is not the case for the numerical frequencies computed at finite m, and this is reflected by the higher-order WKB corrections (2.33) which have a non-zero imaginary part when $\Theta \gtrsim \pi/6$ in the extremal limit (accordingly, from Fig. 2.3 it is also clear that the dashed black and dotted gray lines are distinct near $\Theta \sim \pi/6$). However, for sufficiently large Θ, the higher-order WKB approximation still predicts that PS modes have vanishing imaginary part and $\mathrm{Re}\,\omega \to m\Omega_H^{\rm ext}$ at extremality. This happens for $\Theta \geqslant \Theta_\star^{\rm WKB}$ with $\Theta_\star^{\rm WKB} > \Theta_\star^{\rm eik} \equiv \pi/6$. However, later − see in particular the discussion of Figs. 2.7-2.12 − we will find that it is not entirely clear whether the PS modes do approach $\mathrm{Im}\,\omega \to 0$ and $\mathrm{Re}\,\omega \to m\Omega_H^{\rm ext}$ for large Θ at extremality (although it is probably the case that they indeed do so). On the other hand, we will find that the near-horizon QNM family is very well described by (2.33) close to extremality.

2.2.2 Near-extremal QNM frequencies: a matched asymptotic expansion

Near extremality, the scalar wavefunctions of relevant classes of modes about KN (this is the case *e.g.* for $m = \ell = 2$ modes when Θ is small, but not for the $m = \ell = 0$ modes at any Θ; see Fig. 2.20 for the latter case) are very localized near the horizon and quickly decay away from it, at least near the RN limit. This suggests that we might be able to analytically study the problem within perturbation theory, with the expansion parameter being the off-extremality quantity σ introduced in (2.5) [77–82, 57, 58, 83, 59, 84, 16, 18]. This turns out to be indeed possible if we resort to a matched asymptotic expansion (MAE) whereby we split the spacetime into a near-region (where the wavefunction is mainly localized) and a far region (where the wavefunction is considerably smaller). The near-region is defined as $\frac{r}{r_+} - 1 \ll 1$ and the wavefunction must be regular in this region. In particular it must be regular in ingoing Eddington-Finkelstein coordinates at the event horizon $r = r_+$. On the other hand, the far-region covers the region $\frac{r}{r_+} - 1 \gg \sigma$ and the associated wavefunction must satisfy the outgoing boundary condition at $r \to +\infty$. The two solutions must then be simultaneously valid − and thus the free parameters of the two regions must be matched − in the matching region $\sigma \ll \frac{r}{r_+} - 1 \ll 1$. The latter is guaranteed to exist since the expansion parameter is small, $\sigma \ll 1$. In each of

these regions we find that the radial Klein-Gordon simplifies considerably and can be solved analytically.

We can now formulate and perform the matched asymptotic expansion in detail. As stated above, the expansion parameter of our perturbation theory is the dimensionless off-extremality quantity $\sigma = 1 - \frac{r_-}{r_+}$ defined in (2.5). At extremality ($\sigma = 0$), we numerically find that the modes with slowest decay rate *always* approach $\mathrm{Im}\,\omega = 0$ and $\mathrm{Re}\,\omega = m\Omega_H^{\rm ext}$.[4] Therefore, onwards we assume that the eigenfrequency we search for has an expansion in σ about this superradiant bound:

$$\tilde{\omega} = m\tilde{\Omega}_H^{\rm ext} + \sigma\,\delta\tilde{\omega} + \mathcal{O}(\sigma^2)\,, \tag{2.34}$$

where $\tilde{\omega} = \omega\, r_+$, $\delta\tilde{\omega} = \delta\omega\, r_+$, and our task is to find $\delta\tilde{\omega}$. In (2.34) and onwards, $\tilde{\Omega}_H$ and α always refer to their extremal values although we will drop the super/subscripts 'ext' (present in (2.34)) for notational simplicity. By now, it is clear that it's useful to parameterize the background using the inner and event horizon locations, $r_\pm$. For that, recall that $\Delta = r^2 - 2Mr + a^2 + Q^2$ which can be equivalently written as $\Delta = (r - r_-)(r - r_+)$. Equating these two expressions and their derivatives we can express M and Q as a function of (r_-, r_+, a):

$$M = \frac{1}{2}\,(r_- + r_+)\,, \qquad Q = \sqrt{r_- r_+ - a^2}\,. \tag{2.35}$$

We will insert these relations in the radial Klein-Gordon equation.

Consider first the far-region, $\frac{r}{r_+} - 1 \gg \sigma$. It is then natural to redefine the radial coordinate as

$$y = \frac{r}{r_+} - 1\,, \tag{2.36}$$

in which case the far-region is simply defined as the region $y \gg \sigma$. Inserting (2.36), (2.35) and (2.34) into the radial equation (2.8a) one finds that, to leading order in a σ expansion about extremality, it reduces to

$$y^2 R''(y) + 2yR'(y) + \left[m^2\tilde{\Omega}_H^2\left(6 + \alpha^2 + 4y + y^2\right) - \lambda\right] R(y) \simeq 0. \tag{2.37}$$

[4] In several studies of perturbations of RN, Kerr, KN [77–82, 57, 58, 83, 59, 84, 16, 18] and even de Sitter black holes [188, 165, 189], it was also found that there are near-horizon modes that saturate the superradiant bound $\omega = m\Omega_H$ at extremality. This happens for bosonic perturbations with spin s, *not* only for $s = 0$. Our analysis here is very similar to the one presented in [59] for $s = 0$ (the MAE analysis of NH gravito-electromagnetic modes is considerably more involved than the $s = 0$ case [18]).

Introducing a new radial coordinate $\bar{y}$ and a redefinition of the radial function,

$$\bar{y} = 2\,i\,m\tilde{\Omega}_H\,y\,, \qquad R = e^{-i\,m\tilde{\Omega}_H y} y^{-\frac{1}{2}+i\,\delta} K \tag{2.38}$$

where

$$\delta = \sqrt{(6+\alpha^2)m^2\tilde{\Omega}_H^2 - \frac{1}{4} - \lambda}\,, \tag{2.39}$$

we find that (2.37) is a standard Kummer equation, $\bar{y}K''(\bar{y})+(\mathfrak{b}-\bar{y})K'(\bar{y})-\mathfrak{a}K(\bar{y}) = 0$ with

$$\mathfrak{a} = \frac{1}{2} + i\left(2m\tilde{\Omega}_H + \delta\right)\,, \qquad \mathfrak{b} = 1 + 2i\delta\,. \tag{2.40}$$

Its most general solution is a sum of two independent functions, ${}_1F_1(\mathfrak{a};\mathfrak{b};\bar{y})$ and $\bar{y}^{1-\mathfrak{b}}\,{}_1F_1(\mathfrak{a}-\mathfrak{b}+1;2-\mathfrak{b};\bar{y})$ where ${}_1F_1$ is the Kummer confluent hypergeometric function (a.k.a. of the first kind) [190][5]. Thus, the most general solution of the far-region equation (2.37) is

$$\begin{aligned} R \;=\; & A_1 e^{-i\,m\tilde{\Omega}_H y} y^{-\frac{1}{2}+i\,\delta}\,{}_1F_1\left(\mathfrak{a};\mathfrak{b};2i\,m\tilde{\Omega}_H\,y\right) \\ & + A_2 e^{-i\,m\tilde{\Omega}_H y} y^{-\frac{1}{2}-i\,\delta}\,{}_1F_1\left(\mathfrak{a}-\mathfrak{b}+1;2-\mathfrak{b};2i\,m\tilde{\Omega}_H\,y\right), \end{aligned} \tag{2.41}$$

for arbitrary integration constants A_1 and A_2. Asymptotically, this solution behaves as

$$\begin{aligned} R\big|_{y\to\infty} \;\simeq\; & e^{-i\,m\tilde{\Omega}_H y} y^{-1-2i\,m\tilde{\Omega}_H}\left(A_1\frac{(-2im\tilde{\Omega}_H)^{-\frac{1}{2}-i(\delta+2m\tilde{\Omega}_H)}\Gamma(2i\delta+1)}{\Gamma\left(\frac{1}{2}-i(2m\tilde{\Omega}_H-\delta)\right)}\right. \\ & \left. + A_2\frac{(-2im\tilde{\Omega}_H)^{-\frac{1}{2}-i(2m\tilde{\Omega}_H-\delta)}\Gamma(1-2i\delta)}{\Gamma\left(\frac{1}{2}-i(\delta+2m\tilde{\Omega}_H)\right)}\right) \\ & + e^{i\,m\tilde{\Omega}_H y} y^{-1+2i\,m\tilde{\Omega}_H}\left(A_1\frac{(2im\tilde{\Omega}_H)^{-\frac{1}{2}+i(2m\tilde{\Omega}_H-\delta)}\Gamma(2i\delta+1)}{\Gamma\left(\frac{1}{2}+i(\delta+2m\tilde{\Omega}_H)\right)}\right. \\ & \left. + A_2\frac{(2im\tilde{\Omega}_H)^{-\frac{1}{2}+i(\delta+2m\tilde{\Omega}_H)}\Gamma(1-2i\delta)}{\Gamma\left(\frac{1}{2}+i(2m\tilde{\Omega}_H-\delta)\right)}\right). \end{aligned} \tag{2.42}$$

The first contribution (proportional to $e^{-i\,m\tilde{\Omega}_H y}$) represents an ingoing wave while the second (proportional to $e^{+i\,m\tilde{\Omega}_H y}$) describes an outgoing wave. For the QNM problem we want to impose boundary conditions in the asymptotic region that

[5]There is a third solution $U(\mathfrak{a},\mathfrak{b},y)$, known as the confluent hypergeometric function of the second kind, that is sometimes also used as one of the two independent solutions. It can be written as a linear combination of the two independent solutions that we use as $U(\mathfrak{a},\mathfrak{b},y) = \frac{\pi}{\sin(\pi\mathfrak{b})}\left(\frac{{}_1F_1(\mathfrak{a};\mathfrak{b};y)}{(\mathfrak{b}-1)!(\mathfrak{a}-\mathfrak{b})!} - \frac{{}_1F_1(\mathfrak{a}-\mathfrak{b}+1;2-\mathfrak{b};y)}{(\mathfrak{a}-1)!(1-\mathfrak{b})!}\,y^{1-\mathfrak{b}}\right)$ [190].

keep only the outgoing waves. This fixes A_1 to be

$$A_1 = A_2 e^{\delta\left[\pi+2i\ln(2m\tilde{\Omega}_H)\right]}\frac{\Gamma(-2i\delta)\Gamma\left(\frac{1}{2}-i(2m\tilde{\Omega}_H-\delta)\right)}{\Gamma(2i\delta)\Gamma\left(\frac{1}{2}-i(2m\tilde{\Omega}_H+\delta)\right)}. \tag{2.43}$$

For the matching with the near-region, we will need the small y behaviour of the far-region solution (2.42) with the boundary condition (2.43):

$$R_{\text{far}}\big|_{y\ll 1} \simeq A_2\left(y^{-\frac{1}{2}-i\,\delta}+y^{-\frac{1}{2}+i\,\delta}e^{\pi\delta}(2m\tilde{\Omega}_H)^{2i\delta}\frac{\Gamma(-2i\delta)\Gamma\left(\frac{1}{2}-i(2m\tilde{\Omega}_H-\delta)\right)}{\Gamma(2i\delta)\Gamma\left(\frac{1}{2}-i(2m\tilde{\Omega}_H+\delta)\right)}\right) \tag{2.44}$$

Consider now the near-region $0 \leqslant y \ll 1$. This time we should proceed cautiously when doing the perturbative expansion in $\sigma \ll 1$ since this small expansion parameter can now be of similar order as the radial coordinate y. This is closely connected with the fact that the far-region solution breaks down when $y/\sigma \sim \mathcal{O}(1)$. This suggests that to proceed with the near-region analysis we should define a new radial coordinate as[6]

$$z = \frac{y}{\sigma} = \frac{r-r_+}{r_+-r_-}\,, \tag{2.45}$$

The near-region now corresponds to $0 \leqslant z \ll \sigma^{-1}$. So, in the near-region we simultaneously zoom in around the horizon and approach extremality. Inserting (2.45), (2.35) and (2.34) into the radial equation (2.8a) one finds that (again to leading order in a σ expansion about extremality) it reduces to

$$z(1+z)R''(z)+(1+2z)R'(z)+\left(\frac{\left(2m\tilde{\Omega}_H z+(1+\alpha^2)\,\delta\tilde{\omega}\right)^2}{z(1+z)}+\left(2+\alpha^2\right)m^2\tilde{\Omega}_H^2-\lambda\right)R(z)\simeq 0. \tag{2.46}$$

Introducing a new radial coordinate $\bar{z}$ and a redefinition of the radial function,

$$\bar{z} = -z\,, \qquad R = \bar{z}^{-i\,(1+\alpha^2)\delta\tilde{\omega}}(1-\bar{z})^{i\,[2m\tilde{\Omega}_H-(1+\alpha^2)\delta\tilde{\omega}]}F, \tag{2.47}$$

we find that (2.46) reduces to a standard hypergeometric equation, $(1-\bar{z})\bar{z}F''(\bar{z}) + [c-\bar{z}(a_+ + a_- + 1)]F'(\bar{z}) - a_+a_-F(\bar{z}) = 0$ with

$$a_\pm = \frac{1}{2} + i\left[2m\tilde{\Omega}_H - 2(1+\alpha^2)\delta\tilde{\omega} \pm \delta\right], \qquad c = 1 - 2\,i(1+\alpha^2)\delta\tilde{\omega}\,, \tag{2.48}$$

[6]At the heart of the matching expansion procedure, note that a factor of σ (the expansion parameter!) is absorbed in the new near-region radial coordinate.

and δ defined in (2.39). Its most general solution is a sum of two hypergeometric functions, $F = \bar{C}_1\, {}_2F_1(a_+, a_-; c; \bar{z}) + \bar{C}_2 \bar{z}^{1-c}\, {}_2F_1(a_+ - c + 1, a_- - c + 1; 2 - c; \bar{z})$ [190] (for an arbitrary integration constants $\bar{C}_1, \bar{C}_2$), but regularity at the horizon in Eddington-Finkelstein coordinates requires that we eliminate the solution that is outgoing at the event horizon. So we set $\bar{C}_2 \equiv 0$. Thus, the solution of (2.46) that describes ingoing waves at the event horizon is

$$R = C_1 z^{-i\,(1+\alpha^2)\delta\tilde{\omega}} (1+z)^{i\,[2m\tilde{\Omega}_H - (1+\alpha^2)\delta\tilde{\omega}]}\, {}_2F_1(a_+, a_-; c; -z) \tag{2.49}$$

for arbitrary constant C_1. Later, to match the near-region solution (2.49) with the far-region one, we will need the large $z = \frac{y}{\sigma}$ behaviour of (2.49) which is given by

$$\begin{aligned} R_{\text{near}}\big|_{z\gg 1} \;\simeq\; & C_1 y^{-\frac{1}{2}-i\delta} \frac{\sigma^{\frac{1}{2}+i\delta}\Gamma(-2i\delta)\Gamma\Big(1-2i(1+\alpha^2)\delta\tilde{\omega}\Big)}{\Gamma\left(\frac{1}{2}-2im\tilde{\Omega}_H - i\delta\right)\Gamma\left(\frac{1}{2}-2i\,(1+\alpha^2)\,\delta\tilde{\omega}+2im\tilde{\Omega}_H - i\delta\right)} \\ & + C_1 y^{-\frac{1}{2}+i\delta} \frac{\sigma^{\frac{1}{2}-i\delta}\Gamma(2i\delta)\Gamma\left(1-2i\,(1+\alpha^2)\,\delta\tilde{\omega}\right)}{\Gamma\left(\frac{1}{2}-2im\tilde{\Omega}_H + i\delta\right)\Gamma\left(\frac{1}{2}-2i\,(1+\alpha^2)\,\delta\tilde{\omega}+2im\tilde{\Omega}_H + i\delta\right)} \end{aligned} \tag{2.50}$$

In the near-region we have used the horizon boundary condition to fix one of the two amplitudes of the most general solution. Similarly, in the far-region we have used the asymptotic boundary condition to fix one of the two amplitudes of the most general far-region solution. In each of the regions we are left with a free integration constant, C_1 in the far-region and A_2 in the near-region. These are now fixed in the matching region $\sigma \ll \frac{r}{r_+} - 1 \ll 1$ by requiring that the small radius expansion (2.44) of the far-region matches with the large radius expansion (2.50) of the near-region. Concretely, matching first the coefficients of $y^{-\frac{1}{2}-i\delta}$ of (2.44) and (2.50) requires that

$$A_2 = C_1\, \frac{\sigma^{\frac{1}{2}+i\delta}\Gamma(-2i\delta)\Gamma\left(1-2i\,(1+\alpha^2)\,\delta\tilde{\omega}\right)}{\Gamma\left(\frac{1}{2}-i(2m\tilde{\Omega}_H+\delta)\right)\Gamma\left(\frac{1}{2}+i[2m\tilde{\Omega}_H-\delta-2\,(1+\alpha^2)\,\delta\tilde{\omega}]\right)}\,. \tag{2.51}$$

We can now insert this relation into (2.44) and the final matching, this time of the coefficients of $y^{-\frac{1}{2}+i\delta}$ of (2.44) and (2.50), requires that the following condition holds

$$\beta\,\Gamma\left(\frac{1}{2}+\frac{2i\,m\alpha}{1+\alpha^2}-2i\left(1+\alpha^2\right)\delta\tilde{\omega}-i\delta\right)-1=0 \tag{2.52}$$

$$\text{with}\quad \beta = \sigma^{-2i\delta}\frac{e^{-\pi\delta}\left(\frac{2\alpha m}{1+\alpha^2}\right)^{-2i\delta}\Gamma(2i\delta)^2\Gamma\left(\frac{1}{2}-\frac{2im\alpha}{1+\alpha^2}-i\delta\right)^2}{\Gamma(-2i\delta)^2\Gamma\left(\frac{1}{2}-\frac{2im\alpha}{1+\alpha^2}+i\delta\right)^2\Gamma\left(\frac{1}{2}+\frac{2im\alpha}{1+\alpha^2}-2i\,(1+\alpha^2)\,\delta\tilde{\omega}+i\delta\right)}.$$

Here, we make the important observation that $\sigma \ll 1$ and thus $\beta \propto \sigma^{-2i\delta}$ is generally a very small number, $\beta \ll 1$. In these conditions, (2.52) can be obeyed is if the gamma function multiplying β is very large *i.e.* if the frequency correction $\delta\tilde{\omega}$ is such that the argument of the gamma function is near one of its poles. Recalling that $\Gamma(-p) \to +\infty$ when p is a non-negative integer, the matching condition (2.52) quantizes the frequency correction as

$$\delta\tilde{\omega} \simeq \frac{m\alpha}{(1+\alpha^2)^2} - \frac{\delta}{2\,(1+\alpha^2)} - \frac{i\left(p+\frac{1}{2}\right)}{2\,(1+\alpha^2)}\,, \qquad p = 0, 1, 2, \cdots \tag{2.53}$$

Inserting this quantization into (2.34), we conclude that QNMs that approach $\tilde{\omega} = m\tilde{\Omega}_H^{\rm ext}$ at extremality should have a frequency that is well approximated near extremality by[7]

$$\tilde{\omega}_{\rm MAE} = \frac{m\alpha}{1+\alpha^2} + \sigma\left(\frac{m\alpha}{(1+\alpha^2)^2} - \frac{1}{2\,(1+\alpha^2)}\sqrt{\frac{m^2\alpha^2(6+\alpha^2)}{(1+\alpha^2)^2} - \frac{1}{4} - \lambda} - \frac{i\left(p+\frac{1}{2}\right)}{2\,(1+\alpha^2)}\right) + \mathcal{O}\left(\sigma^2\right), \tag{2.54}$$

where $p = 0, 1, 2, \cdots$ is the radial overtone of the mode. To compare with our numerical results generated using the polar parameterisation (2.5)-(2.6), we should now replace $\sigma = 1 - \mathcal{R}^2$ and $\alpha = \mathcal{R}\sin\Theta$ in (2.54). This approximation should be good for $\mathcal{R} \simeq 1$ and any $0 \leqslant \Theta \leqslant \frac{\pi}{2}$.

Note that if we wish, we can convert (2.54) into units of M by multiplying (2.54) by M/r_+ (since $\omega M = \tilde{\omega} M/r_+$) and expanding it in terms of σ while keeping terms only up to $\mathcal{O}(\sigma)$ (since all our analysis is valid only up to this order). The near-horizon modes (a.k.a. zero damped [57–59] or near-extremal modes) and a matched asymptotic analysis of such modes similar to the one above that leads to their frequencies near-extremality have already been considered for RN, Kerr and KN for several bosonic fields in [77–82, 57, 58, 83, 59, 84, 16, 18]. In the appropriate limits, our frequency (2.54) reduces to the expressions presented in this literature.

In Fig. 2.4 we compare the matched asymptotic expansion $\tilde{\omega}_{\rm MAE}$ (dot-dashed magenta curve) to the exact NH modes (blue diamond curve) of KN for $\mathcal{R} = 0.993$ as we go from RN ($a = 0$, *i.e.* $\Theta = 0$) to Kerr ($Q = 0$, *i.e.* $\Theta = \pi/2$). For most values of $\Theta \equiv \arctan(a/Q)$, $\tilde{\omega}_{\rm MAE}$ is an excellent approximation. There is a sharp change in the behaviour of the matched asymptotic expansion at $\Theta \sim 0.881$, which turns out to be an important feature of this approximation, and is only present for

[7] Note that, as discussed below (2.8b), the eigenvalue λ is related to the eigenvalue Λ of the standard oblate spheroidal equation by $\lambda = \Lambda - \alpha^2\tilde{\omega}^2$ and, in the near-horizon analysis of this subsection, one has $\tilde{\omega} = m\tilde{\Omega}_H^{\rm ext} = m\,\alpha/(1+\alpha^2)$.

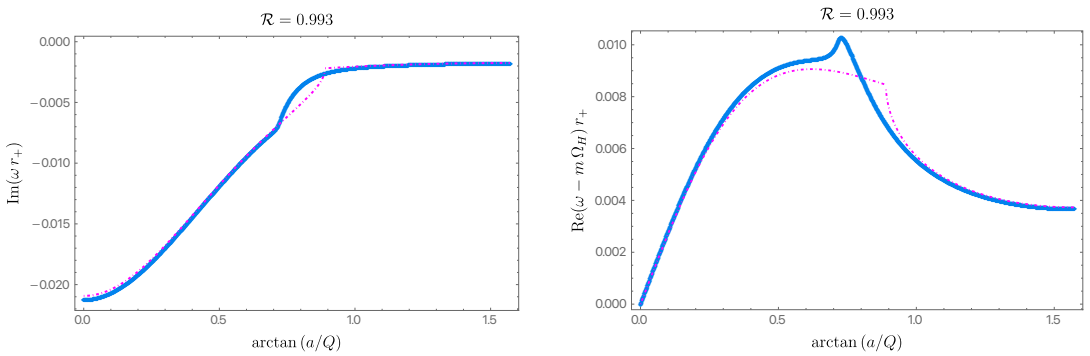

Fig. 2.4: The NH (blue diamonds) family of QNMs with $m = \ell = 2, n = 0$ for a KN family with $\mathcal{R} = 0.993$. We also display the near-extremal frequency $\tilde{\omega}_{\rm MAE}$ for $p = 0$ (dot-dashed magenta line). **Left panel:** Imaginary part of the frequency as a function of Θ. **Right panel:** Real part of the frequency measured with respect to the superradiant bound $m\Omega_H$ as a function of Θ.

certain values of the azimuthal quantum numbers m and ℓ, as already noted in [57–59, 16, 18].

To understand this feature of the matched asymptotic expansion better, in Fig. 2.5 we plot the imaginary (left panel) and real (right panel) parts of the matched asymptotic expansion $\tilde{\omega}_{\rm MAE}$, for several values of $m = \ell = 0, 1, 2, 5$ (yellow, blue, green, red). For $m = \ell \geqslant 2$, as the cases $m = \ell = 2$ and $m = \ell = 5$ in Fig. 2.5 illustrate, this sharp change in behaviour is present, but not for $m = \ell = 0$ or $m = \ell = 1$. This change occurs at a critical value $\Theta_{\rm c}$, indicated by dashed lines, which is the value of Θ at which the argument of the square root in (2.54) changes sign, or equivalently when δ^2 changes sign, where δ is defined by (2.39): δ^2 is negative when $\Theta < \Theta_{\rm c}$ and positive when $\Theta > \Theta_{\rm c}$.

It is important to note that the matched asymptotic expansion we performed captures any modes that approach the superradiant bound $\omega \to m\,\Omega_H$ (with vanishing imaginary part) in the extremal limit, regardless of whether they are associated to 'NH' or 'PS' modes in the RN limit (or any other mode classification we choose). In particular, we will find 'PS modes' that approach the superradiant bound, and when this occurs the matched asymptotic expansion frequency $\tilde{\omega}_{\rm MAE}$ provides an excellent approximation near extremality, even for small values of m and ℓ where the WKB expansion (2.33) might fail to give a good approximation (see the last three plots of the later Fig. 2.7).

In the eikonal limit ($m \to \infty$) and at extremality, one finds that $\Theta_{\rm c}|_{m\to\infty} \to \pi/6 \simeq 0.524$. Interestingly, we can see that this value is in agreement with the eikonal expectation that the PS modes have vanishing imaginary part in the near-extremal limit when $\Theta \geqslant \Theta^{\rm eik}_\star$ (where $\Theta^{\rm eik}_\star \equiv \pi/6$ was introduced in the last paragraph of

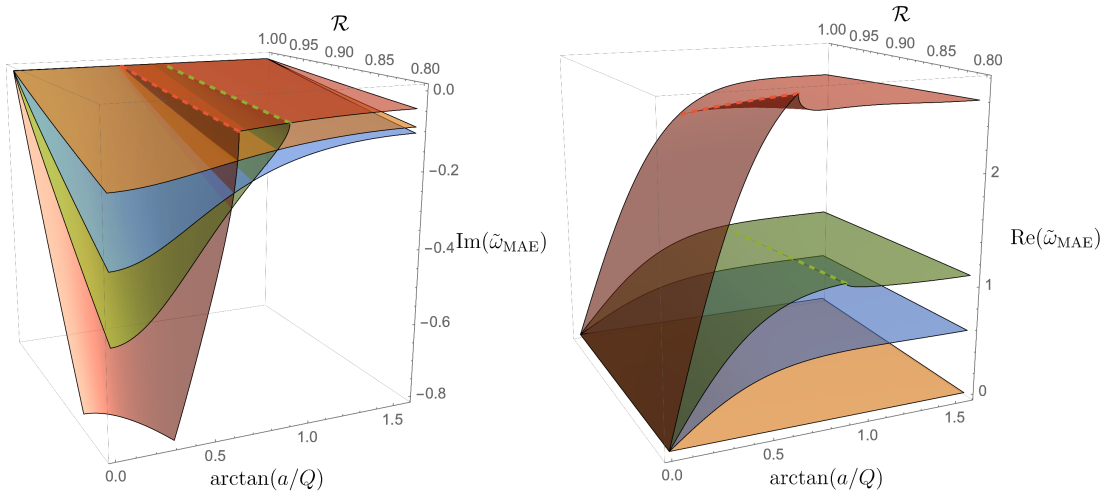

Fig. 2.5: Imaginary (left) and real (right) parts of the matched asymptotic expansion $\tilde{\omega}_{\mathrm{MAE}}$ given by (2.54), for KN families with $\mathcal{R} \geqslant 0.8$, with $m = \ell = 0, 1$ (yellow, blue surfaces) and $m = \ell = 2, 5$ (green, red surfaces). In the latter two cases, representative of when $m = \ell \geqslant 2$, there are two regions with distinct behaviours demarcated by a critical value Θ_{c} indicated by a dashed line.

section 2.2.1.2 and in the discussion of Fig. 2.1). However, as discussed in the same paragraph, this is no longer the case once we include the higher-order WKB corrections (2.33) since this frequency approaches $\omega = m\Omega_H$ at extremality only for $\Theta \geqslant \Theta_\star^{\mathrm{WKB}}$ with $\Theta_\star^{\mathrm{WKB}} > \Theta_\star^{\mathrm{eik}}$. The expectation is that if we extend the large m WKB analysis of section 2.2.1.2 beyond third order $\mathcal{O}(m^{-3})$ to increasingly higher orders (so that it progressively more accurately describes small m modes), one would observe $\Theta_\star^{\mathrm{WKB}}$ approaching $\Theta_{\mathrm{c}} \sim 0.881$ from below. Conversely, we have observed that as $m = \ell$ increases, the associated Θ_{c} approaches $\Theta_\star^{\mathrm{WKB}}$.

For gravito-electromagnetic perturbations in KN [18], there is a separation constant λ_2 which plays the role of δ^2, and there it was shown that the vanishing of λ_2 provides a very good indication of the point where PS modes want to reach vanishing imaginary part in the extremal limit [18]. For the scalar field case, the sign of δ^2 has been shown to at least roughly correspond to whether there are one or two families [59] in the extremal limit, however, establishing whether the sign of δ^2 is a sharp criteria for KN in the scalar field case was not previously studied in detail. Later, when discussing Figs. 2.7−2.14, we will find that 1) PS modes do attempt to approach $\mathrm{Im}\,\omega \to 0$ and $\mathrm{Re}\,\omega \to m\Omega_H^{\mathrm{ext}}$ for large Θ at extremality, and 2) NH modes always start at $\mathrm{Im}\,\omega \to 0$ and $\mathrm{Re}\,\omega \to m\Omega_H^{\mathrm{ext}}$ at extremality for any value of Θ. Proceeding with caution, the critical values $\Theta_\star^{\mathrm{eik}}$ and $\Theta_\star^{\mathrm{WKB}}$ that emerge from the eikonal/WKB analysis and Θ_{c} that emerges from the near-horizon analysis are to be seen only as rough reference values signalling where one expects some change in the qualitative behaviour of the QNM spectra. They

are rough references because these quantities emerge from WKB or near-horizon analytical considerations that are just approximation analyses, but also because these expectations can be subverted by eigenvalue repulsions in KN (which are not present in the RN or Kerr limits), as we discuss next.

2.3 Eigenvalue repulsions

2.3.1 Eigenvalue or level repulsion, avoided crossing or Wigner-Teller effect

Eigenvalue repulsions are ubiquitous in eigenvalue problems, for both classical and quantum mechanical systems, where it goes by the name *level repulsion*, *avoided crossing* or the *Wigner-Teller effect* [184, 185]. For example, in solid state physics eigenvalue repulsion is responsible for the energy gap between different energy bands of simple lattice models [191]. However, this phenomenon has only recently been observed or, at least, correctly understood/identified as such in the QNM spectra of black holes. In this section, we give a brief discussion of this phenomenon using the analogy of a two-level system, and explain why one only expects eigenvalue repulsions to occur in the QNM spectra of black hole families with two or more dimensionless parameters (*e.g.* in Kerr-Newman) but not in black holes parametrised by a single dimensionless parameter (*e.g.* RN or Kerr). We ask the reader to see section 4.1 of [18] for a more thorough treatment of the argument sketched here.

As an example, let us consider $\mathcal{L}_0$ to be an operator schematically representing the eigenvalue problem $\mathcal{L}_0\psi = \omega\,\psi$ given by (2.8a)-(2.8b) subject to QNM boundary conditions, for some fixed value of Θ, *e.g.* RN ($\Theta = 0$). We select two eigenfunctions ψ_1, ψ_2 whose associated eigenvalues ω_1 and ω_2 are distinct but very close in the complex plane. For example, ω_1 could be the dominant PS eigenvalue and ω_2 the dominant NH eigenvalue for some specific RN BH, which never coincide in the complex plane for any value of $\mathcal{R}$ (as discussed later in Fig. 2.6).

Now, we perturb the operator, $\mathcal{L} = \mathcal{L}_0 + \mathcal{K}$, by turning on angular momentum, $\Theta > 0$, and ask how the eigenvalues change. We make the zeroth-order approximation that the perturbed eigenfunctions $\bar{\psi}$ are a linear combination of the unperturbed basis, $\bar{\psi} = c_1\psi_1 + c_2\psi_2$, which leads to the perturbed eigenvalue problem $(\mathcal{L}_0+\mathcal{K})\bar{\psi} =$

$\bar{\omega}\,\bar{\psi}$. The matrix representing this eigenvalue problem can then be written as

$$\begin{bmatrix} \omega_1 + \mathcal{K}_{11} & \mathcal{K}_{12} \\ \mathcal{K}_{21} & \omega_2 + \mathcal{K}_{22} \end{bmatrix} \tag{2.55}$$

where $\mathcal{K}_{ij}$ are the matrix elements of $\mathcal{K}$ in the $\{\psi_1, \psi_2\}$ basis, defined with respect to some suitable inner product, and the eigenvalues $\bar{\omega}_\pm$ of this perturbed equation are given by

$$\bar{\omega}_\pm = \frac{\tilde{\omega}_1 + \tilde{\omega}_2}{2} \pm \sqrt{\frac{(\tilde{\omega}_1 - \tilde{\omega}_2)^2}{4} + \mathcal{K}_{12}\mathcal{K}_{21}}\,, \tag{2.56}$$

where $\tilde{\omega}_i \equiv \omega_i - \mathcal{K}_{ii}$ (no Einstein summation over i). The perturbed eigenvalues $\bar{\omega}_\pm$ can only cross if the argument of the square root vanishes, *i.e.* if and only if

$$\frac{(\tilde{\omega}_1 - \tilde{\omega}_2)^2}{4} + \mathcal{K}_{12}\mathcal{K}_{21} = 0. \tag{2.57}$$

This complex condition gives rise to two real conditions, which both need to be satisfied for an eigenvalue crossing. In general, the matrix elements of the perturbed operator $\mathcal{K}_{ij}$ will depend on the N real black hole parameters. With the exception of some symmetry that reduces the number of conditions required, we thus expect that eigenvalue crossing can only occur on an $N-2$ dimensional subspace. KN is parameterized by two dimensionless parameters $\{\mathcal{R}, \Theta\}$, and hence eigenvalue crossing (in the complex plane) can only occur at isolated points in the parameter space. This simple argument might explain why eigenvalue repulsions have been observed in Kerr-Newman [16, 18], Reissner-Nordström-de Sitter [145] and Myers-Perry-de Sitter (Chapter 3), or accelerating spacetimes [186], but not in RN, Kerr or Schwarzschild [167–175, 78, 176, 48, 177, 178, 180, 181, 57]. It is also important to note that the above analysis leaves room for the following scenario. If the background system has a parameter space with a boundary (e.g. the 1-dimensional extremal boundary in the KN black hole case or the 0-dimensional extremal endpoint in the Kerr and RN cases), two eigenvalue families might be able to meet in the complex plane at this extremal boundary (or at a portion of it if 1-dimensional). This is not an eigenvalue crossing in the complex plane (since it occurs at a boundary) and thus is not ruled out by the above analysis; instead it is a special case where two eigenvalue families meet and *terminate* at a *boundary* of the parameter space.

Having understood (in section 2.2) that the QNM spectra of KN has two families of modes (PS and NH) and that KN is a 2-dimensional parameter family of black holes, we might now expect the existence of one point (or, at most, a few isolated

points) in the KN parameter space where we might see the PS and NH modes trying to approach each other in the frequency complex plane. What might this point be? Well, from the matched asymptotic analysis of section 2.2.2 we know that NH modes always start at $\mathrm{Im}\,\omega \to 0$ and $\mathrm{Re}\,\omega \to m\Omega_H^{\mathrm{ext}}$ at extremality for any value of Θ and there is an associated critical point $\{\mathcal{R}, \Theta_{\mathrm{c}}\} \sim \{1, 0.881\}$.[8] On the other hand, the eikonal and WKB analyses of section 2.2.1, suggest that PS modes want to approach $\mathrm{Im}\,\omega \to 0$ and $\mathrm{Re}\,\omega \to m\Omega_H^{\mathrm{ext}}$ at extremality for $\Theta \geqslant \Theta_\star^{\mathrm{WKB}}$ with $\Theta_\star^{\mathrm{WKB}} > \Theta_\star^{\mathrm{eik}} \equiv \pi/6 \simeq 0.524$ which singles out the special point $\{\mathcal{R}, \Theta_\star^{\mathrm{WKB}}\}$. The expectation is that if we extend the large m WKB analysis of section 2.2.1 to increasingly higher orders so that it progressively describes the small m modes more accurately, one would observe $\Theta_\star^{\mathrm{WKB}}$ approaching Θ_{c} from below. Onwards, for simplicity, let us thus denote this point simply as $\Theta_\star \sim 0.881$. Given the restrictions on eigenvalue crossings argued previously, and the special point $\Theta_\star$ given by our analytic predictions, there are thus three possibilities for the Kerr-Newman QNM spectra:

1. In one of the simplest scenarios, the PS and NH modes have the same frequency at a single point. If so, the MAE and WKB results suggest that this point should be at $\mathcal{R} = 1$ and around $\Theta = \Theta_\star \sim 0.881$.

2. However, since $\mathcal{R} = 1$ happens to be at the 1-dimensional extremal boundary of the KN parameter space, there is also room to actually have both the PS and NH eigenfrequencies meeting and terminating with $\mathrm{Im}\,\omega \to 0$ and $\mathrm{Re}\,\omega \to m\Omega_H^{\mathrm{ext}}$, not only at the single point $\{\mathcal{R}, \Theta_\star\}$ but actually along the portion of the extremal boundary parametrised by $\mathcal{R} = 1$ and $\Theta_\star \leqslant \Theta \leqslant \pi/2$. In fact, we will see that this situation certainly occurs for modes within the same family of QNM: all the overtones of the NH modes (the exact numerical frequencies) meet with $\mathrm{Re}\,\omega = m\Omega_H$ and $\mathrm{Im}\,\omega = 0$ at extremality for RN, Kerr and KN. Therefore, it seems reasonable that two distinct families of QNMs (namely, the PS and NH modes) might also meet and terminate along a 1-parameter portion of the extremal KN boundary ($\mathcal{R} = 1$ and $\Theta_\star \leqslant \Theta \leqslant \pi/2$), perhaps with the appearance of eigenvalue repulsions near-extremality when they do or attempt to do so.

3. The final scenario, that cannot be excluded, is that the PS and NH eigenvalues never coincide, not even at $\{\mathcal{R}, \Theta_\star\}$.

[8] Recall that the quantity Θ_{c} was introduced in the last paragraph of section 2.2.2 (when discussing the cusps in Figs. 2.4 and 2.5), and that $\Theta_\star^{\mathrm{eik}}$ and $\Theta_\star^{\mathrm{WKB}} \geqslant \Theta_\star^{\mathrm{eik}}$ were introduced in the discussion of Fig. 2.1 in the last paragraph of section 2.2.1.2.

What ends up happening in the KN QNM spectra? This question will be addressed in the next section. We will do a detailed numerical search of the $m = \ell = 2$ PS and NH frequencies, some of which will be displayed in Figs. 2.6−2.15. From this analysis, we will conclude that: 1) NH modes indeed exist and always approach $\mathrm{Im}\,\omega \to 0$ and $\mathrm{Re}\,\omega \to m\Omega_H^{\rm ext}$ at extremality, and 2) PS modes indeed seem to be strongly willing to approach $\mathrm{Im}\,\omega \to 0$ and $\mathrm{Re}\,\omega \to m\Omega_H^{\rm ext}$ at extremality for $\Theta > \Theta_\star$. However, intricate eigenvalue repulsions will typically kick in close to extremality and for $\Theta \gtrsim \Theta_\star$ (as a rough indication) which will break the monotony of the system that was present for smaller values of $\mathcal{R}$ and/or Θ.

2.3.2 Eigenvalue repulsions in the scalar field QNMs of KN

The quasinormal mode spectra of the Kerr-Newman black hole has two families of mode. In the Reissner-Nordström (RN) limit (*i.e.* $a = 0$ or $\Theta = 0$) we can undoubtedly associate one of these families to the photon sphere (PS) modes and the other to the near-horizon (NH) modes. This is because when $\Theta = 0$, the PS family is well approximated by $\tilde{\omega}_{\rm WKB}$ in (2.33), while the NH family is well described by $\tilde{\omega}_{\rm MAE}$ in (2.54).

This is illustrated in Fig. 2.6, where we plot the $n = 0$ (orange disks) and $n = 1$ (red disks) PS QNM frequencies as well as $\tilde{\omega}_{\rm WKB}$ given by the black ($n = 0$) and gray ($n = 1$) dashed lines. We see that the latter higher-order WKB curves are on top of the numerical PS curves, indicating that (2.33) provides an excellent approximation for the PS family of RN QNMs and its overtones, and allows one to identify them in the RN limit. Additionally, in Fig. 2.6 we also plot the $n = 0, 1, 2, 3$ (blue, dark-green, brown and green diamonds) NH QNM frequencies and $\tilde{\omega}_{\rm MAE}$ (magenta and red dot-dashed and dashed lines). We see that the latter matched asymptotic expansions approximate the NH frequencies of RN very well when we are close to extremality (*i.e.* as $\mathcal{R} \to 1$). This clearly identifies the NH family of QNMs and their overtones in the RN limit. As pointed out in [59], the PS modes (a.k.a. damped modes in [59]) of RN are very well known in the literature, starting with the WKB analysis of [72]. However, the existence of the NH modes (a.k.a. zero-damped modes in [59]) in RN seems to have been missed until the work of [59], in spite of the seminal work of Teukolsky and Press [77] and Detweiler [78] already suggesting that such family might be present in any black hole with an extremal configuration. Our PS frequencies in Fig. 2.6 agree with those first computed in [72, 192–195]. On the other hand, the NH QNM spectrum in Fig. 2.6 agrees with the data obtained in [59] (see its figures 9 and 10).

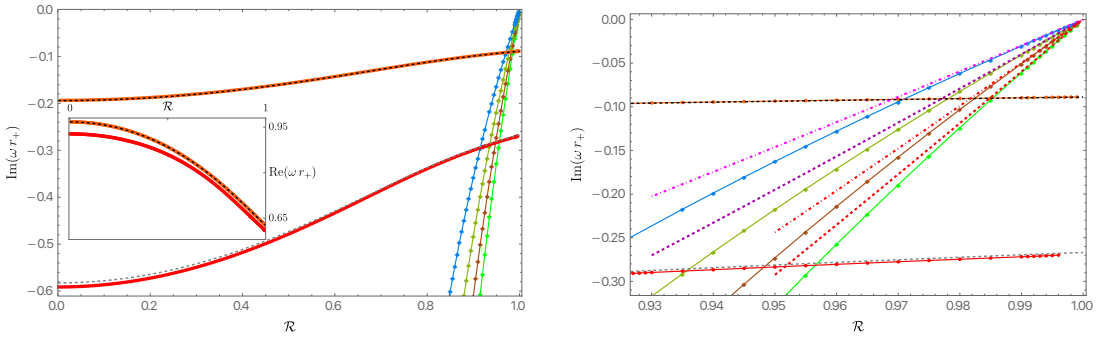

Fig. 2.6: The first few overtone PS and NH families of QNMs with $m = \ell = 2$ for the Reissner-Nordström black hole (*i.e.* the KN black hole with $\Theta = 0$ and thus $Q/r_+ = \mathcal{R}, a = 0$). The orange (red) disk curve is the $n = 0$ ($n = 1$) PS family, while the blue, dark-green, brown and green diamond curves are the NH families with $n = 0$, $n = 1$, $n = 2$ and $n = 3$, respectively. **Left panel:** the main plot displays the imaginary part of the dimensionless frequency as a function of $\mathcal{R}$. On the other hand the inset plot displays the real part of the frequency of the $n = 0$ and $n = 1$ PS families (all the NH families have $\mathrm{Re}\,\omega = 0$ in the RN limit). The black (gray) dashed line that is almost on the top of the $n = 0$ ($n = 1$) PS numerical curve is the analytical WKB approximation $\tilde{\omega}_{\rm WKB}$ given by (2.33). **Right panel:** Zoom of the left panel in the near-extremal region (*i.e.* around $\mathcal{R} \sim 1$ where the NH families approach $\mathrm{Im}\,\tilde{\omega} \to 0$ as $\mathcal{R} \to 1$). This time we also show, as dot-dashed or dashed lines, the near-extremal approximation $\tilde{\omega}_{\rm MAE}$ as from (2.54) for $p = 0, 1, 2, 3$. We see that the latter approximate the NH frequencies very well when we are close to extremality $\mathcal{R} \sim 1$, as expected. (The counterpart of this figure for the Kerr case is displayed in Fig. 2.15).

One final property of the RN QNM spectra that is worth observing in the context of the eigenvalue repulsions discussed in section 2.3.1 is the fact that the several NH overtone frequencies do meet and terminate with $\omega = 0$ at the extremal RN point $\mathcal{R} = 1 = Q/r_+$. So we clearly can have different modes meeting and terminating at the boundary of the RN parameter space.

We will *lock* the color code of Fig. 2.6 for the rest of the figures of this chapter, since this settles a nomenclature to frame our discussions (this rule will not be respected only in Fig. 2.12). That is to say, in all our figures (except Fig. 2.12) we will always use orange and red disks to represent the KN QNM families that continuously connect to the RN $n = 0$ and $n = 1$ PS families of Fig. 2.6, respectively, when $\Theta \to 0$. Similarly, in all our figures we will always use the blue, dark-green, brown and green diamonds to represent the KN QNM families that continuously connect to the RN $n = 0, 1, 2, 3$ NH families of Fig. 2.6, respectively, when $\Theta \to 0$. Moreover, to keep the discussion fluid (but, unfortunately, often misleadingly), we will keep denoting these modes as the PS and NH families. However, we will find that, generically, this sharp distinction between the PS and NH families only holds in (a

neighbourhood of) the Reissner-Nordström limit (*i.e.* for small a/r_+ or small Θ) and is often lost as Θ grows and approaches the Kerr limit ($Q = 0$ *i.e.* $\Theta = \pi/2$). So much that at a certain point it will be more appropriate to denote the different KN QNM families as 'PS-NH' families and their overtones, rather than separate PS or NH families.

To illustrate how the PS and NH families of RN QNM evolve when we extend them to the KN case, we plot the imaginary part (Fig. 2.7) and real part (Fig. 2.8) of the KN QNM frequencies as a function of $\Theta = \arctan(a/Q)$ for the PS (orange disks) and the NH (blue diamonds) families of QNM with $m = \ell = 2$, $n = 0$ for a series of KN families with fixed $\mathcal{R}$. Recall − see (2.5)-(2.6) − that $\mathcal{R}$ is a 'radial' parameter that effectively measures the distance away from extremality, with the extremal KN family being described by $\mathcal{R} = 1$ (and the Schwarzschild solution by $\mathcal{R} = 0$). In Figs. 2.7−2.8 we have selected six KN families at constant $\mathcal{R}$ that illustrate a key feature of the QNM spectra as we progressively move away from extremality. These values are $\mathcal{R} = 0.993$, $\mathcal{R} = 0.992$, $\mathcal{R} = 0.991$, $\mathcal{R} = 0.990$, $\mathcal{R} = 0.985$ and $\mathcal{R} = 0.980$ (please find this value on the top of each plot). For each plot, we increase Θ to follow the $m = \ell = 2, n = 0$ PS and NH QNM families from their RN limit ($\Theta = 0$), shown in Fig. 2.6, all the way up to their Kerr limit ($\Theta = \pi/2$), which will be shown in later Fig. 2.15.

The most relevant property of the system is found in Fig. 2.7, which plots the imaginary part. We see that for $\mathcal{R} \lesssim 0.991$ the blue diamond NH family has smaller $|\mathrm{Im}\,\tilde{\omega}|$ than the orange disk PS family for all values of Θ. However, at $\mathcal{R} \sim 0.991$ (middle-left plot; see in particular the zoom in the inset plot) we see that both the NH and PS curves develop a cusp around $\Theta \sim 0.7$ where the two families approach arbitrarily close. (Hereafter, we denote the piece of the curve to the left/right of this cusp as the '*old left/right branches*' of the PS or NH family). For slightly smaller values of $\mathcal{R}$ the 'old left/right' branches of the NH curve break, and the same happens for the 'old left/right branches' of the PS curve. In particular, for $\mathcal{R} \sim 0.990$ (middle-right plot; see in particular the zoom in the inset plot) we see that the 'old NH left branch' is now smoothly merged with the 'old PS right branch', and a similar trade-off occurs with the other two branches, *i.e.* the 'old PS left branch' is now smoothly merged with the 'old NH right branch'. That is to say, in the small window $0.991 \gtrsim \mathcal{R} \gtrsim 0.990$ the identification of the PS and NH families is no longer clean but fuzzy. Up to the point where it becomes more appropriate to consider the two families of QNMs displayed in Fig. 2.7 as two 'merged PS-NH' mode families that intersect each other by simple crossovers (the $\mathrm{Im}\,\tilde{\omega}$ curves but not the real part) for values $\mathcal{R} < 0.990$, as illustrated in the

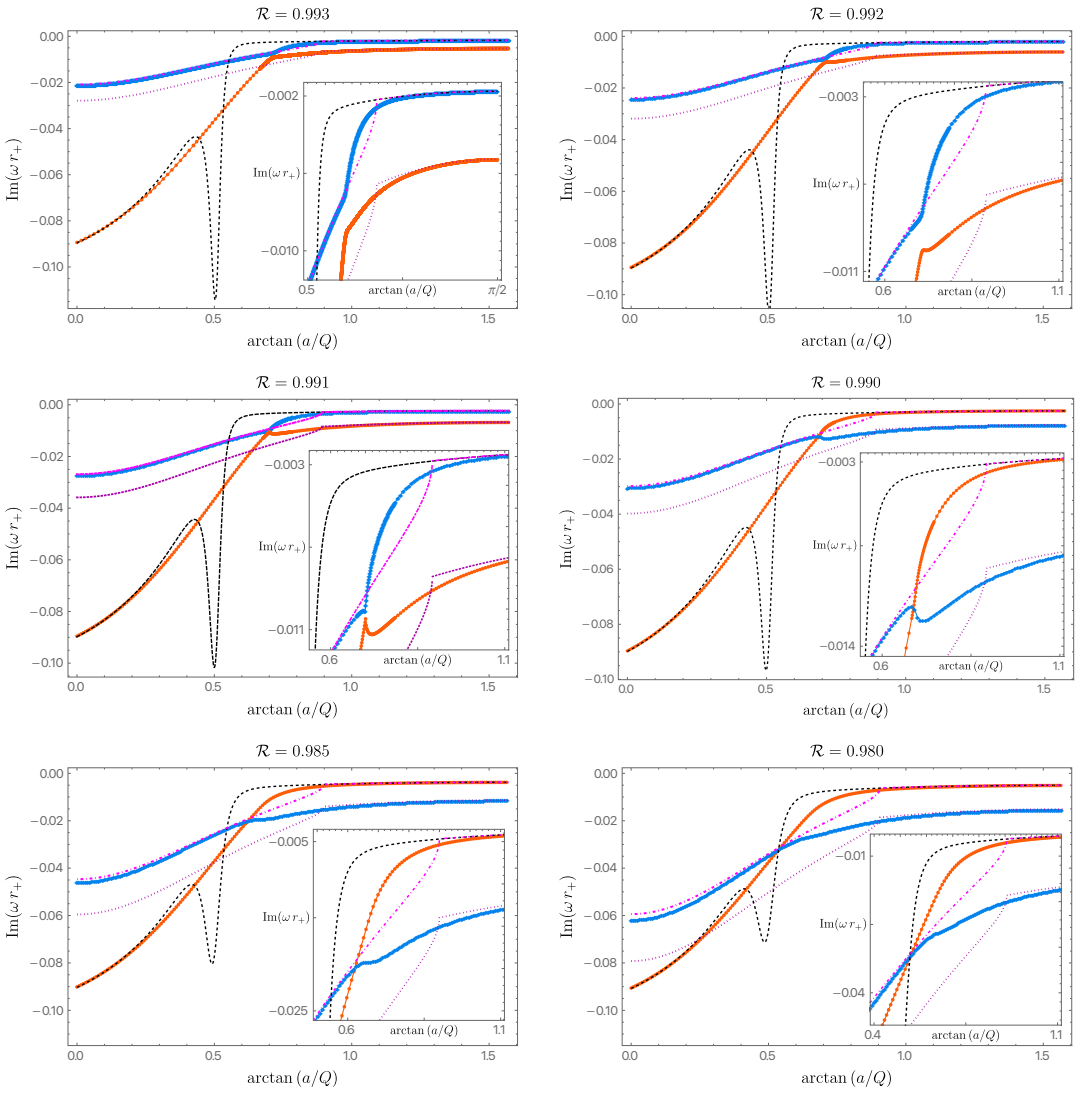

Fig. 2.7: Imaginary part of the frequency as a function of $\Theta = \arctan(a/Q)$ for the PS (orange disks) and the NH (blue diamonds) families of QNMs with $m = \ell = 2, n = 0$ for a KN family with, following the lexicographic order, $\mathcal{R} = 0.993$, $\mathcal{R} = 0.992$, $\mathcal{R} = 0.991$, $\mathcal{R} = 0.990$, $\mathcal{R} = 0.985$ and $\mathcal{R} = 0.980$. We also display the WKB result $\tilde{\omega}_{\rm WKB}$ (dashed black line) and the near-extremal frequency $\tilde{\omega}_{\rm MAE}$ for $p = 0$ (dot-dashed magenta line) and $p = 1$ (dotted dark magenta line).

two bottom plots of Fig. 2.7 for $\mathcal{R} = 0.985$ (bottom-left panel) and for $\mathcal{R} = 0.980$ (bottom-right panel). The non-trivial interaction between the imaginary part of the $m = \ell = 2, n = 0$ NH and PS QNM families is a consequence of the eigenvalue repulsion phenomenon reviewed in the previous section. Eigenvalue repulsions were previously identified in [18] for gravito-electromagnetic perturbations of KN, and we see here that they are also present in the scalar field QNM spectra. The polar parametrisation adopted here for the KN black hole is particularly useful to study this phenomenon.

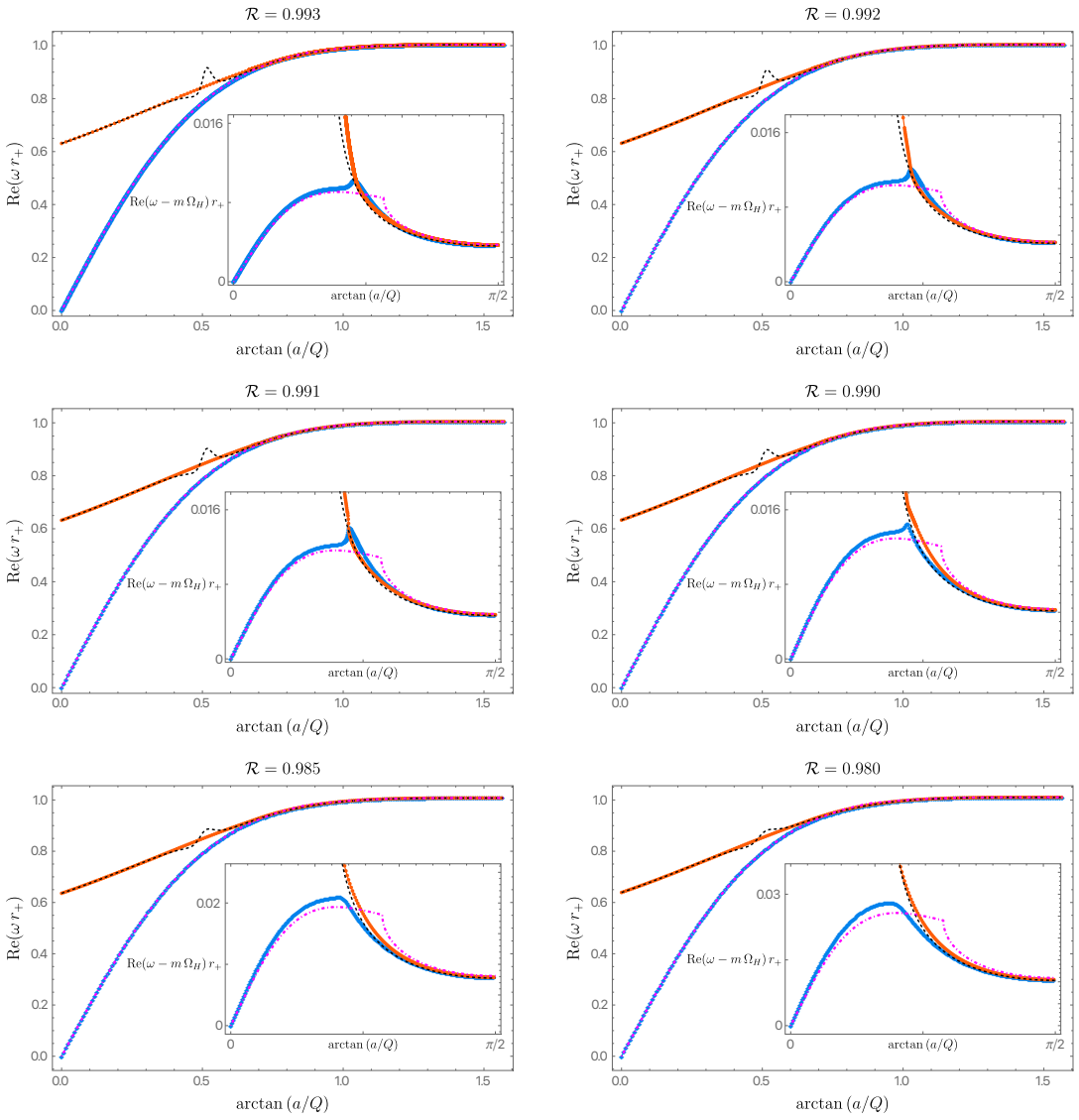

Fig. 2.8: This series of figures is for the same cases reported in Fig. 2.7 but this time we plot the real part of the frequency as a function of Θ for the PS (orange disks) and the NH (blue diamonds) families of QNMs with $m = \ell = 2, n = 0$ for a KN family with, following the lexicographic order, $\mathcal{R} = 0.993$, $\mathcal{R} = 0.992$, $\mathcal{R} = 0.991$, $\mathcal{R} = 0.990$, $\mathcal{R} = 0.985$ and $\mathcal{R} = 0.980$. We also display the WKB result $\tilde{\omega}_{\rm WKB}$ (dashed black line) and the near-extremal frequency $\tilde{\omega}_{\rm MAE}$ for $p = 0$ (dot-dashed magenta line) and $p = 1$ (dotted dark magenta line). In the inset plots, we still show the real part of the frequency but this time measured with respect to the superradiant bound $m\Omega_H$.

Three important observations are still in order. First, note that for small values of Θ, and for any value of $\mathcal{R}$, it is true that the two families of QNM can be unequivocally traced back to the PS and NH QNM families of the RN black hole when $\Theta \to 0$. It is only at intermediate values of Θ (roughly, $\Theta \gtrsim 0.5$, say) that the two curves approximate and develop cusps (for $0.992 \gtrsim \mathcal{R} \gtrsim 0.990$) and finally break/merge to form the two 'PS-NH' curves (for $\mathcal{R} \lesssim 0.990$).

Secondly, notice that the formation of cusps and the associated breakup/merge process between two branches of the old PS and NH families (described above) only occurs at the level of the imaginary part of the frequencies. Indeed, in Fig. 2.8 we analyse the evolution of the real part of the frequency as a function of Θ for the same fixed values of $\mathcal{R}$ as those displayed in Fig. 2.7 and we conclude that nothing special occurs to the real part of the frequency as $\mathcal{R}$ decreases. In particular there is no formation of cusps or breakups/mergers in the range $0.992 \gtrsim \mathcal{R} \gtrsim 0.990$. As discussed in section 2.3.1, this is consistent with the fact that for a 2-parameter family of black holes (KN in our case), two eigenvalues can coincide only at a isolated point (or a discrete set of isolated points) in the parameter space (where the analogue of the two conditions (2.57) are satisfied). Elsewhere, except possibly at a portion of the extremal KN boundary where the modes terminate, the real and imaginary part of the frequency of one family of QNMs cannot be simultaneously the same as those of another QNM family. If we are to summarize our key findings in a single sentence, our numerical data strongly suggests that PS and NH modes can meet and terminate at the portion of the extremal boundary described by $\mathcal{R} = 1$ and $\Theta_\star \lesssim \Theta \leqslant \pi/2$ (with $\Theta_\star \sim 0.881$), but we find no eigenvalue crossing anywhere else away from extremality. Interestingly, the repulsions around the portion of the extremal boundary where the PS and NH modes do (or do attempt to) meet and terminate creates ripple effects relatively far away that can produce intricate interactions between the imaginary part of the frequency of modes of two QNM families like those observed in Fig. 2.7 that could not be anticipated before doing the actual computation. (We will analyse key aspects of this discussion in more detail later when we discuss Fig. 2.12).

There is a third observation that emerges from Figs. 2.7−2.8 which is crucial to interpret the nature of the QNM families. In the plots of these figures we also show the higher-order WKB frequency $\tilde{\omega}_{\rm WKB}$ (dashed black line) as given by (2.33) with $p = 0$, and the near-horizon frequency $\tilde{\omega}_{\rm MAE}$ of (2.54) for $p = 0$ (dot-dashed magenta line) and $p = 1$ (dotted dark magenta line). For small Θ, and independently of the value of $\mathcal{R}$, $\tilde{\omega}_{\rm WKB}$ approximates the orange disk PS curve well; moreover, (2.54) with $p = 0$ is an excellent approximation for the blue diamond NH curve. This is what we expect from the discussions of sections 2.2.1 and 2.2.2. In particular, we used these criteria to unambiguously identify the PS and NH families of modes in the RN limit ($\Theta \to 0$). The situation is however much more intricate in the opposite Kerr limit ($\Theta = \pi/2$). To start with, for $\mathcal{R} \gtrsim 0.991$ (see *e.g.* the first three plots of Figs. 2.7−2.8 for $\mathcal{R} = 0.993, 0.992, 0.991$), the black-dashed $\tilde{\omega}_{\rm WKB}$ describes the orange PS modes well for small Θ, but (and this comes as a surprise)

it fails to do so at large Θ! Instead, at large Θ, $\tilde{\omega}_{\rm WKB}$ describes the blue NH family very well (in particular, in the Kerr limit $\Theta \to \pi/2$)! This is a first indication that the clean criterion used to classify and distinguish PS and NH families in the RN limit becomes absolutely misleading as we approach the Kerr limit. On the other hand, without surprise, in this range $\mathcal{R} \gtrsim 0.991$ the dot-dashed magenta $\tilde{\omega}_{\rm MAE}$ (with $p = 0$) is an excellent approximation to the blue NH family for all $0 \leqslant \Theta \leqslant \pi/2$. However, $\tilde{\omega}_{\rm MAE}$ coincides with $\tilde{\omega}_{\rm WKB}$ for large Θ! This is a second indication that the RN criteria for the PS/NH distinction does not extend to the Kerr limit. Still in the range $\mathcal{R} \gtrsim 0.991$ we have yet another surprise: for large Θ, the orange PS family, that is not well approximated by $\tilde{\omega}_{\rm WKB}$, is instead well described by $\tilde{\omega}_{\rm MAE}$ ... with $p = 1$ (dotted dark magenta line)!! So not only is the orange PS curve not well described by the eikonal/WKB approximation, but it is instead well described by a *higher overtone* MAE frequency: this orange disk family starts at $\Theta = 0$ as a $n = 0$ family but terminates at $\Theta = \pi/2$ with radial overtone $n = 1$![9] Summarizing, for $\mathcal{R} \gtrsim 0.991$, the mode we naively called the ground state NH family (in the RN limit) is simultaneously described by $p = 0$ $\tilde{\omega}_{\rm WKB}$ and $p = 0$ $\tilde{\omega}_{\rm MAE}$ at large Θ, while the mode we naively called the ground state PS family (in the RN limit) is described by $p = 1$ $\tilde{\omega}_{\rm MAE}$ (and $p = 1$ $\tilde{\omega}_{\rm WKB}$) at large Θ. The three conclusive facts above confirm that the criteria used to classify and distinguish QNM families in the RN limit cannot be extended without contradictions/inconsistencies to high values of Θ and, in particular, to the Kerr limit. The PS/NH classification at the RN limit remains valid for small values of Θ but gets absolutely misleading at high values of Θ. Up to the point that it should be dropped because it simply cannot be formulated in equal terms in the Kerr limit.

If not already sufficiently intricate, another level of complexity is added when we move to the region $0.991 \gtrsim \mathcal{R} \gtrsim 0.990$ where the phenomenon of eigenvalue repulsion occurs, as already described in detail previously. Moving further away from extremality, for $\mathcal{R} \leqslant 0.990$, the modes that previously repelled now simply cross (i.e. the imaginary part of the frequency crosses but not the real part) as we increase Θ. One now finds that it is the orange disk mode − that we initially (in the RN limit) called the PS family − that is simultaneously described by $p = 0$ $\tilde{\omega}_{\rm WKB}$ and $p = 0$ $\tilde{\omega}_{\rm MAE}$ at large Θ (this is possible because the original PS modes approach $\mathrm{Im}\,\tilde{\omega} = 0$ at extremality for large Θ)! And the blue diamond curve that was initially (*i.e.* at the RN limit) denoted as the ground state NH family is the one that is now well approximated by $\tilde{\omega}_{\rm MAE}$ with $p = 1$ (not $p = 0$) at large Θ! Altogether,

[9]Note that here we are not including discussions of the $p = 1$ $\tilde{\omega}_{\rm WKB}$. This will be discussed in Figs. 2.13−2.14.

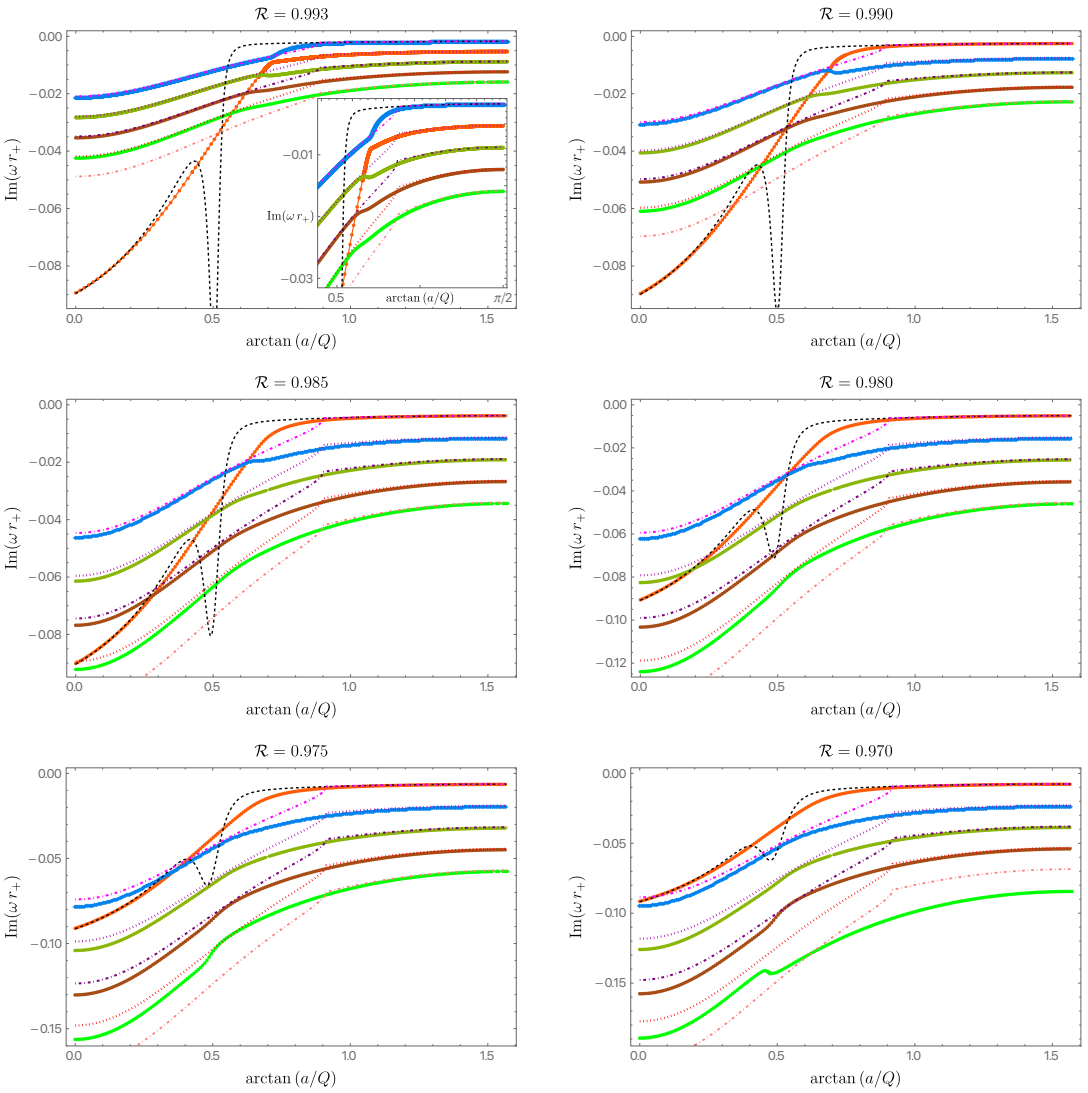

Fig. 2.9: Imaginary part of the frequency as a function of $\Theta = \arctan(a/Q)$ for the PS (orange disks) and the $n = 0, 1, 2, 3$ NH (blue, dark-green, brown, green diamonds) families of QNM with $m = \ell = 2$ for a KN family with $\mathcal{R} = 0.993$, $\mathcal{R} = 0.990$, $\mathcal{R} = 0.985$, $\mathcal{R} = 0.980$, $\mathcal{R} = 0.975$ and $\mathcal{R} = 0.970$ (following the lexicographic order). We also display the WKB result $\tilde{\omega}_{\rm WKB}$ (dashed black line) and the near-extremal frequency $\tilde{\omega}_{\rm MAE}$ for $p = 0, 1, 2, 3$ (dot-dashed magenta, dotted dark magenta, dot-dashed purple, dotted pink, dot-dashed pink lines, respectively).

and with hindsight, it would have been more appropriate to denote all the QNM families simply as an entangled 'PS-NH' family and its radial overtones, with the photon sphere and near-horizon nature of the modes unequivocally disentangling only for small values of Θ as one approaches the Reissner-Nordström limit.

In Figs. 2.7−2.8 we have only displayed the ground state modes, *i.e.* the first overtone ($n = 0$) of the PS family and the first overtone ($n = 0$) of the NH family (as we unambiguously classify them in the RN limit). To further explore the properties of our system, in Fig. 2.9 we display the $n = 0$ PS (orange disks) and $n = 0$ NH

(blue diamonds) curves that were already presented in Fig. 2.7 but, this time, we additionally display the $n = 1, 2, 3$ NH (dark-green, brown, green diamonds) families of QNM with $m = \ell = 2$ for a KN family with $\mathcal{R} = 0.993$, $\mathcal{R} = 0.990$, $\mathcal{R} = 0.985$, $\mathcal{R} = 0.980$, $\mathcal{R} = 0.975$ and $\mathcal{R} = 0.970$ (following the lexicographic order). Moreover, we also display the $p = 0$ WKB result $\tilde{\omega}_{\rm WKB}$ (dashed black line) and the near-extremal frequency $\tilde{\omega}_{\rm MAE}$ for $p = 0, 1, 2, 3$ (dot-dashed magenta, dotted dark magenta, dot-dashed purple, dotted pink, dot-dashed pink lines, respectively). As pointed out above when discussing Fig. 2.7, we see that for $\mathcal{R} \leqslant 0.990$, the blue diamond curve is well approximated by $\tilde{\omega}_{\rm MAE}$ with $p = 0$ for small Θ and then by $\tilde{\omega}_{\rm MAE}$ with $p = 1$ for large Θ. A similar behavior is found in the higher overtone NH families. Indeed, near extremality, *i.e.* for large $\mathcal{R}$, the $n = 1, 2, 3$ NH curves are well described by $\tilde{\omega}_{\rm MAE}$ with $p = 1, 2, 3$ for small Θ but, for large Θ, then are instead well described by $\tilde{\omega}_{\rm MAE}$ with $p = 2, 3, 4$. That is to say, the family that at RN is described by the MAE result with overtone p turns out to become, at large Θ, well approximated by the MAE result with overtone $p + 1$!

So far we have focused our attention in the parameter region $\mathcal{R} \leqslant 0.993$. But we might also ask what happens when we approach extremality ($\mathcal{R} = 1$) even further. This question is addressed in Figs. 2.10-2.11 (where the latter plots are to be seen as a continuation of the former) which describes what happens for $0.993 < \mathcal{R} \leqslant 0.999$, namely for $\mathcal{R} = 0.9940, 0.9950, 0.9955, 0.9960,\ 0.9965, 0.9970$ (Fig. 2.10) and $\mathcal{R} = 0.9975, 0.9980, 0.9985, 0.9990$ (Fig. 2.11); note that unlike in the previous figures here we are increasing $\mathcal{R}$ as we move along the lexicographic order. We see that further eigenvalue repulsions happen. Indeed, when moving from $\mathcal{R} = 0.9950$ (top-right panel of Fig. 2.10) to $\mathcal{R} = 0.9955$ (middle-left panel), one notes an eigenvalue repulsion between the $n = 0$ PS family (orange curve) and the $n = 1$ NH family (dark-green curve). Then, when moving from $\mathcal{R} = 0.9965$ (bottom-left panel of Fig. 2.10) to $\mathcal{R} = 0.9970$ (bottom-right panel), one observes an eigenvalue repulsion between the $n = 0$ PS family (orange curve) and the $n = 2$ NH family (brown curve). Continuing our analysis now in Fig. 2.11, when moving from $\mathcal{R} = 0.9975$ (top-left panel of Fig. 2.11) to $\mathcal{R} = 0.9980$ (top-right panel), we see a further eigenvalue repulsion this time between the $n = 0$ PS family (orange curve) and the $n = 3$ NH family (green curve). Finally, we see clear evidence that a series of further eigenvalue repulsions keep happening at an increasingly higher rate (in the sense that small increments $\mathcal{R}$ produce more repulsions) as we further approach $\mathcal{R} = 1$. Indeed, in the bottom panel of Fig. 2.11 we find that at $\mathcal{R} = 0.9985$, for large Θ, the $n = 0$ PS curve is now below the $n = 5$ NH curve and then, at $\mathcal{R} = 0.9990$, for large Θ, the $n = 0$ PS curve is now below the $n = 8$ NH

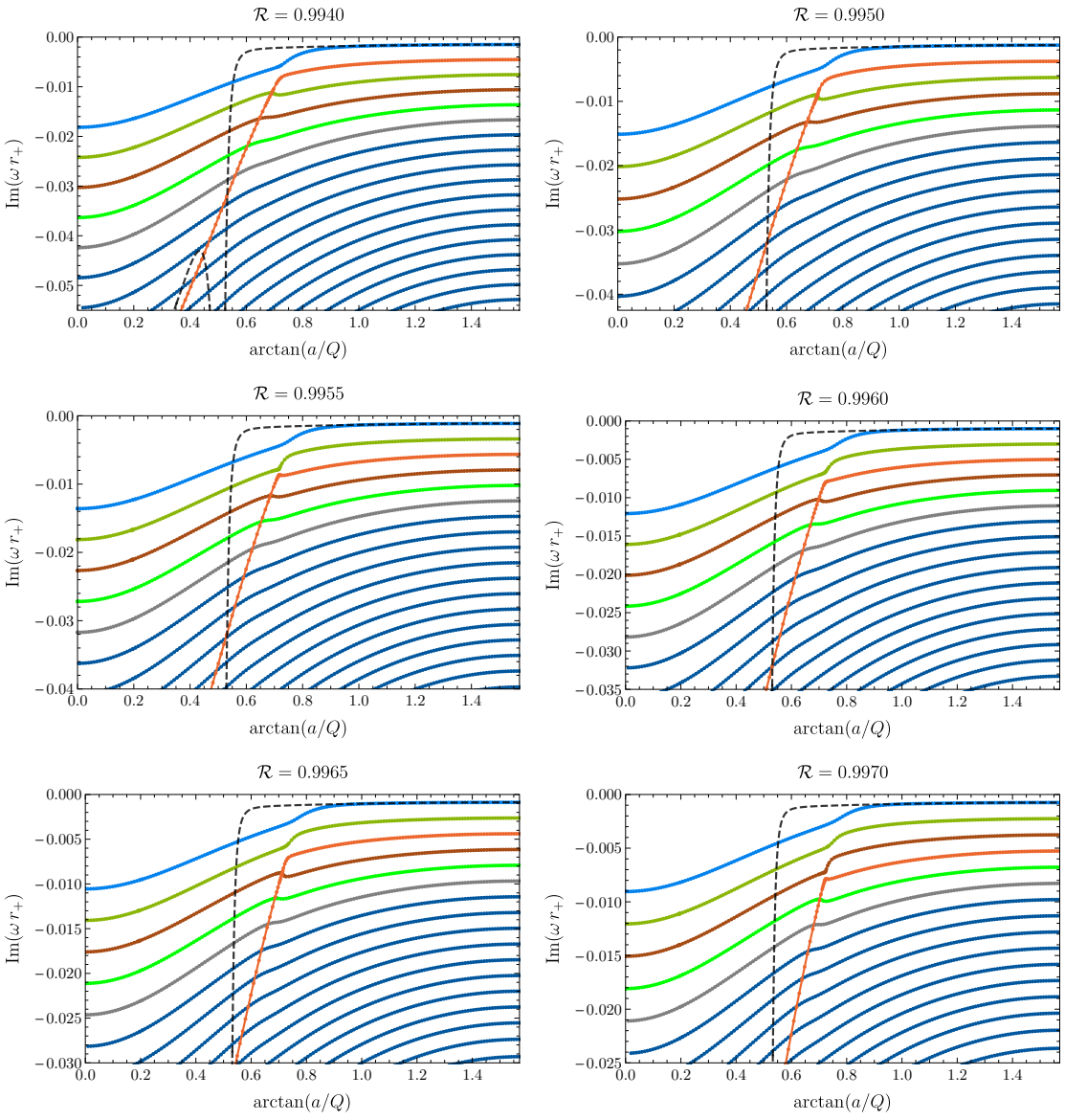

Fig. 2.10: Imaginary part of the frequency as a function of $\Theta = \arctan(a/Q)$ for the $n = 0$ PS (orange disks) and the $n = 0, 1, 2, 3, 4, \cdots, 16$ NH (blue, dark-green, brown, green and, for $n \geqslant 4$, dark-blue diamonds) families of QNM with $m = \ell = 2$ for a KN family with $\mathcal{R} = 0.9940$, $\mathcal{R} = 0.9950$, $\mathcal{R} = 0.9955$ and $\mathcal{R} = 0.9960$, $\mathcal{R} = 0.9965$ and $\mathcal{R} = 0.9970$ (following the lexicographic order). We also display the WKB result $\tilde{\omega}_{\mathrm{WKB}}$ for $n = 0$ (dashed black line). (This series of plots continues in Fig. 2.11 for larger $\mathcal{R}$).

curve. This overwhelmingly suggests that as $\mathcal{R} \to 1$, there is a (possibly infinite) cascade of eigenvalue repulsions where, for large Θ, the $n = 0$ PS curve gets below the n-th overtone NH curve for an increasingly higher value of n (possibly with $n \to \infty$).

Altogether, from the analyses of Figs. 2.7-2.11 there is a fundamental property that emerges and that should be further highlighted and discussed. The orange

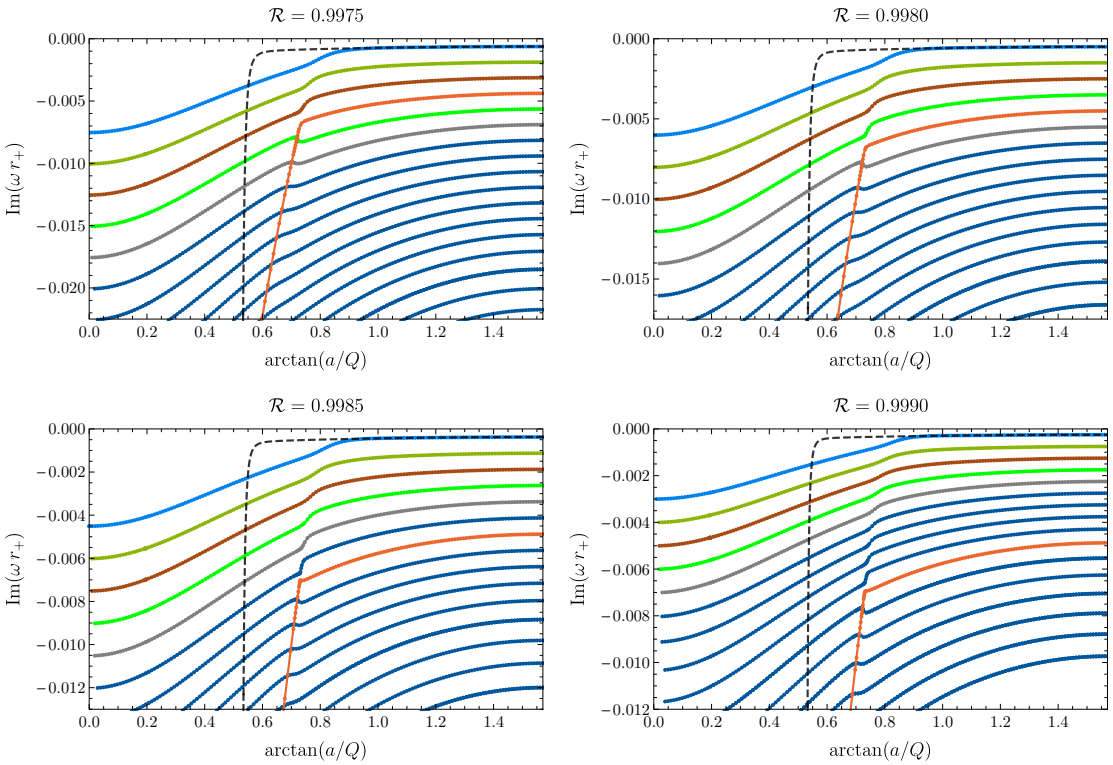

Fig. 2.11: Continuation of Fig. 2.10, this time for KN families with $\mathcal{R} = 0.9975$, $\mathcal{R} = 0.9980$, $\mathcal{R} = 0.9985$ and $\mathcal{R} = 0.9990$ (following the lexicographic order).

$n = 0$ photon sphere mode (as we identify it in the RN limit and trace forward for higher values of Θ) seems to be trying to reach $\mathrm{Re}\,\tilde{\omega} = m\tilde{\Omega}_H^{\mathrm{ext}}$ and $\mathrm{Im}\,\tilde{\omega} = 0$ at extremality and for sufficiently large Θ — note that the scale of the vertical axis is changing between Figs 2.7-2.11. This would be in line with the WKB analysis (and its NH limit) which predicts that PS modes should indeed have this behaviour as $\mathcal{R} \to 1$ and for $\Theta \geqslant \Theta_\star \gtrsim \Theta_\star^{\mathrm{WKB}} > \pi/6$ (see the dashed WKB line in previous figures), where $\Theta_\star$ was introduced in the second to last paragraph of section 2.3.1 (recall also footnote 8). But the second KN family of QNMs − namely the NH family − already sits at $\mathrm{Re}\,\tilde{\omega} = m\tilde{\Omega}_H^{\mathrm{ext}}$ and $\mathrm{Im}\,\tilde{\omega} = 0$ at extremality (and for any value of $0 \leqslant \Theta \leqslant \pi/2$, not only for $\Theta_\star \leqslant \Theta \leqslant \pi/2$). So, making contact with the three possible scenarios enumerated in the end of section 2.3.1, our numerical data seems to be suggesting that in the KN QNM spectra there are *no* eigenvalue crossings in isolated *non*-extremal points of the parameter space. Instead, we are seeing evidence that two families of eigenvalues (the PS and NH modes as we identify them in the RN limit and their overtones) can meet and *terminate* along a continuous portion of the KN extremal boundary (very much like several QNM overtones already meet and terminate at the extremal endpoint of the RN and Kerr black holes). To gather more evidence in favour of this scenario, it is thus worthy to analyse in more detail how the PS modes (attempt to) force their pathway towards

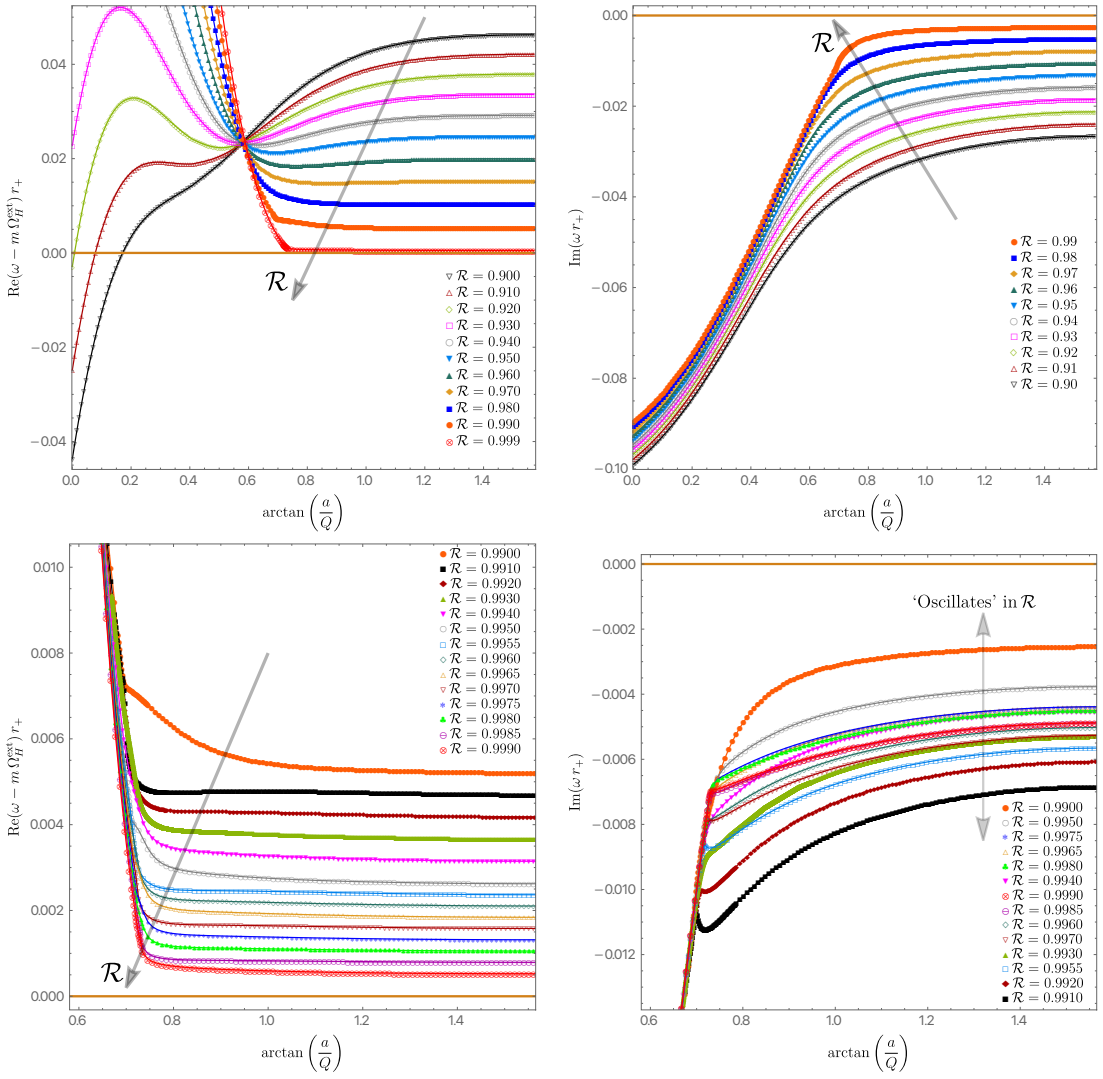

Fig. 2.12: Information about the real (left) and imaginary (right) parts of the photon sphere (PS) frequency as a function of Θ for several fixed values of $\mathcal{R}$. Namely, in the top panels ones has curves for $0.90 \leqslant \mathcal{R} \leqslant 0.999$ (top-left) or for $0.90 \leqslant \mathcal{R} \leqslant 0.99$ (top-right); see exact values of $\mathcal{R}$ and associated color code in the legends of the plots. On the other hand, in the bottom panels we focus our attention closer to extremality, in the region $0.990 \leqslant \mathcal{R} \leqslant 0.999$.

$\tilde{\omega} = m\tilde{\Omega}_H^{\mathrm{ext}}$ at extremality. For that we collect some of the data of Figs. 2.7-2.11 in a single plot where we show the evolution of the PS mode frequency as a function of Θ for several fixed values of $\mathcal{R}$. This is done in Fig. 2.12. In the top panels we show the evolution of the PS family when we are not too close to extremality, namely for $0.90 \leqslant \mathcal{R} \leqslant 0.99$ (in intervals of 0.01); the same monotonic behaviour is observed in the evolution for smaller values of $\mathcal{R}$ but we do not show it here (see later Fig. 2.16 with the full phase space). On the other hand, in the bottom panels we plot the same quantities but this time for families of KN black holes that are even closer to extremality in the region $0.990 \leqslant \mathcal{R} \leqslant 0.999$, namely we plot several

curves with constant $\mathcal{R}$ from 0.990-0.995 in intervals of 0.001 and 0.996-0.999 in intervals of 0.0005 (see legends in the plots). In the right panels of Fig. 2.12 we plot the imaginary part of the frequency, $\mathrm{Im}\,\tilde{\omega}$, as a function of Θ. On the other hand, in the left panels, instead of simply plotting the real part of the frequency, we plot $\mathrm{Re}\,\tilde{\omega} - m\tilde{\Omega}_H^{\rm ext}$ where $\tilde{\Omega}_H^{\rm ext}$ is the extremal value ($\mathcal{R} = 1$) of the frequency for a given Θ as given by (2.4)-(2.6): $\tilde{\Omega}_H^{\rm ext} = \alpha_{\rm ext}/(1+\alpha_{\rm ext}^2) = \sin\Theta/(1+\sin^2\Theta)$. This quantity has the advantage that it vanishes when $\mathrm{Re}\,\tilde{\omega} \to m\tilde{\Omega}_H^{\rm ext}$ at extremality.

From the top panels of Fig. 2.12 we see that the PS frequency indeed attempts to approach $\mathrm{Re}\,\tilde{\omega} = m\tilde{\Omega}_H^{\rm ext}$ and $\mathrm{Im}\,\tilde{\omega} = 0$ for $\Theta > \Theta_\star$ as we keep decreasing the distance to extremity (i.e. as we approach $\mathcal{R} = 1$ from below), where $\Theta_\star$ is roughly around 0.8 (doing a rough extrapolation of the $\mathcal{R} = 0.999$ curve all the way up to $\mathrm{Im}\,\tilde{\omega} = 0$). But around $\mathcal{R} \sim 0.99$, the system 'realizes' that the PS modes are dangerously approaching the NH modes and eigenvalues repulsions (reported in Figs. 2.7-2.11) kick in. In more detail, for $\mathcal{R} > 0.9$, the bottom-left panel of Fig. 2.12 shows that, interestingly, the real part of the PS frequencies still keeps monotonically approaching $m\tilde{\Omega}_H^{\rm ext}$ as $\mathcal{R}$ increases from 0.990 to 0.999 following a pattern that seems to be blind to any worries of level repulsion. But, perhaps to avoid eigenvalue crossing in the complex plane as $\mathcal{R} \to 1$, the $\mathrm{Im}\,\tilde{\omega}$ (see bottom-right panel) reacts and starts 'oscillating' in $\mathcal{R}$, i.e. for $\mathcal{R} \gtrsim 0.990$ one finds that $|\mathrm{Im}\,\tilde{\omega}|$ no longer decreases monotonically towards zero with increasing $\mathcal{R}$. Instead, for a small increment of $\mathcal{R}$ (and fixed Θ), sometimes $|\mathrm{Im}\,\tilde{\omega}|$ decreases and other times it increases in such a way that in practice (for the values of $\mathcal{R} \leqslant 0.999$ that we computed), for $\Theta > \Theta_\star$, it stays in between the top orange disk curve (with $\mathcal{R} = 0.990$) and the bottom black square curve (with $\mathcal{R} = 0.991$). This is eigenvalue repulsion in action at its best.

What happens if we approach even further extremality, i.e. if we plunge into the region $0.999 < \mathcal{R} \leqslant 1$? We have not attempted to explore this region. To put into context, in the Kerr limit, the line of constant $\mathcal{R} = a/r_+ = 0.999$ already corresponds, in mass units, to $a/M \simeq 0.999999$. So we have not attempted to increase this value even further since it becomes very costly computationally. Furthermore, whether the PS modes do or do not reach $\mathrm{Im}\,\omega \to 0$ and $\mathrm{Re}\,\omega \to m\Omega_H^{\rm ext}$ at extremality for $\Theta \geqslant \Theta_\star \simeq 0.881$ is a lesser question, since even if it does, it does so with an $|\mathrm{Im}\,\tilde{\omega}|$ that is always larger than (or equal to) the $|\mathrm{Im}\,\tilde{\omega}|$ of the NH modes (i.e. they approach at smaller rate) and thus they are not the dominant modes in this region of the parameter space. It should however be noticed that, in the QNM spectra of Kerr, [58] report the existence of modes whose $|\mathrm{Im}\,\tilde{\omega}|$ has 'damped oscillations' in $\mathcal{R}$ and approaches zero at extremality

(see the discussion of figure 3 of [58]). Moreover, similar damped oscillations of $\mathrm{Im}\,\tilde{\omega}$ as extremality is approached was observed in the (charged) scalar field QNM spectra of Reissner-Nordström-de Sitter [189] (see discussion of figures 9-12 of [189]; especially the latter). So we cannot exclude the possibility (also very much suggested by the WKB analysis of section 2.2.1) that the 'oscillations' observed in the bottom-right plot of Fig. 2.12 persist all the way to extremality with an exponential decay envelope (sufficiently close to extremality) such that the curves ultimately hit $\mathrm{Im}\,\omega \to 0$ and $\mathrm{Re}\,\omega \to m\Omega_H^{\rm ext}$ at extremality ($\mathcal{R}=1$) for $\Theta > \Theta_\star$. It is very tempting to claim it is the case and we believe it is for the above reasons. If so, the PS and NH modes meet and terminate, with $\mathrm{Im}\,\omega \to 0$ and $\mathrm{Re}\,\omega \to m\Omega_H^{\rm ext}$, at extremality $\mathcal{R}=1$ for $\Theta > \Theta_\star$ (this is the third possibility enumerated in the end of our discussion of section 2.3.1). A similar behaviour was observed for the gravito-electromagnetic modes of KN [16, 18].

For completeness, we may now ask whether the eigenvalue repulsions observed in Figs. 2.7-2.12 between the $n=0$ PS (orange disks) and NH families also extend to the higher PS overtones, namely for $n=1$ (or higher). The answer is yes, and in fact the eigenvalue repulsions in the $n=1$ PS family are already very visible further away from extremality. In detail, we address this question in Figs. 2.13−2.14, where the latter plots are to be seen as a continuation of the former. In particular, Fig. 2.13 displays the cases $\mathcal{R}=0.975$, $\mathcal{R}=0.970$, $\mathcal{R}=0.965$, $\mathcal{R}=0.960$, $\mathcal{R}=0.955$ and $\mathcal{R}=0.950$ (following the lexicographic order) and then Fig. 2.14 continues this series of plots to even smaller values of $\mathcal{R}$ for the values $\mathcal{R}=0.940$, $\mathcal{R}=0.935$, $\mathcal{R}=0.930$, $\mathcal{R}=0.925$, $\mathcal{R}=0.920$ and $\mathcal{R}=0.915$.[10] In these figures we always plot the imaginary part of the frequency as a function of Θ for the $m=\ell=2$ modes, and we display the $n=0$ (orange disks) and $n=1$ (red disks) PS families together with the $n=0,1,2,3$ NH (blue, dark-green, brown and green diamonds) families of QNMs. Moreover, we also plot the higher-order WKB frequency $\tilde{\omega}_{\rm WKB}$ − as given by (2.33) − with $p=0$ (dashed black line) and with $p=1$ (dashed gray line), and the near-extremal frequency $\tilde{\omega}_{\rm MAE}$ − as given by (2.54) − for $p=0,1,2,3$ (dot-dashed magenta, dotted dark magenta, dot-dashed purple, dotted pink, dot-dashed pink lines, respectively). We conclude that a series of eigenvalue repulsions (with characteristic cusp formation followed by breakup/merge of distinct branches), similar to those described in Fig. 2.7, do occur, namely between:

[10] Recall that the color code was introduced in Fig. 2.6 for the RN case ($\Theta=0$). Then we *locked* this color code and, at fixed $\mathcal{R}$, we increase Θ to follow each QNM family from its RN limit ($\Theta=0$) until its Kerr limit ($\Theta=\pi/2$). Further recall that the nomenclature PS/NH refers to the nature of the modes in the RN limit.

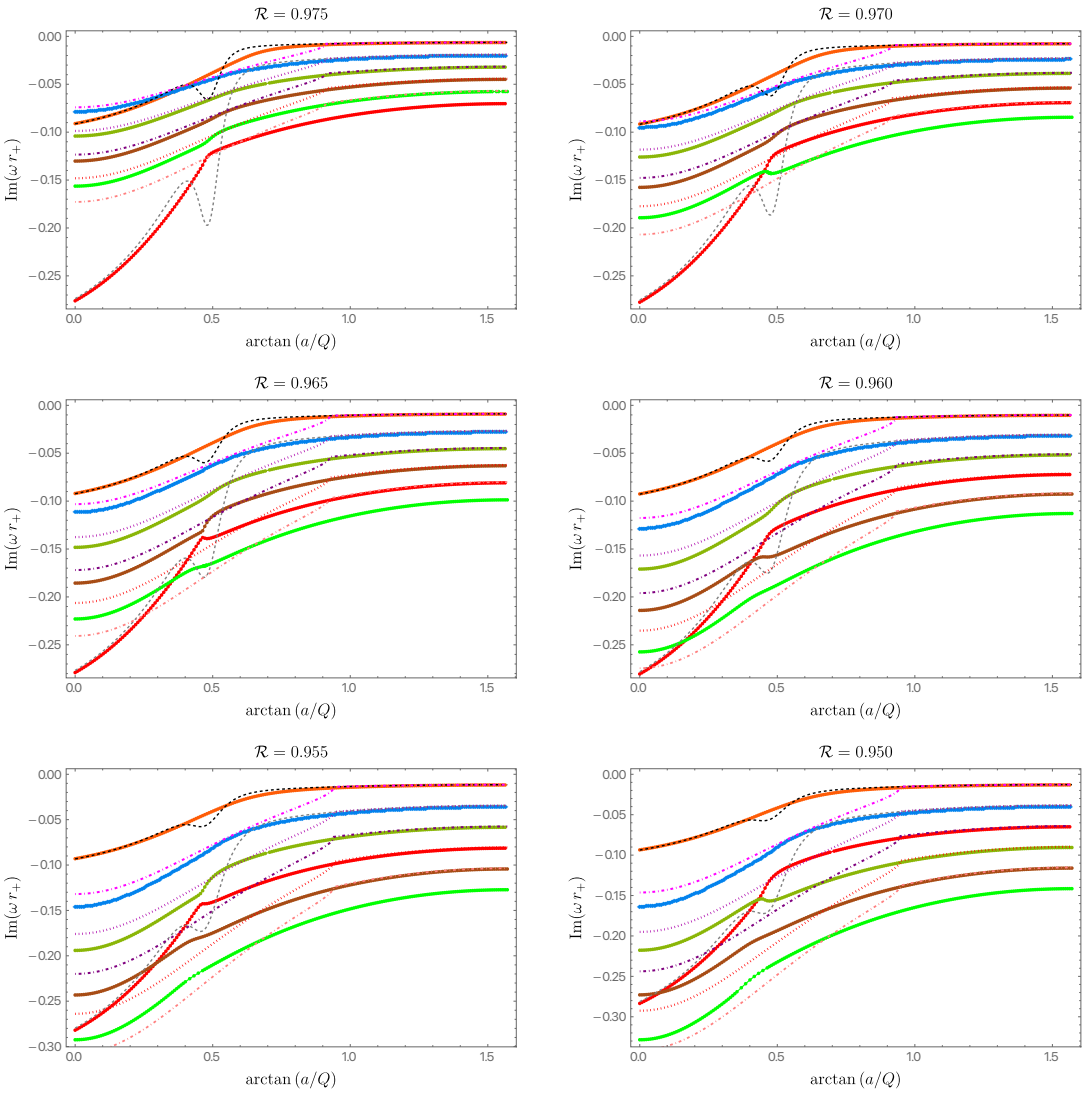

Fig. 2.13: Imaginary part of the frequency as a function of $\Theta = \arctan\,(a/Q)$ for the $n = 0$ PS (orange disks), $n = 1$ PS (dark-red disks; not present in Figs. 2.7−2.9) and the $n = 0, 1, 2, 3$ NH (blue, dark-green, brown and green diamonds) families of QNMs with $m = \ell = 2$ for a KN family with $\mathcal{R} = 0.975$, $\mathcal{R} = 0.970$, $\mathcal{R} = 0.965$, $\mathcal{R} = 0.960$, $\mathcal{R} = 0.955$ and $\mathcal{R} = 0.950$ (following the lexicographic order). We also display the WKB result $\tilde{\omega}_{\rm WKB}$ for $n = 0, 1$ (dashed black and dashed gray lines, respectively) and the near-extremal frequency $\tilde{\omega}_{\rm MAE}$ for $p = 0, 1, 2, 3$ (dot-dashed magenta, dotted dark magenta, dot-dashed purple, dotted pink, dot-dashed pink lines, respectively). (This series of plots continues in Fig. 2.14 for smaller $\mathcal{R}$).

- The $n = 1$ PS red curve and $n = 3$ NH green curve ($0.975 \gtrsim \mathcal{R} \gtrsim 0.970$ in Fig. 2.13).

- The $n = 1$ PS red curve and $n = 2$ NH brown curve ($0.965 \gtrsim \mathcal{R} \gtrsim 0.960$ in Fig. 2.13).

- The $n = 1$ PS red curve and $n = 1$ NH dark-green curve ($0.955 \gtrsim \mathcal{R} \gtrsim 0.950$ in Fig. 2.13).

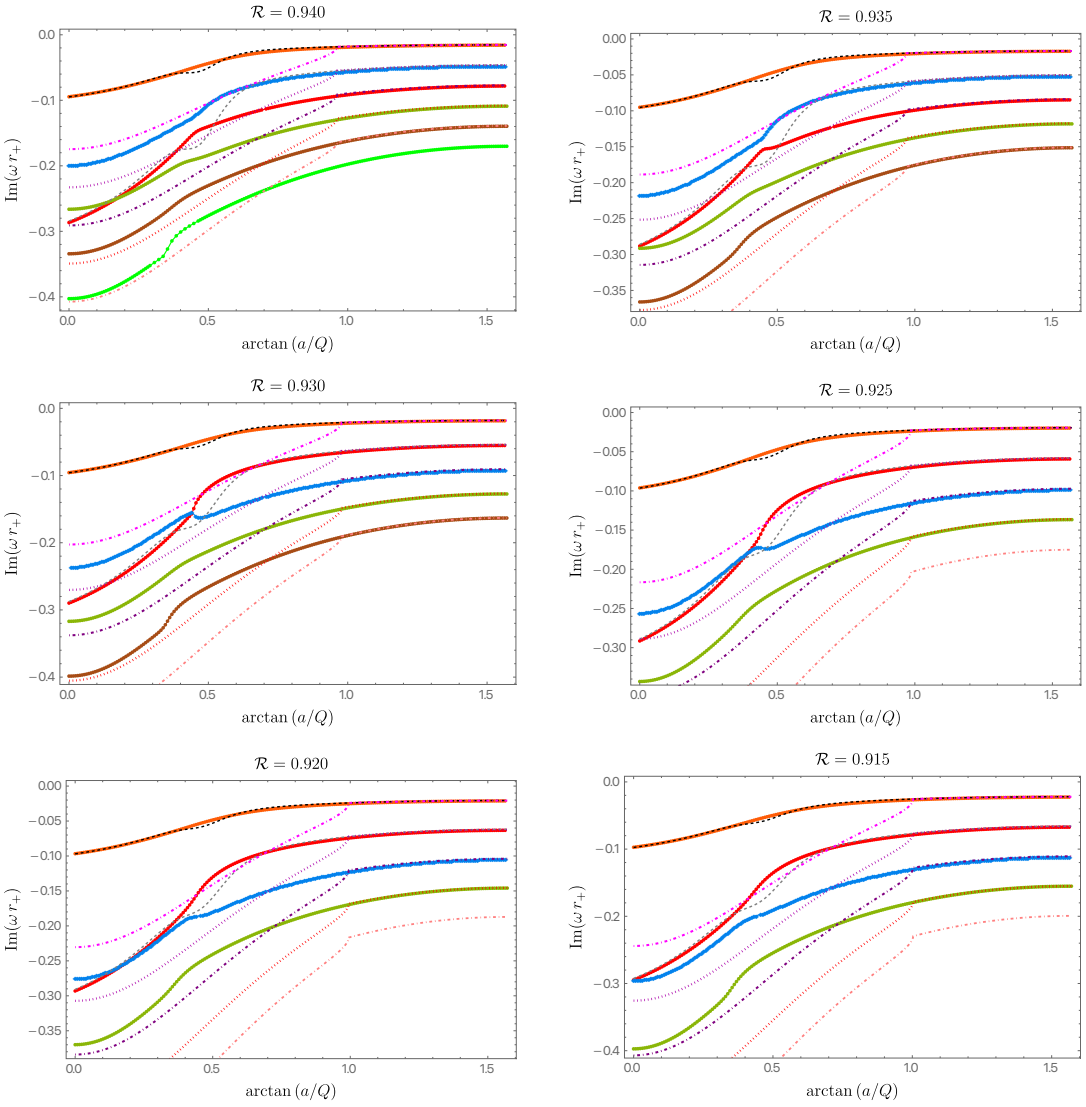

Fig. 2.14: This series of plots continues the one started in Fig. 2.13 but this time for $\mathcal{R} = 0.940$, $\mathcal{R} = 0.935$, $\mathcal{R} = 0.930$, $\mathcal{R} = 0.925$, $\mathcal{R} = 0.920$ and $\mathcal{R} = 0.915$ (following the lexicographic order).

- The $n = 1$ PS red curve and $n = 0$ NH blue curve ($0.935 \gtrsim \mathcal{R} \gtrsim 0.930$ in Fig. 2.14).

This shows that the eigenvalue repulsion phenomena observed in Figs. 2.7−2.8 for the $n = 0$ PS and $n = 0$ NH families is not unique. Instead, it is a common feature for other overtones.

We started our discussion of the KN QNM spectra with the RN limit ($\Theta = 0$; see Fig. 2.6). It is thus enlightening to terminate our journey with a discussion of the 'opposite' Kerr limit ($\Theta = \pi/2$). Therefore, in Fig. 2.15 we display the $m = \ell = 2$ QNM spectra for the Kerr black hole. In the top panel, we show the two families with the lowest $|\mathrm{Im}\,\tilde{\omega}|$ for the full range $0 \leqslant \mathcal{R} \leqslant 1$. These are families that, except

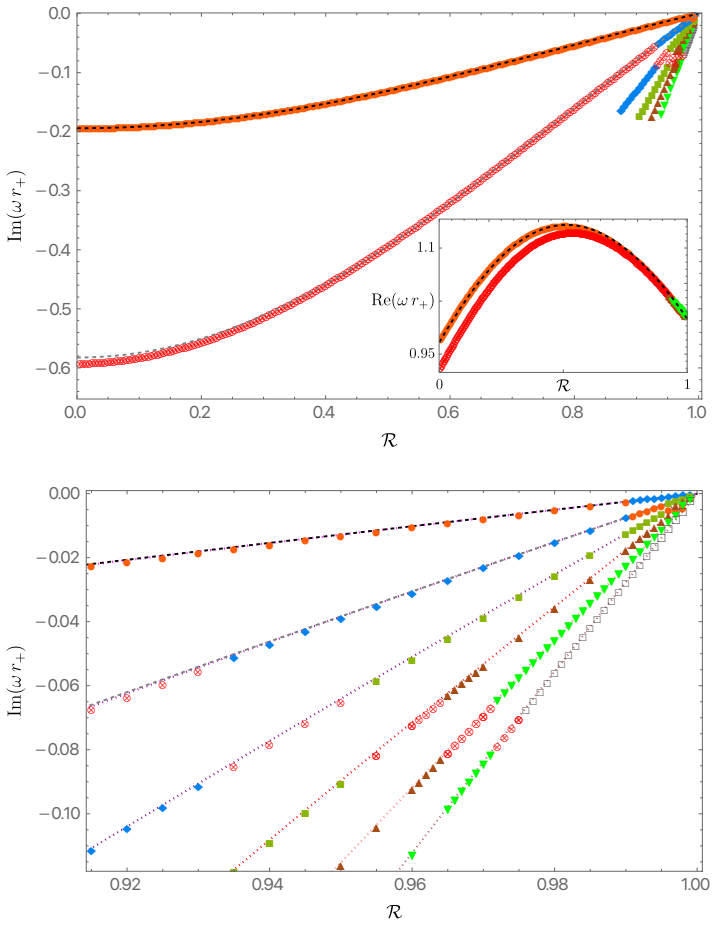

Fig. 2.15: The first few overtone PS-NH families of QNMs with $m = \ell = 2$ for the Kerr black hole (*i.e.* the KN black hole with $\Theta = \pi/2$ and thus $a/r_+ = \mathcal{R}$). The orange ● and red ⊗ are points that connect smoothly, when we decrease Θ from $\Theta = \pi/2$ down to $\Theta = 0$, to the $n = 0$ and $n = 1$ PS family of the RN black hole, while the blue ◆, dark-green ■, brown ▲, green ▼ and gray □ points connect smoothly to the NH families of the RN black hole with $n = 0, 1, 2, 3, 4$, respectively. **Top panel:** the main plot displays the imaginary part of the dimensionless frequency as a function of $\mathcal{R}$. On the other hand, the inset plot displays the real part of the frequency. The black (gray) dashed line that is almost on the top of the orange ● and red ⊗ numerical points are the analytical WKB approximation $\tilde{\omega}_{\rm WKB}$ given by (2.33) with $p = 0, 1$. **Bottom panel:** Zoom of the left panel in the near-extremal region (*i.e.* around $\mathcal{R} \sim 1$) where all the overtone NH families approach $\mathrm{Im}\,\tilde{\omega} \to 0$ as $\mathcal{R} \to 1$. This time we also show, as dotted magenta/purple lines, the near-extremal approximation $\tilde{\omega}_{\rm MAE}$ as can be read from (2.54) for $p = 0, 1, 2, 3, 4, 5$. We see that the latter approximate the 'PS-NH' frequencies very well when we are close to extremality (*i.e.* as $\mathcal{R} \to 1$), as expected. (The counterpart to this figure for the RN case is displayed in Fig. 2.6).

in a small neighbourhood around extremality ($\mathcal{R}=1$), are smoothly connected to the $n=0$ and $n=1$ PS families in the RN limit. However, for the same reasons discussed above for KN, in the special Kerr case ($\Theta=\pi/2$) it is still true that it is more appropriate to denote the modes of Fig. 2.15 as the $n=0$ PS-NH family (orange $\bullet$ curve) and an $n=1$ PS-NH family (red $\otimes$ curve). Indeed, on one hand, for the full range of $\mathcal{R}$ these families are very well approximated by the high order WKB approximation $\tilde{\omega}_{\rm WKB}$, namely by (2.33) with $p=0$ (black dashed line on top of orange $\bullet$ curve) and with $p=1$ (gray dashed line almost on top of the red $\otimes$ curve). This seems to support the idea that these are photon sphere modes. On the other hand, this classification is challenged by what happens near extremality ($\mathcal{R}\to 1$). Indeed, note that in the bottom panel of Fig. 2.15 we also display the magenta dot-dashed lines that are the analytical MAE approximation $\tilde{\omega}_{\rm MAE}$ given by (2.54) with $p=0$ and $p=1$ (and with $p=2,3,4,5$). We see that, sufficiently close to extremality, this MAE approximation is also on top of the orange $\bullet$ and the red $\otimes$ curves of the top panel. So, from this perspective, we could instead say that the orange $\bullet$ and red $\otimes$ curves (as best identified in the top panel) are NH families. Altogether, since near-extremality of Kerr (or of KN for large Θ, as shown previously) the orange $\bullet$ and red $\otimes$ curves are simultaneously well described by $\tilde{\omega}_{\rm WKB}$ and $\tilde{\omega}_{\rm MAE}$, it is more appropriate (as advocated previously) to denote these modes as a single 'PS-NH' family of QNMs with several overtones $n=0,1,\cdots$, *all* of which approach (the higher overtones with higher slope) $\mathrm{Im}\,\tilde{\omega}=0$ and $\mathrm{Re}\,\tilde{\omega}=\tilde{\Omega}_H^{\rm ext}$ at extremality. In the top panel of Fig. 2.15, in addition to the first two overtone families with $n=0,1$, we also present the next four overtones with $n=2,3,4,5$ but, in these cases, we just show the curves near extremality for $\mathcal{R}\gtrsim 0.85$. These extra four overtone curves are also simultaneously well described by $\tilde{\omega}_{\rm WKB}$ and $\tilde{\omega}_{\rm MAE}$ (with $p\geqslant 2$). The $n=0$ and $n=1$ 'PS-NH' curves in Fig. 2.15 agree with the frequencies of the $\ell=m=2$ scalar field QNMs first computed in figures 3 and 4 of [179] and also reproduced previously in figures 7 and 8 of [180] (the higher overtones in Fig. 2.15 also agree with [180]; recall that we convert our units ωr_+ into ωM using (2.2)).

This observation that in the Kerr black hole the PS and NH families lose their individual identity and merge into a single 'PS-NH' family and its overtones is better illustrated if we focus our attention in the near-extremal region. We do this in the bottom panel of Fig. 2.15, by zooming into the region $\mathcal{R}\gtrsim 0.91$ of the top panel. In this plot we identify the first 6 overtone families of the top panel using the color code convention of the RN QNMs described in footnote 10. Looking into the details that are not clear in the top panel, we first notice that the $n=0$

overtone (top curve) is essentially filled with orange ● except for $\mathcal{R} \geqslant 0.991$ where it is instead continued with blue ◆. So this Kerr $n = 0$ PS-NH curve − that is simultaneously well described by $\tilde{\omega}_{\rm WKB}$ (black dashed line) and $\tilde{\omega}_{\rm MAE}$ (magenta dotted line) − can be seen has being formed out of solutions (points) that connect smoothly to either the PS and NH families in the RN limit ($\Theta = 0$). Similarly, the $n = 1$ PS-NH overtone curve (second from top) is filled with red ⊗ (which are $n = 1$ PS modes in RN), blue ◆ (which are $n = 0$ NH modes in RN), orange ● (that are $n = 0$ PS modes when traced back to RN) and finally a few dark-green ■ (that are $n = 1$ NH modes in RN) points. Comparing these first two curves on the bottom panel, we identify the trade-off that occurs at $0.990 \lesssim \mathcal{R} \lesssim 0.991$: see the few blue ◆ that are on the $n = 0$ 'PS-NH' curve (that is otherwise dominated by the orange ●) and the few orange ● points in the $n = 1$ 'PS-NH' curve. This is nothing but the eigenvalue repulsion already documented in detail (for KN including the $\Theta = \pi/2$ case) in Fig. 2.7. Indeed, the transitions between the orange ● and the blue ◆ branches in Fig. 2.15 map to the cusp formation and consequent mergers of 'old left/right' branches of Fig. 2.7.

Moreover, as we move along the sequence of curves that describe the $n = 1, 2, 3, 4, 5$ 'PS-NH' families, we also clearly identify the eigenvalue repulsions between the red ⊗ modes, *i.e.* the $n = 1$ PS modes in the RN limit, and the $n = 0, 1, 2, 3, 4$ NH modes in the RN limit described, respectively, by the blue ◆, dark-green ■, brown ▲, green ▼ and gray □ points. This series of eigenvalue repulsions were already identified and studied in detail in the discussions of Figs. 2.13−2.14. For example, the trade-off between the red ⊗ and blue ◆ around $\mathcal{R} \sim 0.93$ when we move from the $n = 1$ to the $n = 2$ 'PS-NH' curves is in a one-to-one correspondence with the cusp/merger observed in the transition between the plots of $\mathcal{R} = 0.0935$ and $\mathcal{R} = 0.0930$ of Fig. 2.14. As another example, the trade-off between the red ⊗ and dark-green ■ around $\mathcal{R} \sim 0.95$ when we move from the $n = 2$ to the $n = 3$ 'PS-NH' curves is in a one-to-one correspondence with the cusp/merger observed in the transition between the plots of $\mathcal{R} = 0.0955$ and $\mathcal{R} = 0.0950$ of Fig. 2.13. And the trade-off between the red ⊗ and brown ▲ around $\mathcal{R} \sim 0.965$ when we move from the $n = 3$ to the $n = 4$ 'PS-NH' curves is in a one-to-one correspondence with the cusp/merger observed in the transition between the plots of $\mathcal{R} = 0.0965$ and $\mathcal{R} = 0.0960$ of Fig. 2.13.[11]

[11]The following observations might further help interpreting the bottom panel of Fig. 2.15. In this plot, let us fix our attention at constant $\mathcal{R} = 0.92$: we identify the orange ●, red ⊗ and blue ◆ that are observed at $\Theta = \pi/2$ (Kerr limit) in the bottom-left plot of Fig. 2.14. As another example, consider now $\mathcal{R} = 0.94$ in Fig. 2.15: we identify the orange ●, blue ◆, red ⊗ and dark-green ■ also seen at $\Theta = \pi/2$ in the top-left plot of Fig 2.14. As a final example, consider this time $\mathcal{R} = 0.97$ in Fig. 2.15: we identify the orange ●, blue ◆, dark-green ■, brown ▲, red ⊗

An important feature that emerges from Fig. 2.15 is that one could say the families denoted as $n = 0$ and $n = 1$ PS modes in RN limit are completely 'swallowed' by near-horizon modes in the extremal Kerr limit, and we simply have the entangled 'PS-NH' curves (describing several overtones) shown in the bottom panel of Fig. 2.15. Another property of the Kerr QNM spectra worth mentioning in the context of the eigenvalue repulsion discussion of section 2.3.1 is the fact that the several overtone PS-NH frequencies do meet and terminate with $\mathrm{Im}\,\omega \to 0$ and $\mathrm{Re}\,\omega \to m\Omega_H^{\rm ext}$ at the extremal Kerr point $\mathcal{R} = 1 = a/r_+$. So we clearly can have different modes meeting and terminating at the boundary of the Kerr parameter space.

As a conclusion or reflection to settle ideas after the above detailed discussions, it is perhaps enlightening to again observe the $m = \ell = 2$ QNM spectra of the $\Theta = 0$ RN black hole (Fig. 2.6) and its counterpart in the $\Theta = \pi/2$ Kerr black hole (Fig. 2.15), keeping in mind the color code nomenclature fixed in footnote 10. In the RN case, the PS families and the NH families extend all the way to extremality while preserving their individual identity. However, eigenvalue repulsions entangle the PS and NH modes as we turn on angular momentum, so that by the time we reach the Kerr case we instead have the 'PS-NH' family of modes and their radial overtones.

2.4 QNM spectra of scalar field perturbations in Kerr-Newman

In the previous section we focused our attention on the region of KN parameter space relevant to eigenvalue repulsions (typically the near-extremal region for large Θ). For completeness, we now discuss the QNM spectra for the whole $(\mathcal{R}, \Theta)$ parameter space of KN, for both $m = \ell = 2$ and, this time, also $m = \ell = 0$ scalar field modes. Recall that the $m = \ell = 2$ QNM spectra is important because it should and does capture properties (*e.g.* eigenvalue repulsions) that are in common with the gravito-electromagnetic perturbations of KN [182, 17, 16, 18]. On the other hand, the $m = \ell = 0$ QNM spectra is relevant because these angular quantum numbers match the spin 0 of the scalar field.

and green ▼ that are observed at $\Theta = \pi/2$ in the top-right plot of Fig 2.13. This exercise further helps understanding how several overtones of what we call PS and NH families of the RN QNM spectra ($\Theta = 0$; see Fig. 2.6) entangle between each other as Θ increases to collectively generate, in an intricate combination, the single 'PS-NH' QNMs (and its overtones) of the Kerr black hole when one reaches $\Theta = \pi/2$.

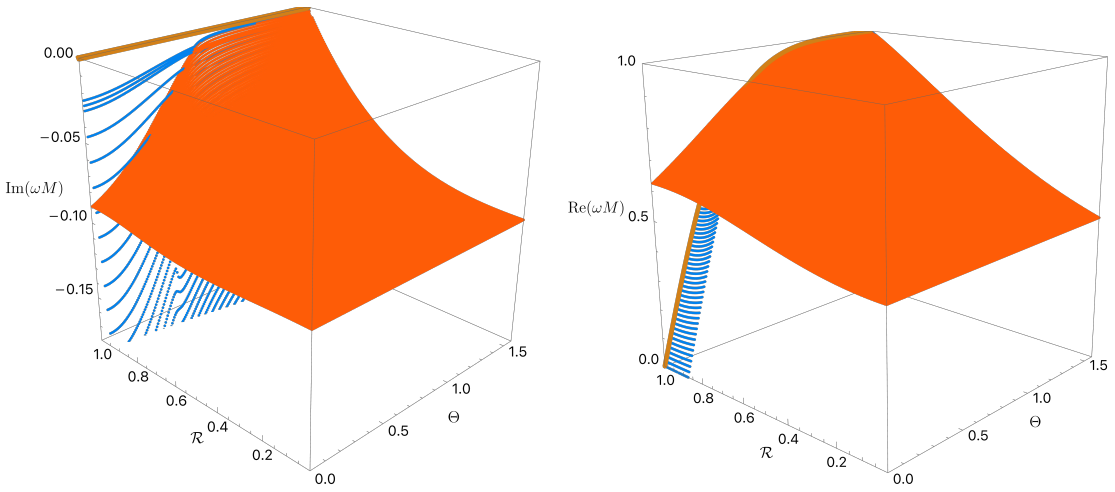

Fig. 2.16: Dominant $m = \ell = 2$ QNMs of the KN black hole parametrised by the 'polar' parameters $(\mathcal{R}, \Theta)$. The orange (blue) surface describes the QNM family that reduces to the $n = 0$ PS (NH) modes in the RN limit. The light brown curve at $\mathcal{R} = 1$ has $\mathrm{Re}(\omega M) = m\Omega_H$ and $\mathrm{Im}\,\omega = 0$. **Left panel:** Imaginary part of the dimensionless frequency (in mass units) as a function of $\{\mathcal{R}, \Theta\}$. **Right panel:** Real part of the dimensionless frequency as a function of $\{\mathcal{R}, \Theta\}$. In both panels we only display the NH modes for $0.875 \leqslant \mathcal{R} \leqslant 1$ (since they plunge very deeply to very negative values of $\mathrm{Im}\,(\omega M)$ for smaller values of $\mathcal{R}$).

As discussed previously, we choose to parametrize the KN family using the 'polar' quantities $\{\mathcal{R}, \Theta\}$, such that the dimensionless rotation α and charge $\tilde{Q}$ are given by (2.6), *i.e.* $\alpha = \mathcal{R}\sin\Theta$ and $\tilde{Q} = \mathcal{R}\cos\Theta$. Thus, Θ ranges from the Reissner-Nordström solution ($\Theta = 0$) to the Kerr solution ($\Theta = \pi/2$). On the other hand, $\mathcal{R}$ is an off-extremality measure, such that extremality of KN (and hence RN and Kerr) is at $\mathcal{R} = 1$, while $\mathcal{R} = 0$ describes the Schwarzschild BH.

2.4.1 The QNM spectra of $m = \ell = 2$ modes

In Fig. 2.16 we consider the full parameter space ($\mathcal{R} \in [0, 1]$ and $\Theta \in [0, \pi/2]$) of the KN black hole and we plot the two $\ell = m = 2$ modes that can dominate the spectra (*i.e.* that can have the smallest $|\mathrm{Im}(\omega M)|$) in some region of the phase space.

In Fig. 2.16 and all figures of this section we choose to provide the dimensionless frequency in units of the mass (ωM), because this is the standard unit in astrophysical studies.[12] Still following the color convention of footnote 10, the orange surface

[12]The intricate properties of the spectra due to the eigenvalue repulsions are however best seen if we use units of r_+. This is the reason we used this unit in previous figures. To convert ωr_+ into ωM we use (2.2).

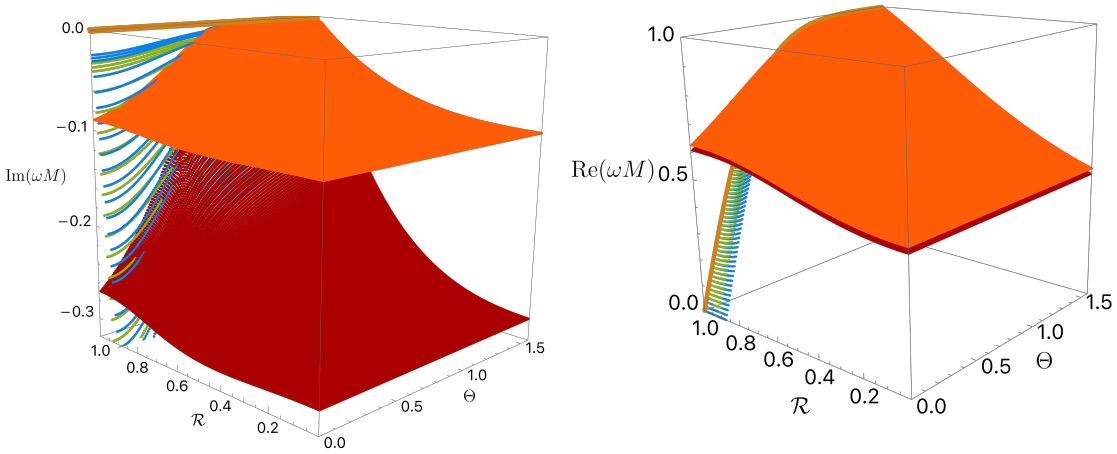

Fig. 2.17: In addition to the two surfaces (orange and blue) already presented in Fig. 2.16, we also display the red family of modes that connect to the $n = 1$ PS family of modes in the RN limit, and the dark-green surface which describes the modes that connect to the $n = 1$ NH family in the RN limit.

is the family of modes that connects to the $n = 0$ PS family of modes in the RN limit, and is typically well approximated by the high order WKB approximation $\tilde{\omega}_{\rm WKB}$, namely by (2.33) with $p = 0$. On the other hand, the blue surface describes the modes that connect to the $n = 0$ NH family in the RN limit, and is typically well approximated by the MAE frequency $\tilde{\omega}_{\rm MAE}$ given by (2.54) with $p = 0$. The light brown curve at $\mathcal{R} = 1$ in Fig. 2.16 has $\mathrm{Im}\,\omega = 0$ and $\mathrm{Re}\,\omega = m\Omega_H$. As already concluded from the analysis of Figs. 2.7 and 2.9, Fig. 2.16 clearly shows that the orange family is the dominant mode (*i.e.* it has smaller $|\mathrm{Im}(\omega M)|$) in most of the parameter space except in a small neighbourhood around extremality $\mathcal{R} \sim 1$ where the blue family dominates. Note that the $\Theta = 0$ plane of Fig. 2.16 is the RN spectrum shown in Fig. 2.6, and the $\Theta = \pi/2$ plane of Fig. 2.16 is the Kerr spectrum of Fig. 2.15 (after converting units $\omega r_+ \to \omega M$ and keeping only the orange and blue modes of those earlier figures). Finally, several planes at constant $\mathcal{R}$ of Fig. 2.16 can be found in previous figures, *e.g.* in Figs. 2.7−2.8.

For completeness, in Fig. 2.17 we again display the two QNM families of Fig. 2.16, but this time we also add the next two subdominant modes. Namely, the red family of modes that connects to the $n = 1$ PS family of modes in the RN limit and that is typically well approximated by the high order WKB approximation $\tilde{\omega}_{\rm WKB}$ with $p = 1$, and the dark-green surface which describes the modes that connect to the $n = 1$ NH family in the RN limit and which is typically well approximated by the

MAE frequency $\tilde{\omega}_{\rm MAE}$ with $p = 1$.[13]

Concluding, the scalar field $m = \ell = 2$ QNM spectra is qualitatively similar to that of gravito-electromagnetic perturbations of KN [16, 18]. For example, this is evident when we compare the scalar field Fig. 2.17 with the gravito-electromagnetic Fig. 15 of [18]. The intricate properties associated to eigenvalue repulsions are also similar for the two sectors of perturbations. However, since the scalar field perturbations are described by a single pair of radial/angular ODEs (instead of a coupled pair of PDEs), and using the polar parametrisation of the KN parameter space introduced in this chapter, we were able to explore fine-tuned details of the eigenvalue repulsions that were not so easy to extract in the gravito-electromagnetic case of [16, 18].

A comparison between our findings and those of [59], where the scalar QNM spectra of KN was also analysed and the existence of two families of QNMs was extensively discussed, is in order. Overall, our study is complementary to the one of [59] (see also [57, 58, 85, 196]), but it offers a fresh perspective of the RN/KN/Kerr QNM spectra, identifies and studies the features of eigenvalue repulsions, and helps to clarify the Kerr QNM spectra from the perspective of the RN QNM spectra. For each pair $\{\ell, m\}$ of quantum numbers, Refs. [57–59] define the quantity $\mu = \frac{m}{\ell+1/2}$. Furthermore, these references analyse the properties of the Schrödinger potential of the system in the eikonal limit, namely its maximum and whether it is located outside the event horizon. From this analysis, [57–59] conclude that there a separatrix curve $\mu = \mu_c(\tilde{a}) \gtrsim 0.74$ (where the lower bound holds in the Kerr limit) such that the qualitative behaviour of the QNM spectra is distinct depending on whether $\{\ell, m\}$ are such that $\mu \lesssim \mu_c(\tilde{a})$ or $\mu \gtrsim \mu_c(\tilde{a})$. In Appendix A, we provide a complementary first-principles analysis that (also) identifies this separatrix curve $\mu_c(\tilde{a})$ (and agrees with the one found in [57–59]). In our analysis we use the fact that the near-horizon geometry of the extremal KN black hole (NHEKN) is a spacetime similar to $AdS_2 \times S^2$ (remaining a solution of the Einstein equation). This NHEKN geometry has an $SL(2,R) \times U(1)$ isometry group, where the $U(1)$ is inherited from the axisymmetry of the KN solution and the $SL(2,R)$ extends the KN time-translation symmetry. The Klein-Gordon equation in this NHEKN geometry (which can be equivalently obtained taking the near-horizon limit of the Klein-Gordon equation of the extremal KN) naturally reduces to the equation for a scalar field in AdS_2 with an effective mass that depends on $\{\ell, m\}$. In AdS_2, the

[13] Again, the planes $\Theta = 0$ and $\Theta = \pi/2$ in Fig. 2.17 are given by the RN and Kerr plots displayed in Fig. 2.6 and Fig. 2.15, respectively (after unit conversion), and several planes at constant $\mathcal{R}$ of Fig. 2.17 can be found in previous figures, namely in Figs. 2.13−2.14.

scalar field mass must be higher than the 2-dimensional Breitenlöhner-Freedman (BF) bound for the solutions to have finite energy [197, 198]. This AdS_2 BF bound turns out to define the separatrix boundary $\mu = \mu_c(\tilde{a})$ − see in particular Table A.1 and (A.11) − that is essentially the same 1-parameter curve that was found in [57–59] by looking at the location of the maxima of the eikonal Schrödinger potential of the KN Klein-Gordon problem. These two criteria are in close numerical agreement despite the fact that $\mu_c(\tilde{a})$ is strictly-speaking only valid in the eikonal limit (as discussed further in Appendix A). We will revisit this connection to the near-horizon geometry again later, in Chapter 3, where we find a BF bound violation of the near-horizon geometry is an (approximate) indication of whether strong cosmic censorship is respected in Myers-Perry de Sitter spacetimes, as it indicates the near-extremal behaviour of the merged PS-NH modes.

As stated above, [57–59] found that the qualitative behaviour of the QNM spectra is significantly different depending whether $\{\ell, m\}$ are such that $\mu \lesssim \mu_c(\tilde{a})$ or $\mu \gtrsim \mu_c(\tilde{a})$ which is closely related with whether the near-horizon quantity δ^2 defined in (2.39), i.e. the argument of the square root in (2.54), is negative or positive. Our results confirm this is the case. In particular, for the $\ell = m = 2$ modes ($\mu = 0.8$) we are discussing in this section, one is in the regime $\mu \lesssim \mu_c(\tilde{a})$ for $\Theta < \Theta_\star$ and $\mu \gtrsim \mu_c(\tilde{a})$ for $\Theta \geqslant \Theta_\star$ (where recall that $\Theta_\star \simeq 0.881$). For $\mu \gtrsim \mu_c(\tilde{a})$, [57–59] find that the QNM spectra has only zero-damped modes (ZDMs), i.e. modes whose imaginary part of the frequency approaches zero at extremality ($\mathcal{R} \to 1$). Essentially, this is consistent with our analysis for $\Theta \geqslant \Theta_\star$ if, very close to extremality, the PS modes indeed approach $\tilde{\omega} = m\tilde{\Omega}_H^{\text{ext}}$ (please see detailed discussion of the bottom panels of Fig. 2.12 that we do not repeat here) as do the NH modes. We would however emphasize that for $\Theta \geqslant \Theta_\star$ (i.e. $\mu \gtrsim \mu_c(\tilde{a})$) there are not one but two families of modes that have a distinct origin when we trace them back to the RN case (as we discuss next). On the other hand, for smaller $\Theta < \Theta_\star$, in agreement with [59], we find that the system has (in the nomenclature of [57–59]) both ZDMs and damped modes (DMs) that approach a finite $\text{Im}\,\tilde{\omega}$ at extremality) as summarized in the top panel of Fig. 2.12 and in Figs. 2.7-2.11. We emphasize that these DMs are the PS modes that become ZDMs for $\Theta > \Theta_\star$. This and the differences between the two regimes $\mu \lesssim \mu_c(\tilde{a})$ and $\mu \gtrsim \mu_c(\tilde{a})$ are clearly observed in Figs. 2.16-2.17: in short, the NH surfaces always end in the extremal brown line, while the PS modes do not do so for $\Theta < \Theta_\star$.

One should also provide an important clarification that helps bridge our findings with those of [57–59] and avoid an apparent inconsistency. In regimes $\mu \lesssim \mu_c(\tilde{a})$ where there are both ZDMs and DMs, [57–59] state that far away from extremality

the system only has a DM family which exists all the way till extremality. But, at a critical value of $\mathcal{R}$, these references state that the DM family '*bifurcates*' into two branches: one continues to describe DMs till extremality while the other only exists above this critical $\mathcal{R}$ and describes ZDMs. We find that this is because [57–59] effectively considered modes that have not only fixed $\{\ell, m\}$ but also *fixed* overtone p. On the other hand, by construction, in our analysis we always fix $\{\ell, m\}$ (but *not* the overtone p) and, starting from the PS and NH modes at the RN limit ($\Theta = 0$), we follow these modes as Θ grows till reaching the Kerr limit ($\Theta = \pi/2$). This is a continuous process where no bifurcations are observed (although we have eigenvalue repulsions with the associated cusp formations and break/trade-off/merge of branches). That is to say, at each fixed Θ we always have two modes, below and above any possible critical $\mathcal{R}$. However, the fact that we do not observe bifurcations in our analysis is not inconsistent with the analysis of [57–59, 85, 196]. The key observation here is that the overtone number p of the continuous curves/surfaces we follow effectively changes as we march in Θ when eigenvalue repulsions kick in. For example (among many others described previously), the overtone of the orange PS and blue NH curves in Fig. 2.7 change when making the transition $\mathcal{R} = 0.991 \to \mathcal{R} = 0.990$ (middle panels). If we insist on fixing our attention on modes with fixed overtone, we would interpret some results as being a 'bifurcation' in an $\mathrm{Im}\,\omega$ vs Θ plot and this was the approach followed in [57–59]. We do not do so and thus, instead of a bifurcation, we do observe two surfaces intersecting or crossing in an $\mathrm{Im}\,\omega$ vs $\{\Theta, \mathcal{R}\}$ plot (or two curves crossing in a $\mathrm{Im}\,\omega$ vs Θ plot); note that it is only $\mathrm{Im}\,\omega$, but not $\mathrm{Re}\,\omega$, that coincides along the crossing.

2.4.2 The QNM spectra of $m = \ell = 0$ modes

The focus of this chapter so far has been the $m = \ell = 2$ QNMs due to their close analogy with the gravito-electromagnetic perturbations computed in [16, 18, 182]. However, for completeness, in this section we consider QNMs with $m = \ell = 0$ since these quantum numbers match the spin of the scalar field perturbations. Moreover, these modes are important as they dominate the $m = \ell = 2$ modes (*i.e.* they have smaller $|\mathrm{Im}(\omega M)|$) in certain regions of the parameter space.

Perturbations with $m = 0$ have an enhanced $t \to -t$ symmetry, so QNM frequencies form pairs $\{\omega, -\omega^*\}$. When $m = 0$, the WKB approximation $\tilde{\omega}_{\rm WKB}$ in (2.33) is not valid (for obvious reasons since it is an expansion at large m), however the matched asymptotic expansion $\tilde{\omega}_{\rm MAE}$ (2.54) remains a very good approximation provided

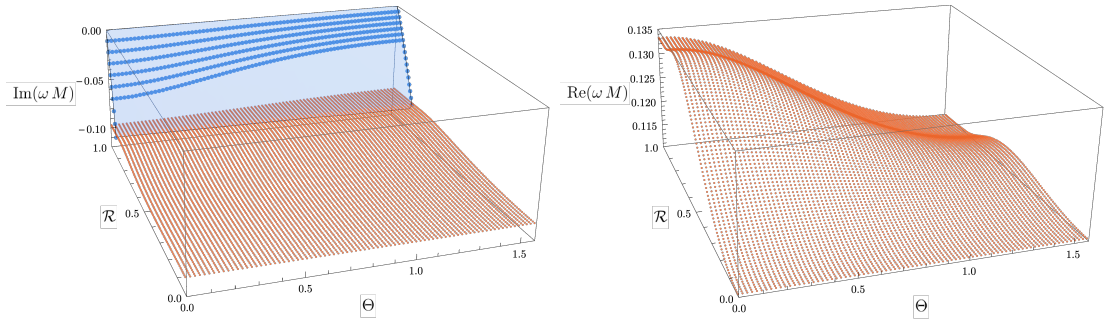

Fig. 2.18: The frequency of the slowest-decaying PS (orange disk) and NH (blue disk) QNMs with $m = \ell = 0$ for the whole parameter space $\{\mathcal{R}, \Theta\}$ of KN. **Left panel:** The imaginary parts of the frequency. With the exception of the Kerr and RN limits, only the NH modes down to $\mathcal{R} = 0.94$ were found, due to computational limitations. The blue surface represents the extrapolation of the points found until the intersection with the PS modes. **Right panel:** The real part of the PS frequencies. The NH frequencies always have zero real part.

we are close to extremality, and simplifies as follows. When $m = 0$, the angular equation (2.8b) at extremality can be solved exactly, with the angular eigenvalue $\lambda_{\rm ext}^{(m=0)} = \ell(\ell+1)$, where $\ell = 0, 1, 2, \ldots$ denotes the number of zeros of the angular eigenfunction, as usual. The MAE frequency (2.54) simplifies to

$$\tilde{\omega}_{\rm MAE}^{(m=0)} = -\frac{i(\ell+p+1)}{2(1+\alpha^2)}\sigma + \mathcal{O}(\sigma^2), \qquad p = 0, 1, 2, \ldots . \tag{2.58}$$

This frequency is purely imaginary, for all $\Theta = \arctan(a/Q)$, in contrast to the $m = l = 2$ case. Since the PS frequencies remain complex (as we will discuss later), this hints at a major difference between the $m = \ell = 2$ and $m = \ell = 0$ QNM spectra: in the latter there are no eigenvalue repulsions. Consequently, for $m = \ell = 0$ we can always unambiguously identify the photon sphere (PS) and near-horizon (NH) modes in the full parameter space of KN (not only in the RN limit). These properties can be seen in Fig. 2.18 where we display the spectrum of KN QNMs with $m = \ell = 0$ for all $(\mathcal{R}, \Theta)$. We have found the full spectrum of the PS modes (orange disks), however the NH modes (blue disks) have proven to be much more difficult to find numerically, and we have only computed those down to $\mathcal{R} = 0.94$, except in the RN ($\Theta = 0$) and Kerr ($\Theta = \pi/2$) limits. For intermediate values of Θ, the blue surface in the left panel of Fig. 2.18 represents the extrapolation of the NH data till the point they intersect with the PS modes and become subdominant.

For clarity, the QNM spectra in the special RN ($\Theta = 0$) and Kerr ($\Theta = \pi/2$) limits are displayed in Fig. 2.19, as well as the matched asymptotic expansion frequency approximation (2.58). For Kerr (RN), the PS modes are orange triangles

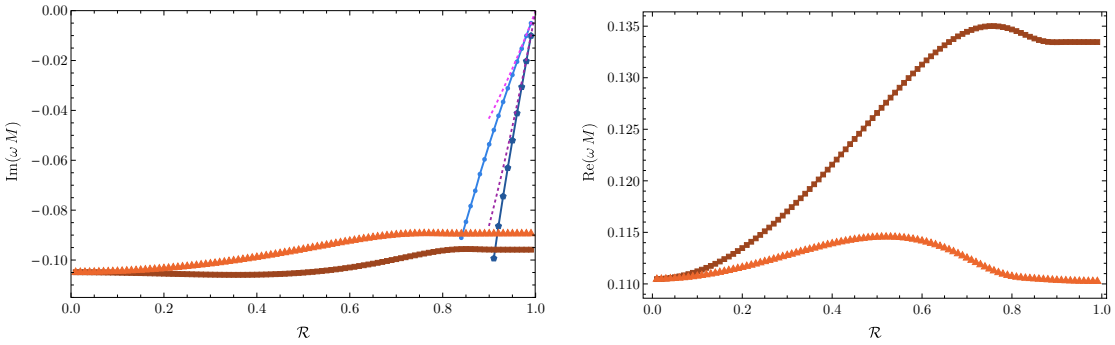

Fig. 2.19: The frequency of the slowest-decaying PS and NH QNMs in the RN ($\Theta = 0$) and Kerr ($\Theta = \pi/2$) limits. For Kerr (RN), the PS modes are orange triangles (brown squares) and the NH modes are light blue disks (dark blue pentagons). **Left panel:** The imaginary parts of the frequency. The dashed magenta and dotted purple lines emerging from $\mathcal{R} = 1$ describe the matched asymptotic expansion $\tilde{\omega}_{\rm MAE}^{(m=l=0)}$ (2.58) for $p = 0$ and $p = 1$, respectively. **Right panel:** The real part of the PS frequencies for Kerr and RN. The NH modes always have zero real part.

(brown squares) and the NH modes are light blue disks (dark blue pentagons), with the matched asymptotic expansion $\tilde{\omega}_{\rm MAE}^{(m=\ell=0)}$ of (2.58) with $p = 0$ represented by a dashed magenta (dotted purple) line. Note that the QNM spectra only depends weakly on Θ, most likely because these are axisymmetric perturbations, and therefore are not significantly affected by the angular momentum of KN. In the RN case, our PS frequencies (brown squares) in Fig. 2.19 agree with those first computed in [72, 192–195]. On the other hand, to the best of our knowledge, the RN NH QNM spectrum (dark blue pentagons) is first computed exactly (within numerical accuracy) in Fig. 2.19 (their existence is predicted in [59]; see however the discussion in the next paragraph). In the Kerr case, our PS frequencies (orange triangles) in Fig. 2.19 agree with those first computed in [73, 180] (see figure 6 of [180]). On the other hand, as far as we know, the Kerr NH spectrum (light blue disks) is first computed exactly (within numerical accuracy) in Fig. 2.19 (their existence follows from the analysis of [48, 57, 58]).

In agreement with the matched asymptotic expansion $\tilde{\omega}_{\rm MAE}^{(m=0)}$ in (2.58), the real part of the NH modes is zero. In contrast, the PS modes are always complex with $|\,\mathrm{Re}(\omega M)| > 0.11$ across the full parameter space. Therefore, there is no single point in the KN parameter space where the PS and NH frequencies can coincide (not even at extremality), strongly suggesting that the associated phenomenon of eigenvalue repulsion should also be absent. Indeed, unlike the $m = \ell = 2$ case, for the $m = \ell = 0$ modes we find no evidence of the presence of eigenvalue repulsions in the spectra. In particular, the PS family never develops cusps or intricate features

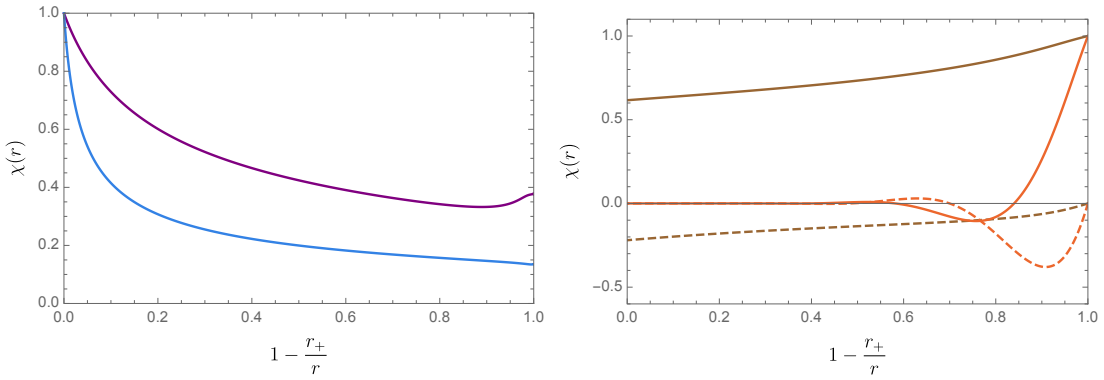

Fig. 2.20: Typical eigenfunctions $\chi(r)$ of KN QNMs with $m = \ell = 0$. $\chi(r)$ is the redefined radial function as in (2.10). **Left panel:** NH eigenfunctions for $\mathcal{R} = 0.95$ (purple) and $\mathcal{R} = 0.99$ (blue) at $\Theta = \pi/4$. The dominant NH eigenfunctions are purely real, peaked at the horizon radius $r = r_+$, with no zeros. **Right panel:** Real part (solid lines) and imaginary part (dashed lines) of the PS eigenfunctions for $\mathcal{R} = 0.8$ (brown) and $\mathcal{R} = 0.99$ (orange). The PS eigenfunctions are complex with non-zero support at large r, and the number of zeros depends on the distance to extremality.

that could be a sign of eigenvalue repulsions: the imaginary part of the frequency always increases monotonically with $\mathcal{R}$ and Θ (this is the reason we found no need to push our numerics further to find more NH modes than those in Fig. 2.18).

Given the lack of eigenvalue repulsions, we can unambiguously identify NH modes throughout the KN parameter space, by tracing them to the extremal limit $\mathcal{R} \to 1$ where we can compare them to the matched asymptotic expansion (2.58) (see the left panel of Fig. 2.19), unlike the $m = \ell = 2$ modes. A similar phenomenon occurs in other black hole spacetimes, such as higher-dimensional Kerr-dS (Myers-Perry-dS) that we study in the next chapter, where eigenvalue repulsions between the PS and NH modes occur when $m \neq 0$, but not for $m = 0$.

The two QNM families can also be distinguished by their eigenfunctions. In Fig. 2.20 we plot the eigenfunctions $\chi(r)$ as defined by (2.10) for the dominant NH modes (left panel) and PS modes (right panel) at a representative value of $\Theta = \pi/4$. The eigenfunctions of the NH modes are purely real (blue and purple curves for $\mathcal{R} = 0.95$ and 0.99, respectively, at $\Theta = \pi/4$), peaking at the horizon radius $r = r_+$, and becoming increasingly peaked as we approach extremality $\mathcal{R} \to 1$. Furthermore, the eigenfunctions of the dominant NH modes do not have any zeros. In contrast with the NH modes, the PS modes (orange and brown curves for $\mathcal{R} = 0.8$ and 0.99, respectively, for $\Theta = \pi/4$ in right panel of Fig. 2.20) have both real and imaginary parts. Far away from extremality the PS eigenfunction

is nearly flat, with no zeroes, but becomes oscillatory, with the number of zero crossings increasing the closer we approach extremality.[14]

Compared to the $m = \ell = 2$ modes, the PS family of $m = \ell = 0$ modes is always subdominant, *i.e.* with larger $|\mathrm{Im}\,\omega|$ than the corresponding PS QNM at any point in the KN parameter space. On the other hand, at least near extremality, the NH modes with $m = \ell = 0$ dominate modes with $m = \ell = 2$. However, the difference in imaginary part between the two shrinks as $\mathcal{R}$ decreases.

As in the previous subsection, it is appropriate to make contact between our findings and those of [57–59]. In terms of the quantity $\mu_c(\tilde{a})$ introduced in the discussion below Fig. 2.17 of subsection 2.4.1 (and originally in [57–59]), the $\ell = m = 0$ modes satisfy the condition $\mu < \mu_c(\tilde{a})$ in the whole range of $\{\mathcal{R}, \Theta\}$. Refs. [57–59] do not present results for the scalar $\ell = m = 0$ Kerr or RN modes displayed in Fig. 2.19, but do discuss in detail other cases (including with spin $s = 1, 2$ in the Dudley-Finley approximation) in the same class $\mu < \mu_c(\tilde{a})$. As explained in the last paragraph of subsection 2.4.1, Refs. [57–59] fix not only $\{\ell, m\}$ but also the overtone p when describing/interpreting their results (unlike in our analysis). Consequently, [57–59] describe cases like the one in Figs. 2.18-2.19 as a 'bifurcation' happening in the $\mathrm{Im}\,\omega$ plot along a $\mathcal{R}(\Theta)$ line (or at a point $\mathcal{R}_c$ in the Kerr or RN case) close to extremality, while in our analysis (where we do not constrain the overtone to be fixed" we see that there is simply a "crossing" of two surfaces (or curves in the RN/Kerr limits) that intersect along the curve $\mathcal{R}(\Theta)$ (or along a point in RN/Kerr); note that it is only $\mathrm{Im}\,\omega$, but not $\mathrm{Re}\,\omega$, that coincides along the "crossing". Thus the two analyses are consistent and not contradictory once we identify the conditions underlying the selected choice of language. The compatibility of our findings and those of [57–59] is further confirmed when we analyse the results (for a gravitational mode with $\ell = 2$ and $m = 1$ that fits in the $\mu < \mu_c(\tilde{a})$ class) of figure 8 of [58], which reproduces figure 3.b of [48] (the latter was the first instance where the simultaneous existence of zero-damped and damped modes was observed).

[14] On the other hand, when $m = \ell = 2$, the NH modes acquire an imaginary part, but otherwise the NH and PS eigenfunctions are qualitatively similar to those in Fig. 2.20 in the Kerr and RN limits. However, due to the eigenvalue repulsions, they can smoothly transition from one type to another as we vary Θ, such that the NH-type eigenfunctions in the RN limit become PS-type in the Kerr limit, and vice versa. Essentially, in the regions of the parameter space where eigenvalue repulsions occur, we cannot use the eigenfunctions to distinguish the nature of the modes.

Chapter 3

Strong cosmic censorship in higher-dimensions

In asymptotically-flat spacetimes, there is growing evidence that strong cosmic censorship is respected for initial data close to Reissner-Nordström [113–116] and Kerr [117, 118]. Ultimately, this is due to the well-known infinite blueshift effect near the Cauchy horizon and the associated Price law [119, 27]. However, for positive cosmological constant ($\Lambda > 0$) there is a competing redshift associated with the gravitational potential well of asymptotically de Sitter spacetimes. As a result of the delicate competition between these two effects, the decay of generic linear perturbations depends on the magnitude of the imaginary part of the slowest-decaying quasinormal mode (QNM) of the system [111, 112]. Indeed, in recent years, a large body of work indicates that initial data close to Reissner-Nordström−de Sitter (RNdS) violates SCC [86, 89, 122][1] [2], while Kerr-dS does not [94].

Perhaps the strongest motivation to study SCC for initial data close to Reissner-Nordström−dS is the fact that, in many respects, the RNdS black hole appears to be a (much simpler) toy model for initial data close to Kerr-dS. Thus it might come as a surprise that SCC is violated for initial data close to RNdS but not for initial data close to Kerr-dS. However, there is an important distinction between the two, which is best fleshed out if we recall the parallel between the two spacetimes. In particular, *charged* scalar fields of mass μ and charge q around a Reissner-Nordström-dS black hole have been shown to lead to a violation of SCC for any

[1] See Sections 1.2-1.3 for more details on this, in particular regarding the charged scalar field.

[2] In the conclusion (Chapter 5), we discuss potential ways in that SCC in RNdS can be rescued, including the effect of quantum corrections and and the "rough formulation" of strong cosmic censorship.

finite value of q [122]. If, however, we take (the rather unphysical limit) $q \to +\infty$, these violations disappear altogether [122]. For Kerr-dS, the analog of q is the azimuthal quantum number m, which counts the number of nodes of the scalar perturbation along the direction of rotation. However, unlike RNdS, for Kerr-dS we are forced to consider initial data with arbitrarily large m, and it is this data that ends up saving SCC in Kerr-dS.

It remains, however, a mystery as to why the quasinormal mode spectrum of Kerr-dS black holes at large m behaves just so as to save SCC. It could have been that the large m behaviour was such that SCC would still be violated: it just so happens that, after a long calculation, it is not! One might then wonder whether this is a result one can derive for a large class of rotating black holes, perhaps by studying the universal properties of rotating near-horizon geometries. Whatever the mechanism might be, it appears to depend on the details of the near-horizon geometry. However, it has been argued in [199, 200] that initial data close to Kerr-Newman-dS black holes will generically violate SCC if the black hole charge is large enough. This shows, to some extent, that not all rotating black holes necessarily preserve SCC and that preserving SCC cannot be a universal property of *all* rotating near-horizon geometries.

In this chapter, instead of turning on charge, we change yet another dial: the spacetime dimension d. As a first step in this direction, it was shown that scalar field perturbations of RNdS in $d = 5, 6$ violate SCC (much alike in the $d = 4$ case), with the expectation that this conclusion does not change in even higher dimensions [201]. RNdS black holes have, however, been shown to be unstable in dimensions $d \geqslant 6$ [202–204, 145]. As a second step, here we consider scalar field perturbations of Myers-Perry−de Sitter (MPdS), *i.e.* the higher-dimensional extension of the Kerr-de Sitter solution. For simplicity, we restrict our analysis to odd d spacetime dimensions and to black holes with equal angular momentum. In this case the resulting line element is cohomogeneity-1, *i.e.* it depends non-trivially on only the radial coordinate. We will find that Christodoulou's formulation of SCC holds in cohomogeneity-1 MPdS, very much like in the $d = 4$ Kerr-dS case. The generic considerations of [205] further indicate that this result extends to other, perhaps all, MPdS solutions. Together with [201] we thus have strong evidence in favour of the following universal result for perturbations excited by scalar fields: for arbitrary spacetime dimensions in de Sitter, Christodoulou's formulation of SCC holds in dynamically stable, vacuum, rotating black hole solutions of the Einstein equations, but can be violated if charged matter is included. We note, however,

that the leading WKB behaviour is spin independent, and thus the result quoted above could indeed also be true for gravitational perturbations.

As stated above, the question of SCC in de Sitter backgrounds is intimately linked to quasinormal modes [206–209, 111, 210, 211], so we naturally also take the opportunity to discuss some aspects of the QNM spectra of MPdS. In particular, we want to identify all possible families of QNMs in MPdS (for a given set of relevant wave quantum numbers) and, ultimately, the family with the slowest decaying QNM at each point in the 2-parameter space of MPdS. For that we resort to a numerical computation of the QNM spectra in the full parameter space (using the pseudospectral collocation methods described in Section 1.5) but also to analytical analyses (in the appropriate corners of the parameter space) to elucidate the physical origin of each family.

In the previous chapter, we found that asymptotically flat, four-dimensional spacetimes which admit a Cauchy horizon (the Kerr-Newman family and its Kerr and Reissner-Nordström limits) have two distinct families of QNMs: the *photon sphere* (PS) modes and *near-horizon* (NH) modes. Both the PS and NH modes are also present in rotating asymptotically de Sitter black holes in higher dimensions. We will verify (by direct comparison with the numerical results) that the PS mode correspondence (1.19) described in Section 1.1 still holds in rotating black holes in higher dimensions. To capture the NH modes with an analytic approximation, we perform a matched asymptotic expansion similar to that of Kerr-Newman, but with a slight variation. We find the eigenfunction near the horizon as before, but then match it with a *vanishing* wavefunction solution far from the horizon. We will highlight the link between the NH modes we find and the near-horizon geometry of the extremal spacetime.

In asymptotically de Sitter spacetimes, unlike in the $\Lambda = 0$ case, there is a third family of QNM modes: the *de Sitter* (dS) family. The frequency of these modes approaches the QNM mode frequency of pure de Sitter space in the limit where the mass and the angular momentum of MPdS vanish. In $d = 4$, dS modes have a weak dependence on the black hole parameters. We will find that this is no longer true in higher dimensions.

In cohomogeneity-1 Myers-Perry-de Sitter, axisymmetric mode perturbations (*i.e.* with azimuthal quantum number $m = 0$) feature all three families. However, for $m \neq 0$, we will find that the PS and NH modes will typically (but not always) merge into a single family. This family generally dominates, *i.e.* has more slowly decaying modes than the dS family. As a result, we will be able to use both our eikonal and

near-horizon approximations in tandem to study SCC. No less interestingly, we also find that in certain regions of the parameter space some of these families will exhibit eigenvalue repulsions, similar to those observed for the scalar QNMs of Kerr-Newman in the previous chapter, and for gravito-electromagnetic perturbations of Kerr-Newman in [212]. However, there the eigenvalue repulsions occurred between the NH and PS modes, while in MPdS the interactions primarily occur between the NH and dS modes.

The plan of this chapter is as follows. In Section 3.1 we review the main properties of cohomogeneity-1 Myers-Perry-de Sitter black holes. We use separation of variables to study the Klein-Gordon equation for scalar fields in this background, and describe the numerical scheme used to solve for the scalar field perturbations. In Section 3.2, we derive analytic approximations for the three families of QNM − dS, PS and NH − that can be present in MPdS for regions of the parameter space that are susceptible to such analytical approximations. For completeness, and because the QNMs show significant dependence on the spacetime dimension, we study the QNM spectra of higher-dimensional Schwarzschild-de Sitter black holes in Section 3.3. Then, in Section 3.4, we describe important features of the MPdS QNM spectra, after comparing our numerical results with the aforementioned analytical approximations. Finally, in Section 3.5 we tackle the question of whether or not strong cosmic censorship holds in cohomogeneity-1 MPdS black holes. Some details of the NH modes are deferred to Appendix B and we discuss the numerical convergence of our results in Appendix C.

3.1 Scalar perturbations of cohomogeneity-1 Myers-Perry−de Sitter

3.1.1 Cohomogeneity-1 Myers-Perry−de Sitter black holes

The Myers-Perry black hole is a stationary and axisymmetric spacetime in $d \geqslant 4$ dimensions, parametrised by a mass parameter M and angular momentum parameters a_i in each of the $n = \left\lfloor \frac{d-1}{2} \right\rfloor$ rotational planes [213]. For general a_i this black hole has the isometry group $\mathbb{R} \times U(1)^n$. However, in the *equal angular momenta* case $a_i = a$ and in odd dimensions (only), the symmetry is enhanced to $\mathbb{R} \times U(n)$. Consequently, the resulting metric is *cohomogeneity-1*, *i.e.* it depends non-trivially on only the radial coordinate. This is in contrast to Kerr (and even-dimensional

Myers-Perry with or without equal angular momenta) which has non-trivial angular dependence. Thus, cohomogeneity-1 Myers-Perry black holes are easier to study than Kerr.

Myers-Perry can be generalised to include a cosmological constant Λ. This solution was first found in $d = 5$ (the Hawking-Hunter-Taylor black hole [214]), and generalized later to arbitrary dimensions [215, 216], and they retain all the symmetries discussed above in the $\Lambda = 0$ case. We will focus on the equal angular momenta Myers-Perry−de Sitter spacetime in odd dimensions, $d = 2N + 3$, where $N \geqslant 1$ is an integer, abbreviating it to simply MPdS when unambiguous. In Boyer-Lindquist-like (BL) coordinates[3] $x_a = (t, r, \psi, x_i)$, the metric can be written as [217]

$$ds^2 = -\frac{f(r)}{h(r)}dt^2 + \frac{1}{f(r)}dr^2 + r^2 h(r)\Big(d\psi + \mathcal{A} - \Omega(r)\,dt\Big)^2 + r^2 d\Sigma^2 \tag{3.1}$$

where

$$f(r) = 1 - \frac{r^2}{L^2} - \frac{2M}{r^{2N}}\left(1 + \frac{a^2}{L^2}\right) + \frac{2Ma^2}{r^{2N+2}}, \tag{3.2}$$

$$h(r) = 1 + \frac{2Ma^2}{r^{2N+2}}, \qquad \Omega(r) = \frac{2Ma}{r^{2N+2}h(r)}, \tag{3.3}$$

with L being the de Sitter radius, and we have expressed the sphere S^{2N+1} as a fibration (parametrised by ψ) over $\mathbb{CP}^N$, with Fubini-Study metric $d\Sigma^2 = \hat{g}_{ij}dx^i dx^j$, where the latin indices run over the $\mathbb{CP}^N$ coordinates $1, \ldots, 2N$. The volume element is $\sqrt{-g} = r^{2N+1}\sqrt{\hat{g}}$. The one-form $\mathcal{A} = \mathcal{A}_i dx^i$ is a local potential for the Kähler form $\mathcal{J}$ on $\mathbb{CP}^N$, *i.e.* $d\mathcal{A} = 2\mathcal{J}$. In the $N = 1$ case, $\mathbb{CP}^1$ is isomorphic to S^2, so we can introduce the standard spherical polar coordinates $(x_1, x_2) = (\theta, \phi)$, with

$$\hat{g} = \frac{1}{4}\left(d\theta^2 + \sin^2\theta\, d\phi^2\right), \qquad \mathcal{A} = \frac{1}{2}\cos\theta\, d\phi. \tag{3.4}$$

See Appendix B of [218] for an explicit construction of $\hat{g}_{ij}$ and $\mathcal{A}$ for $N > 1$.

We assume that the mass parameter M is positive, and we can also assume that the angular momentum $a \geqslant 0$ without loss of generality due to the $t - \psi$ symmetry. The positive real roots of $f(r)$ define the horizon radii. From Descartes' rule of signs, we can show that $f(r)$ has either three or one positive real roots, counted with multiplicity. Since asymptotically de Sitter black holes must have at least

[3] These are related to the *unified* Boyer-Lindquist coordinates of [215, 216] by the transformations $r^2 \to (r^2 + a^2)\left(1 + a^2/L^2\right)^{-1}$ and $M \to M(1 + a^2/L^2)^{N+2}$.

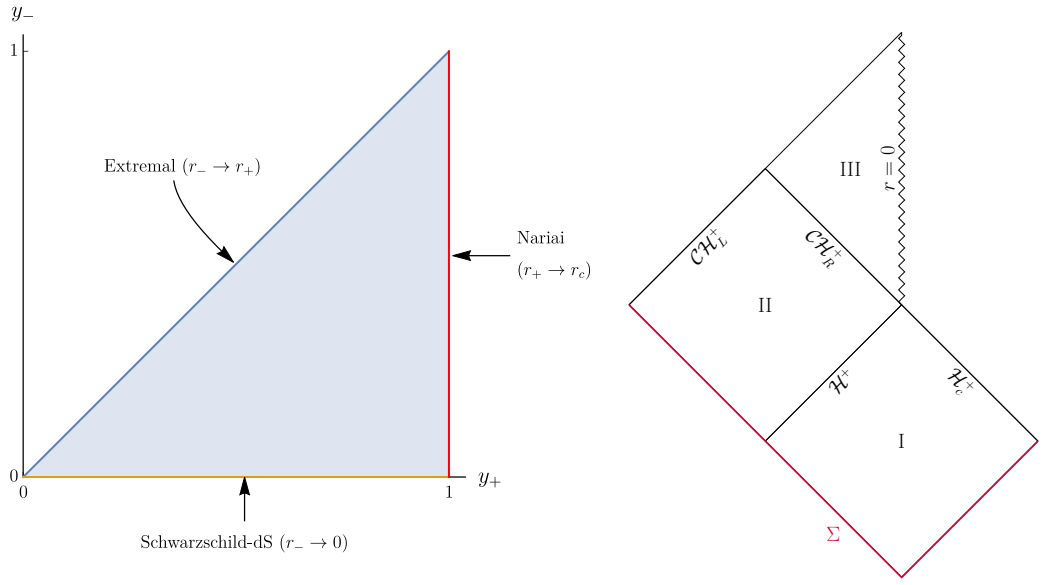

Fig. 3.1: Left panel: Parameter space of equal angular momenta Myers-Perry−de Sitter in terms of the dimensionless variables (y_+, y_-), and the relevant limits. **Right panel:** Globally hyperbolic portion of non-extremal MPdS with Cauchy surface Σ, and its analytic extension beyond the right Cauchy horizon $\mathcal{CH}^+_R$. The event horizon $\mathcal{H}_+$ and cosmological horizon $\mathcal{H}^+_c$ are also shown.

two roots, we require that $f(r)$ has a single zero at each of the three positive real roots $r_- \leqslant r_+ \leqslant r_c$, which define the Cauchy horizon (r_-), event horizon (r_+) and cosmological horizon (r_c). This requirement restricts the parameter space (M, a, L). Since $f(r)$ is negative in the limit $r \to \infty$, we see that $f(r)$ is positive for $r_- < r < r_+$ and negative for $r_+ < r < r_c$. The surface gravity at each horizon $r_i \in \{r_-, r_+, r_c\}$ is

$$\kappa_i \equiv \frac{|f'(r_i)|}{2r_i h(r_i)}. \tag{3.5}$$

We can express L, M and a in terms of r_-, r_+, r_c using the three conditions $f(r_i) = 0$. The Einstein equations are invariant under the scaling $g \to \lambda^2 g$ and $L \to \lambda L$, with $\lambda \in \mathbb{R}$, which we can use to construct dimensionless quantities in units of r_c. For example,

$$y_- \equiv \frac{r_-}{r_c}, \qquad y_+ \equiv \frac{r_+}{r_c}, \qquad \alpha \equiv \frac{a}{r_c}. \tag{3.6}$$

It follows that the MPdS black hole is a 2-parameter solution. We can choose, as we will often do, to parametrise the MPdS solution using the dimensionless parameters (y_+, y_-) where $y_+ \in [0, 1]$ and $0 \leqslant y_- \leqslant y_+$. This parameter space is plotted in the left panel of Fig. 3.1, with the relevant limits indicated. Extremality occurs when $y_- \to y_+$, at which κ_+ and κ_- vanish, *i.e.* the black hole has vanishing temperature.

Alternatively, for $d = 5$, we will sometimes instead parametrise MPdS using (y_+, α) where $0 \leqslant \alpha \leqslant \alpha_{\rm ext}$ ($\alpha_{\rm ext}$ is the value of α at extremality). We will find it useful to do so because it emphasises the relationship with Kerr-dS. In $d = 5$ we can express y_- in terms of (y_+, α) using[4]

$$y_-^2 = -\frac{1+y_+^2}{2} + \frac{1}{2}\sqrt{(1-y_+)^2 - \frac{4y_+^4}{\alpha^2 - y_+^2(1-\alpha^2)}}, \qquad (d=5) \tag{3.7}$$

and the extremal value of the rotation parameter (for which the temperature of the event horizon vanishes) is given by

$$\alpha_{\rm ext}^{d=5} = \frac{y_+\sqrt{1+2y_+^2}}{\sqrt{2}(1+y_+^2)}. \tag{3.8}$$

Let us now describe the causal structure of cohomogeneity-1 MPdS black holes in odd d. The relevant piece of its Penrose diagram is shown in the right panel of Fig. 3.1. Region I is the exterior region described by the metric (3.1) with $r_+ < r < r_c$. We define ingoing Eddington-Finklestein (EF) coordinates (v, r, ψ', x_i),

$$dv = dt + \frac{\sqrt{h(r)}}{f(r)}dr, \qquad d\psi' = d\psi + \Omega(r)\frac{\sqrt{h(r)}}{f(r)}dr, \tag{3.9}$$

in terms of which the metric is

$$ds^2 = -\frac{f(r)}{h(r)}\,dv^2 + \frac{2}{\sqrt{h(r)}}\,dv\,dr + r^2h(r)\left(d\psi' + \mathcal{A} - \Omega(r)\,dv\right)^2 + r^2 d\Sigma^2. \tag{3.10}$$

This is regular at the future event horizon $\mathcal{H}^+$, and the metric in region I can be analytically continued to region II where $r_- < r < r_+$. Converting to outgoing Eddington-Finklestein coordinates (u, r, ψ'', x_i),

$$du = dt - \frac{\sqrt{h(r)}}{f(r)}dr, \qquad d\psi'' = d\psi - \Omega(r)\frac{\sqrt{h(r)}}{f(r)}dr, \tag{3.11}$$

the metric is the same as (3.10) with the usual change of sign $dv\,dr \to -du\,dr$, and we can use these coordinates to analytically continue beyond the Cauchy horizon into region III where $r < r_-$. The causal structure is the same as Kerr-de Sitter (Kerr-dS) and Reissner-Nordström-de Sitter (RNdS). There is also a left Cauchy horizon $\mathcal{CH}_L^+$, however in the context of gravitational collapse it is occluded by the matter region, so we do not consider it here.

[4]Similar relations to (3.7) and (3.8) hold for arbitrary odd d but it is not enlightening to explicitly display them here.

3.1.2 Klein-Gordon equation in MPdS

We want to study massive scalar field perturbations, with mass μ, on a fixed MPdS background (3.1), which are governed by the Klein-Gordon equation

$$\nabla_a \nabla^a \Phi - \mu^2 \Phi = 0. \tag{3.12}$$

In the context of strong cosmic censorship, the scalar field has been found to be a good proxy for linearised gravitational perturbations in both RNdS and Kerr-dS [94, 86, 89]. To study linear mode perturbations, we make the following separation ansatz in BL coordinates (3.1),

$$\Phi = e^{-i\omega t + im\psi} \mathcal{R}(r) Y(x_i), \tag{3.13}$$

which introduces the frequency ω and azimuthal quantum number m of the perturbation. Using this ansatz, the Klein-Gordon equation separates, with the angular eigenfunction $Y(x_i)$ satisfying a charged Laplace equation on $\mathbb{CP}^N$ with charge m and with eigenvalue λ,

$$(\mathcal{D}^2 + \lambda) Y(x_i) = 0, \qquad \mathcal{D} \equiv \hat{\nabla} - im\mathcal{A}, \tag{3.14}$$

where $\hat{\nabla}$ is the covariant derivative on $\mathbb{CP}^N$. The eigenfunctions $Y(x_i)$ were studied in [219], and regularity requires that the eigenvalues are quantised as [219]

$$\lambda = l(l+2N) - m^2, \qquad l = 2k + |m|, \qquad k = 0, 1, 2, \ldots \tag{3.15}$$

Here l labels the total angular momentum of the mode. The radial equation reduces to

$$\mathcal{R}''(r) + \left(\frac{1+2N}{r} + \frac{f'}{f} \right) \mathcal{R}'(r) + \frac{1}{f} \left(\frac{h}{f}(\omega - m\Omega)^2 - \frac{\lambda}{r^2} - \frac{m^2}{r^2 h} - \mu^2 \right) \mathcal{R}(r) = 0. \tag{3.16}$$

We will need to solve this eigenvalue equation to find the eigenfrequencies ω of the system. For that, we require that Φ obeys QNM boundary conditions, namely Φ must be regular in ingoing coordinates (3.9) at the future event horizon $\mathcal{H}^+$ and regular in outgoing coordinates (3.11) at the cosmological horizon $\mathcal{H}_c^+$. In BL coordinates (3.1), this translates to the requirement that the the radial

eigenfunction must behave as

$$\mathcal{R}(r) \sim \begin{cases} (r-r_+)^{-i\frac{\omega-m\Omega(r_+)}{2\kappa_+}}\hat{\mathcal{R}}_{(+)} & \text{as} \quad r \to r_+\,, \\ (r_c-r)^{-i\frac{\omega-m\Omega(r_c)}{2\kappa_c}}\hat{\mathcal{R}}_{(c)} & \text{as} \quad r \to r_c\,, \end{cases} \tag{3.17}$$

for some functions $\hat{\mathcal{R}}_{(+)}$ and $\hat{\mathcal{R}}_{(c)}$ that are smooth at r_+ and r_c, respectively. These boundary conditions turn out to be the same as four-dimensional de Sitter black holes (1.17), *i.e.* there is no dimensional dependence.

3.1.3 Numerical setup

To prepare the radial Klein-Gordon equation (3.16) to be solved numerically, we redefine $\mathcal{R}(r)$ so that the only solutions which are regular at the boundaries are those which obey QNM boundary conditions (3.17), hence the only solutions that converge numerically are QNMs. A Frobenius analysis[5] at $r = r_+$ yields solutions of the form

$$\mathcal{R}\big|_{r=r_+} \sim c_1\,(r-r_+)^{-i\frac{\omega-m\Omega(r_+)}{2\kappa_+}}\hat{\mathcal{R}}_{(1,+)} + c_2\,(r-r_+)^{i\frac{\omega-m\Omega(r_+)}{2\kappa_+}}\hat{\mathcal{R}}_{(2,+)}, \tag{3.18}$$

for some constants c_i and functions $\hat{\mathcal{R}}_{(i,+)}$ which are analytic at r_+. Similarly, at the cosmological horizon,

$$\mathcal{R}\big|_{r=r_c} \sim c_1'\,(r_c-r)^{i\frac{\omega-m\Omega(r_c)}{2\kappa_c}}\hat{\mathcal{R}}_{(1,c)} + c_2'\,(r_c-r)^{-i\frac{\omega-m\Omega(r_c)}{2\kappa_c}}\hat{\mathcal{R}}_{(2,c)}\,, \tag{3.19}$$

where $\hat{\mathcal{R}}_{(i,c)}$ are analytic at r_c. The first term in (3.18) and the second term in (3.19) obey the QNM boundary conditions (3.17), but not the other two. So we have to eliminate the latter. For that we make the redefinition

$$\mathcal{R}(r) = (r-r_+)^{-i\frac{\omega-m\Omega(r_+)}{2\kappa_+}}(r_c-r)^{-i\frac{\omega-m\Omega(r_c)}{\kappa_c}}\,\mathcal{Q}(r)\,, \tag{3.20}$$

such that $\mathcal{R}(r)$ obeys QNM boundary conditions (3.17) at both boundaries if $\mathcal{Q}(r)$ is analytic (*i.e.* the singular solutions are never captured by the numerical function $\mathcal{Q}(r)$ which is necessarily analytic). We also introduce the compact dimensionless radial coordinate

$$y = \frac{r-r_+}{r_c-r_+} \tag{3.21}$$

such that the event horizon is at $y = 0$ and the cosmological horizon is at $y = 1$. Finally, we perform a Taylor expansion of the resulting ODE at each boundary,

[5] A similar Frobenius analysis is discussed in detail in section 3.5.

to get Dirichlet and Robin boundary conditions at $y = 0$ and $y = 1$, respectively, which we impose at the matrix level after discretisation. These are purely for numerical convenience, to guard against zero cancellation at the boundaries, and do not change the resulting solution, since they follow directly from the equations of motion. A detailed discussion of this type of *derived boundary condition* can be found in [166]. The explicit expression for the final ODE fully prepared for numerical evaluation is long and unenlightening, so we do not write it here.

Working now with dimensionless quantities, as defined in (3.6), the resulting ODE is a quadratic eigenvalue problem in the frequency $\tilde{\omega} = \omega\, r_c$, *i.e.* the coefficients depend quadratically on $\tilde{\omega}$. To solve this numerically, we use the direct eigenvalue method when we want to find the full spectrum, and the Newton-Raphson method to reach numerically difficult regions. Both were described in Section 1.5.

3.2 Quasinormal mode families of Myers-Perry−de Sitter

Ideally, the first step in classifying the QNM spectra is to identify some corner or window of the parameter space where we can find analytic expressions for the frequencies (in some approximation). This can help identify the physical nature of the modes and eventually already hint at the existence of different families of QNMs, and it can further be used to test the numerical results. In this section we derive approximations in the de Sitter ($a \to 0$, $r_+ \to 0$), eikonal ($m = l \to \infty$) and near-extremal limit ($r_- \to r_+$).

3.2.1 de Sitter modes

When $a \to 0$, $r_+ \to 0$, the MPdS black hole reduces to the pure de Sitter spacetime. Scalar perturbations in this background, *i.e.* the pure de Sitter (dS) modes, must be regular at the origin and at the cosmological horizon. The d-dimensional dS modes have been studied previously [220]. In $d = 2N + 3$ dimensions, the pure dS modes have the frequency spectrum

$$\omega_{dS}\, r_c = -i\,(l + 2n), \qquad \text{(for all } d\text{)} \tag{3.22}$$

$$\omega_{dS}^{\text{even}}\, r_c = -i\left[l + 2(n + N + 1)\right], \qquad \text{(even } d \text{ only)} \tag{3.23}$$

for radial overtone $n = 0, 1, 2, \ldots$. In odd dimension d, N is an integer, and so the second set of modes $\omega_{dS}^{\text{even}}$ is a subset of the first. However, in even dimensions d, N is a half integer and thus the second mode set (3.23) is distinct from the first described by (3.22). This property of dS modes plays an important role in the mode spectrum of Schwarzschild-de Sitter and MPdS, as we will discuss, in particular, in Section 3.3.

3.2.2 Photon sphere modes

When a de Sitter spacetime possesses an event horizon, there is another family of QNMs, the photon sphere (PS) modes, reviewed in Section 1.1. The nomenclature derives from the fact that, in the eikonal limit $|m| = l \to \infty$, the frequencies of these modes (which exist for any l, m) are related to the properties of unstable circular photon orbits of the background by the PS correspondence (1.19). In four dimensions this correspondence is well studied, both numerically and analytically [221–224, 94, 86, 89]. In higher dimensions this is not as well documented[6]. We will verify that this correspondence also holds for cohomogeneity-1 MPdS black holes.

We use the Lagrangian formalism, solving directly for null geodesics which are independent of the $\mathbb{CP}^N$ coordinates, but only rotate in the fiber direction ψ. For example, in the $N = 1$ ($d = 5$) case, this corresponds to geodesics with $\dot{\theta} = \dot{\phi} = 0$ in the (θ, ϕ) coordinates of (3.4). For all N, the Lagrangian describing such geodesics is

$$\mathcal{L} = -\frac{f(r)}{2h(r)}\,\dot{t}^2 + \frac{1}{2f(r)}\,\dot{r}^2 + \frac{r^2 h(r)}{2}\left(\dot{\psi} - \Omega(r)\,\dot{t}\right)^2 \tag{3.24}$$

where the dot indicates a derivative with respect to the affine parameter τ of the null geodesic and the background functions f, h, Ω are defined in (3.2)-(3.3). We can associate a conserved energy E and angular momentum L_ψ to translations in the t and ψ Killing directions, respectively:

$$E \equiv \frac{f}{h}\,\dot{t} + \Omega\, L_\psi, \qquad\qquad L_\psi \equiv r^2 h(\dot{\psi} - \Omega\,\dot{t}). \tag{3.25}$$

[6]This correspondence has been derived explicitly for static spacetimes in arbitrary dimensions [74], but this was not generalised to rotating spacetimes.

Substituting these into the Lagrangian and noting that null geodesics have $\mathcal{L} = 0$, we arrive at the radial Schrödinger equation with potential V_{eff}:

$$\dot{r}^2 + V_{\text{eff}}(r) = 0, \qquad V_{\text{eff}}(r) \equiv {L_\psi}^2 f\left(\frac{1}{r^2 h} - \frac{h}{f}\left(b^{-1} - \Omega\right)^2\right) \tag{3.26}$$

where we have defined the impact parameter $b \equiv \frac{L_\psi}{E}$. Unstable circular orbits have $V_{\text{eff}}(r_0) = V'_{\text{eff}}(r_0) = 0$. First solving $V'_{\text{eff}}(r_0) = 0$ gives two possible values for the impact parameter

$$b^\pm = \frac{a\sqrt{2(N+1)M}}{\sqrt{2(N+1)M} \pm r_0^N}. \tag{3.27}$$

Substituting this back into the effective potential and now requiring $V_{\text{eff}}(r_0) = 0$, we find that the orbit radii r_0 are the (relevant) roots of a polynomial of order $2(N+1)$:

$$L^2 r_0^2\Big[2(N+1)M + r_0^N(r_0^N \pm 2\sqrt{2(N+1)M})\Big] = 2a^2 M\Big[NL^2 - (N+1)r_0^2\Big] \tag{3.28}$$

with the $\pm$ sign corresponding to the signs of $b^\pm$. For $N = 1$ this is a quartic polynomial, which we can solve explicitly, but for $N > 1$ we can only find the orbit radii r_0 numerically.[7] We find that only two solutions have $r_+ < r_0 < r_c$, with the physical solution corresponding to the minus sign in (3.28) and thus to b^-. The imaginary part of the photon sphere modes (1.19) is proportional to the principal Lyapunov exponent, which characterises the instability time scale of the geodesic. It can be computed from the second derivative of the effective potential [74]

$$\lambda_{\text{L}} = \sqrt{-\frac{V''_{\text{eff}}(r)}{2\dot{t}^2}}\bigg|_{r=r_c} \tag{3.29}$$

and the real part is proportional to the angular velocity of the null orbit, $\Omega_0 = \frac{\mathrm{d}\psi}{\mathrm{d}t} = \frac{\dot{\psi}}{\dot{t}}$, which can be computed from (3.25). Explicitly, these two quantities are given by

$$\Omega_0 = \frac{1}{b^-}, \qquad \lambda_{\text{L}} = \frac{\sqrt{2N}}{|b^-|}\left|1 + \frac{a\,(b^-)^2}{r_c^2(N+1)(a-b^-)}\right|. \tag{3.30}$$

Note that expressions involving the black hole parameters (M, a, L) can be written in terms of (y_+, y_-) using (B.1) in Appendix B. The solution to (3.28) with the larger angular velocity Ω_0 (*i.e.* larger real part) corresponds to the *corotating* PS modes, while the other with smaller Ω_0 describes the *counter-rotating* PS

[7] Note that using (3.27) and (3.28) we can express the mass and AdS radius in terms of the orbit parameters as $M = \frac{(b^\pm)^2 r_0^{2N}}{2(N+1)(a-b^\pm)^2}$ and $L = r_0\sqrt{\frac{N+1}{N-(b^\pm)^{-2}(N+1)r_0^2}}$, which are useful to simplify our final expressions.

modes. The corotating modes have smaller r_0, *i.e.* are closer to the event horizon, and so intuitively they are less stable, with smaller λ_L. Indeed, the corotating modes always dominate, *i.e.* they have smaller $|\,\mathrm{Im}(\omega)|$ than their counter-rotating partner.

In Section 3.5, we will verify that the eikonal approximation (1.19) and (3.30), although strictly valid in the limit $|m| = l \to \infty$, also gives a very good approximation for the PS modes even when $|m| = l$ is of $\mathcal{O}(1)$.

3.2.3 Near-horizon geometry and near-horizon modes

There is another limit where we can compute QNMs using analytical methods. Indeed, near-extremal black holes typically have a set of modes known as near-horizon (NH) modes. This nomenclature follows from the fact that these NH modes characteristically have a wavefunction that is highly localised around the event horizon (when near extremality), and they have frequencies approaching $\mathrm{Im}(\omega) \to 0$ and $\mathrm{Re}(\omega) \to m\Omega(r_+)$ in the strict extremal limit. In subsection 3.2.3.3, we will use a matched asymptotic expansion method to analytically capture these NH modes, whereby we match the solution of the Klein-Gordon equation in the near-horizon region of near-extremal MPdS with a trivial solution in the far-region.

Before deriving the near-horizon modes, we do a small digression in subsections 3.2.3.1−3.2.3.2, and we find the near-horizon geometry of extremal MPdS and the associated effective AdS_2 Breitenlöhner-Freedman (BF) bound. The motivation to do so is twofold. Firstly, the BF bound naturally appears in the expressions for the NH frequencies and it will ultimately provide a criterion to find QNMs that preserve strong cosmic censorship. Moreover, for completeness, we take the opportunity to discuss and test a theorem about instabilities arising from perturbations of near-horizon geometries [144, 149] that is relevant in the context of our study.

Let us review some details about the near-horizon geometry that were briefly discussed in Section 1.4. In the near-horizon limit, the geometry of extremal black holes, including MPdS, can be expressed locally as a product of AdS_2 times a compact space [144], even though MPdS is asymptotically de Sitter. In this limit, the Klein-Gordon equation in the near-horizon geometry reduces to an effective scalar field equation on pure AdS_2 space with a certain effective mass μ_{eff} and charge q_{AdS}. It is well known that in AdS_2 (with radius L_{AdS}), a scalar field perturbation is normalisable even if its squared mass μ^2_{AdS} is negative, provided that it obeys the 2-dimensional BF bound $\mu^2_{\text{AdS}} L^2_{\text{AdS}} \geqslant -\frac{1}{4}$ [147, 148]. On the other hand, the

scalar field on AdS_2 is not stable if its mass is below the 2-dimensional BF bound. However, a violation of the effective AdS_2 BF bound of the near-horizon geometry of extreme MPdS does not *necessarily* imply an instability of the scalar field on the full d-dimensional MPdS black hole geometry.

For asymptotically flat or AdS black holes, a conjecture by Durkee and Reall [144] (proven by Hollands and Ishibashi in [149]) states that a sufficient (but not necessary) condition for this near-horizon AdS_2 BF bound violation to develop into an instability of the extremal black hole is that the unstable mode preserves a certain symmetry already present in the background geometry. In the case of rotating black holes, this is that the perturbation is axisymmetric, $m = 0$. Assuming there is such an instability, one expects that it also extends away from extremality, by continuity. For Myers-Perry-AdS, near-horizon instabilities triggered by a violation of the near-horizon AdS_2 BF bound have been studied in detail in [217, 144]. Strictly speaking, the proof established in [149] only applies to asymptotically flat or AdS black holes, but is somehow trivial to extend the proof in the asymptotically flat context to black holes living in the static patch of dS. Indeed, in [149], slices that extend from $\mathcal{H}^+$ to $\mathcal{I}^+$ were considered and appropriate boundary conditions were given so that the *canonical energy* of [225] obeys a certain balance equation that plays a crucial role in the proof. Such a balance equation can still be obtained in the context of black holes living in the static patch of dS by imposing boundary conditions on $\mathcal{H}^+_c$ that are similar to those imposed on $\mathcal{H}^+$. If one further restricts to perturbations that preserve axisymmetry, the desired result follows.[8] Recent numerical results seem to corroborate the previous extension and show that an effective AdS_2 BF bound violation explains the instability of $d \geqslant 6$ Reissner-Nordström−de Sitter black holes [146] so it is worthwhile to check whether $m = 0$ modes in MPdS can lead to a violation of the 2-dimensional BF bound, and eventually to an instability in MPdS (in subsection 3.2.3.2 we will find that this is not the case).

3.2.3.1 Near-horizon geometry of MPdS

To find the near-horizon geometry of the extremal MPdS black hole, we start with (3.10) at extremality $r_- = r_+$, where $f(r)$ has a double root $r = r_- = r_+$, and zoom into the horizon by the coordinate transformations

$$r \to r_+ + \epsilon\, R, \qquad t \to \frac{\tilde{T}}{\epsilon}, \qquad \psi \to \Psi + \Omega(r_+)\frac{\tilde{T}}{\epsilon}. \tag{3.31}$$

[8] We thank S. Hollands for discussions on this point.

Taking the limit $\epsilon \to 0$, i.e. keeping only the leading contribution of an expansion in small ϵ, we obtain the near-horizon geometry

$$ds^2 = -\frac{f''(r_+)}{2h(r_+)} R^2\, d\tilde{T}^{\,2} + \frac{2}{f''(r_+)}\,\frac{dR^2}{R^2} + r_+^2 h(r_+)\left(d\Psi + \mathcal{A} - R\Omega'(r_+)\, d\tilde{T}\right)^2 + r_+^2\, d\Sigma^2. \tag{3.32}$$

We can make the AdS_2 structure more explicit by a further change of coordinates, similarly to [144]. We define the constants

$$L_{\mathrm{AdS}}^2 \equiv \left.\frac{2}{f''(r_+)}\right|_{\mathrm{ext}}, \qquad \tilde{\Omega} \equiv \left.\Omega'(r_+)\sqrt{h(r_+)}\right|_{\mathrm{ext}}, \tag{3.33}$$

and rescale the time coordinate $\tilde{T} \to L_{\mathrm{AdS}}^2\sqrt{h(r_+)}T$, to get the near-horizon geometry in (T, R, Ψ, x_i) coordinates

$$ds^2 = L_{\mathrm{AdS}}^2\left(-R^2\, dT^2 + \frac{dR^2}{R^2}\right) + r_+^2 h(r_+)\left(d\Psi + \mathcal{A} - R\,\tilde{\Omega} L_{\mathrm{AdS}}^2\, dT\right)^2 + r_+^2\, d\Sigma^2\,. \tag{3.34}$$

This near-horizon geometry is still a solution of the d-dimensional Einstein-dS equations. On the other hand, the AdS_2 part parametrised by (T, R) satisfies the 2-dimensional Einstein-AdS equations with $R = -2L_{\mathrm{AdS}}^{-2}$.

3.2.3.2 Perturbations of the near-horizon geometry and the AdS_2 BF bound

Linear mode solutions of the Klein-Gordon equation on the near-horizon geometry (3.34), with the Fourier decomposition $\Phi = e^{-i\omega T + im\Psi}\chi(R)$, must satisfy the ODE

$$R^2\,\chi'' + 2R\,\chi' - \left[\frac{(\omega^2 - m\tilde{\Omega}L_{\mathrm{AdS}}^2 R)^2}{R^2} - L_{\mathrm{AdS}}^2\left(\mu^2 + \frac{\lambda}{r_+^2} + \frac{m^2}{r_+^2 h(r_+)}\right)\right]\chi = 0. \tag{3.35}$$

We can write this as a massive charged Klein-Gordon equation on pure AdS_2,

$$\left(\tilde{\nabla} - iq_{\mathrm{AdS}}A(R)\right)^2\Phi = L_{\mathrm{AdS}}^2\left(\mu^2 + \frac{\lambda}{r_+^2} + \frac{m^2}{r_+^2 h(r_+)}\right)\Phi, \qquad A(R) = -R\, dT\,, \tag{3.36}$$

if we make the identification $q_{\mathrm{AdS}} = -m\, L_{\mathrm{AdS}}^2\tilde{\Omega}$. Here $\tilde{\nabla}$ is the covariant derivative on pure AdS_2 associated to the metric

$$ds^2_{\mathrm{AdS}_2} = L_{\mathrm{AdS}}^2\left(-R^2\, dT^2 + \frac{dR^2}{R^2}\right), \tag{3.37}$$

and $\tilde{\nabla} - iq_{\rm AdS}A(R)$ is the gauge covariant derivative of a scalar field with effective charge $q_{\rm AdS}$ in the AdS_2 background with a homogeneous electric field $A(R)$. The latter descends from the $dT\,d\Psi$ component of the metric in the original near-horizon solution (3.34).

Asymptotically, as $R \to \infty$, the solutions of (3.35) behave as $\chi \sim R^{-\Delta_\pm}$ where the 2-dimensional conformal dimensions $\Delta_\pm$ are

$$\Delta_\pm = \frac{1}{2} \pm \frac{1}{2}\sqrt{1 + 4{\mu_{\rm eff}}^2 L^2_{\rm AdS}}, \qquad {\mu_{\rm eff}}^2 \equiv \mu^2 + \frac{\lambda}{r_+^2} + \frac{m^2}{r_+^2 h(r_+)} - L^2_{\rm AdS} m^2 \tilde{\Omega}^2. \tag{3.38}$$

In order for such solutions to not oscillate at infinity (*i.e.* to be normalisable; with finite energy), we require that $\Delta_\pm$ is real. This requirement defines the AdS_2 BF bound of the near-horizon geometry:

$${\mu_{\rm eff}}^2 L^2_{\rm AdS} \geqslant -\frac{1}{4}. \tag{3.39}$$

In summary, by taking the near-horizon limit of extreme MPdS, we have found the effective near-horizon AdS_2 radius $L_{\rm AdS}$, charge $q_{\rm AdS}$ and mass $\mu_{\rm eff}$, which are explicitly given in terms of (N, y_+) by:

$$L^2_{\rm AdS} = \frac{r_c^2 y_+^2}{2(N+1)} \frac{1 - y_+^{2N+2}(2 - y_+^2 + N(1-y_+^2))}{N(1-y_+^2)(1+y_+^{2N+2}) - 2y_+^2(1-y_+^{2N})}, \tag{3.40}$$

$$q_{\rm AdS} = \frac{L^2_{\rm AdS}}{r_c^2} \frac{2m}{y_+^2} \sqrt{\frac{N(1-y_+^2) - y_+^2(1-y_+^{2N})}{(1-y_+^2)(1-y_+^{2N+2})}}, \tag{3.41}$$

$${\mu_{\rm eff}}^2 = \mu^2 + \frac{1}{r_c^2}\left(\frac{\lambda}{y_+^2} - \frac{m^2}{y_+^2}\frac{N}{N+1}\frac{1 - y_+^{2N+2}(2 - y_+^2 + N(1-y_+^2))}{N(1-y_+^2)(1+y_+^{2N+2}) - 2y_+^2(1-y_+^{2N})}\right). \tag{3.42}$$

In the UV region of the full geometry, excitations in asymptotically d-dimensional dS spacetimes have finite energy (*i.e.* are stable) if and only if $\mu \geqslant 0$. However, in the IR region, these can correspond to an effective mass $\mu_{\rm eff}$ in the near-horizon region, as defined in (3.38) and (3.42), that violates the AdS_2 BF bound (3.39) of the near-horizon geometry. Since ${\mu_{\rm eff}}^2$ is minimised when $\mu = 0$, we will restrict considerations to the massless scalar field $\mu = 0$ on MPdS from now on.

For the axisymmetric modes $m = 0$ the effective mass (3.38) is always non-negative, and hence there is no AdS_2 BF bound violation (that could be relevant to the previously discussed theorem about near-horizon instabilities [144, 149]). Since that theorem provides a sufficient but not necessary condition for instability, we cannot make any conclusions about the stability of MPdS, but we indeed do not find any instabilities when $m = 0$.

We will also be interested in modes with non-zero m, which *can* violate the BF bound (3.39). Of particular interest will be the behaviour in the eikonal limit where $m = l$ is large. Recall that, analogously to the spherical harmonics, the $\mathbb{CP}^N$ angular eigenvalues λ of (3.14) can be labeled by m and l, with $|m| \leqslant l$. For a fixed m, one can show that ${\mu_{\text{eff}}}^2$ is minimised when $l = |m|$, *i.e.* a BF bound violation will first occur for the maximally corotating modes. Furthermore, the BF bound can always be violated for sufficiently large $m = l$. Recall that in this $m \neq 0$ case the background symmetry is not preserved, and it follows from the analysis of Durkee-Reall and Hollands-Ishibashi [144, 149] that a violation of the AdS_2 BF bound says nothing about the existence of eventual instabilities in the full MPdS geometry. Yet, one might expect that a BF bound violation can signal some transition boundary of the physical properties of the system. Indeed, in the previous chapter, for Kerr-Newman, we found that this was indeed the case, where a BF bound violation indicated the critical ratio of charge to angular momentum a/Q at which the PS and NH modes merge to form a single family in the near-extremal limit. We will see that a similar behaviour occurs in MPdS (with some differences), as we will see in the discussion of the results of Fig. 3.12 and Table 3.1 of section 3.5.

3.2.3.3 Near-horizon modes

To find the near-horizon (NH) modes in an off-extremality expansion, we use a matched asymptotic expansion, which is motivated by the following considerations. From our numerical results we find that close to extremality, where $r_- \to r_+$, NH eigenfunctions are very much localized near the event horizon and very quickly decay as we move away from it towards the cosmological horizon. To obtain a good analytical approximation that well describes the NH mode solutions of the Klein-Gordon equation we can then split the spacetime into a near-region, localized around the horizon, and a far-region, that extends all the way up to the cosmological horizon. In the near-region, a double series expansion of the Klein-Gordon equation around the extremal black hole and, simultaneously, about the event horizon yields an hypergeometric equation which we can solve analytically to find the near-region eigenfunction. We then match this solution with the far-region eigenfunction which, from the above observations and in a "poor-man" approximation, can be taken to be approximately the trivial vanishing solution to leading order in the expansion. The matching and boundary conditions fix the amplitudes of the eigenfunctions and quantise the frequency of the NH modes. To validate our matched asymptotic expansion and to simultaneously identify the NH modes, we

compare this analytical expression for the frequency with the numerical data. In the literature there are systems where a similar strategy proved to be very useful and successful [89, 226, 122, 227].

The explicit derivation presented here is for $N = 1$ (for clarity of the presentation), but the approach generalises, and the main result that we present in the end is valid for all N. We start by defining

$$\sigma = 1 - \frac{r_-}{r_+}, \qquad x = 1 - \frac{r}{r_+}, \qquad z = x\,\sigma\,. \tag{3.43}$$

Small σ corresponds to taking the near-extremal limit, while small $x = z/\sigma$ corresponds to a zoom into the horizon (note that $x \leqslant 0$ and $z \leqslant 0$). We will take the $\sigma \to 0$ limit while holding z fixed to zoom in the near-extremal solution around the horizon. To zeroth order in the σ-expansion, we look for modes (the NH modes) whose frequency at extremality is purely real and satisfies the superradiant bound, $\omega = m\,\Omega(r_+)|_{\rm ext}$. This suggests that (3.43) should be accompanied by the σ-expansion in the frequency,

$$\omega = m\,\Omega(r_+)\big|_{\rm ext} + \sigma\,\delta\omega\,, \tag{3.44}$$

where we will have to determine the next-to-leading order frequency correction $\delta\omega$. Inserting (3.43)−(3.44) into the (massless) Klein-Gordon equation (3.16) and taking the limit $\sigma \to 0$ while holding z fixed, we can show that the leading order contribution of the expansion is a hypergeometric equation for $\chi(z)$ if we perform the field redefinition

$$R(z) = z^A(1-z)^B\chi(z) \tag{3.45}$$

where A and B are given by

$$A = -i\left(\frac{m\sqrt{1+y_+^2}(1+3y_+^2+4y_+^4)}{8(1+2y_+^2)(1-y_+^4)} + \frac{y_+\sqrt{(1+y_+^2)(1+2y_+^2)}}{2\sqrt{2}(1-y_+^2)}\,\delta\tilde{\omega}\right), \tag{3.46}$$

$$B = i\left(\frac{m(1+3y_+^2)(3+4y_+^2)}{8\sqrt{1+y_+^2}(1+2y_+^2)(1-y_+^2)} - \frac{y_+\sqrt{(1+y_+^2)(1+2y_+^2)}}{2\sqrt{2}(1-y_+^2)}\,\delta\tilde{\omega}\right), \tag{3.47}$$

where we have introduced the dimensionless frequency correction $\delta\tilde{\omega} \equiv r_c\,\delta\omega$. In these conditions, the general solution of the system is a sum of hypergeometric functions ${}_2F_1$ [228]:

$$\chi(z) = C_{(1)}\,{}_2\mathrm{F}_1(a_+, a_-, c; z) + C_{(2)}z^{1-c}\,{}_2\mathrm{F}_1(a_+ - c + 1, a_- - c + 1, 2 - c; z), \tag{3.48}$$

for some constants $C_{(1)}$ and $C_{(2)}$, and the coefficients $a_\pm$ and c are expressed in terms of the effective mass $\mu_{\rm eff}$ and AdS_2 radius $L_{\rm AdS}$ given in (3.40)-(3.42), as well as y_+ and m as:

$$\begin{aligned} a_\pm &= \frac{1}{2} \pm \frac{1}{2}\sqrt{1+4\mu_{\rm eff}^2 {L_{\rm AdS}}^2} + \frac{im\sqrt{1+y_+^2}(1+4y_+^2)}{4(1-y_+^2)(1+2y_+^2)} - \frac{iy_+\sqrt{(1+y_+^2)(1+2y_+^2)}}{\sqrt{2}(1-y_+^2)}\,\delta\tilde{\omega}, \\ c &= 1 - \frac{im\sqrt{1+y_+^2}(1+3y_+^2+4y_+^4)}{4\sqrt{1+y_+^2}(1-y_+^2)(1+2y_+^2)} - \frac{iy_+\sqrt{1+3y_+^2+2y_+^4}}{\sqrt{2}(1-y_+^2)}\,\delta\tilde{\omega}. \end{aligned} \tag{3.49}$$

Using ${}_2\mathrm{F}_1(\alpha,\beta,\gamma,0) = 1$, the leading order behaviour of $R(z)$ near the event horizon $z=0$ is

$$R\big|_{z\to 0^-} \simeq C_{(1)}\, z^A + C_{(2)}\, z^{-A}. \tag{3.50}$$

The first (second) term describes an ingoing (outgoing) wave at the event horizon $z=0$. We want the solution that is regular in ingoing Eddington-Finklestein coordinates (3.9) so we set $C_{(2)}=0$ in (3.48).

Formally, we should now find the *far-region* wavefunction in some approximation (tailored to an analytical treatment) that is valid far from the event horizon all the way up to the cosmological horizon, and match it with the near-horizon solution to find the QNMs, as we did for Kerr-Newman in Chapter 2. In MPdS, it turns out that it is difficult to solve the far-region equations analytically, so we will take the simpler heuristic approach of matching the near-region eigenfunction with a vanishing far-region wavefunction, motivated by our observation that the near-horizon modes are highly peaked near the horizon. In spite of being a "poor-man" matched asymptotic expansion, we will find *à posteriori* that this simple analysis yields an approximation that agrees extremely well with our numerics. The edge of the near-horizon region where the matching is done is at $z\to-\infty$. Using the following relationship between the coefficients,

$$A + B - a_\pm = -\frac{1}{2} \mp \frac{1}{2}\sqrt{1+4{\mu_{\rm eff}}^2 L_{\rm AdS}^2}, \tag{3.51}$$

we can expand the near-region hypergeometric function for large negative z, to get

$$\begin{aligned} R\big|_{|z|\gg 1} \simeq\ & (-z)^{-\frac{1}{2}-\frac{1}{2}\sqrt{1+4{\mu_{\rm eff}}^2 L_{\rm AdS}^2}} \frac{\Gamma(a_- - a_+)\Gamma(c)}{\Gamma(c-a_+)\Gamma(a_-)} \\ & + (-z)^{-\frac{1}{2}+\frac{1}{2}\sqrt{1+4{\mu_{\rm eff}}^2 L_{\rm AdS}^2}} \frac{\Gamma(a_+ - a_-)\Gamma(c)}{\Gamma(c-a_-)\Gamma(a_+)}. \end{aligned} \tag{3.52}$$

Thus, the behaviour of the two contributions depends on the real part of each exponent. The expression $\sqrt{1+4{\mu_{\rm eff}}^2 L_{\rm AdS}^2}$ is always either positive or imaginary,

and so the first term in (3.52) always vanishes far away from the event horizon. When ${\mu_{\rm eff}}^2 L^2_{\rm AdS} \geqslant 0$ the second term diverges as $|z|$ grows large. Since we want to match the large radius expansion (3.52) of the near-region with a vanishing far-region wavefunction, we must require that the coefficient of the second term vanishes identically. This happens if one of the arguments of the gamma functions in the denominator is a non-positive integer since $\Gamma(-n) = \infty$, $n \in \mathbb{N}_0$. That is to say, we require $a_+ = -n$, for $n = 0, 1, 2, \ldots$ which gives a quantisation condition for $\delta\tilde{\omega}$. Namely, for $N = 1$, the frequency of the NH modes should be well approximated by

$$\omega_{\rm NH}^{(N=1)} r_c \simeq \frac{m}{y_+\sqrt{2(1+2y_+^2)}} - i\,\frac{1-y_+^2}{y_+\sqrt{2(1+y_+^2)(1+2y_+^2)}}\Bigg[i\,\frac{m(1+4y_+^2)\sqrt{1+y_+^2}}{2(1-y_+^2)(1+2y_+^2)} + 1 + 2n + \sqrt{1 - \frac{m^2(1+2y_+)^2}{2(1-y_+^2)(1+2y_+^2)} + \frac{\lambda(1+2y_+^2)}{1-y_+^2}}\Bigg]\sigma + \mathcal{O}\left(\sigma^2\right) . \tag{3.53}$$

Note that $\sigma = 1 - y_-/y_+$ can be expressed in terms of (y_+, α) using (3.7). The calculation so far is strictly valid for $N = 1$ but it generalizes *mutatis mutandis* for all N. At the end of the day, for any $d = 2N + 3$, the frequency of the NH modes can be written as

$$\omega_{\rm NH} \simeq m\,\Omega(r_+)|_{\rm ext} + \left[m\Omega_{(1)} - \frac{i}{2}\left(1 + 2n + 2iq_{\rm AdS} + \sqrt{1 + 4{\mu_{\rm eff}}^2 {L_{\rm AdS}}^2}\right)\kappa_{(1)}\right]\sigma + \mathcal{O}\left(\sigma^2\right) \tag{3.54}$$

where we have defined the first-order coefficients of the Taylor expansion of $\Omega(r_+)$ and κ_+:

$$\Omega_{(1)} \equiv \left.\frac{d\Omega(r_+)}{d\sigma}\right|_{\sigma=0}, \qquad \kappa_{(1)} \equiv \left.\frac{d\kappa_+}{d\sigma}\right|_{\sigma=0}. \tag{3.55}$$

Explicit expressions for $\Omega_{(1)}$ and $\kappa_{(1)}$ as a function of N and y_+ are given in (B.3) of Appendix B. Apart from the angular velocity and surface gravity, $\omega_{\rm NH}$ only depends on the black hole parameters via the effective mass $\mu_{\rm eff}$, charge $q_{\rm AdS}$ and AdS_2 radius $L_{\rm AdS}$ which characterize the near-horizon geometry and its perturbations. In general, $\omega_{\rm NH}$ is complex, but in the axisymmetric case $m = 0$, $q_{\rm AdS}$ vanishes and the BF bound (3.39) is never violated, so the resulting modes are purely imaginary:

$$\omega_{\rm NH}^{(m=0)} r_c \simeq -\frac{i}{2}\left(1 + 2n + \sqrt{1 + 4{\mu_{\rm eff}}^2 {L_{\rm AdS}}^2}\right)\kappa_{(1)}\,\sigma + \mathcal{O}\left(\sigma^2\right). \tag{3.56}$$

This expression is again valid for all N.

In the next section, we will use (3.54) to help identify the NH family of QNMs, and simultaneously (3.54) will verify some of our numerical results.

3.3 Quasinormal modes of higher-dimensional Schwarzschild-de Sitter

To discuss strong cosmic censorship in equal angular momenta MPdS black holes, it is necessary to carefully study the quasinormal mode spectra, and we will highlight the main features in Section 3.4. However, even before studying the QNMs of the MPdS, we have to start with the QNM spectra of its non-rotating limit, the Schwarzschild-dS black hole, to understand which features of the QNM spectra originate from a change in dimension. Since there are no detailed studies of the QNMs of higher-dimensional Schwarzschild-dS in the literature, we highlight some key properties here. In this section (only) we will also consider even dimensions, as the Schwarzschild-dS QNM spectra differs substantially for even and odd dimensions. We do not aim to present the full QNM spectra of Schwarzschild-dS for all dimensions, but just the main features that we have identified and that seem worth highlighting. In particular, those that help us further understand features of the MPdS spectra.

Taking the limit $a \to 0$ of the MPdS metric (3.1), we recover the metric for $d = 5$ Schwarzschild-dS, with a $\mathbb{CP}^1$ angular part that is isomorphic to a 2-sphere S^2:

$$ds^2 = -f(r)dt^2 + \frac{1}{f(r)}\,dr^2 + r^2(d\psi + \frac{1}{2}\cos\theta\, d\phi)^2 + \frac{r^2}{4}(d\theta^2 + \sin^2\theta\, d\phi^2), \quad (3.57)$$

$$f(r) = 1 - \frac{2M}{r^2} - \frac{r^2}{L^2}. \quad (3.58)$$

Note that due to spherical symmetry we can label perturbations by the total angular momentum l alone, using $\lambda = l(l + 2N) - m^2$ from equation (3.15) to eliminate the explicit dependence on m. In general, there are two distinct mode families in Schwarzschild-dS. These are the de Sitter (dS) modes, which reduce to (3.22)-(3.23) in the limit $y_+ \to 0$, and the photon sphere (PS) modes, which are well approximated by (1.19) in the eikonal limit $|m| = l \to \infty$. Schwarzschild-dS has no extremal limit and thus there are no near-horizon (NH) modes in its QNM spectra.

Taking the limit $a \to 0$ of the effective potential for null geodesics in MPdS (3.26) and setting $N = 1$, the solutions to $V_{\text{eff}}(r_0) = V'_{\text{eff}}(r_0) = 0$ are $r_0 = 2\sqrt{M}$ and

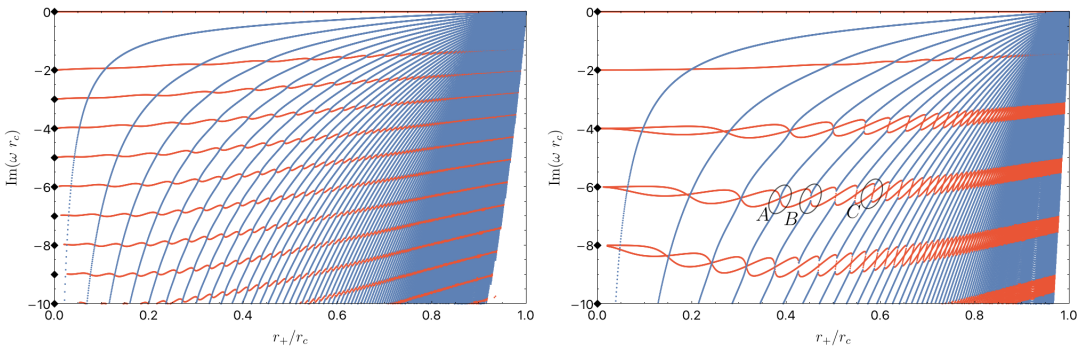

Fig. 3.2: QNM spectrum for $d = 4$ (left) and $d = 5$ (right) Schwarzschild-dS with $m = l = 0$ (several radial overtones $n = 0, 1, 2, 3, 4, 5, \ldots$ are displayed). There are purely imaginary dS modes (red) and complex PS modes (blue). The modes of pure dS space (3.22)-(3.23) are indicated by black diamonds at $r_+ = 0$. In $d = 5$ (right panel) the pure dS frequencies are degenerate, but the dS curves split as r_+/r_c increases above zero, while they are always non-degenerate in $d = 4$ (left panel). The points A, B, C indicate three mode crossings/mergers plotted in detail in Fig. 3.3.

$b^{\pm} = \pm 2L\left(\frac{L^2}{2M} - 4\right)^{-1/2}$. The corresponding eikonal approximation (1.19) to the PS modes is therefore

$$\omega_{\rm PS}\, r_c \simeq \frac{y_+^2 - 1}{2y_+\sqrt{1 + y_+^2}} \left[\pm l + i\sqrt{2}\left(n + \frac{1}{2}\right)\right]. \tag{3.59}$$

One can also derive an approximation for the modes in the Nariai limit $y_+ \to 1$ (see e.g. the supplementary material in [86]), but we will not do this here, since there is no extra family of QNMs associated to it: the Nariai analysis simply captures the PS family.

The $d = 5$ QNM spectra are shown in Fig. 3.2 for $d = 4$ (left panel) and $d = 5$ (right panel) Schwarzschild-dS with $m = l = 0$.[9] There are dS modes with purely imaginary frequencies (red curves with increasing radial overtone $n = 0, 1, 2, 3, 4, 5, \ldots$ from top to bottom), whose eigenvalues are smoothly connected to the frequencies of pure de Sitter space (3.23)-(3.22) (indicated by black diamonds) in the limit $r_+ \to 0$. There also exist PS modes with complex frequencies (blue curves with increasing radial overtone $n = 0, 1, 2, 3, 4, 5, \ldots$ from top-left to bottom-right), which we have identified by marching each QNM to $m = l = 20$, where they are in excellent agreement with the eikonal approximation (3.59).

[9]It becomes very difficult to find the full quasinormal mode spectrum as we approach the two limits of the parameter space: de Sitter ($r_+ = 0$) and Nariai ($r_+ = r_c$), so some modes have not been resolved in those limits, although they certainly do exist.

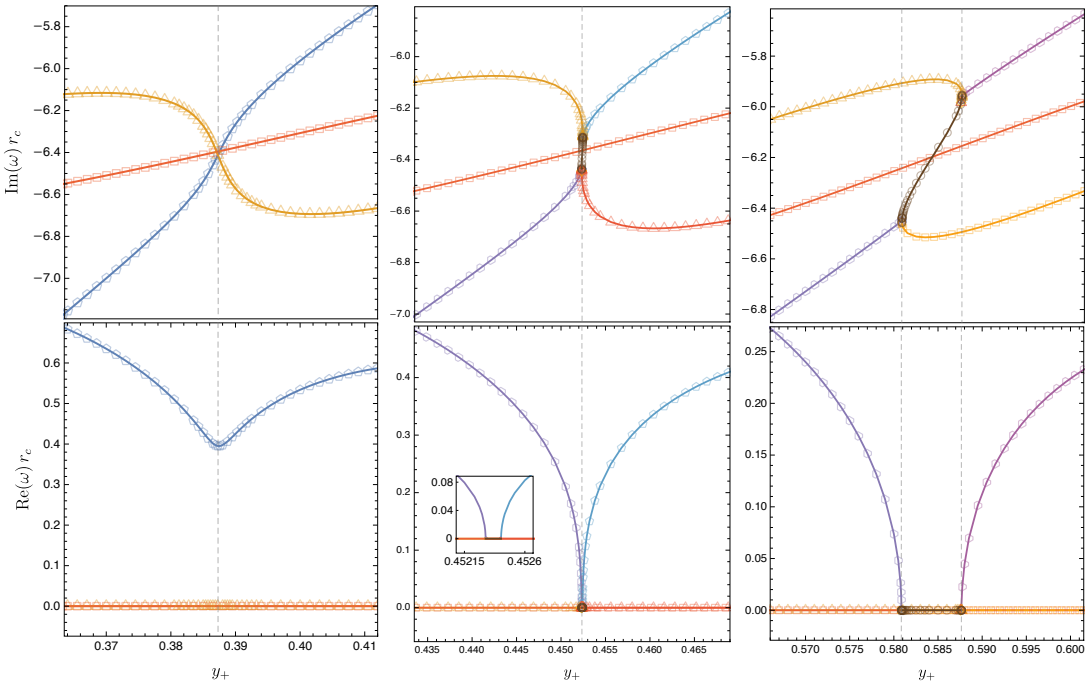

(a) Mode crossing at A **(b)** Close merger at B **(c)** Mode merger at C

Fig. 3.3: Imaginary (top panel) and real (bottom panel) parts of the $l = m = 0$ QNM frequency spectra of the $d = 5$ Schwarzschild-dS black hole of the right panel of Fig. 3.2, but this time zoomed-in around the regions A, B and C identified in Fig. 3.2. The red/yellow/brown modes are purely imaginary frequency dS modes and the blue/purple pentagon curves describe complex frequency PS modes. The inset plot in the middle-bottom figure (b) is an enlarged plot at the merge region to show that it is a very short-lived merge rather than a crossing.

Comparing the left ($d = 4$) and right ($d = 5$) panels of Fig. 3.2, the main difference going from $d = 4$ to $d = 5$ can be found in the dS curves. To start with, in $d = 4$ we have roughly two times more dS curves than in $d = 5$, in agreement with the discussion of (3.23)-(3.22). Indeed, in the $r_+ \to 0$ limit, all negative imaginary integers (except $-i$) are frequencies of pure dS spacetime in $d = 4$ but, in $d = 5$, the frequencies of pure dS are given only by the even negative integers. The next difference occurs when we let r_+/r_c increase. For $d = 4$, there is a single curve departing from each overtone of pure dS, but in $d = 5$ two intertwining curves emerge as r_+/r_c increases (except the $N = 0, 1$ dS modes). This can be partially explained by the degeneracy of the pure de Sitter modes (3.22-3.23). In odd dimensions $d = 2N + 3$, the $(N + 1)$-th pure de Sitter mode (counting the zero mode) and higher overtones are degenerate and these degenerate modes split as we move away from pure de Sitter. However, this intertwining behaviour of the dS modes appears to be unique to $d = 5$ (and not shared by the $d = 7, 9, 11, \ldots$ case).

To better understand the intertwining structure of $d = 5$ Schwarzschild-dS, the

three regions A, B and C in the right panel of Fig. 3.2 are enlarged in Fig. 3.3. The dS modes are represented by orange triangles and/or red squares, while the PS modes are described by the blue or purple pentagons. At region A (top-left panel) both dS modes merely cross each other and the PS mode. The PS modes have a real part that dips to a finite value at the crossing (bottom-left panel), but don't become purely imaginary (the dS modes always have frequencies with zero real part). Increasing y_+ to region B (middle panels), the real part of the PS mode drops to zero (bottom-middle panel), and the orange triangle dS curve merges with the PS curve (middle panels). The red square dS curve passes through the other two without interaction (top-middle panel) Further increasing y_+ till region C (right panels), we see two bifurcation points (with 3 curves departing from each one). Looking at the imaginary part (top-right panel) of Fig 3.3c, the PS mode in the bottom-left splits (at the first bifurcation point) into the orange triangle dS curve and a new 'bridge' mode (brown circles bridging the two bifurcation points in the right panels) with purely imaginary frequencies. This bridge mode then extends up and to the right till the second bifurcation point where the other branches of the orange triangle dS and PS curves also meet. Again, the red square dS curve passes through the other two without interaction. Similar bridge modes were observed in the QNM spectra of Reissner-Nordstöm−dS black holes in higher dimensions [146].

Let us now consider what happens when $d > 5$. In Fig. 3.4 we plot the QNM spectra of Schwarzschild-dS in dimensions $d = 6, 7, 8, 9$ for $l = m = 0$. The several overtones of the PS curves (blue squares) have a qualitative behaviour similar to that found in $d = 4$ and $d = 5$ of Fig. 3.2. Moreover, the even-dimensional results are qualitatively similar to $d = 4$ (left panel of Fig. 3.2) for both the PS and dS modes. In $d = 7$, the degenerate dS modes still split as r_+/r_c increases above zero and tend to develop a wavy shape, however they do not have the same intertwining behaviour observed in $d = 5$ (right panel of Fig. 3.2). In fact, we do not observe intertwining behaviour between two dS curves in any other dimension other than $d = 5$, at least up to $d = 11$. The behaviour of the dS modes in $d = 5$ is thus very unique.

In $d = 9$ and higher, we find some exceptional modes which do not have the standard characteristics of dS or PS modes, as can be seen in the $d = 9$ plot in the bottom-right panel of Fig. 3.4. The red and blue curves still describe the same families as before: purely imaginary dS modes and complex frequency PS modes, respectively. However, the purple/magenta and orange/brown modes do not fit the standard classification. The purple/magenta modes are PS modes with complex

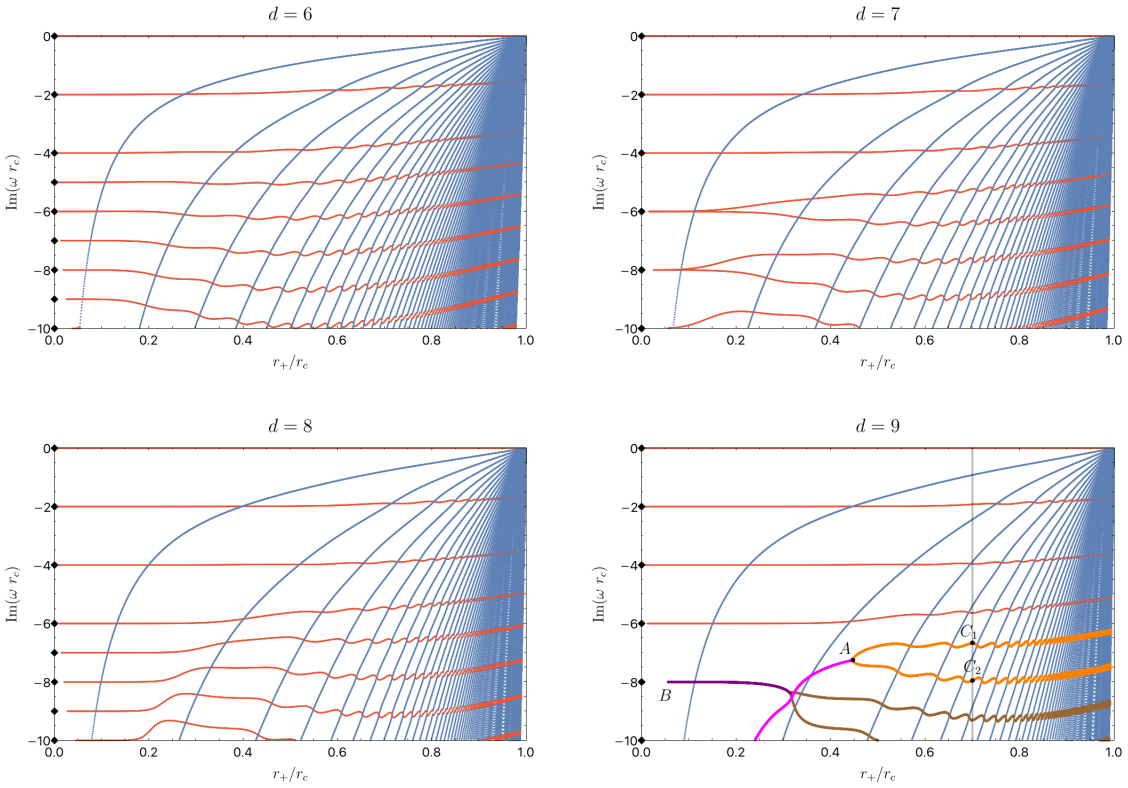

Fig. 3.4: QNM spectrum of Schwarzschild-dS in $d = 6, 7, 8, 9$ dimensions, with $l = m = 0$. Red modes are purely imaginary dS modes and the blue modes are complex PS modes. The orange/brown modes are purely imaginary but not connected directly to the dS limit when $r_+ \to 0$. The purple/magenta modes are PS modes with complex frequency that do not vanish in the Nariai limit $r_+ \to r_c$. The pure dS frequencies at $r_+ = 0$ are indicated by black diamonds. These are exceptional modes in the sense that we do not observe similar modes for $d < 9$ at least in the first few radial overtones.

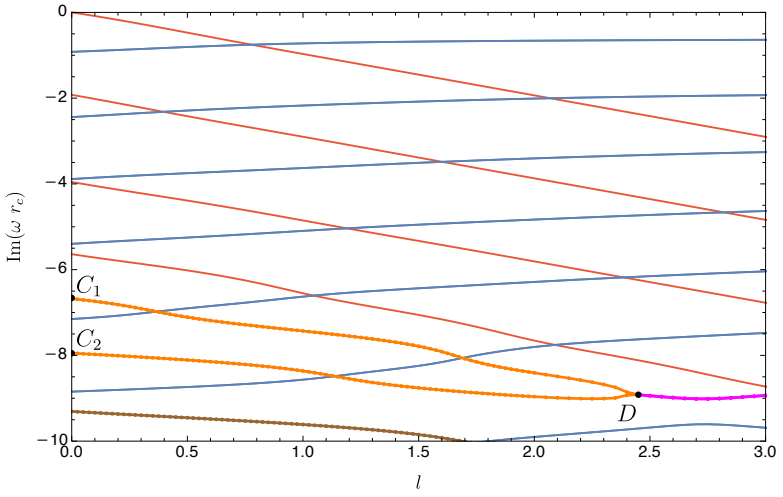

Fig. 3.5: Marching the QNM spectra of Fig. 3.4 from $m = l = 0$ all the way up to $m = l = 3$ for fixed $y_+ = 0.7$. The points C_1 and C_2 are those already present in the bottom-right panel of Fig. 3.4 (see vertical grey line). The red modes are the usual purely imaginary dS modes and the blue modes are PS modes with complex frequency (we have tracked them up to $m = l = 20$ to compare with the eikonal limit of PS modes). The orange curves starting at C_1 and C_2 have purely imaginary frequency and join at point D. For higher m, the magenta curve starting at D has complex frequencies and it is a PS mode in the sense that for larger $l = m$ it agrees well with the eikonal approximation.

frequency (see discussion of Fig. 3.5 below), but unlike the other PS modes, they do not have a standard PS behaviour at small y_+ or a vanishing imaginary part in the Nariai limit, $r_+/r_c \to 1$. Instead, these frequencies behave like those of pure dS space as r_+/r_c grows large. For example, the magenta curve splits at A into a pair of imaginary modes (orange) which behave much like dS modes, with a non-vanishing ω in the Nariai limit. The magenta and purple modes appear to have different behaviours in the limit $r_+ \to 0$. The magenta mode is suppressed (*i.e.* $|\mathrm{Im}(\omega r_c)|$ becomes large as y_+ decreases), while the purple mode appears to tend towards the pure dS frequency, with $\mathrm{Im}(\omega\, r_c) = -8i$. However, this region is difficult to resolve to the left of point B. To further clarify the properties of the exceptional families that pass though points A, C_1 and A, C_2 in Fig. 3.5 we do the following exercise. We fix $y_+ = 0.7$, which is described by the vertical grey line in bottom-right panel of Fig. 3.4 when $l = m = 0$. In particular, in the exceptional orange curves this selects points C_1 and C_2 with $l = m = 0$. Then, in Fig. 3.5, we run a code that marches over $m = l$ from $m = l = 0$ (where C_1 and C_2 lay) all the way up to $l = m = 3$. We see that in this path, the two orange curves starting at C_1 and C_2 merge at point D into a single magenta curve that then extends to $m = l = 3$ and beyond (not shown). Extending this plot even further to, say, $m = l = 20$ we can compare it with the eikonal limit of the PS modes and conclude that the magenta curve is a high overtone PS mode (like the blue curves in Fig. 3.4 and Fig. 3.5). So as l increases the curves AC_1 and AC_2 of Fig. 3.4 are connected to PS modes, although for $l = m = 0$ they do not have the standard $\mathrm{Im}(\omega) \to 0$ behaviour as $y_+ \to 0$. This illustrates how intricate the QNM spectra of Schwarzschild-dS can become for higher overtones, especially for large d.

The quasinormal mode spectrum of other asymptotically dS spacetimes (e.g MPdS or Reissner-Nordstöm−dS) will similarly contain modes which defy the standard classification in higher dimensions, as confirmed in the Reissner-Nordstöm−dS study of [146]. One might wonder why this is not visible in studies of SCC for higher-dimensional RNdS [201]. In the context of strong cosmic censorship, the $n = 1$ mode is the dominant dS mode. This is the only mode which is not paired, and it has a much weaker dependence on the black hole parameters. Indeed, all of the effects we have described are present only for subdominant modes, and so are not relevant for SCC.

3.4 Quasinormal mode spectra of equal angular momenta MPdS

Having now discussed the QNM spectra of higher-dimensional Schwarzschild-de Sitter, we are now ready to turn on angular momentum and consider Myers-Perry-de Sitter. In Section 3.2 we used analytical methods, strictly valid in certain windows of the black hole or angular harmonic parameters, to identify three possible families of quasinormal modes: the de Sitter (dS), photon sphere (PS) and near-horizon (NH) QNM families. Strictly speaking, we do not know if these 3 families are distinct or whether e.g. two of them describe the same family that happens to be captured by two distinct analytical analysis in different "corners" of the parameter space. In this section (and in section 3.5) we do a numerical search of the quasinormal modes of MPdS black holes. This numerical scan of the QNMs is done completely independently of our analytic approximations. However, after collecting the data we compare our numerical results with the analytical approximations of Section 3.2, in the regime of parameters where the analytical approximations are valid, to identify the origin of each family of QNMs that we find.

In the previous chapter, we found that in Kerr-Newman black holes there is only a sharp distinction between the PS and NH modes in certain regions of the parameter space, in particular near the Reissner-Nordström limit. Elsewhere, the distinction between the two families is much less clear due to *eigenvalue repulsions*. In particular, this means that we can have e.g. PS surfaces that, when approaching the NH surface, 'break' into two branches and each one of the two branches then merges smoothly with what was (in other regions) a NH branch (the NH surface itself also breaks into two pieces). Instead of ending with one PS and one NH family of modes we have what we can call two 'combined PS-NH' families (describing different overtones) with a frequency gap between them. In this study of the QNM spectra of MPdS, we also observe eigenvalue repulsions, similar to those in Kerr-Newman, although not just between the PS and NH families but also between the dS and NH modes.

It is not our aim to do a detailed study of QNMs of MPdS, since we just need to identify the modes that enforce SCC in MPdS, and this only requires finding a dominant QNM family that does the job. Instead, we present a selection of results that illustrate the key features of MPdS QNMs. Recall, from the discussions in Section 3.1, that the MPdS black hole is a 2-parameter solution and we can take these two parameters to be either (y_+, y_-) or be $(y_+, \alpha) \equiv (r_+, a)/r_c$ (where

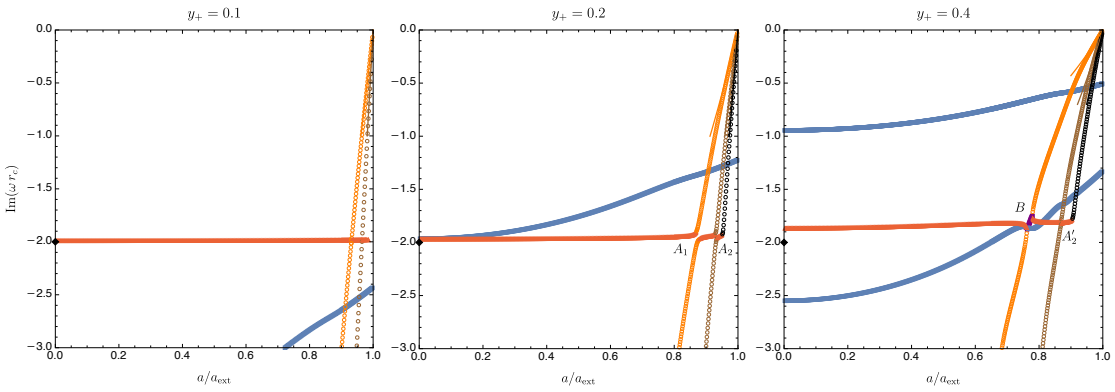

Fig. 3.6: QNM spectrum for $d = 5$ MPdS with $m = l = 0$ and $y_+ = 0.1$ (left), 0.2 (middle) and 0.4 (right). The red triangle curve is the dS mode (with $n = 0$). In the limit $(y_+ \to 0, a \to 0)$ these reduce to the QNMs of pure dS space (3.22), indicated by a black diamond. The blue square curves are the complex PS modes (with $n = 0$; we also show the PS curve with $n = 1$ in the right panel). The orange/brown/black circle curves are the $n = 0, 1, 2$ harmonics of the NH modes, respectively, with analytic approximations (3.53) given by solid lines. Eigenvalue repulsions occur at A_1, A_2, A_2' and further subdominant modes (not shown). The complex purple mode at B does not fit into any of the three families: it simply provides a "bridge" between two points where, at each one, 3 curves bifurcate from.

$0 \leqslant \alpha \leqslant \alpha_{\mathrm{ext}}$, with α_{ext} being the value of α at extremality). Typically we will display 2-dimensional plots where we plot the frequency as a function of one of the parameters while keeping the second black hole parameter fixed. Altogether, our selection of plots allows us to infer how the complete 3-dimensional plot $(y_+, \alpha, \omega\, r_c)$ looks like.

Let us start with the axisymmetric $m = l = 0$ modes in $d = 5$ MPdS, displayed in Fig. 3.6. For small $y_+ = 0.1$ (left panel) we identify 3 distinct QNM families: the dS (red triangle curve), PS (blue square curve) and NH (orange and brown circles) families. The PS family has complex frequencies. In the NH case, we display not only the curve with radial overtone $n = 0$ (orange disks) but also the family with $n = 1$ (brown circles), and they all have purely imaginary frequencies (for $m = 0$). The dS red triangle curve (with purely imaginary frequencies) approaches the pure $(y_+ = 0)$ dS normal mode (3.23) when $\alpha \to 0$ (black diamond). On the other hand the $n = 0$ (orange) and $n = 1$ (brown) circle NH curves match very well with the NH analytic approximation (3.53) (described by the solid lines) which are valid near extremality $\alpha/\alpha_{\mathrm{ext}} \lesssim 1$.

Still in Fig. 3.6, as we increase y_+ to 0.2 (middle panel), the dS modes clearly merge with the NH modes as α approaches extremality. This first occurs near A_1, between the $n = 0$ dS and $n = 0$ NH modes, leaving a gap region in the eigenvalue spectrum of the 'old' $n = 0$ NH curve (by 'old' we mean w.r.t. the left panel). To

the right of A_1 we see that a small branch of the 'old' $n = 0$ dS curve now provides a bridge that connects the bottom section of the 'old' $n = 0$ NH curve (on the left/bottom) with the top/right half of the 'old' $n = 1$ NH curve. Then, for even larger α we see that around A_2 there is a branch of the 'old' $n = 0$ dS curve that now provides a bridge between a branch of the 'old' $n = 1$ NH mode (on the left) and a branch of the 'old' $n = 2$ NH mode (on the right). In fact, similar bridges continue to exist (although not displayed) as we approach $\alpha \to \alpha_{\text{ext}}$ between the 'old' n and $n + 1$ NH overtones, not just the $n = 0 \to n = 1$ and $n = 1 \to n = 2$ overtones that are displayed. Altogether, these features are characteristic of the phenomenon of eigenvalue repulsion, and Fig. 3.6 illustrates how intricate this phenomenon can be.

The spectra become even more intricate when y_+ increases further, e.g. at $y_+ = 0.4$ (right panel of Fig. 3.6). Indeed, we find that in region B the $n = 0$ dS mode (red triangles to the left of B) merges with the 'old' $n = 0$ NH mode (orange circles below B) and, at the very same point, a small purple bridge bifurcates and extends to the right and up till a new point where 3 lines merge again: this time it is the purple bridge, and the other 'halves' of the 'old' $n = 0$ NH (orange circles) and the 'old' $n = 0$ dS curve (red triangles). For larger α, the latter then merges with the 'old' $n = 1$ NH family (much like the middle panel). Note that all of this occurs in a region where one also finds the $n = 1$ PS curve (blue square curve on the bottom) that seems to go through crossovers without significant interaction. Again, we see how eigenvalue repulsions can make the spectra very elaborate.

To start discussing the modes with $m > 0$ it is important to first recall that when $m = l = 0$, the NH frequencies are purely imaginary while the PS frequencies are complex, so they clearly form two distinct families of QNM, as was seen in Fig. 3.6. However, for $m \neq 0$, the PS modes with $m = l$ split into corotating and counter-rotating modes, as first discussed in the eikonal limit in section 3.2.2. As in the eikonal limit, the counter-rotating mode always has a frequency with smaller imaginary part than the corotating PS mode for a given overtone n.[10] Remarkably, we find that when $m \neq 0$, *typically* (*with an exception* to this rule discussed below) the corotating PS modes turn out to *merge* with the NH modes and they form a single unified family (plus its overtones) that we can denote as the 'PS-NH' family. This is very similar to what we found in Kerr-Newman, most closely analogous to the Kerr limit, but with some important differences. See also [212] for a discussion

[10]Note that the $t - \psi$ symmetry of MPdS means that we need only consider modes with $m \geqslant 0$, as long as we study both signs of $\text{Re}(\omega)$. When $a = 0$ this enhances to a $t \to -t$ symmetry and the QNM frequencies form pairs of $\{\omega, -\omega^*\}$.

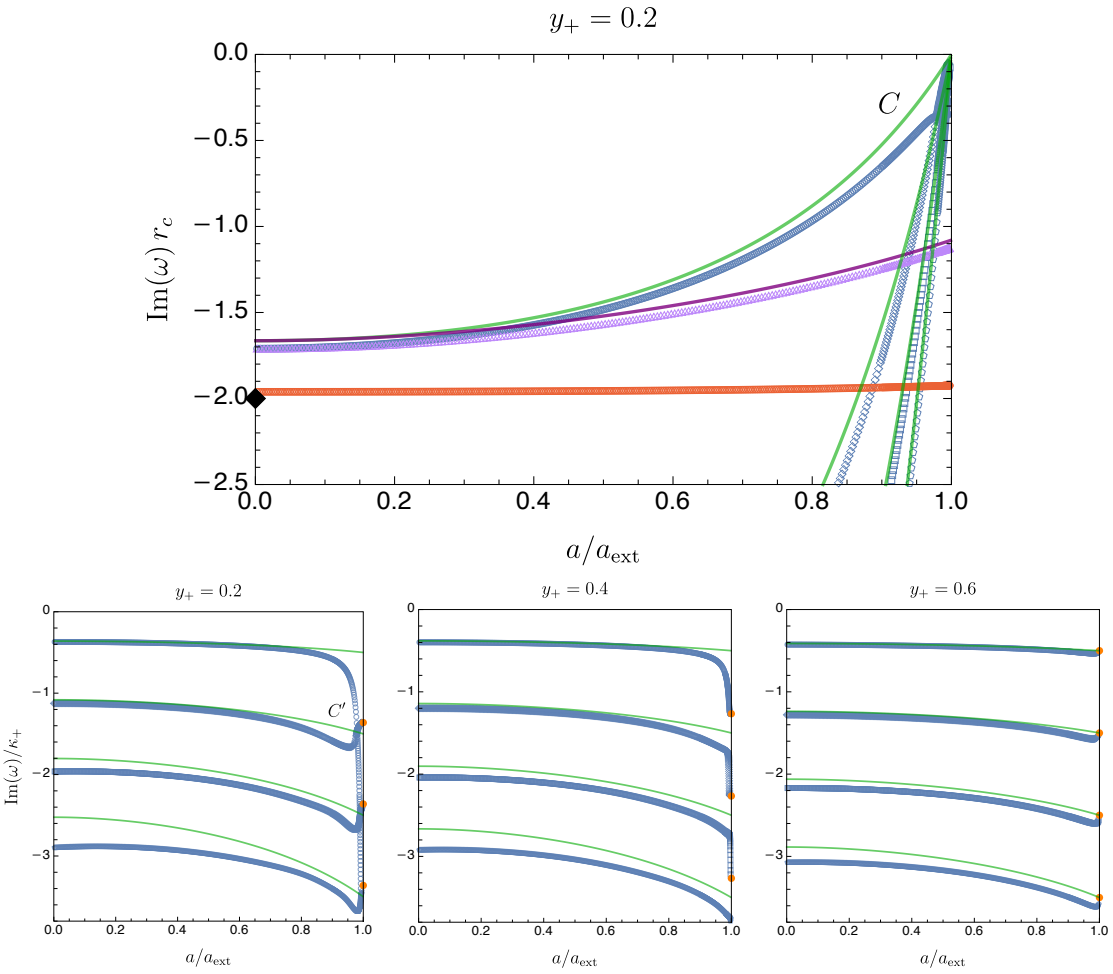

Fig. 3.7: QNM spectrum for $d = 5$ MPdS with $m = l = 2$. Typically, the corotating PS and NH modes (blue circles, diamonds, squares and pentagons) have merged to become a single PS-NH family: in all plots we display the first 4 overtones of this unified family. The only exception is the blue circle curve in the top of the left panel which describes a $n = 0$ corotating PS mode, not a PS-NH mode since it is not captured by a NH analysis. The top panel is for $y_+ = 0.2$ and the frequency is normalized in units of r_c. In this top panel we also display the counter-rotating PS QNMs (magenta triangle curve), and the dS modes (red circles). The corotating and counter-rotating eikonal approximations (1.19) are described by the the solid green and purple lines, respectively. For reference, the pure dS frequency (3.22) with $y_+ = a = 0$ is represented by the black diamond. The bottom panels are normalised in units of κ_+ to differentiate the near-extremal behaviour of the different overtones $n = 0, 1, 2, 3$ of the PS-NH family with $y_+ = 0.2$ (left), $y_+ = 0.4$ (middle) and $y_+ = 0.6$ (right). The NH approximation (3.53) at $a = a_{\mathrm{ext}}$ (for $n = 0, 1, 2, 3$ from top to bottom) are represented by the orange disks in the bottom panels. (In the bottom panel the dS modes and counter-rotating PS modes are not shown).

of eigenvalue repulsions in the gravito-electromagnetic QNMs of Kerr-Newman. To illustrate the unification of the corotating PS and NH modes, we plot the frequency spectra for $d = 5$ MPdS with $m = l = 2$ and $y_+ = 0.2$, in the top panel of Fig. 3.7. The four blue curves with circles, diamonds, squares and pentagons are the corotating PS modes with radial overtone $n = 0, 1, 2, 3$ (from left/top to right). As expected, this classification is consistent with the eikonal analytical result $\omega_{\rm WKB}$ obtained in (1.19) which is represented by the solid green curves for $n = 0, 1, 2, 3$. The magenta triangle curve is the $n = 0$ counter-rotating PS curve and it is also well approximated by the counter-rotating eikonal frequency $\omega_{\rm WKB}$ of (1.19) (solid purple curve). Finally, the red square curve in the top panel of Fig. 3.7 is the $n = 0$ dS QNM family, clearly identified by the fact that it approaches the pure dS frequency (3.22) when $a \to 0$ (black diamond).

An important property of the top panel of Fig. 3.7 is the fact that there are no extra curves which we could associate to a third independent family[11]. We only have the dS family and the unified 'PS-NH' family (and their overtones); the PS and NH modes do not exist separately. This is because, unlike the $m = l = 0$ case in Fig. 3.6, the NH modes at extremality (*i.e.* at $a = a_{\rm ext}$) or nearby − as unambiguously identified by the analytical approximation $\omega_{\rm NH}$ in (3.54) − can always be traced back to a corotating PS mode when we move away from extremality. Indeed, the blue PS-NH curves in Fig. 3.7 (top and bottom panels) are *simultaneously* well approximated by $\omega_{\rm WKB}$ in (1.19) and, near-extremality, by $\omega_{\rm NH}$ of (3.54). This is better seen in the bottom-left panel of Fig. 3.7 for $y_+ = 0.2$. Here we choose a different normalization for the frequency: we plot the dimensionless frequency in units of the surface gravity κ_+. We make this choice because at extremality both $\omega_{\rm NH}$ and κ_+ go to zero but their ratio is finite (and changes with n). Therefore, these properties help identifying the NH approximation $\omega_{\rm NH}$ of (3.54) (orange disks at $a/a_{\rm ext} = 1$ for $n = 0, 1, 2, 3$)[12]. We indeed see that, typically, the unified PS-NH blue curves terminate at extremality at the NH orange disks and, away from extremality, are also well approximated by the solid green corotating PS line described by $\omega_{\rm WKB}$ in (1.19). Still in the bottom panel of Fig. 3.7 we see that these conclusions also hold for $y_+ = 0.4$ (middle panel) and $y_+ = 0.6$ (right panel) and actually for all other values of y_+ (not shown).

[11]We emphasise that we did an exhaustive direct numerical search for eigenvalues using *Mathematica's built-in routine Eigensystem* (as described in Section 1.5) but we found no other frequencies besides the ones that are displayed in Fig. 3.7 (in the range shown and excluding even higher overtones $n \geqslant 4$). That is, we found no third family of QNMs besides the two main families (dS and unified PS-NH) displayed in the top panel of Fig. 3.7.

[12]Note that, since we are plotting ω/κ_+, the first-order accurate approximation (3.53) only gives us the value of $\omega_{\rm NH}/\kappa_+$ at extremality, and not away from it.

A second important property that is observed in the plots of Fig. 3.7 is that there is an "exception to the rule" described in the previous two paragraphs. Namely, for small $y_+ \lesssim 0.3$, e.g. $y_+ = 0.2$ in the top and bottom-left panels, we see that the $n = 0$ corotating PS mode is the only solution that is *not* also captured by the NH description. Indeed, as seen on the top panel, the $n = 0$ corotating PS curve (unlike for $n \geqslant 1$) does *not* have $\mathrm{Im}(\omega r_c) \to 0$ (neither does it have $\mathrm{Re}(\omega) \to m\Omega|_{\rm ext}$, although this is not shown) as extremality is approached. Instead $\mathrm{Im}(\omega r_c)$ goes to a finite value as $a \to a_{\rm ext}$. This is better seen in the bottom-left panel, since the $n = 0$ corotating PS curve plunges into $\mathrm{Im}(\omega)/\kappa_+ \to -\infty$ as $a \to a_{\rm ext}$ because $\kappa_+ \to 0$ in this limit but $\mathrm{Im}(\omega)$ is finite. In particular, this means that this particular mode, and only this one (and only for small y_+), is not described by $\omega_{\rm NH}$ with $n = 0$ in (3.54). This also means that near extremality (see regions C in top panel or C' in bottom-left panel) the $n = 0$ corotating PS mode trades dominance with the $n = 1$ corotating PS mode. Indeed, from $\alpha = 0$ all the way up to a critical α near-extremality, the $n = 0$ corotating PS QNM is the one with the smallest $|\mathrm{Im}(\omega r_c)|$, but above this critical α and all the way to extremality, it is instead the $n = 1$ corotating PS QNM that has the smallest $|\mathrm{Im}(\omega r_c)|$. An interesting property that follows from the previous one is that the $n = 0$ NH approximation $\omega_{\rm NH}$ of (3.54) actually describes the extremal limit of the $n = 1$ (not $n = 0$) PS curve: see orange disk nearby point C' in bottom-left panel. Similarly, the $n = 1, 2$ NH approximation $\omega_{\rm NH}$ describes the extremal limit of the $n = 2, 3$ (not $n = 1, 2$) unified PS-NH curves, respectively. Interestingly this "exception to the rule" ceases to hold for larger values of y_+ namely for $y_+ \gtrsim 0.3$: see e.g. the cases $y_+ = 0.4$ (middle panel) and $y_+ = 0.6$ (right panel) of Fig. 3.7. That is, in these cases, we have unified PS-NH curves, with $\omega_{\rm NH}$ (with overtone n) describing the extremal limit of the blue curves (with the same overtone n), and the $n = 0$ PS-NH QNM is the one that dominates the spectra for all values of $a/a_{\rm ext}$.

Note that, as Fig. 3.7 illustrates, the eikonal approximation $\omega_{\rm WKB}$ of (1.19) (solid green curves), although strictly valid only for $|m| = l \to \infty$, is nevertheless already a good approximation for $m = l = 2$ as long as we are away from extremality. However the PS-NH family is no longer well approximated by the eikonal approximation in the near-extremal limit, although the approximation gets better even in this region as y_+ increases. Close to extremality, the PS-NH frequencies are better approximated by $\omega_{\rm NH}$ in (3.54) (orange disks in Fig. 3.7). In fact, we can find the difference between the analytical NH prediction (3.54) and the eikonal prediction (1.19) exactly at extremality. Interestingly, we find that the value of y_+ at which this difference vanishes turns out to be given by the value of y_+ that saturates

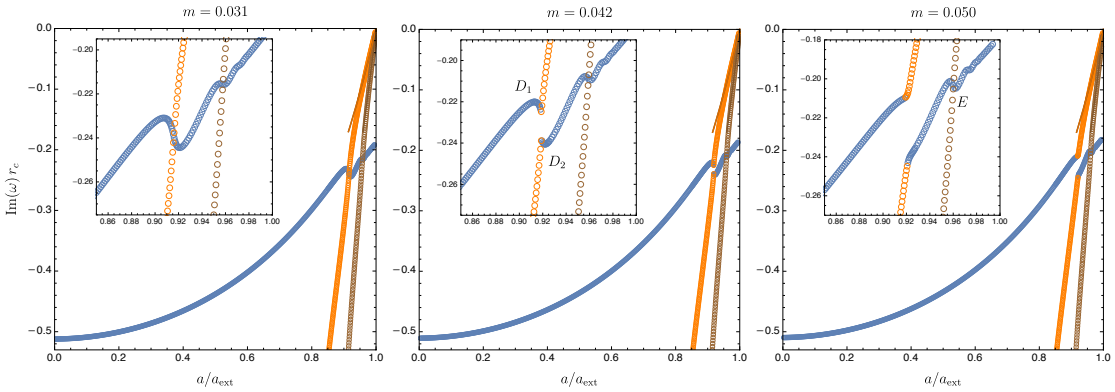

Fig. 3.8: PS modes (blue circles) merging with the $n = 0$ NH mode (orange circles) as $m = l$ increases, in $d = 5$ MPdS with $y_+ = 0.6$. The $n = 1$ NH mode (brown circles) merges later, by $m \simeq 0.125$. The inset figures are enlargements of the merging region. The NH approximations (3.53) for the $n = 0$ and $n = 1$ overtones are indicated by solid orange and brown lines, respectively. The dS modes and counter-rotating PS modes are not shown in these plots.

the AdS_2 BF bound of the near-horizon geometry, $1 + 4{\mu_{\rm eff}}^2 L^2_{\rm AdS} = 0$, where $\mu_{\rm eff}$ is given by (3.42). For $(N = 1, m = l = 2)$, the AdS_2 BF bound is saturated at $y_+ \sim 0.54$. We postpone a detailed discussion of this observation to section 3.5.

The fact that the PS and NH modes typically merge in a single PS-NH family for $m > 0$ in MPdS might be considered puzzling. How can it be that for $m = 0$ the system has three distinct QNM families (dS, PS and NH) and for $m > 0$ there are typically only two (dS and PS-NH)? We can address and settle this question with the following strategy. Regularity of the $\mathbb{CP}^N$ harmonics requires that the angular eigenvalues λ are given by (3.14) with *integer* m. But nothing prevents us from doing an exercise where we search numerically for the eigenfrequencies of the problem when the value of m is not an integer. This would simply describe the eigenfrequencies of singular modes which are physically irrelevant. But we can learn important lessons from this academic exercise: we start with the PS and NH modes of $m = 0$ (displayed e.g. in Fig. 3.6) and see how these curves evolve as we increase m incrementally. We do this in Fig. 3.8 for $d = 5$ MPdS with $y_+ = 0.6$. In the left panel we display the spectra for $m = 0.031$. In this case, the $n = 0$ corotating PS family (blue circles), the $n = 0$ NH family (orange circles) and the $n = 1$ NH family (brown circles) are still very much distinct families as in the $m = 0$ case of Fig. 3.6 (we do not show the dS modes in Fig. 3.8). However, as we increase m, the $n = 0$ PS curve breaks into two branches, and the same happens to the $n = 0$ NH curve. This is clearly seen e.g. in the middle panel of Fig. 3.8 for $m = 0.042$. And the left-branch of the 'old' (w.r.t. the left panel) $n = 0$ PS curve merges smoothly with the upper-branch of the 'old' $n = 0$ NH curve at point D_1, while the lower-branch

of the 'old' $n = 0$ NH curve merges smoothly with the right-branch of the 'old' $n = 0$ PS curve at the point D_2. Effectively, the PS and NH families loose their individual identities and the two 'old' PS and NH curves become two PS-NH curves with a eigenfrequency gap D_1D_2 appearing between the two new PS-NH curves. This is nothing but another manifestation of the eigenvalue repulsion phenomenon observed in Fig. 3.6. As m keeps increasing, the gap D_1D_2 keeps increasing and similar breakups, merges and gaps will keep happening between the $n = 0$ PS curve and 'old' NH curves with overtone $n \geqslant 1$ as suggested in the right panel of Fig. 3.8 for $m = 0.05$. For example, although not shown, the breakout/merger between the $n = 0$ PS curve and the $n = 1$ NH curve occurs for $m \simeq 0.125$, as the region E in the right panel already suggests will happen. After this exercise, we finally understand why for $m = 0$ we have three families of QNMs but only two families for $m > 0$. Once we reach $m = 1$ all of the sub-dominant PS and NH modes (at least those with $n = 0, 1, 2, 3$) will have merged in the same fashion and we get the homogeneous picture previously presented for $m = 2$ in the bottom-right panel of Fig. 3.7. There is a striking similarity to the eigenvalue repulsions observed in Kerr-Newman, compare for example with Fig. 1 of [212] [13]. It seems likely that the underlying mechanism is the same.

Although we have focused our discussion on $d = 5$ black holes in this section, similar properties occur for higher spacetime dimensions d. However, there are also differences, some of which can be traced back to the fact that the QNM spectrum of Schwarzschild-dS black holes (*i.e.* the limit $a = 0$) changes when d increases, especially when d changes from odd to even, as discussed in Section 3.3.

3.5 Strong cosmic censorship in MPdS. Discussion of the results

We are finally ready to discuss strong cosmic censorship in cohomogeneity-1 Myers-Perry−de Sitter black holes. The Christodoulou formulation of strong cosmic censorship states that the maximal Cauchy development cannot be extended beyond the Cauchy horizon as a weak solution of the Einstein equations or matter fields [108]. For the scalar field, this translates to the requirement that the scalar field is not in the Sobolev space H^1_{loc} near the Cauchy horizon. In four

[13] Ref. [212] is the study of gravito-electromagnetic QNMs of Kerr Newman. The eigenvalue repulsion behaviour is essentially the same as the scalar QNMs of Chapter 2, but the parameterisation Q/r_+ in that figure is more closely analogous to a/a_{ext} used here.

dimensional de Sitter black holes, it has been shown that the decay rate of generic linear perturbations is governed by the imaginary part of the *slowest*-decaying quasinormal mode, relative to the surface gravity κ_- at the Cauchy horizon [121].

In terms of $\beta = \mathrm{Im}(\omega)/\kappa_-$ defined in (1.26) of section 1.3, it was shown for RNdS and (slowly-rotating) Kerr-dS in [121] that the scalar field is in H^1_{loc} if $\beta > \frac{1}{2}$ (see also [94] regarding Kerr-dS with arbitrary rotation). We will now argue that the requirement is the same for MPdS. Consider a quasinormal mode defined in region I (see the left panel of Fig. 3.1),

$$\Phi = e^{-i\omega t} e^{im\psi} Y(x_i) \tilde{R}(r). \tag{3.60}$$

Changing to ingoing EF coordinates (3.9), the metric is regular at the event horizon $\mathcal{H}^+$ and Φ can be analytically continued into region II of Fig. 3.1. Then, using (3.11) to change to outgoing EF coordinates (v, r, ψ'', x_i), which are regular at the Cauchy horizon $\mathcal{CH}^+$, we get

$$\Phi = e^{-i\omega v} e^{im\psi''} Y(x_i) R(r), \tag{3.61}$$

where $R(r)$ includes the original contribution $\tilde{R}(r)$ from region I but has additional factors from the coordinate transformations. In outgoing EF coordinates, the massless radial equation (3.16) reads

$$R''(r) + \left(\frac{2N+1}{r} + \frac{2i\sqrt{h}}{f}(\omega - m\Omega) + \frac{f'}{f} \right) R'(r) \\ - \frac{1}{f}\left[\frac{m^2}{r^2 h} + \frac{\lambda}{r^2} - \frac{i}{r^{2N+1}} \partial_r \left(r^{2N+1} \sqrt{h}\, (\omega - m\Omega) \right) \right] R(r) = 0. \tag{3.62}$$

This equation has regular singular points at the roots of $f(r)$, *i.e.* at the horizon radii. In particular, we know from section 3.1 that $f(r)$ has a single zero at $r = r_-$, so we can factor $f(r)$ as $f(r) = (r - r_-)\Delta(r)$. The remaining terms in (3.62), including Δ, are all analytic and non-zero at r_-. Hence, we can perform a Frobenius expansion around $r = r_-$. Fuch's theorem [228] asserts that there exists a solution with a non-zero radius of convergence

$$R(r) = A\, \hat{R}_{(1)}(r) + B\, (r - r_-)^s \hat{R}_{(2)}(r), \tag{3.63}$$

for some constants A and B, where $\hat{R}_{(1,2)}(r)$ are analytic and non-zero at $r = r_-$, and $s \equiv i(\omega - m\Omega_-)/\kappa_-$ is the non-trivial solution of the indicial equation. Φ is in the Sobolev space H^1_{loc} if $R(r)$ and its first derivative are locally square integrable.

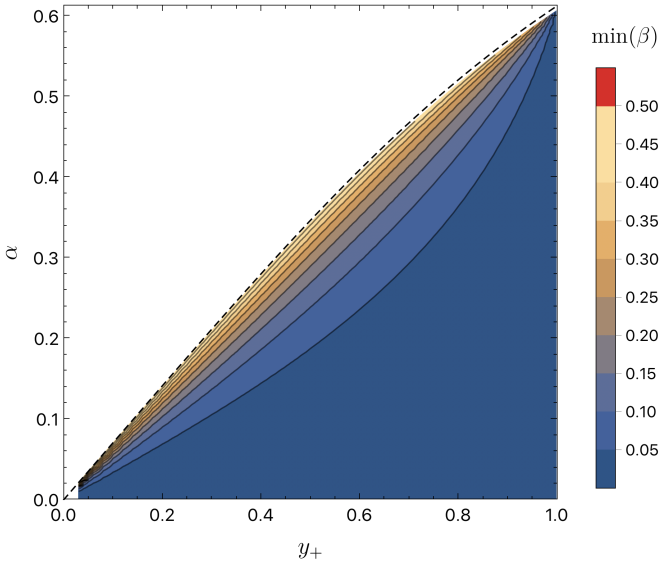

Fig. 3.9: Plot of $\min(\beta)$ for the full spectrum of quasinormal modes of $d = 5$ MPdS with $m = l = 10$ as computed by numerically solving the eigenvalue problem. There are two families of modes, the PS-NH modes and the dS modes. We find that the PS-NH modes are dominant for the entire parameter space, since the dS modes are suppressed for large $m = l$. The dashed black line represents extremality $r_- \to r_+$. One finds that $\min(\beta) < 1/2$ for the whole parameter space.

Since $\hat{R}_{(i)}$ are analytic, the only relevant factor is $(r - r_-)^s$, which is locally square integrable if and only if $\mathrm{Re}(2s) > -1$. In terms of β, we can write this condition as $\beta > \frac{1}{2}$. In other words, to prove that Christodoulou's formulation of strong cosmic censorship is respected, we 'just' need to show that, for the whole parameter space, at least one family of QNMs is not in H^1_{loc}, *i.e.* there exists a QNM family with $\beta \leqslant \frac{1}{2}$.

In the eikonal limit $|m| = l \to \infty$, the quasinormal mode spectrum is dominated by the PS family of modes (actually, the PS-NH modes, following the findings of the previous section), which are well approximated by ω_{WKB}, as defined in (1.19). We first check that the corresponding β_{WKB} computed using (1.26) satisfies $\beta_{\mathrm{WKB}} < \frac{1}{2}$. This result *per se* should establish that Christodoulou's SCC is preserved in equal angular momenta MPdS since we would have found a QNM family with $\beta \leqslant 1/2$ in the whole range of the parameter space. However, to make such a strong claim we must ensure that the eikonal approximation is really valid, *i.e.* we have to compare it with the exact numerical frequencies, a task that can be completed only at finite m. From the previous section we already know that the eikonal approximation is reasonably good when extrapolated to finite m but here it is fundamental that we find a family that has exactly $\beta \leqslant 1/2$ everywhere. So, in practice, we need to numerically compute the dominant QNMs of MPdS at finite m for the whole

parameter space and check that there is indeed at least one m for which $\beta \leqslant 1/2$ everywhere. In this process, we will have the opportunity to further quantify how good the eikonal approximation (1.19) is when extrapolated to finite m. Moreover, we want to complete this exercise for several dimensions d to find whether there is a critical dimension where the validity of SCC could change.

Recall that we have corotating and counter-rotating PS modes, including in the eikonal limit, but the norm of the imaginary part of the frequency of the corotating modes is always smaller than the counter-rotating ones (for a given overtone). So we just need to consider the corotating PS modes (*i.e.*, typically, the corotating PS-NH modes). Inserting $\omega_{\rm WKB}$, as read from (1.19) and (3.30), and the surface gravity κ_-, as computed from (3.5), into (1.26) we can compute $\beta_{\rm WKB}$ for any odd spacetime dimension d. We find that, just as in Kerr-dS [94], $\beta_{\rm WKB}$ is bounded less than $\frac{1}{2}$ away from extremality, only approaching $\beta_{\rm WKB} = \frac{1}{2}$ at extremality. It turns out that, across the range of dimensions we tested ($d \leqslant 15$), $\beta_{\rm WKB}$ is a non-increasing function of the dimension, *i.e.* for every point (y_+, y_-) in the parameter space, $\beta_{\rm WKB}(y_+, y_-; d) \leqslant \beta_{\rm WKB}(y_+, y_-; d+2)$. Hence we expect that $\beta_{\rm WKB} \leqslant \frac{1}{2}$ also holds true for $d > 15$. However, this conclusion does not necessarily extend to the exact PS or PS-NH modes at finite m near-extremality, because the eikonal result fails to be a good approximation in the near-extremal regime for small m (more below).

After this simple but enlightening and encouraging eikonal exercise, we should now confirm that the exact numerical solutions of the eigenvalue problem indeed yield $\beta \leqslant 1/2$, *at least* for a sufficiently high $m = l$ family of QNMs. We start by doing this for $l = m = 10$ and for the whole parameter space (y_+, α) of $d = 5$ MPdS (with the parameter space discretised into about 2700 points). As discussed in section 3.4, when $m > 0$ the individual PS and NH families that exist for $m = 0$ typically lose their identity (except for small values of y_+ if $m = l$ is small) and become a single PS-NH family for each radial overtone n. Here, since we are working in the eikonal limit $m = l \to \infty$, we are only interested in the PS-NH family with the lowest overtone (since it has smaller β), and this family of modes dominates for the entire parameter space over the second QNM family of the system (the dS family). The smallest value of β at each point of the phase space is plotted in Fig. 3.9. The closest we approach extremality in this plot is $\alpha/\alpha_{\rm ext} = 0.99$ or $r_-/r_+ = 0.98$. All the points tested have $\beta < \frac{1}{2}$, with a maximum of $\beta \simeq 0.488$. Hence, we conclude that for $l = m = 10$ one has $\beta < 1/2$, as predicted by the eikonal approximation. To quantify the accuracy of the WKB approximation when extrapolated to such a finite m, we compute $\Delta_{\rm WKB} \equiv \frac{\beta_{\rm WKB} - \beta}{\frac{1}{2} - \beta}$, where $\beta_{\rm WKB}$

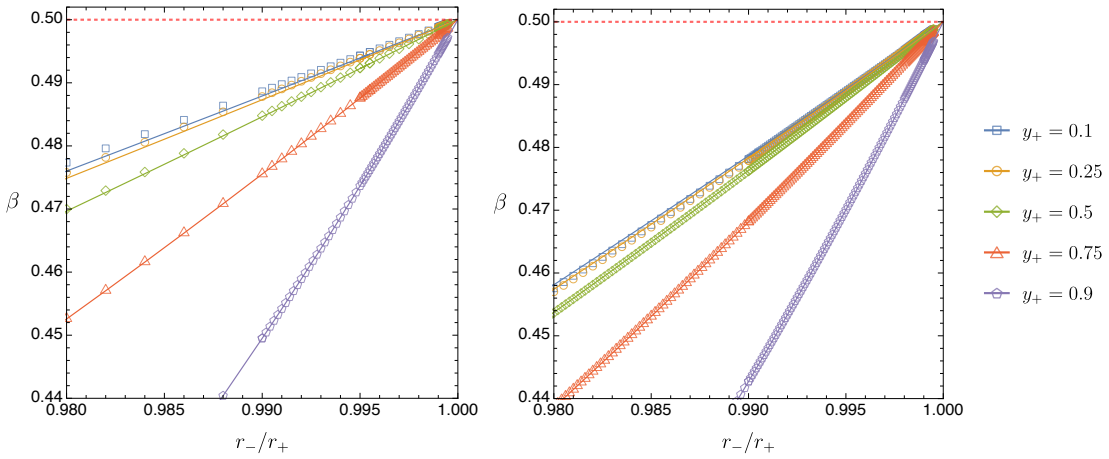

Fig. 3.10: β for the dominant QNMs near extremality in $d = 5$ MPdS with $m = l = 10$ (left panel) and $d = 11$ with $m = l = 30$ (right panel), compared to the eikonal approximation (1.19) of the PS modes (solid lines). The horizontal red dashed line indicates $\beta = \frac{1}{2}$. In both plots, the closest we approach extremality is $r_-/r_+ = 0.9995$.

is the eikonal approximation (1.19) and β is the numerical value. We find that $-0.07 < \Delta_{\rm WKB} < 10^{-11}$ for $d = 5$, *i.e.* up to numerical accuracy the true value of β is never larger than that of the eikonal approximation $\beta_{\rm WKB}$.

However, to claim that $\beta \leqslant 1/2$ for the whole parameter space we should still stretch our numerical analysis even closer to extremality, *i.e.* even closer than what we do in Fig. 3.9 where we have reached 'only' $\alpha/\alpha_{\rm ext} = 0.99$ or $r_-/r_+ = 0.98$. For that we can focus our attention on lines of constant $y_+ = r_+/r_c$ and push the numerical collection of data as close as possible to extremality where $r_- = r_+$. We do this for $d = 5$ and $m = l = 10$ in the left panel of Fig. 3.10 for several lines of constant $0 < y_+ < 1$ identified in the legend[14]. We also display, as solid lines, the eikonal approximation $\beta_{\rm WKB}$ as read from (1.19). We conclude that all solutions approach $\beta = 1/2$ from below as extremality is approached. Moreover, we also find that the eikonal approximation very well describes this approach even for a relatively small value such as $m = 10$ (note that the approximation is better for large y_+).

We find similar results when we repeat the analysis but this time for $d = 7, 9, 11$, although we need to pick families with higher $m = l$ as d increases to still have $\beta \leqslant 1/2$ everywhere (for reasons explained below). As an example, in the right panel of Fig. 3.10 we present the results for $m = l = 30$ in $d = 11$.

[14]A convergence test is given in Appendix C for the $d = 5$ case at $r_- = 0.9995\, r_+$.

Altogether, we conclude that there is at least one family of $m = l$ QNMs for which the spectral gap satisfies the condition $\beta \leqslant 1/2$ in the whole parameter space of MPdS for odd $d \leqslant 11$ (and most probably also above). It follows that Christodoulou's formulation of strong cosmic censorship holds for equal angular momenta $d > 4$ MPdS black holes, very much alike in the $d = 4$ Kerr-dS case [94]. This is the main result of this chapter.

As the above discussions indicate, it is very easy to find that $\beta < 1/2$ away from extremality; however it is much more difficult to stretch the numerical code to prove that we have $\beta \leqslant 1/2$ all the way up to extremality. However, even without resorting to a numerical analysis, we can establish analytically that there are modes that have $\beta \leqslant 1/2$ in the whole parameter space if $m = l$ is sufficiently large, for any d. While doing so, we can also find a criterion that tells us how large $m = l$ needs to be (for a given d) to have a family of QNMs that approach $\beta = 1/2$ at extremality. We discuss how this can be done in the rest of this section. As emphasized previously, for $m \neq 0$ and sufficiently large y_+, the PS and NH modes do not exist as separate families; instead they combine to form what we call the PS-NH family. This means that the PS-NH QNMs are simultaneously well approximated by the eikonal approximation $\omega_{\rm WKB}$ in (1.19) and by the NH approximation $\omega_{\rm NH}$ of (3.54). The eikonal approximation (1.19) is a good approximation as long as we are far away from extremality but it deviates from the exact result as we approach extremality and this deviation gets higher for small y_+ and higher d. On the other hand − and this is a key observation for our purposes − the NH approximation (3.54) becomes more and more accurate as we approach extremality and this is precisely the region where we want to have a solid proof that β does not exceed 1/2 for at least a family of modes. Thus, using the fact that $q_{\rm AdS}$ defined in (3.41) is real, it follows from (3.54) and (1.26) that, for all $d = 2N + 3$, $\beta_{\rm NH}$ is given by

$$\beta_{\rm NH} \simeq \frac{1}{2} + \frac{1}{2}\,{\rm Re}\left(\sqrt{1 + 4{\mu_{\rm eff}}^2 L_{\rm AdS}^2}\right). \tag{3.64}$$

Based on this near-horizon approximation, the PS-NH modes will have $\beta > \frac{1}{2}$ at extremality unless the near-horizon AdS_2 BF bound is violated. Conversely, to have $\beta \leqslant 1/2$ (at and away from extremality) and thus a family of modes that enforce SCC, one must violate the AdS_2 BF bound. For a MPdS BH of fixed y_+ and dimension $d = 2N + 3$, the violation of the AdS_2 BF bound can occur if m is above a critical value $m_{\rm crit}$. More concretely, choosing $l = m$ and using $L_{\rm AdS}$ and $\mu_{\rm eff}$ as given in (3.42), we find that in order to have an AdS_2 BF bound violation,

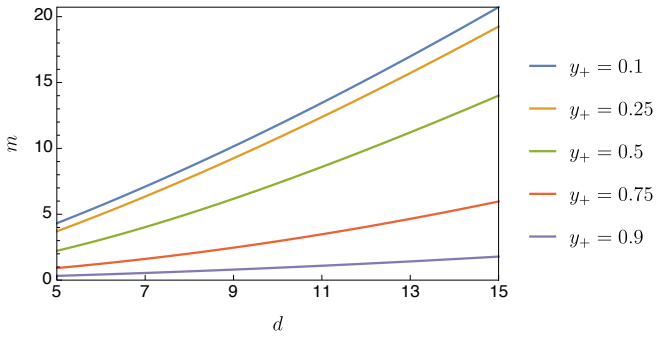

Fig. 3.11: Critical value $m_{\rm crit}$ given by (3.65) above which we have a BF bound violation. $m_{\rm crit}$ is plotted as a function of dimension d for a range of fixed y_+.

we must have $m > m_{\rm crit}$ where

$$m_{\rm crit} = \frac{(N+1)\left(\sqrt{2}+\sqrt{N+2}\right)}{\sqrt{2}N} \frac{2y_+^2\left(y_+^{2N}-1\right) - N\left(y_+^2-1\right)\left(y_+^{2N+2}+1\right)}{1-(N+2)y_+^{2N+2}+(N+1)y_+^{2N+4}}\,, \tag{3.65}$$

which, for a fixed dimension, has a finite maximum given by

$$\max(m_{\rm crit}) = \frac{N+1}{\sqrt{2}}\left(\sqrt{2}+\sqrt{N+2}\right). \tag{3.66}$$

We plot $m_{\rm crit}$ as a function of the dimension d for several values of y_+ in Fig. 3.11. Note that $m_{\rm crit}$ increases for higher dimensions, and smaller y_+. For example, for $d = 5$ one has $m_{\rm crit} \sim 5$ but for $d = 11$ one has $m_{\rm crit} \sim 13$ (or even higher if $y_+ \to 0$). Coming back to Fig. 3.10 this explains why for $d = 5$ it was sufficient to look at $m = l = 10$ modes to attain $\beta \leqslant 1/2$ everywhere, but for $d = 11$ we had to use a higher $m = l = 30$ to obtain modes with $\beta \leqslant 1/2$ everywhere.

To illustrate how $m_{\rm crit}$ and the associated AdS_2 BF bound violation is closely (but not sharply) related to modes with $\beta \leqslant \frac{1}{2}$ near extremality, we give β for the dominant QNM at $r_-/r_+ = 0.99$ in Table 3.1, while varying both $m = l$ and the dimension d, for $y_+ = 0.25$ (left table) and $y_+ = 0.75$ (right table). We conclude that AdS_2 BF bound violation is a necessary (but not sufficient) condition for $\beta \leqslant \frac{1}{2}$ near extremality. Indeed, modes that violate the AdS_2 BF bound are those below the zigzag line $m = m_{\rm crit}$ in Table. 3.1, and we see that these modes with $m > m_{\rm crit}$ typically have $\beta \leqslant \frac{1}{2}$. However, this is not always the case: some modes with m just above $m_{\rm crit}$ can still have $\beta > \frac{1}{2}$. Once β crosses below $\frac{1}{2}$, there is a sharp change in behaviour (in the sense that increasing m produces very small changes in the value of β) and all of the modes with larger m are approaching $\frac{1}{2}$ from below.

	dimension d					
m	5	7	9	11	13	15
0	**0.99**	**0.99**	**0.99**	**0.99**	**0.99**	**0.99**
2	**1.34**	**1.18**	**1.11**	**1.07**	**1.05**	**1.02**
4	**0.54**	**1.13**	**1.13**	**1.10**	**1.07**	**1.06**
6	0.49	**0.63**	**1.05**	**1.09**	**1.08**	**1.07**
8	0.49	0.49	**0.73**	**1.02**	**1.06**	**1.06**
10	0.49	0.49	**0.54**	**0.81**	**1.01**	**1.05**
12	0.49	0.49	0.49	**0.61**	**0.87**	**1.00**
14	0.49	0.48	0.48	**0.52**	**0.68**	**0.91**
16	0.49	0.48	0.48	0.48	**0.57**	**0.76**
18	0.49	0.48	0.48	0.48	**0.51**	**0.63**
20	0.49	0.48	0.48	0.48	0.49	**0.56**

	dimension d					
m	5	7	9	11	13	15
0	**0.96**	**0.96**	**0.96**	**0.97**	**0.97**	**0.97**
2	0.48	0.50	**0.72**	**1.00**	**1.05**	**1.05**
4	0.48	0.47	0.47	**0.52**	**0.67**	**0.88**
6	0.48	0.47	0.47	0.47	0.49	**0.57**
8	0.48	0.47	0.47	0.47	0.47	0.48
10	0.48	0.47	0.47	0.47	0.47	0.46
12	0.48	0.47	0.47	0.47	0.47	0.46
14	0.48	0.47	0.47	0.47	0.47	0.46
16	0.48	0.47	0.47	0.47	0.47	0.46
18	0.48	0.47	0.47	0.47	0.47	0.46
20	0.48	0.47	0.47	0.47	0.47	0.46

TABLE 3.1: β for the dominant QNM of MPdS at $r_-/r_+ = 0.99$ (*i.e.* at 99% of extremality) and $y_+ = 0.25$ (left) and $y_+ = 0.75$ (right), for a range of $m = l$ and dimensions d. The zigzag line describes the boundary $m = m_{\text{crit}}$ as given by (3.65). Modes above this line (*i.e.* those with smaller m) respect the AdS_2 BF bound; below it the BF bound is violated. Bold values have $\beta > \frac{1}{2}$ and the others have $\beta \leqslant \frac{1}{2}$.

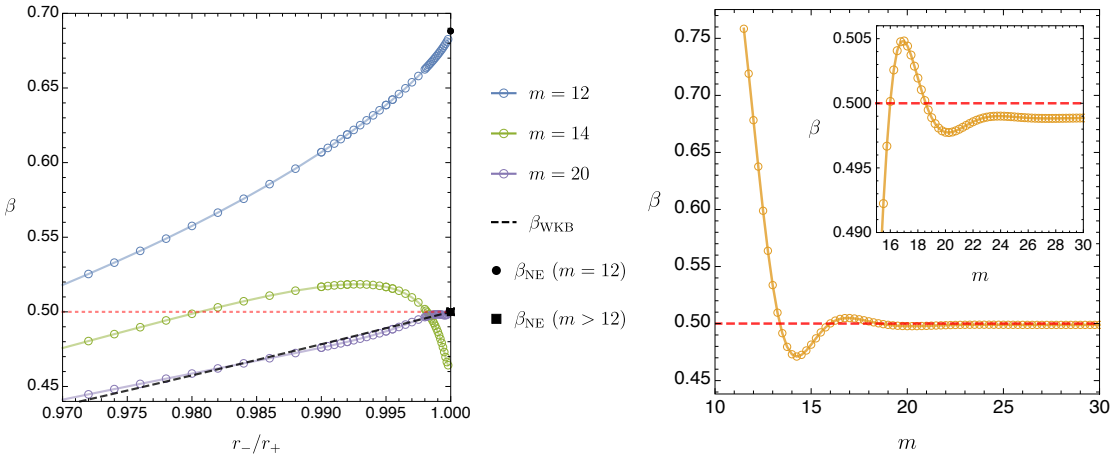

Fig. 3.12: Left panel: Dominant QNMs (PS-NH modes) near extremality for $d = 11$ MPdS with $y_+ = 0.25$, for varying $m = l$. The black dashed line is the eikonal approximation β_{WKB}. The black disk and black square at $r_-/r_+ = 1$ are β_{NH} for $m = 12$ and $m > 12$, respectively, as given by (3.64). The BF bound is saturated at $m \simeq 12.4$ so $\beta_{\text{NH}} = \frac{1}{2}$ for $m \geqslant 13$. **Right panel:** β as a function of m for $d = 11$ MPdS with $y_+ = 0.25$ and $r_- = 0.9995\, r_+$. For large m, β converges to a value with $\beta < \frac{1}{2}$ (see the inset plot, which is an enlargement), however β oscillates around this value for smaller m.

We now analyse what happens when we approach extremality even closer, namely as close as $r_-/r_+ = 0.9998$. As an illustrative example, we do this in Fig. 3.12 for a $d = 11$ ($N = 4$) MPdS black hole with $y_+ = 0.25$, for which $m_{\rm crit} \simeq 12.4$. For modes with $m < m_{\rm crit}$, e.g. the blue curve $m = 12$ in Fig. 3.12, there is no BF violation and accordingly we have $\beta > \frac{1}{2}$ at extremality (note that the near-horizon approximation (3.64) is highly accurate in this case: see black disk $\beta_{\rm NE}$ ($m = 12$) in the plot). For $m > m_{\rm crit}$ the situation is more complicated. For m slightly above $m_{\rm crit}$, e.g. for the $m = 14$ green curve in the left panel of Fig. 3.12, we find that the behaviour of $\beta(r_-/r_+)$ is not monotonic; β can first reach a maximum above $\frac{1}{2}$ before decreasing below $\frac{1}{2}$ at extremality. However, when m is well above $m_{\rm crit}$ e.g. for the $m = 20$ red curve in the left panel of Fig. 3.12, the modes have $\beta \leqslant \frac{1}{2}$ everywhere as they approach extremality. To understand this non-monotonicity better, in the right panel of Fig. 3.12 we fix the distance to extremality to be close to the minimum we reached, namely $r_-/r_+ = 0.9995$ and we plot β as a function of m for $d = 11$ MPdS with $y_+ = 0.25$. We see that β oscillates around $\frac{1}{2}$ for moderate values of m but ultimately converges to a value below $\frac{1}{2}$ as m grows large. Interestingly, but not perhaps not surprisingly (since the underlying physics is similar), a similar behaviour is observed in the discussion of SCC for a charged scalar field in Reissner-Nordström-dS when we plot β as a function of the scalar field charge (which is the analogue of m in charged system); see Fig. 9 of [122]). Just like in [122], we could probably try to capture the behaviour of $\beta(m)$ using a WKB expansion at large m with the oscillations around $\beta = 1/2$ only captured after including non-perturbative contributions to the analysis via a Borel resummation (*i.e.* a resurgence analysis) of the WKB expansion.

To conclude, we summarize our main SCC results. MPdS black holes with $m > 0$ typically have two families of QNMs: the dS and PS-NH families. For sufficiently large m, the latter always has smaller $|\mathrm{Im}(\omega)|$ than the dS family so the PS-NH modes are the ones relevant for strong cosmic censorship. We found that there is at least one family of $m = l$ QNMs for which the spectral gap satisfies the condition $\beta \leqslant 1/2$ in the whole parameter space of MPdS for odd $d \leqslant 11$ (and most probably even higher dimensions). It follows that Christodoulou's formulation of strong cosmic censorship holds for equal angular momenta $d > 4$ MPdS black holes, very much like in the $d = 4$ Kerr-dS case [94]. This is the main result. For each dimension $d = 2N + 3$ we found a (necessary but not sufficient) criterion, based on the violation of the AdS_2 BF bound associated to the near-horizon geometry of the extremal MPdS, to find how large $m = l$ needs to be to ensure that we have at least one family of PS-NH modes with $\beta \leqslant 1/2$ everywhere. Strictly speaking,

our numerical analysis covered only the range $0.1 \leqslant y_+ \leqslant 0.9$ and $0 \leqslant a/a_{\rm ext} \lesssim 1$ of the 2-dimensional parameter space of MPdS. So it seems that we missed cases near the endpoints of $y_+ \in [0,1]$. However, we have complemented our numerical analysis with an (approximate) analytic analysis that covers the corners of the phase space which are not easy to explore numerically. Namely, we used the eikonal approximation (1.19) and the NH approximation (3.64)-(3.65). We have only discussed SCC in equal angular momenta MPdS black holes in odd spacetime dimensions d. However, the generic considerations of [205] further indicate that this result extends to other, perhaps all, MPdS solutions. Together with [201] we thus have strong evidence that for arbitrary spacetime dimensions in de Sitter and for scalar induced perturbations, Christodoulou's formulation of SCC holds in dynamically stable, vacuum, rotating black hole solutions of the Einstein equations, but can be violated in the presence of charged matter. We stress, however, that the leading eikonal behaviour is spin independent, and thus the result quoted above could indeed also be true for gravitational perturbations.

Chapter 4

Phase diagram of the charged black hole bomb

The black hole bomb setup was designed by Zel'dovich [138] and Press and Teukolsky [137] (see also [229]) very much in the aftermath of having understood the mathematical theory of black hole perturbations around a Kerr black hole. It emerged naturally from the fact that superradiant scattering unavoidably occurs in rotating black holes with angular velocity Ω, as discussed in section 1.4. For a Kerr black hole, if a scalar wave with frequency ω and azimuthal number m satisfying $\omega < m\Omega$ is trapped near the horizon by the potential of a box (for example), the multiple superradiant amplifications and reflections can lead to an instability. The wave keeps extracting energy and angular momentum from the black hole interior and these accumulate between the horizon and the cavity. Press and Teukolsky assumed that this build up of radiation pressure would raise to levels that could no longer be supported by the box and the latter would eventually break apart. But the black hole bomb system does not necessarily need to have such a dreadful end. Actually, more often than not, a black hole instability is a pathway to find new solutions that are stable to the original instability, have more entropy (for given energy and angular momentum) and are thus natural candidates for the endpoint or metastable states of the instability time evolution. This is certainly the case for superradiant fields trapped by the AdS gravitational potential [230–235] or massive fields in asymptotically flat black holes [236]. So we can expect the same in the original black hole bomb system.

Motivated by these considerations, we would like to find the full phase diagram of solutions that can exist in the original black hole bomb system. By this, we mean

to find all possible stationary solutions of the theory with boundary conditions that confine the scalar field inside the box. These would be the non-linear version of the floating solutions in equilibrium that are described in [137]. This certainly requires solving PDEs. Therefore, here we start by considering a simpler system that still has a superradiant scalar field trapped inside a box but those properties can be found by simply solving ODEs. This is possible if we first place a Reissner-Nordström black hole (RN BH) with chemical potential μ inside a box and then perturb it with a scalar field with charge q and frequency ω. As long as $\omega < q\mu$, a superradiant instability will also develop leading to the charged version of the black hole bomb system [139]. We thus want to find the phase diagram of static solutions of this system, including those with a scalar condensate floating above the horizon. The latter hairy solutions might have higher entropy than the original RN BH for a given energy and charge where they coexist. If so they would be a natural candidate for the endpoint of the charged black hole bomb instability, as long as we check that we can build boxes − with an Israel stress tensor [237–240] that satisfies the relevant energy conditions [241] − that holds the internal radiation pressure without breaking apart. This will further guarantee that we can insert this boxed system in an exterior Reissner-Nordström background, as required by Birkhoff's theorem [242, 243].

Looking into the details of this programme we immediately find new physics. Indeed, a linear perturbation analysis of the Klein-Gordon equation on an RN BH finds that the system is not only unstable to superradiance but also to a near-horizon instability, discussed in Section 1.4. In this context, it is also known as a *scalar condensation instability*, and it was originally found by Gubser [244] in planar AdS backgrounds (in a study that initiated the superconductor holographic programme), see *e.g.* [162, 163, 245]. The superradiant and near-horizon instabilities are typically entangled for generic RN BHs but there are two corners of the phase space where they disentangle and reveal their origin. Indeed, extremal RN BHs with arbitrarily small horizon radius only have a superradiant instability since the near-horizon instability is suppressed as inverse powers of the horizon radius. In the opposite corner, RN BHs with a horizon radius close to the box radius only have a near horizon instability.

Analysing the setup of the black hole bomb system leads to the observation that the theory also has horizonless solutions if we remove the RN BH but leave the scalar field inside a box with a Maxwell field. Indeed, we can certainly perturb a Klein-Gordon field in a cavity and the frequencies that can fit inside it will be naturally quantized and real. This suggests that, within perturbation theory, we can

then back-react this linear solution to higher orders where it will source non-trivial gravito-electric fields that are regular inside (and outside) the box [246]. These are the boson stars of the theory, also known as solitons (depending on the chosen $U(1)$ gauge; see *e.g.* [247] for a review on boson stars). This perturbative analysis is bound to capture only small mass/charge boson stars. But a full numerical nonlinear analysis can identify the whole phase space of boson stars [248]. This analysis further reveals that the phase diagram of boson stars is quite elaborate, with distinct boson star families. In particular, it finds that the phase diagram of solitons depends non-trivially on a total of four critical scalar field charges. Two of them can be anticipated using simple heuristic arguments on the aforementioned superradiant and near-horizon instabilities, but the two others only emerge after solving the non-linear equations of motion.

Coming back to our main subject of study, an RN BH placed inside a box is also the starting point to discuss and find the hairy BHs of the theory. The latter have a scalar condensate floating above the horizon that is balanced against gravitational collapse by electric repulsion. A box with appropriate Israel junction conditions and stress tensor [237–240] should be able to confine the scalar condensate in its interior, and it should then be possible to place the whole boxed system in a background whose exterior solution is the RN solution. Here, we confirm that this is indeed the case and we find the full phase diagram of static solutions of the charged black hole bomb system. It turns out that the aforementioned four critical scalar electric charges play a relevant role also in the phase diagram of hairy BHs. Indeed, this diagram is qualitatively distinct depending on which one of the four available windows of critical charges the scalar charge q falls into. Ultimately, the reason for this dependence follows from the fact − that we will establish− that all hairy BHs that have a zero horizon radius limit choose to terminate on the boson star of the theory (which is fully specified once q is given), in the sense that the zero entropy hairy BHs have the same (Brown-York [249] quasilocal) mass and charge as the boson star. In our system, this materializes the idea that, often, small hairy BHs can be thought of as a small BH (RN or Kerr BH) placed on top of a boson star, as long as they have the same thermodynamic potential (chemical potential or angular velocity) to have the two constituents in thermodynamic equilibrium.

One of the four hairy BH families that we find here was already identified in the perturbative analysis of [246]. This is the only family of hairy BHs that extends to arbitrarily small mass and charge, thus making it prone to be captured by the perturbative analysis about an empty box with an electric field. But the other

three families and their intricate properties cannot be captured by such a theory because they are not perturbatively connected to the zero mass/charge solution.

Perhaps the most important property of the hairy BHs of the charged black hole bomb is that, when both coexist, they *always* have higher entropy than the RN BH that has the *same* mass and charge. Therefore, we will conclude that hairy BHs are always the preferred thermodynamic phase of the theory in the microcanonical ensemble.

Very much like black holes confined in a box can be the a starting point to discuss certain aspects of black hole thermodynamics [250–256] they should also be useful to understand generic superradiant systems where distinct (including perhaps some astrophysical) potential barriers confine fields [137]. These two are related since the hairy solutions describe non-linear systems where the central solution is in thermodynamic equilibrium with the floating scalar radiation. In particular, we can expect that hairy solutions of the charged black hole bomb provide a toy model with *some* universal features for the phase diagram of other confined unstable systems. Actually, we find that the present phase diagram shares many common features with the phase diagram of superradiant hairy blacks holes in global anti-de Sitter [257–259, 163, 260–263].

The plan of this chapter is as follows. In section 4.1 we summarize in two figures the main properties of the phase diagram of hairy black holes and boson stars. In section 4.2 we formulate the exact setup of our system. The discussion only includes aspects that guarantee that our exposition is self-contained and more details can be found in [246]. In section 4.3 we explicitly construct the hairy black hole solutions in the four relevant windows of scalar charge that, together with the boson star study of [248], allow us to arrive to the conclusions summarized in section 4.1. Finally, in section 4.4 we explain how data of the hairy solution inside the box can be used to find the Israel stress tensor of the cavity surface layer and be matched with the exterior Reissner-Nordstöm solution.

4.1 Summary of phase diagram of boson stars and BHs in a cavity

Einstein−Maxwell−Scalar theory, with boundary conditions such that the scalar field is confined inside a box of radius L in an asymptotically flat background, is fully specified once we fix the mass and charge q of the scalar field. We consider

massless scalar fields with dimensionless electric charge $e = qL$ (the system has a scaling symmetry that allows us to measure all physical, *i.e.* dimensionless, quantities in units of L). By Birkhoff's theorem [242, 243] [1], outside the cavity the hairy solutions we search for are necessarily described by the RN solution. Thus, we just need to find the hairy solutions inside the box and then confirm that the Israel junctions conditions required to confine the scalar condensate inside the cavity, while having an exterior RN solution, correspond to an Israel energy-momentum stress tensor (proportional to the extrinsic curvature jump across the box layer [237–240]) that is physical, *i.e.* that satisfies relevant energy conditions [241].

Since the solution outside the box is described by the RN solution, we cannot use the Arnowitt-Deser-Misner (ADM) mass M and charge Q [264] to differentiate the several solutions of the theory. However, we can use the Brown-York quasilocal mass $\mathcal{M}$ and charge $\mathcal{Q}$ [249], computed at the box location and normalized in units of L, and associated phase diagram $\mathcal{Q}$-$\mathcal{M}$ to display and distinguish the solutions of the theory. These quasilocal quantities obey their own first law of thermodynamics that is used to (further) check the results. In the quasilocal phase diagram, the extremal RN 1-parameter family of BHs (with horizon inside the box) provides a natural reference to frame our discussions. In particular, because distinct solutions often pile-up in certain regions of the phase diagram, for clarity we will find it useful to plot $\Delta\mathcal{M}/L$ *vs* $\mathcal{Q}/L$ where $\Delta\mathcal{M} = \mathcal{M} - \mathcal{M}\big|_{\text{ext RN}}$ is the mass difference between the hairy solution and the extremal RN that has the *same* $\mathcal{Q}/L$. Therefore, in this phase diagram $\mathcal{Q}$-$\Delta\mathcal{M}$, the horizontal line with $\Delta\mathcal{M} = 0$ represents the extremal RN BH solution. Its horizon at R_+ fits inside the box of radius L if $R_+ \leqslant 1$ (which corresponds to $\mathcal{Q}/L \leqslant 2^{-1/2}$) and non-extremal RN BHs exist above this line. However, horizons of non-extremal RN BHs fit inside the box ($R_+ \leqslant 1$) if and only if their quasilocal charges are to the left of the red dashed line that we will display in our $\mathcal{Q}$-$\Delta\mathcal{M}$ diagrams. Actually, it turns out that this line also represents the maximal quasilocal charge that hairy solutions enclosed in the box can have.

We find that the spectrum of hairy black holes and boson stars of the theory is qualitatively distinct depending on whether e is smaller or bigger than four critical scalar field charges — e_{NH}, e_γ, e_c and e_{S} — which obey the relations $0 < e_{\text{NH}} < e_\gamma < e_c < e_{\text{S}}$.

[1] Birkhoff's theorem for Einstein-Maxwell theory states that the unique spherically symmetric solution of the Einstein-Maxwell equations with non-constant area radius function r (in the gauge (4.2)) is the Reissner-Nordström solution. If r is constant then the theorem does not apply since one has the Bertotti-Robinson ($AdS_2 \times S^2$) solution.

Two of these critical charges, $e_{\rm NH}$ and $e_{\rm S}$, can be identified simply studying linear scalar field perturbations about an RN BH in a box. Such RN BHs can be parametrised by the chemical potential μ and dimensionless horizon radius $R_+ = r_+/L$. These parameters are constrained to the intervals $0 \leqslant \mu \leqslant \mu_{\rm ext}$ (with the upper bound being the extremal configuration) and $0 < R_+ \leqslant 1$. Boxed RN BHs become unstable − the black hole bomb system − if e is above the instability onset charge $e_{\rm onset}(\mu, R_+)$. Instead of displaying $e_{\rm onset}(\mu, R_+)$, it proves to be more clear to display the 2-dimensional plot $e_{\rm onset}(R_+)$ for fixed values of μ. A sketch of this plot is given in the left panel of Fig. 4.1 (which reproduces the exact results in Fig. 2 of [245]). The minimal onset charge is attained for extremal RN black holes ($\mu = \mu_{\rm ext}$): this is the orange curve that connects points $(0, e_{\rm S})$ and $(1, e_{\rm NH})$. For completeness, in the left panel of Fig. 4.1 we also sketch the onset charge curves (green dashed) for two non-extremal RN BHs at fixed $\mu < \mu_{\rm ext}$. Naturally, this onset charge increases as we move away from extremality. Moreover, we see that the (extremal) minimal onset curve terminates at two critical charges that, actually, can be computed analytically:

- $e = e_{\rm NH} = \frac{1}{2\sqrt{2}} \sim 0.354$. This is the charge above which scalar fields can trigger a violation of the near horizon AdS_2 Breitenlöhner-Freedman (BF) bound [197, 244, 162, 163] of the extremal RN black hole whose horizon radius approaches, from below, the box radius. For details on how to derive this critical charge please refer to Section III.B of [245].

- $e = e_{\rm S} = \frac{\pi}{\sqrt{2}} \sim 2.221$. This is the critical charge above which scalar fields can drive arbitrarily small RN BHs unstable via superradiance. For a detailed analysis that leads to this critical charge, please see Section III.A of [246].

The system has two other critical charges, e_γ and e_c, that are uncovered when we do a detailed scan of the boson stars (a.k.a. solitons) of the theory. This task was completed in detail in the companion paper [248]. A phase diagram that summarizes the relevant properties for the present study is displayed in the right panel of Fig. 4.1 [248]. Note that it stores in a single plot the solitons for *different theories*, *i.e.* for several distinct values of e. Two families of ground state boson stars (*i.e.* with smallest energy for a given charge) where found in [248]. One is the *main or perturbative boson star family* which can be found within perturbation theory if we back-react a normal mode of a Minkowski cavity to higher orders. In the right panel of Fig. 4.1, these are the solitons that are continuously connected to $(\mathcal{Q}, \Delta\mathcal{M}) = (0, 0)$. The other one is the *secondary or non-perturbative soliton*

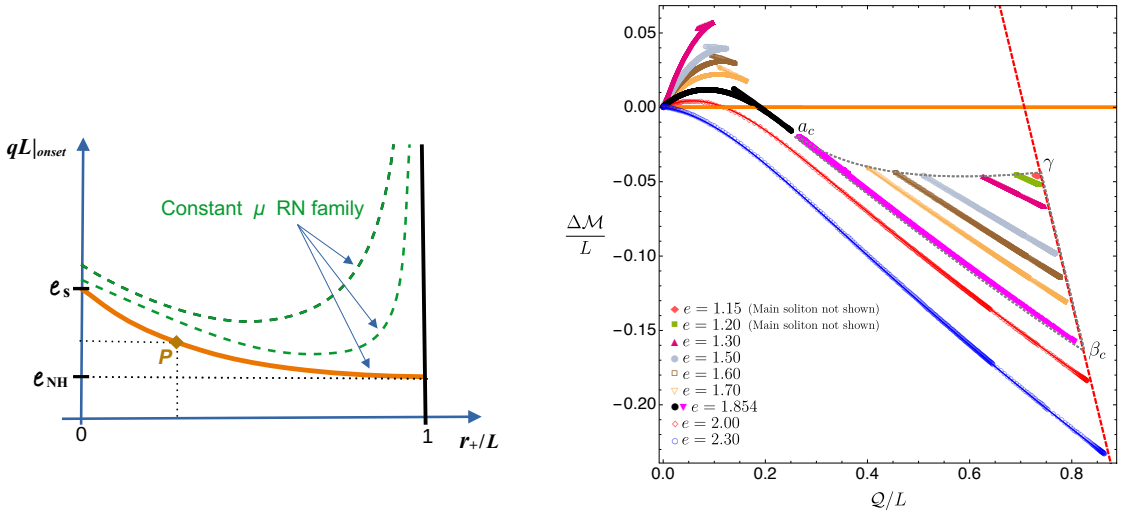

Fig. 4.1: Left panel: Sketch of the scalar field electric charge $e_{\rm onset} = qL|_{\rm onset}$ as a function of the horizon radius $R_+ = r_+/L$ of RN BHs in a box (sketched from Fig. 2 of [245]). The orange curve in the bottom − that starts at $(R_+, e) = (0, e_{\rm S})$ and terminates at $(R_+, e) = (1, e_{\rm NH})$ − describes the *minimal* onset charge (which occurs at extremality, $\mu = \mu_{\rm ext}$). That is, (non-)extremal RN BHs can be unstable if an only if e is higher than the one identified by this orange onset curve. On the other hand, if we pick an RN family with constant $\mu < \mu_{\rm ext}$, for instability, we need e to be higher than the associated green dashed line $e(R_+)|_{{\rm const}\ \mu}$ also shown. In particular, we see that if we chose a charge in the range $e_{\rm NH} \leqslant e \leqslant e_{\rm S}$, RN BHs are unstable if and only if they are between the orange minimal onset curve and the horizontal line to the right of point P (gold diamond). **Right panel:** a survey of boson stars for different values of e, for $e \geqslant e_\gamma$ [248]. For a given $e \in [e_\gamma, e_c[$ we have the main (perturbatively connected to $(0,0)$) and secondary (non-perturbative) solitons (which only exist in the region bounded by the auxiliary grey dashed closed curve $a_c\beta_c\gamma$). The secondary soliton curve with e just above e_γ is close to the point γ, while the soliton with $e = 1.854$, just below e_c, is the magenta curve (very close to $a_c\beta_c$). Note that the gap in $\mathcal{Q}/L$ between the main soliton and the secondary one starts very large at $e = e_\gamma$ but then decreases and goes to zero precisely at $e = e_c$.

family. In Fig. 4.1, these are the solitons that exist only above a critical $\mathcal{Q}$ and terminate at the red dashed line. The main/perturbative soliton family exists for any value of $e > 0$ (the system has a symmetry that allows us to consider only $e > 0$). However, the secondary/non-perturbative soliton only exists for scalar field charges that are in the window $e_\gamma \leqslant e < e_c$. These are the solitons enclosed in the region $a_c\beta_c\gamma$ (*i.e.* inside the auxiliary grey dashed closed line with these vertices). They only exist above $e_\gamma \sim 1.13$ (see point γ) and below $e_c \simeq 1.854 \pm 0.0005$ (see line $a_c\beta_c$ just below the magenta line). Below e_γ the non-perturbative solitons do not exist because they no longer fit inside the box. Above e_c, the gap between the two soliton families ceases to exist, *i.e.* the non-perturbative soliton merges with the perturbative soliton, and the ground state boson stars of the theory extend

from the origin all the away to the red dashed line (see *e.g.* the red diamond curve with $e = 2$ or the blue circle curve with $e = 2.3$ in Fig. 4.1). Summarizing, the main/perturbative soliton has a Chandrasekhar limit for $0 < e < e_c$ but extends from the origin all the way to the red dashed line for $e \geqslant e_c$. On the other hand, the ground state secondary/non-perturbative soliton only exists in the window $e_\gamma \leqslant e < e_c$.

In the following sections we will find the hairy black holes of the Einstein–Maxwell–Klein-Gordon theory. We will conclude that, whenever the hairy black holes have a zero horizon radius limit, they terminate on a soliton. Accordingly, the phase diagram of solutions depends on the above four critical scalar field charges. Our main findings are summarized in the phase diagram sketches of Fig. 4.2 and the properties of these phase diagrams depend on the following 5 windows of scalar charge e:

1. $e < e_{\rm NH} = \frac{1}{2\sqrt{2}} \sim 0.354$. From the left panel of Fig. 4.1, one concludes that RN is stable for $e < e_{\rm NH}$ and thus no hairy BHs exist. The only non-trivial solutions of the theory are the RN BH and the main/perturbative boson star which has a Chandrasekhar limit (see details in [248]).

2. $e_{\rm NH} \leqslant e < e_\gamma \sim 1.13$. The phase diagram $\mathcal{Q}$-$\Delta\mathcal{M}$ of solutions for this window is sketched in the top-left panel of Fig. 4.2. The only boson star of the theory is the main/perturbative family $OABC\cdots$ (already present for $e < e_{\rm NH}$) with its Chandrasekhar limit A and a series of cusps $A, B, C, \cdots$ and associated zig-zagged branches whose properties were studied in detail in [248]. As the left panel of Fig. 4.1 indicates, RN BHs are now unstable for sufficiently large R_+ (*i.e.* $\mathcal{Q}$) if sufficiently close to extremality (see diamond point P and region bounded by the horizontal line to the right of P and the minimal onset curve). The onset of the instability translates into the yellow curve $P\alpha$ in the top-left panel of Fig. 4.2 and RN BHs below this onset curve $P\alpha$ (and above the extremal horizontal straight line $OP\alpha$) are unstable. Hairy BHs exist inside the region bounded by the closed curve $P\alpha\beta$. They merge with RN BHs at the onset $P\alpha$ of the instability and they extend for lower masses all the way down to the blue dashed line $P\beta$ where they terminate at *finite* entropy and *zero* temperature because the Kretschmann curvature at the horizon blows up. They are also constrained to be to the left of the red dashed line $\alpha\beta$ because the horizon of the hairy BH must fit inside the cavity with unit normalized radius. Note that for this window of e there is no dialogue between the hairy boson star and the hairy BH families.

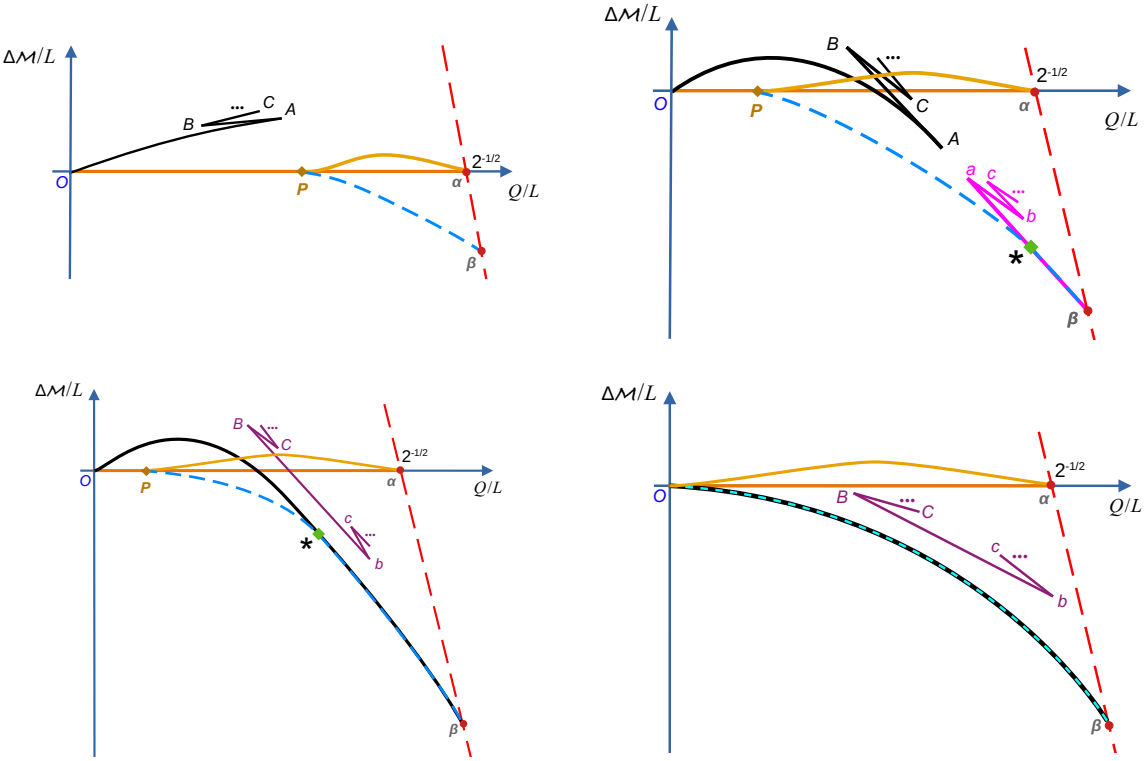

Fig. 4.2: Sketch of the quasilocal phase diagram for black holes and solitons and as we span relevant windows of scalar field charge e. The critical charges are such that $0 < e_{\rm NH} < e_\gamma < e_c < e_{\rm S}$. The quantity $\Delta\mathcal{M}$ is the quasilocal mass difference between a given solution and an extremal RN BH that has the *same* quasilocal charge $\mathcal{Q}/L$. Hence the orange line at $\Delta\mathcal{M} = 0$ describes the extremal RN solution that must have $\mathcal{Q}/L \leqslant 2^{-1/2}$ to fit inside the box. The red dashed line represents the maximal quasilocal charge of solutions that can fit inside the box. It intersects the extremal RN line at $\mathcal{Q}/L = 2^{-1/2}$. Non-extremal RN BHs confined in the box have $\Delta\mathcal{M} > 0$ and fill the triangular region bounded by $\mathcal{Q} = 0$ and by the orange and red dashed lines (not shown completely). The main soliton family is always given by black curves that start at O. The secondary soliton family is given either by magenta or purple curves. Hairy black holes exist in the region $P\alpha\beta$ enclosed by the yellow merger line $P\alpha$ (between hairy and RN BHs), the blue curve $P\beta$ where the curvature grows large and the red line $\alpha\beta$. **Top-left panel:** case $e_{\rm NH} < e < e_\gamma$. **Top-right panel:** $e_\gamma \leqslant e < e_c$. **Bottom-left panel:** case $e_c \leqslant e < e_{\rm S}$. **Bottom-right panel:** case $e \geqslant e_{\rm S}$.

A representative example of a black hole bomb system with a charge $e = 1$ in this window $e_{\rm NH} \leqslant e < e_\gamma$ will be discussed in detail in section 4.3.1 and Fig. 4.3.

3. $e_\gamma \leqslant e < e_c \simeq 1.854 \pm 0.0005$. The phase diagram $\mathcal{Q}$-$\Delta\mathcal{M}$ of solutions for this window is sketched in the top-right panel of Fig. 4.2. Besides the main/perturbative family $OABC\cdots$ of boson stars (black line), the system now has the secondary/non-perturbative family $\beta abc\cdots$ of boson

stars (magenta line) and there is a gap Aa between these two families. Precisely at e_γ, this gap Aa is the largest and the non-perturbative boson star family reduces to a single point β on top of the red-dashed line (*i.e.* it coincides with point γ in right panel of Fig. 4.1). As e grows beyond e_γ, the gap Aa decreases and it vanishes precisely at $e = e_c$ where the two ground state soliton families merge into a single one (for details of this merger please see [248]).

As before, hairy BHs exist in the region enclosed by the closed line $P\alpha\beta$ with the yellow curve $P\alpha$ being again the instability onset curve where the scalar condensate vanishes and hairy BHs merge with the RN BH family. As before, the hairy BHs also extend for smaller masses all the way down to the singular blue dashed line $P\beta$ where the Kretschmann curvature at the horizon diverges. But this time, this singular curve $P\beta \equiv P \star \beta$ splits into two segments. Hairy BHs terminating in the trench $P\star$ do so at *finite entropy* and *zero temperature*, as all the hairy BHs with $e < e_c$. However, hairy BHs terminating at the trench $\star\beta$ do so at *zero entropy* and *infinite temperature*. In such a way that in the $\mathcal{Q}$-$\Delta\mathcal{M}$ phase diagram, this hairy BH trench $\star\beta$ *coincides* with the secondary/non-perturbative soliton (magenta line between $\star$ and β). In this sense, we can say that hairy BHs with large charge ($\mathcal{Q} \geqslant \mathcal{Q}_\star$) terminate on the non-perturbative soliton. This point $\star$ coincides with β in the limit $e \to e_\gamma$ and it diverges away from β as e moves away from e_γ towards e_c.

A representative example of a black hole bomb system with a charge $e = 1.85$ in this window $e_\gamma \leqslant e < e_c$ will be discussed in detail in section 4.3.2 and Figs. 4.4–4.6.

4. $e_c \leqslant e < e_{\rm S} = \frac{\pi}{\sqrt{2}} \sim 2.221$. The phase diagram $\mathcal{Q}$-$\Delta\mathcal{M}$ of solutions for this window is sketched in the bottom-left panel of Fig. 4.2. At $e = e_c$ the perturbative and non-perturbative boson star families merge and for $e \geqslant e_c$ the boson star ground state is always the perturbative family $O\beta$ (black curve) that extends from the origin to the red dashed line. There is also a secondary family of boson stars $\cdots CBbc \cdots$ (purple curve) but it is not the ground state family and it plays no role in the description of hairy BHs. Therefore we do not discuss it further (see [248] for details).

Hairy BHs exist inside the closed line $P\alpha\beta$. Again, the yellow curve $P\alpha$ is the instability onset curve where hairy BHs merge with the RN BH family. The hairy BHs extend for smaller masses all the way down to the singular blue dashed line $P \star \beta$ where the Kretschmann curvature at the horizon

diverges. Hairy BHs terminating in the trench $P\star$ do so at *finite entropy* and *zero temperature*, while hairy BHs terminating at the trench $\star\beta$ do so at *zero entropy* and *infinite temperature*. In the $\mathcal{Q}$-$\Delta\mathcal{M}$ phase diagram, this hairy BH trench $\star\beta$ *coincides* with the perturbative soliton (black line between $\star$ and β). In this sense, hairy BHs with large charge ($\mathcal{Q} \geqslant \mathcal{Q}_\star$) terminate on the perturbative soliton. As e increases above e_c, points P and $\star$ move to the left of the phase diagram, *i.e.* to lower values of $\mathcal{Q}$ and they approach the origin O as $e \to e_{\rm s}$.

A representative example of a black hole bomb system with a charge $e = 2$ in this window $e_c \leqslant e < e_{\rm s}$ will be discussed in detail in section 4.3.3 and Figs. 4.7−4.9.

5. $e \geqslant e_{\rm s}$. The phase diagram $\mathcal{Q}$-$\Delta\mathcal{M}$ of solutions for this window is sketched in the bottom-right panel of Fig. 4.2. Precisely at $e_{\rm s}$, the slope $\mathrm{d}\Delta\mathcal{M}/\mathrm{d}\mathcal{Q}$ of the main/ perturbative boson star family (black curve $O\beta$) vanishes at the origin and for $e \geqslant e_{\rm s}$, perturbative boson stars always have $\Delta\mathcal{M} < 0$. Not less importantly, at and above $e_{\rm s}$, all extremal RN BHs are unstable, *i.e.* point P seen in the plots for $e < e_{\rm s}$ hits the origin O. Consequently, hairy BHs now exist for all values of $\mathcal{Q}$ (that can fit inside the cavity), *i.e.* in the 2-dimensional region with boundary $O\alpha\beta$. And, for any $\mathcal{Q}$, hairy BHs bifurcate from RN at the instability onset $O\alpha$ (yellow curve) and extend for smaller masses till they terminate − with zero entropy, and divergent temperature and Kretschmann curvature − along a curve (blue dashed line) that *coincides* with the boson star curve $O\beta$ (black curve).

   A representative example of a black hole bomb system with a charge $e = 2.3$ in this window $e \geqslant e_{\rm s}$ will be discussed in detail in section 4.3.4 and Figs. 4.10−4.12.

Independently of e, a universal property of hairy BHs is that, when they coexist with boxed RN BHs, they always have higher entropy than the boxed RN BH with the same quasilocal mass and charge. That is to say, in the phase space region where they exist, hairy BHs are always the dominant phase in microcanonical ensemble. Moreover, hairy BHs are stable to the superradiant mode that drives the boxed RN BH unstable. It follows from these observations and the second law of thermodynamics (Section 1.4) that the endpoint of the superradiant/near horizon instability of the boxed RN BH, when we do a time evolution at constant mass and charge, should be a hairy BH. It would be interesting to confirm this doing time evolutions along the lines of those done in [265–267].

The present work can be seen as the final study of a sequel of works on the charged black hole bomb system. Ref. [245] started by studying the linear superradiant and near-horizon instabilities of the boxed RN BH. This identified the zero-mode and growth rates of these instabilities. The hairy boson stars and hairy BHs were found within perturbation theory in [246]. As expected, this perturbative analysis is valid only for small condensate amplitudes and small horizon radius and thus it is able to capture only small energy/charge hairy solutions. Therefore, for the solitons, the perturbative analysis can capture the main or perturbative boson star family at small mass/charge. But it misses: 1) the existence of the Chandrasekhar limit and cusps of this family, 2) the existence of the secondary or non-perturbative boson star family, and 3) it misses the existence of two important critical charges e_γ and e_c where the non-perturbative soliton starts existing and merges with the perturbative family. These properties were only identified once the Einstein−Maxwell−Klein-Gordon equation was solved fully non-linearly in [248]. On the other hand, the perturbative analysis of [246] also finds the hairy BHs that, for $e \geqslant e_{\rm s}$, are perturbatively connected to a Minkowski spacetime with a cavity. By construction, these perturbative hairy BHs reduce, in the zero horizon radius limit, to the boson star of the theory. However, the perturbative analysis of [246] says nothing about the hairy BHs of the theory when $e < e_{\rm s}$. In this chapter, we fill this gap.

In the introduction we already mentioned that the potential barrier that confines the scalar condensate in our boxed or black hole bomb system might be a good toy model for other systems with potential barriers that provide confinement. In particular, we find that the phase diagram of hairy boson stars and BHs in the black hole bomb system is qualitatively similar to the one found for asymptotically anti-de Sitter solitons [257–259, 163, 260–263]. In this latter case, the AdS boundary conditions act as a natural gravitational box with radius inversely proportional to the cosmological length that provides bound states. In this sense, our work also complements and completes previous AdS studies since the existence range of the secondary/non-perturbative boson star family, its merger with the main/perturbative soliton at $e = e_c$, and the fact that hairy BHs can also terminate on this soliton family for $e_\gamma \leqslant e < e_c$ was not established in detail in [257–259, 163, 260].

4.2 Setting up the black hole bomb boundary value problem

The setup of our problem was already discussed in the perturbative analysis of the problem in [246]. Here, to have a self-contained exposition, we discuss only the key aspects needed to formulate the problem and the strategy to compute physical quantities without ambiguities. We ask the reader to see [246] for details.

4.2.1 Einstein-Maxwell gravity with a confined scalar field

We consider the action for Einstein−Maxwell−Klein-Gordon theory, as in Section 1, but now with a (massive) charged scalar field:

$$S = \frac{1}{16\pi G_N}\int \mathrm{d}^4x\sqrt{g}\left(\mathcal{R} - \frac{1}{2}F_{\mu\nu}F^{\mu\nu} - 2D_\mu\phi(D^\mu\phi)^\dagger + m^2\phi\phi^\dagger\right), \tag{4.1}$$

where $\mathcal{R}$ is the Ricci scalar, A is the Maxwell gauge potential, $F = \mathrm{d}A$, $D_\mu = \nabla_\mu - iqA_\mu$ is the gauge covariant derivative of the system, and ϕ is a complex scalar field with mass m and charge q. We consider only massless scalar fields, although it is certainly possible to extend our analysis to $m > 0$.

We want to find the black hole solutions of (4.1) that are static, spherically symmetric and asymptotically flat. $U(1)$ gauge transformations allow us to work with a real scalar field and a gauge potential that vanishes at the horizon. Further choosing the Schwarzschild gauge, an *ansatz* with the desired symmetries is then

$$\begin{aligned} \mathrm{d}s^2 &= -f(r)\mathrm{d}t^2 + g(r)\mathrm{d}r^2 + r^2\mathrm{d}\Omega_2^2, \\ A_\mu\mathrm{d}x^\mu &= A(r)\mathrm{d}t, \qquad \phi = \phi^\dagger = \phi(r), \end{aligned} \tag{4.2}$$

with $\mathrm{d}\Omega_2^2$ being the metric for the unit 2-sphere (expressed in terms of the polar and azimuthal angles $x = \cos\theta$ and φ). The scalar field is forced to be confined inside a box of radius L. The system then has a scaling symmetry that allows us to normalize coordinates ($T = t/L, R = r/L$) and thermodynamic quantities in units of L, and place the box at radius $R = 1$ [246].

In these conditions, the equations of motion that follow from (4.1) can be found in [246]. These are a set of three ordinary differential equations for the fields $f(R)$, $A(R)$ and $\phi(R)$, and an algebraic equation that expresses $g(R)$ as a function

of the other 3 fields and their first derivatives. Well-posedness of the boundary value problem requires that we give boundary conditions at the horizon and asymptotic boundary of our spacetime. Additionally, we must specify Israel junction conditions at the timelike hypersurface $\Sigma = R - 1 = 0$ where the box is located. Again, our hairy BHs have vanishing scalar field at and outside this box, $\phi(R \geqslant 1) = 0$.

The horizon, with radius $R = R_+ = \frac{r_+}{L}$ is the locus $f(R_+) = 0$. We have three second order ODEs and thus there are six free parameters when we do a Taylor expansion about the horizon. Regularity demands Dirichlet boundary conditions that set three of these parameters to zero. We are thus left with only three constants f_0, A_0, ϕ_0 (say) such that the regular fields have the Taylor expansion around the origin:

$$\begin{aligned} f(R_+) &= f_0(R - R_+) + \mathcal{O}((R - R_+)^2), \\ A(R_+) &= A_0(R - R_+) + \mathcal{O}((R - R_+)^2), \\ \phi(R_+) &= \phi_0 + \mathcal{O}((R - R_+)^2). \end{aligned} \tag{4.3}$$

Consider now the asymptotic boundary of our spacetime, $R \to \infty$. The scalar field vanishes outside the box, $\phi = 0$, and the equations of motion have the solution: $f^{out}(R) = c_f - \frac{M_0}{R} + \frac{\rho^2}{2R^2}$, $A_t^{out}(R) = c_A + \frac{\rho}{R}$ and $g^{out}(R) = c_f / f^{out}(R)$ (onwards, the superscript ^{out} represents fields outside the cavity). Here, c_f, M_0, c_A and ρ are arbitrary parameters, *i.e.* we have an asymptotically flat solution for any value of these constants. However, the theory has a second scaling symmetry ($e = qL$)

$$\begin{gathered} \{T, R, x, \varphi\} \to \{\lambda_2 T, R, x, \varphi\}, \qquad \{e, R_+\} \to \{e, R_+\}, \\ \{f, g, A_t, \varphi\} \to \{\lambda_2^{-2} f, g, \lambda_2^{-1} A_t, \varphi\}, \end{gathered} \tag{4.4}$$

that we use to set $c_f = 1$ so that $f|_{r\to\infty} = 1$ (and $g^{out} = 1/f^{out}$) [246]. Outside the box the solution to the equations of motion is then

$$f^{out}(R)\big|_{R\geqslant 1} = 1 - \frac{M_0}{R} + \frac{\rho^2}{2R^2}\,, \qquad A_t^{out}(R)\big|_{R\geqslant 1} = c_A + \frac{\rho}{R}\,, \qquad \phi^{out}(R)\big|_{R\geqslant 1} = 0\,. \tag{4.5}$$

As required by Birkhoff's theorem for the Einstein-Maxwell theory [242, 243], this is the Reissner-Nordström (RN) solution. The leftover free constants in (4.5), M_0, c_A, ρ, will be determined only after we have the solution inside the cavity and specify the Israel junctions conditions at the latter.

Some of the parameters in (4.5) are related to the ADM conserved charges [264].

Indeed, the dimensionless ADM mass and electric charge of the system are ($G_N \equiv 1$):[2]

$$M/L = \lim_{R\to\infty} \frac{R^2 f'(R)}{2\sqrt{f(R)g(R)}} = \frac{M_0}{2}, \qquad Q/L = \lim_{R\to\infty} \frac{R^2 A_t'(R)}{2f(R)g(R)} = -\frac{\rho}{2}. \quad (4.6)$$

These ADM conserved charges measured at the asymptotic boundary include the contribution from the energy-momentum content of the cavity that confines the scalar hair. In the next subsection we discuss the properties of this box.

In these conditions, hairy BHs of the theory are a 2-parameter family of solutions that we can take to be the horizon radius R_+ and the value of the (interior) derivative of the scalar field at the box, $\epsilon \equiv \phi'^{\,in}\big|_{R=1^-}$.

As mentioned in section 4.1, it follows from Birkhoff's theorem that in the asymptotic region our solutions are necessarily described by the RN solution. Therefore, the ADM mass M and charge Q cannot be used to distinguish the several solutions of the theory. It is thus natural to instead use the Brown-York quasilocal mass $\mathcal{M}$ and charge $\mathcal{Q}$, measured at the box, to display our solutions in a phase diagram of the theory [249]. From section II.C of [246], the Brown-York quasilocal mass and charge contained inside a 2-sphere with radius $R = 1$ are ($G_N \equiv 1$)[3]

$$\mathcal{M}/L = R\left(1 - \frac{1}{\sqrt{g(R)}}\right)\Big|_{R=1}, \qquad \mathcal{Q}/L = \frac{R^2 A_t'(R)}{2\sqrt{g(R)}f(R)}\Big|_{R=1}. \quad (4.7)$$

The thermodynamic description of our solutions is complete after defining the chemical potential, temperature and entropy:

$$\mu = A(1) - A(R_+)\,, \qquad T_H L = \lim_{R\to R_+} \frac{f'(R)}{4\pi\sqrt{f(R)g(R)}}, \qquad S/L^2 = \pi R_+^2, \quad (4.8)$$

where we work in the gauge $A(R_+) = 0$. These quantities must satisfy the quasilocal form of the first law of thermodynamics:

$$\mathrm{d}\mathcal{M} = T_H\,\mathrm{d}S + \mu\,\mathrm{d}\mathcal{Q}, \quad (4.9)$$

which is used to check our solutions.

[2]Note that the Maxwell term in action (4.1) is $\frac{1}{2}F^2$, not the perhaps more common F^2 term. It follows that the extremal RN BH satisfies the ADM relation $M = \sqrt{2}|Q|$, instead of $M = |Q|$ that holds when the Maxwell term in the action is F^2. Extremal RN BHs have $\mu = \sqrt{2}$ where μ is the chemical potential of the BH, and RN BHs exist for $0 < \mu \leqslant \sqrt{2}$.

[3]The Brown-York quasilocal quantities reduce to the ADM ones when we evaluate the former at $R \to \infty$.

As explained before, for reference we will often compare the hairy families of solutions against extremal RN BHs. RN BHs confined in a cavity can be parametrised by the horizon radius R_+ and the chemical potential μ, and their quasilocal mass and charge are [246]

$$\mathcal{M}/L\big|_{RN} = 1 - \frac{\sqrt{2}(1-R_+)}{\sqrt{2-(2-\mu^2)R_+}}, \qquad \mathcal{Q}/L\big|_{RN} = \frac{\mu R_+}{\sqrt{2}\sqrt{2-(2-\mu^2)R_+}}. \quad (4.10)$$

where $0 < R_+ \leqslant 1$ (for the horizon to be confined inside the box) and $0 \leqslant \mu \leqslant \mu_{\rm ext}$, with extremality reached at $\mu_{\rm ext} = \sqrt{2}$. Note that at extremality one has $\mathcal{M}/L = R_+$ and $\mathcal{Q}/L = R_+/\sqrt{2}$. On the other hand, for any μ, when $R_+ = 1$ one has $\mathcal{M}/L = 1$ and $\mathcal{Q}/L = 2^{-1/2}$.

4.2.2 Description of the box: Israel junction conditions and stress tensor

So far, we discussed the boundary conditions at the horizon and asymptotic boundaries. However, hairy BHs are solutions that join an interior spacetime ($R < 1$; with superscript ^{in}) with the known RN exterior background (4.5) ($R > 1$; with superscript ^{out}). So, in practice we simply need to find the interior solution. For that, we need to integrate our equations of motion in the domain $R \in [R_+, 1]$. Therefore, we must specify appropriate conditions at the outer boundary of our integration domain, *i.e.* at $R = 1$. Next, we detail the procedures required to do this.

At and outside the box, *i.e.* for $R \geqslant 1$, the scalar field must vanish. However, its derivative when approaching the cavity from inside, *i.e.* as $R \to 1^-$, is finite (except for the trivial RN solution) and we will label this quantity ϵ:[4]

$$\phi^{in}\big|_{R=1} = \phi^{out}\big|_{R=1} = 0, \qquad \phi^{out}(R) = 0, \qquad \phi'^{\,in}\big|_{R=1} \equiv \epsilon. \quad (4.11)$$

That is, inside the box the scalar field is forced to have the Taylor expansion $\phi\big|_{R=1^-} = \epsilon(R-1) + \mathcal{O}\left((R-1)^2\right)$. We are forcing a jump in the derivative of the scalar field normal to the cavity timelike hypersurface Σ. This can be done only if we further impose junction conditions at Σ on the gravito-electric fields as discussed next.

[4]Our theory has the symmetry $\phi \to -\phi$ so we can focus our attention only on the case $\epsilon > 0$.

The box is the timelike hypersurface $\Sigma = R - 1 = 0$. It has outward unit normal $n_\mu = \partial_\mu \Sigma / |\partial \Sigma|$ ($n_\mu n^\mu = 1$) and coordinates $\xi^a = (\tau, \theta, \varphi)$. An observer in the interior of Σ measures the time $T^{\rm in}(\tau) = \tau$ and the induced line element and gauge 1-form at Σ are

$$\begin{aligned} \mathrm{d}s^2|_{\Sigma^{in}} &= h^{in}_{ab}\,\mathrm{d}\xi^a \mathrm{d}\xi^b = -f^{in}|_{R=1}\mathrm{d}\tau^2 + \mathrm{d}\Omega_2^2\,, \\ A_t|_{\Sigma^{in}} &= a^{in}_a \mathrm{d}\xi^a = A^{in}_t|_{R=1}\mathrm{d}\tau\,, \end{aligned} \tag{4.12}$$

where h^{in}_{ab} is the induced metric in Σ and a^{in}_a is the induced gauge potential in Σ. Meanwhile, from the perspective of an observer outside the cavity, Σ is parametrically described by $R = 1$ and $T^{out}(\tau) = N\tau$ (so, N is a reparametrisation freedom parameter) so that the induced line element and gauge 1-form for this observer are

$$\begin{aligned} \mathrm{d}s^2|_{\Sigma^{out}} &= h^{out}_{ab}\,\mathrm{d}\xi^a \mathrm{d}\xi^b = -N^2 f^{out}|_{R=1}\mathrm{d}\tau^2 + \mathrm{d}\Omega_2^2\,, \\ A_t|_{\Sigma^{out}} &= a^{out}_a \mathrm{d}\xi^a = N A^{out}_t|_{R=1}\mathrm{d}\tau\,, \end{aligned} \tag{4.13}$$

Ideally, we would like to have a smooth crossing of Σ, whereby the induced gravitational h_{ab} and gauge a_a fields and their normal derivatives are continuous across Σ. That is to say, the Israel junction conditions should be obeyed [237–240]:

$$a^{in}_a\big|_{R=1} = a^{out}_a\big|_{R=1}\,, \tag{4.14a}$$
$$h^{in}_{ab}\big|_{R=1} = h^{out}_{ab}\big|_{R=1}\,; \tag{4.14b}$$
$$f^{in}_{aR}\big|_{R=1} = f^{out}_{aR}\big|_{R=1}\,, \tag{4.14c}$$
$$K^{in}_{ab}\big|_{R=1} = K^{out}_{ab}\big|_{R=1}; \tag{4.14d}$$

where $h_{ab} = g_{ab} - n_a n_b$ is the induced metric at Σ and $K_{ab} = h_a{}^\mu h_b{}^\nu \nabla_\mu n_\nu$ is the extrinsic curvature.

In the absence of the scalar condensate, we can set $N = 1$ and all the junction conditions (4.14) are satisfied. However, our hairy solutions are continuous but not differentiable at $R = 1$: they satisfy the conditions (4.14a)-(4.14c) but not (4.14d). Since the extrinsic curvature condition is violated, our hairy solutions are singular at Σ. But this singularity simply signals the presence of a Lanczos-Darmois-Israel surface stress tensor $\mathcal{S}_{ab}$ at the hypersurface layer proportional to the difference of

the extrinsic curvature across the hypersurface [237–240]:

$$\mathcal{S}_{ab} = -\frac{1}{8\pi}\Big([K_{ab}] - [K]h_{ab}\Big), \tag{4.15}$$

where K is the trace of the extrinsic curvature and $[K_{ab}] \equiv K^{out}_{ab}\big|_{R=1} - K^{in}_{ab}\big|_{R=1}$. This surface tensor is the pull-back of the energy-momentum tensor integrated over a small region around the hypersurface Σ, *i.e.* it is obtained integrating the appropriate Gauss-Codazzi equation [237–240, 268]. It is also given by the jump across Σ of the Brown-York surface tensor [249] (see also discussion in [246]). Essentially, (4.15) describes the energy-momentum tensor of the cavity (the "internal structure" of the box) that is needed to confine the scalar field. Since the two Maxwell junction conditions (4.14a)-(4.14b) are satisfied, our hairy solutions will have a surface layer with no electric charge.

The strategy to find the hairy BHs of the theory can now be outlined. The hairy solution inside the box is found integrating numerically the coupled system of three ODEs in the domain $R \in [R_+, 1]$. This is done while imposing the boundary conditions (4.3) at the horizon and, at the box, we impose $\phi(1^-) = 0$ and use the scaling symmetry (4.4) to set $f(1^-) = 1$. After this task, we can compute the quasilocal charges (4.7) and the other thermodynamic quantities (4.8) of the system. To find the solution in the full domain $R \in [R_+, \infty]$ we impose the three junction conditions (4.14a)-(4.14c) at the box to match the interior solution with the outer solution (described by the RN solution (4.5)). This operation finds the parameters M_0, C_A, ρ in (4.5) as a function of the reparametrisation freedom parameter N introduced in (4.13). The Israel stress tensor $\mathcal{S}^b_a$ is just a function of N and, if $\phi^{in} \neq 0$, we cannot choose N to kill all the components of $\mathcal{S}^b_a$ (there are two non-vanishing components, $\mathcal{S}^t_t$ and $\mathcal{S}^\theta_\theta = \mathcal{S}^\varphi_\varphi$). In this process, we have arbitrary freedom to choose N. This simply reflects the freedom we have to select the energy-momentum content of the box needed to confine the scalar condensate. We should however, make a selection that respects some or all the energy conditions [241]. Once this choice is made, we can finally compute the ADM mass and charge (4.6) of the hairy solution which, necessarily, includes the contribution from the box.

4.2.3 Numerical scheme

The hairy BHs we seek are a 2-parameter family of solutions, that we can take to be the horizon radius R_+ and the scalar field amplitude $\epsilon \equiv \phi'(R = 1)$ as defined in

(4.11). In practice, we set up a two dimensional discrete grid where we march our solutions along these two parameters. In other words, we give R_+ and ϵ as inputs of our numerical code, and in the end of the day we read the horizon parameters f_0, A_0, ϕ_0 in (4.3), and the values of the derivative of f and the value of A and its derivative at the box, $R = 1$. Typically, we start near the merger with the RN BH where a good seed (approximation) for the Newton-Raphson method we use is the RN BH itself but with a small perturbation that also excites the scalar field.

We find it convenient to introduce a new radial coordinate

$$y = \frac{R - R_+}{1 - R_+} \tag{4.16}$$

so that the event horizon is at $y = 0$ and the box at $y = 1$. The equations of motion now depend explicitly on R_+.

Moreover, we also find useful to redefine the fields as

$$f = y\, q_1(y), \qquad A = y\, q_2(y), \qquad \phi = -(1 - y)\, q_3(y) \tag{4.17}$$

which automatically imposes the boundary conditions (4.3) at the horizon. We now use the scaling symmetry (4.4) to set $f(1^-) = 1$ and introduce the scalar amplitude (4.11) at the box. This can be done through imposing the boundary conditions

$$q_1(1) = 1, \qquad q_3(1) = \epsilon. \tag{4.18}$$

The other boundary conditions for $q_{1,2,3}$ are derived boundary conditions in the sense that they follow directly from evaluating the equations of motion at the boundaries $y = 0$ and $y = 1$ [156]. Under these conditions, the hairy BHs are described by smooth functions $q_{1,2,3}$ that we search for numerically.

To solve our boundary value problem numerically, we use the standard Newton-Raphson algorithm with pseudospectral collocation, as described in Section 1.5. Since we are using pseudospectral methods, and our functions are analytic, our results have exponential convergence with the number of grid points. We check this is indeed the case, and the thermodynamic quantities that we display have, typically, 8 decimal digit accuracy. We further use the quasilocal first law (4.9) (typically, obeyed within an error smaller than $10^{-3}\%$) to check our solutions.

4.3 Phase diagram of the charged black hole bomb system

The properties of the hairy black holes of the charged black hole bomb system are closely linked to the superradiant/near-horizon instability of RN black holes[5], so we first highlight some features of this instability to provide the context needed to interpret the hairy black hole phase diagram (see [245] for details).

In the left panel of Fig. 4.1 we sketch (from [245]) the scalar field instability onset charge $e_{\rm onset} = q_{\rm onset} L$ as a function of R_+ for three families of RN black holes with constant chemical potential μ, *i.e.* the minimum scalar charge needed for a black hole with (R_+, μ) to be unstable. We can see that the near-horizon charge $e_{\rm NH}$ is a lower bound for an RN instability, *i.e.* caged RN BHs are always stable when $e < e_{\rm NH}$. Correspondingly, we also find no hairy black holes when $e < e_{\rm NH}$. At the other end, all extremal RN black holes, no matter their R_+, are unstable at or above the superradiant charge $e_{\rm S}$. In between these two critical charges $e_{\rm NH} < e < e_{\rm S}$ we have a window of horizon radii $R_+ \in [R_+|_P, 1]$ within which sufficiently near-extremal RN black holes are unstable. In equivalent words, for $e_{\rm NH} < e < e_{\rm S}$, extremal RN BHs are unstable for quasilocal charges in the range $\mathcal{Q}/L \in [(\mathcal{Q}/L)|_P, 2^{-\frac{1}{2}}]$. In the upcoming phase diagrams we will indicate the instability onset curve as a yellow curve $P\alpha$ and, when applicable, we will also use a gold diamond point P to identify the minimum charge for instability. The onset curve starts at point P where it intersects the extremal RN curve and terminates at point α with $\mathcal{Q}/L = 2^{-\frac{1}{2}}$ (*i.e.* $R_+ = 1$) where it intersects again the extremal RN curve.

In all our plots $\mathcal{M}$ and $\mathcal{Q}$ are the Brown-York quasilocal mass and charge (4.7) of the system, measured at the location of the box. Different solutions tend to pile-up in certain regions of the $\mathcal{Q}$-$\mathcal{M}$ diagram (as illustrated in Fig. 4.10). Thus, the distinction between different solutions becomes clearer if we use instead $\Delta\mathcal{M} = \mathcal{M} - \mathcal{M}\big|_{\rm ext\,RN}$ which is the quasilocal mass difference of a hairy solution with an extremal RN that has the *same* quasilocal charge $\mathcal{Q}$. Thus, in our $\mathcal{Q}$-$\Delta\mathcal{M}$ plots, the horizontal orange line $O\alpha$ with $\Delta\mathcal{M} = 0$ describes the extremal RN BH. It is constrained to have $\mathcal{Q}/L \leqslant 2^{-\frac{1}{2}}$ (point α) in order to fit inside the box (this extremal line will be represented by a dark red line in the 3-dimensional plots $\mathcal{Q}$-$\Delta\mathcal{M}$-S).

[5]For a general RN black hole the superradiant and near-horizon instabilities are entangled, so we will simply refer to an RN instability, regardless of the origin.

From the RN quasilocal charges (4.10), in the quasilocal $\mathcal{Q}-\mathcal{M}$ plot, the region that represents RN BHs with horizon radius inside the box is the triangular surface bounded by the lines $\mathcal{Q}=0$, $\mathcal{M}=\sqrt{2}\mathcal{Q}$ and $\mathcal{M}/L=1$. Therefore, in the $\mathcal{Q}-\Delta\mathcal{M}$ plane, non-extremal RN BHs with $R_+\leqslant 1$ are those inside the triangular region bounded by $\mathcal{Q}=0$, $\Delta\mathcal{M}=0$ and $\Delta\mathcal{M}/L=1-\sqrt{2}\mathcal{Q}/L$. The boundary $\mathcal{Q}=0$ describes the Schwarzschild limit, $\Delta\mathcal{M}=0$ is the extremal RN boundary and the latter curve is

$$(\mathcal{Q}/L,\Delta\mathcal{M}/L)=\left(L^{-1}\mathcal{Q}\big|_{\text{ext RN}},1-L^{-1}\mathcal{M}\big|_{\text{ext RN}}\right)=\left(\frac{R_+}{\sqrt{2}},1-R_+\right) \tag{4.19}$$

where $\mathcal{M}\big|_{\text{ext RN}}$ and $\mathcal{Q}\big|_{\text{ext RN}}$ are given by (4.10) with $\mu=\mu_{\text{ext}}=\sqrt{2}$. The red dashed line in the forthcoming $\mathcal{Q}-\Delta\mathcal{M}$ plots is this parametric curve (4.19) with R_+ *allowed to take also values above 1.* Indeed, it turns out that the most charged solutions we find approach this dashed red line (4.19) (in the limit where scalar condensate amplitude approaches infinity). In this sense, for a given quasilocal mass (smaller than 1), this red dashed line (4.19) represents the maximal quasilocal charge that confined solutions can have, with or without scalar hair.

As discussed in our summary of results (section 4.1), the charged black hole bomb system has a total of four critical scalar field charges. Besides $e_{\text{NH}}=\frac{1}{2\sqrt{2}}\sim 0.354$ and $e_{\text{S}}=\frac{\pi}{\sqrt{2}}\sim 2.221$ discussed above, the two others are $e_\gamma\sim 1.13$ and $e_c\sim 1.8545\pm 0.0005$. Accordingly, the phase diagram of hairy boson stars and hairy black holes depends on the value of e compared to these four fundamental critical charges of the system. Thus, in the next subsections, we describe the properties of hairy solutions in the following four windows of scalar field charge: 1) $e_{\text{NH}}\leqslant e<e_\gamma$, 2) $e_\gamma\leqslant e\leqslant e_c$, 3) $e_c\leqslant e<e_{\text{S}}$, and 4) $e\geqslant e_{\text{S}}$. For concreteness, we will display results for a representative value of e for each one of these windows, namely: 1) $e=1$ (section 4.3.1), 2) $e=1.85$ (section 4.3.2), 3) $e=2$ (section 4.3.3), and 4) $e=2.3$ (section 4.3.4). Altogether, these results (and others not presented) will allow us to extract the conclusions summarized in section 4.1.

4.3.1 Phase diagram for $e_{\text{NH}}\leqslant e<e_\gamma$

The left panel of Fig. 4.3 is the phase diagram $\mathcal{Q}$-$\Delta\mathcal{M}$ for $e=1$, representative of the range $e_{\text{NH}}\leqslant e<e_\gamma$. The black disk curve describes the only family of boson stars of the theory for this (range of) e which is the main/perturbative family. This corresponds to the black curve $OABC\cdots$ (already present for $e<e_{\text{NH}}$) with its Chandrasekhar limit A and a series of cusps $A,B,C,\cdots$ and associated zig-zagged

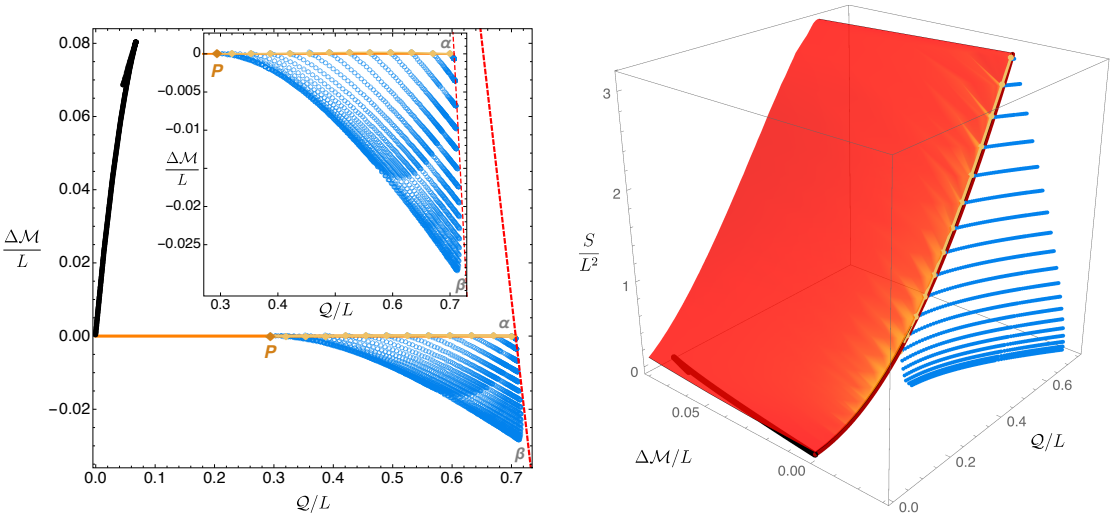

Fig. 4.3: Phase diagrams for Einstein-Maxwell theory with a scalar field charge $e = 1$ ($e_{\rm NH} \leqslant e < e_\gamma$) in a Minkowski box. **Left panel:** Quasilocal mass difference $\Delta\mathcal{M}/L$ as a function of the quasilocal charge $\mathcal{Q}/L$. The black disk curve is the main/perturbative soliton family, the orange line is the extremal RN BH (RN black holes exist above it), and the blue circles describe hairy black holes. The yellow curve is the superradiant onset curve of RN (just above but very close to the extremal RN curve with the two merging at P and α). It agrees with the hairy solutions in the limit where these have $\epsilon = 0$ (no scalar condensate) and thus merge with RN family. The red dashed line with negative slope signals solutions with $\Delta\mathcal{M}/L = 1 - \sqrt{2}\mathcal{Q}/L$ *i.e.* black holes with horizon radius $R_+ = 1$ (above this value they do not fit inside the cavity). **Right panel:** Dimensionless entropy S/L^2 as a function of the quasilocal charge and mass difference. RN BHs are the two parameter red surface with extremality described by the 1-parameter curve $\Delta\mathcal{M} = 0$ (dark red). The instability onset is described by the yellow curve (very close to extremality) and RN between these two curves are unstable. When they coexist with RN BHs, for a given $(\mathcal{Q}, \mathcal{M})/L$, hairy BHs (blue dots) always have more entropy than RN, *i.e.* they dominate the microcanonical ensemble. For $e_{\rm NH} \leqslant e < e_\gamma$, hairy BHs terminate at an extremal BH (*i.e.* with zero temperature) and finite entropy (and divergent horizon curvature). The soliton (black dots) with zero entropy is also shown.

branches sketched in the top-left panel of Fig. 4.2. The properties of this boson star were already studied in much detail in [248] so we do not expand further. Our interest here are the hairy BHs.

The horizontal orange curve $OP\alpha$ with $\Delta\mathcal{M} = 0$ is the extremal RN BH family with $\mathcal{Q}/L \leqslant 2^{-\frac{1}{2}}$ and boxed non-extremal BHs exist above this line and to the left of the red dashed line (4.19) to fit inside the cavity, as detailed above. The yellow curve $P\alpha$, that intersects and terminates at the extremal RN curve precisely at P and α, describes the instability onset curve of RN BHs as computed using linear analysis in [245]. It coincides with the merger line of hairy BHs with RN BHs, as it had to. Indeed, recall that hairy BHs can be parametrised by their horizon radius

R_+ and the scalar field amplitude ϵ. When $\epsilon = 0$ we recover the 1-parameter family $P\alpha$ of RN BHs at the onset of the instability. RN BHs are unstable below this onset curve $P\alpha$ all the way down to the horizontal extremal line also labeled $P\alpha$. This region is extremely small for this value of e but it will be wider as e increases.

Hairy BHs (blue circles) exist inside the closed line $P\alpha\beta$. That is, they exist below the onset curve $P\alpha$ and to the left of the red $\alpha\beta$ dashed line (4.19), all the way down till they reach a line $P\beta$ where the Kretschmann curvature scalar evaluated at the horizon $K|_{\mathcal{H}} = R_{abcd}R^{abcd}\big|_{R_+}$ grows large without bound. This occurs at finite R_+ and thus at *finite entropy* $S/L^2 = \pi R_+^2$, and the *temperature vanishes* along this boundary curve $P\beta$. The entropy is however not constant along this singular extremal boundary curve (in practice, the last curve we plot has $R_+ = 0.1$ but it should extend a bit further down in the region close to $\alpha\beta$). We typically find that lines of constant R_+ extend all the way to the red $\alpha\beta$ dashed line (4.19), but the latter is only reached in the limit $\epsilon \to \infty$. This makes it harder to extend our solution to regions even closer to $\alpha\beta$ (a fixed step in ϵ corresponds to an increasingly smaller progression in $\mathcal{Q}$ as $\alpha\beta$ is approached). Hairy BHs do not exist for $\mathcal{Q} < \mathcal{Q}|_P$, in agreement with the linear analysis of the left panel of Fig. 4.1, and there is clearly no relation between the hairy BHs and the boson star of the theory when $e = 1$ and, more generically, for $e_{\rm NH} \leqslant e < e_\gamma$.

Because point P does not coincide with the origin O, hairy BHs with $e_{\rm NH} \leqslant e < e_\gamma$ were not found in the perturbative analysis of [246]. Indeed, this perturbative analysis only captures hairy BHs that have small mass and charge.

The right panel of Fig. 4.3 plots the same phase diagram as the left panel but this time with the entropy S/L^2 on the extra vertical axis. The latter is the appropriate thermodynamic potential to discuss the preferred thermal phases of the microcanonical ensemble: for a given quasilocal mass $\mathcal{M}/L$ and charge $\mathcal{Q}/L$ fixed, the dominant phase is the one with the largest entropy. The red surface represents (a subset[6]) of RN BHs, both stable and unstable with the boundary line of stability being again the yellow dotted curve, here very close to the extremal RN BH (dark red with $\Delta\mathcal{M} = 0$). In the $S = 0$ plane we find the perturbative boson star (black curve). The blue dots fill the 2-dimensional surface that describe hairy BHs (which merge with RN along the yellow line). Again we see (not very clearly but it will be more clear for higher e) that hairy BHs coexist with RN black holes in the region between the onset and extremal RN curves. In this case, we

[6]We just plot the portion of the RN surface with $\Delta\mathcal{M} < 0.085$ that covers the region where the boson star also exists.

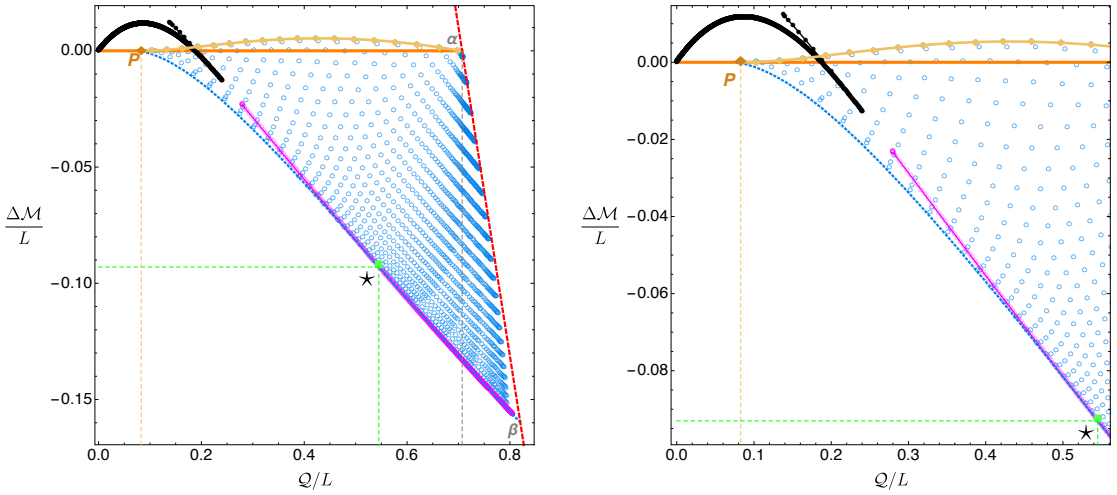

Fig. 4.4: Phase diagram for Einstein theory with a scalar field charge $e = 1.85$ ($e_\gamma \leqslant e < e_c$) in a Minkowski box. The blue circles describe hairy black holes, the black disk (magenta circle) curve is the soliton main (secondary) family, and the orange line is the extremal RN BH (non-extremal RN BHs exist above it). The yellow curve is the superradiant onset curve of RN. As it could not be otherwise, it agrees with the hairy solutions in the limit where these have $\epsilon = 0$ and thus merge with RN family. The dashed vertical line is at $\mathcal{Q} = 2^{-1/2}$ which is the maximum local charge that an extremal RN BH can have while fitting inside a box with radius $R = 1$. The red dashed line (4.19) describes the boundary for black holes that can fit inside the cavity with radius $R = 1$. The green solid square labeled with a star ($\star$) has $(\mathcal{Q}_\star, \mathcal{M}_\star, \Delta\mathcal{M}_\star) \sim (0.545, 0.678, -0.093)$. The auxiliary blue dotted curve $P \star \beta$ in the bottom describes the line where hairy BHs terminate with unbounded horizon curvature. Hairy BHs that terminate in the trench $P\star$ of this auxiliary curve do so at finite entropy and vanishing temperature. On the other hand, hairy BHs that terminate in the trench segment $\star\beta$ (that coincides with magenta soliton line) do so at zero entropy and large (possibly infinite) temperature.

find that hairy black holes always have a larger entropy than the corresponding RN BHs with same $\mathcal{M}/L$ and $\mathcal{Q}/L$. So they are the thermodynamically preferred phase in the microcanonical ensemble.

Hence, it follows from the second law of thermodynamics that hairy BHs with $(\mathcal{Q}, \mathcal{M})$ between the RN onset and extremality curves are natural candidates for the endpoint of the RN superradiant/near-horizon instability when we do a time evolution of the instability where we preserve the mass and charge of the system.

4.3.2 Phase diagram for $e_\gamma \leqslant e < e_c$

In Fig. 4.4 we display the phase diagram when $e = 1.85$, which is representative of the range $e_\gamma \leqslant e < e_c$ that we sketched in the top-right panel of Fig. 4.2. As a first observation we note that, besides the main or perturbative boson star family

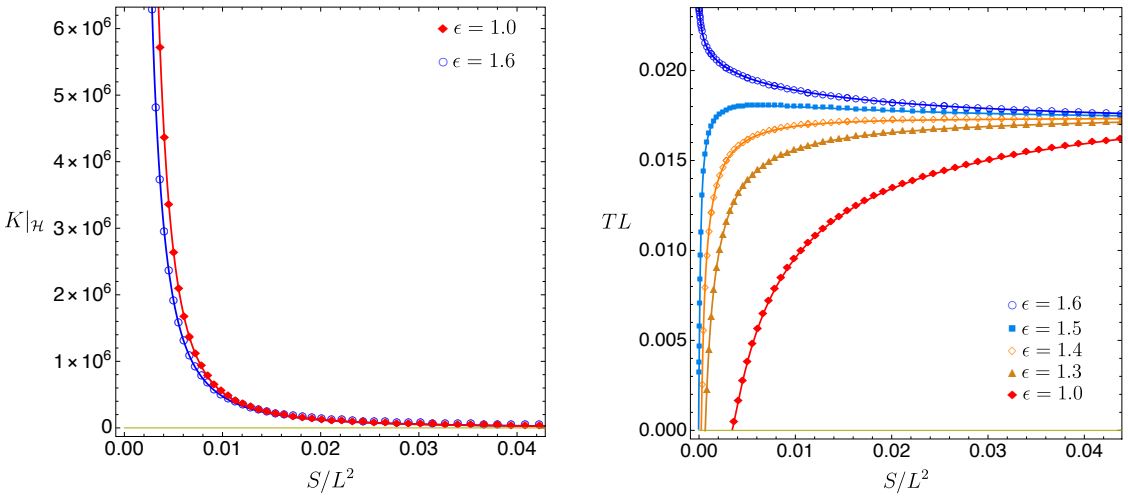

Fig. 4.5: Kretschmann curvature at the horizon (left panel) and temperature (right panel) as a function of the entropy ($S/L^2 = \pi R_+^2$) for several hairy BH families with constant scalar amplitude ϵ and scalar field charge $e = 1.85$ ($e_\gamma \leqslant e < e_c$).

(black curve) already present for $e < e_\gamma$, the diagram now also has the magenta line that starts at finite $\mathcal{Q}$, passes though point $\star$, and terminates at point β on the red dashed line. This is the secondary or non-perturbative family of boson stars. On its left side, this family has itself a series of cusps and zig-zagged secondary branches denoted as $B, C, \cdots$ in the sketch of the top-right panel of Fig. 4.2 (not displayed in Fig. 4.4). These details are not relevant here, and we ask the reader to see [248] for an exhaustive study of boson stars' properties. It is however important to emphasize that this secondary/non-perturbative family exists (as a ground state family) only for $e_\gamma \leqslant e < e_c$, thus explaining the origin of the critical charges e_γ and e_c. At $e = e_c$ the magenta line of Fig. 4.4 merges with the black line (see section 4.3.3). On the other hand, as we decrease e below e_c one finds that the gap $\Delta\mathcal{Q}$ between the black and magenta families increases, and the "length" of the magenta line decreases because the left endpoint of this curve approaches β. It keeps doing so till it only exists on a very small neighbourhood of the red dashed line and, at $e = e_\gamma$, this line shrinks to the single point β. Below e_γ, the non-perturbative family ceases to exist (as seen in section 4.3.1). Essentially because it no longer fits inside the cavity. This discussion is better illustrated in the right panel of Fig. 4.1: 1) if we collect all non-perturbative solitons in a single plot, we find that they exist only in the window $e_\gamma \leqslant e < e_c$ and they fill the area bounded by the auxiliary dashed lines $a_c\beta_c\gamma$; 2) very close to e_c the non-perturbative soliton is almost on top of the auxiliary curve $a_c\beta_c$; and 3) on the opposite end, as $e \to e_\gamma$, the perturbative soliton line shrinks to the point γ on the red dashed line.

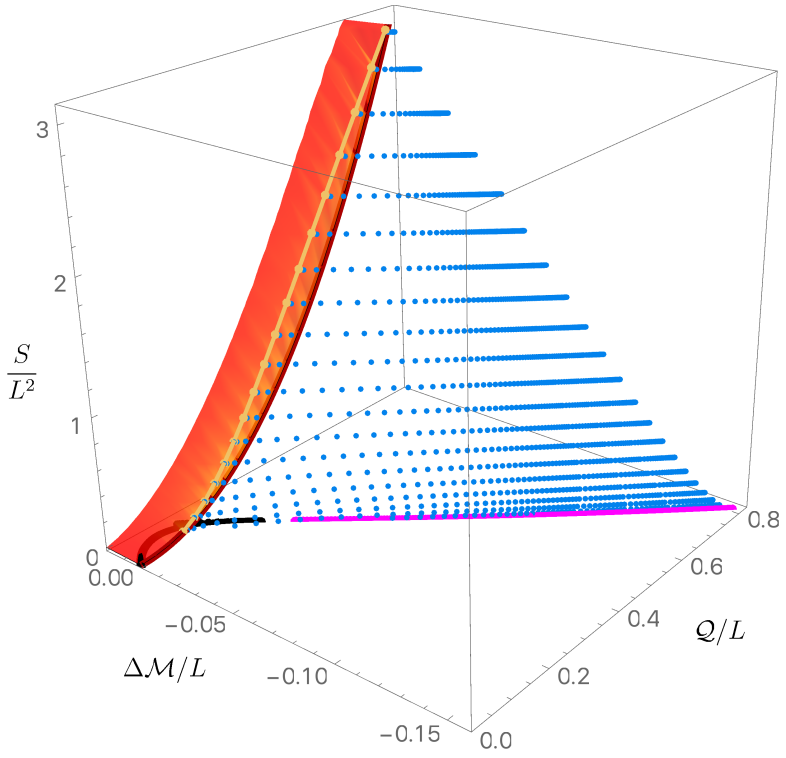

Fig. 4.6: Entropy as a function of the quasilocal charge and mass difference for Einstein theory with a scalar field charge $e = 1.85$ ($e_\gamma \leqslant e < e_c$) in a Minkowski box. The red surface represents RN BHs in the range $0 \leqslant \Delta\mathcal{M} < 0.02$ (they extend for higher $\Delta\mathcal{M}$) with the dark red line with $\Delta\mathcal{M} = 0$ being the extremal RN BH family. The yellow line describes the merger line between RN BHs and hairy BHs, and RN BHs between this line and the dark red extremal line are unstable. The blue disks describe hairy BHs and the black (magenta) lines with $S = 0$ describe the main (secondary) soliton family. When they coexist with RN BHs, for a given $(\mathcal{Q}, \mathcal{M})/L$, hairy BHs always have more entropy than RN, *i.e.* they dominate the microcanonical ensemble.

What are the consequences of these boson star discussions for the hairy BHs? Hairy BHs with $e = 1.85$ are the blue circles in Fig. 4.4. As before, they exist in the area bounded by $P\alpha\beta$, where $P\alpha$ is the merger yellow line with RN BHs and coincides with the instability onset curve of [245], and $\alpha\beta$ is a segment of the red dashed line (4.19). Starting at the onset curve $P\alpha$ and moving down, *e.g.* along constant $\mathcal{Q}$ lines, we find that hairy BHs terminate at the line $P\beta$ (or $P \star \beta$). This is the blue dashed line in Fig. 4.4 which describes hairy BHs with minimum entropy/horizon radius for a given charge. Along this line, the Kretschmann curvature scalar evaluated at the horizon $K|_{\mathcal{H}}$ grows very large (most probably, $K|_{\mathcal{H}} \to \infty$). To illustrate this, in the left panel of Fig. 4.5 we plot $K|_{\mathcal{H}}$ as a function of the entropy $S/L^2 = \pi R_+^2$ as we approach the line $P\beta$ (at small S) along curves of constant scalar amplitude ϵ (shown in the legends). Indeed, for small S/L^2 the curvature is growing very large.

So far the phase diagram of hairy BHs looks similar to the one for $e_{\rm NH} \leqslant e < e_\gamma$ (section 4.3.1). However, for $e_\gamma \leqslant e < e_c$ we now find that the way hairy BHs terminate along the singular curve differs substantially depending on whether it ends to the left or to the right of the green square point $\star$ in Fig. 4.4 (with $\mathcal{Q}_\star/L \simeq 0.545$ for $e = 1.85$). When the hairy BHs terminate along $P\star$, they do so at *finite entropy* and *vanishing temperature*. On the other hand, hairy BHs that terminate along $\star\beta$ do so at *vanishing entropy* and *large (possibly infinite) temperature*. To illustrate this, in the right panel of Fig. 4.5 we plot the temperature TL as a function of the entropy $S/L^2 = \pi R_+^2$ as we follow hairy BH families that approach the singular line $P\beta$ at (different; see legends) constant scalar amplitude ϵ. Point $\star$ has $(\mathcal{Q}_\star, \Delta\mathcal{M}_\star) \sim (0.545, -0.093)$ which corresponds to $(R_+, \epsilon)\big|_\star = (0, 1.55 \pm 0.05)$. Hairy BHs with $\epsilon < \epsilon_\star$ terminate at $P\star$, while hairy BHs with $\epsilon > \epsilon_\star$ end at $\star\beta$. The right panel of Fig. 4.5 indeed shows that hairy BHs with $\epsilon < \epsilon_\star$ approach $P\star$ at finite S/L^2 and with $TL \to 0$ (like all hairy BHs of section 4.3.1), while those with $\epsilon > \epsilon_\star$ approach $\star\beta$ with $S \to 0$ and $TL \to \infty$.

Another important conclusion that emerges from Fig. 4.4, is that hairy BHs which have a zero horizon radius limit terminate precisely along the segment $\star\beta$ of the secondary/non-perturbative soliton family. This means that hairy BHs terminate with the *same* $\mathcal{Q}$ and $\mathcal{M}$ as the non-perturbative soliton (but the gravito-electric and scalar fields of the two solutions are different). On the other hand, those that end at $P\star$ do so in a manner that is very similar to the way the hairy BHs with $e_{\rm NH} \leqslant e < e_\gamma$ terminate (section 4.3.1).

We find that the critical charge $\mathcal{Q}_\star(e)$ decreases as e grows from e_γ till e_c. As explained when discussing the right plot of Fig. 4.1, the non-perturbative soliton line shrinks to the point β when $e \to e_\gamma$. Thus, our expectation is that the critical charge $\mathcal{Q}_\star$ also reaches $\mathcal{Q}\big|_\beta$ when $e \to e_\gamma^+$. That is to say, we expect that hairy black holes are connected to the non-perturbative soliton as soon as it exists. However, determining numerically $\mathcal{Q}_\star$ in this limit is very difficult, since hairy BHs near β have very large values of ϵ.

The hairy BHs with $e_\gamma \leqslant e < e_c$ we find were not captured by the perturbative analysis of [246] because they do not extend to arbitrarily small mass and charge.

In Fig. 4.6, we plot the thermodynamic potential of the microcanonical ensemble − the entropy S/L^2 − as a function of $\mathcal{Q}$ and $\Delta\mathcal{M}$. In the $S = 0$ plane we find the perturbative boson star (black curve) and, for larger $\mathcal{Q}$ and after a gap, the non-perturbative boson star (magenta curve). As before, the red surface describes the RN BH family parametrised by R_+ and μ as in (4.10) and with $S/L^2 = \pi R_+^2$. It

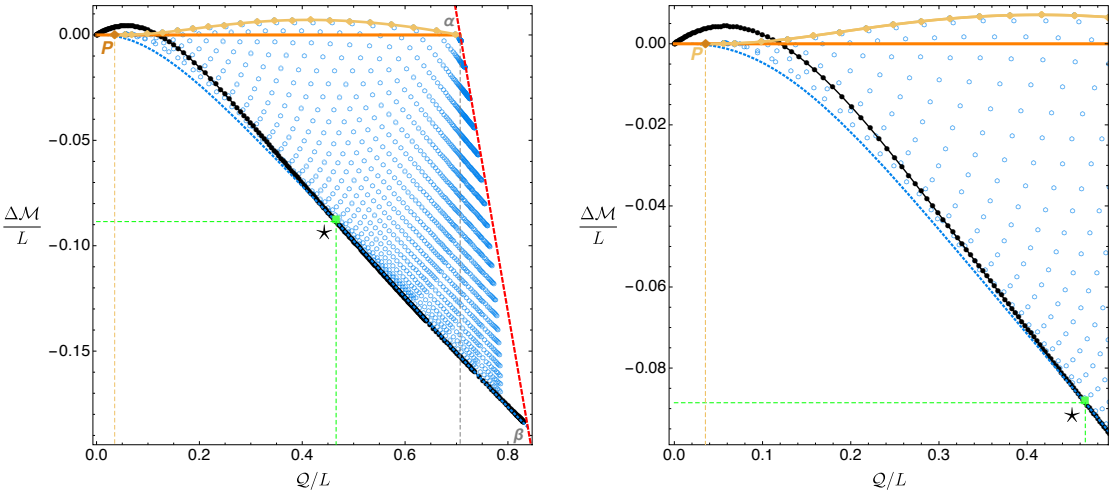

Fig. 4.7: Phase diagram for Einstein theory with a scalar field charge $e = 2$ ($e_c \leqslant e < e_{\rm S}$) in a Minkowski box. As before, the blue circles describe hairy black holes, the black disk curve is the soliton main family, and the orange line is the extremal RN BH (RN black holes exist above it). The gray and red dashed curves have the same interpretation as in Fig. 4.4. The green solid square labeled with a star ($\star$) has $(\mathcal{Q}_\star, \mathcal{M}_\star, \Delta\mathcal{M}_\star) \sim (0.466, 0.659, -0.0886)$. The auxiliary blue dotted curve $P \star \beta$ in the bottom describes the line where hairy BHs terminate with unbounded horizon curvature. Hairy BHs that terminate in the trench $P\star$ of this auxiliary curve have zero temperature ($T = 0$) and finite entropy $S/L = \pi R_+^2$. On the other hand, hairy BHs that terminate in the trench segment $\star\beta$ (that coincides with the black soliton line) have zero entropy and large (possibly infinite) temperature. Note that these $\star\beta$ terminal hairy BHs have the same $(\mathcal{Q}, \Delta\mathcal{M})$ as the main soliton family with $\mathcal{Q} > \mathcal{Q}_\star$.

terminates at the dark red extremal curve with $\Delta\mathcal{M} = 0$. We only plot the portion of the RN surface with $\Delta\mathcal{M} < 0.02$ that covers the region where the perturbative boson star also exists. Unstable RN BHs are those between the instability onset (yellow dotted curve) and the extremal RN dark red curve. The blue dots fill the 2-dimensional surface that describes hairy BHs. It merges with RN BHs along the yellow dotted curve and then extends to lower $\Delta\mathcal{M}$ with an entropy that is always larger the the RN BH with the same $\mathcal{Q}$ and $\mathcal{M}$ (when they coexist). Therefore, hairy BHs are the thermodynamically dominant phase in the microcanonical ensemble. Consequently, from the second law of thermodynamics, hairy BHs with $(\mathcal{Q}, \mathcal{M})$ between the RN onset and extremality curves are candidates for the endpoint of the RN superradiant/near-horizon instability when in a time evolution of the RN instability at constant mass and charge.

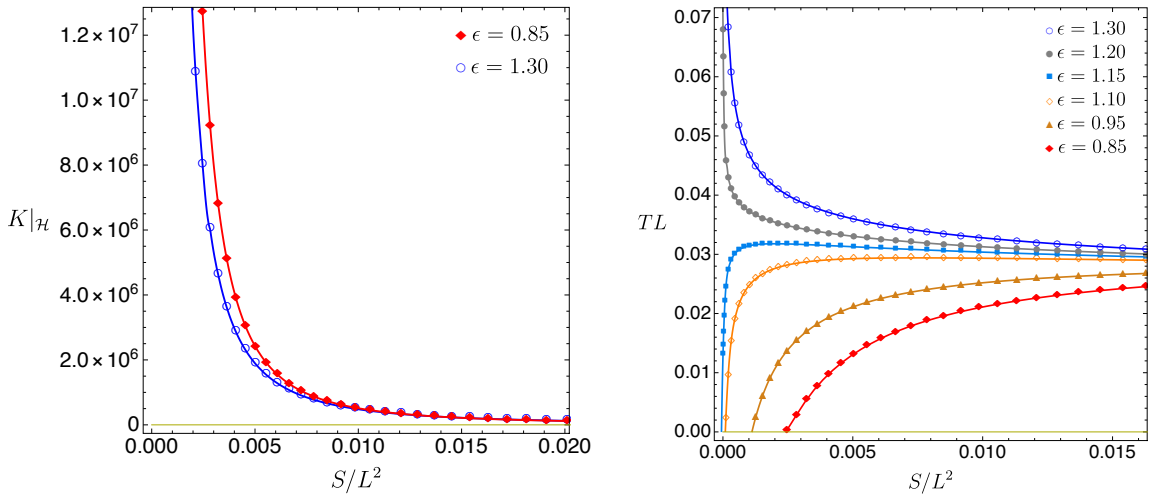

Fig. 4.8: Kretschmann curvature at the horizon (left panel) and temperature (right panel) as a function of the entropy ($S/L^2 = \pi R_+^2$) for hairy BH families with fixed ϵ and scalar field charge $e = 2$ ($e_c \leqslant e < e_{\rm S}$).

4.3.3 Phase diagram for $e_c \leqslant e < e_{\rm s}$

In Fig. 4.7 we give the phase diagram for $e = 2$. This is the case we choose to illustrate the solution spectra in the range $e_\gamma \leqslant e < e_c$ that we sketched in the bottom-left panel of Fig. 4.2. Comparing with the diagram of Fig. 4.4 we immediately notice that the magenta line representing the non-perturbative soliton family is no longer present in Fig. 4.7. This is because at $e = e_c$, the perturbative and non-perturbative boson star families (*i.e.* the black and magenta lines of Fig. 4.4) merge and for $e \geqslant e_c$ the main or perturbative boson star family no longer has a Chandrasekhar mass limit and now extends from the origin O all the way to β in the red dashed line. This merger at e_c occurs in an interesting elaborated manner. In particular, going back to top-right sketch of Fig. 4.2, at $e = e_c$ the secondary zig-zagged branches $\cdots CBA$ of the perturbative (black) soliton also merge with the secondary zig-zagged branches $abc\cdots$ of the non-perturbative (magenta) soliton. As a consequence, for $e \geqslant e_c$ there is also a secondary soliton $\cdots CBbc\cdots$ (purple line in bottom-left of Fig. 4.2) that has higher energy than the perturbative (black) soliton $P\beta$. This secondary family is not displayed in Fig. 4.7 because it plays no role on the discussion of hairy BHs of the theory. The reader can find a detailed discussion of soliton's properties across the transition at $e = e_c$ in [248].

Since the colour code and associated labeling in Fig. 4.7 is the same as in Figs. 4.3 and 4.4 we can now immediately discuss the hairy BHs. Again they exist in the

area enclosed by $P\alpha\beta$ filled with the blue circles. They merge with the RN family along the yellow dotted line $P\alpha$ when the scalar condensate vanishes, which agrees with the RN instability curve found in [245]. The hairy BHs then exist all the way down to the blue dashed line $P\beta$ (or $P\star\beta$) which, for a given charge, identifies the hairy BH that has minimum entropy/horizon radius. The Kretschmann curvature evaluated at the horizon $K|_{\mathcal{H}}$ diverges. For a given charge, $P\beta$ identifies the hairy BHs with minimum entropy/horizon radius and $K|_{\mathcal{H}}$ grows very large along it. This is confirmed in the left panel of Fig. 4.8: as we approach $P\beta$ (at small S) along lines of of constant scalar amplitude ϵ (identified in the legends), $K|_{\mathcal{H}}$ is growing very large.

Point $\star$ with charge $\mathcal{Q}_\star \simeq 0.466$ describes a transition point. Hairy BHs that end to the left of this point along $P\star$ do so at finite S with $T \to 0$. However, one has $S \to 0$ and $T \to \infty$ when the hairy BHs terminate along $\star\beta$ with $\mathcal{Q} > \mathcal{Q}_\star$. This is confirmed in the right panel of Fig. 4.8 where we plot the temperature TL as a function of the entropy $S/L^2 = \pi R_+^2$ as we follow different families of constant scalar amplitude hairy BHs that approach the singular line $P\beta$. Point $\star$ has $(\mathcal{Q}_\star, \Delta\mathcal{M}_\star) \sim (0.466, -0.0886)$ which corresponds to $(R_+, \epsilon)\big|_\star = (0, 1.175 \pm 0.005)$. Hairy BHs with $\epsilon < \epsilon_\star$ have $\mathcal{Q} < \mathcal{Q}_\star$ and terminate at $P\star$, while hairy BHs with $\epsilon > \epsilon_\star$ have $\mathcal{Q} > \mathcal{Q}_\star$ and end at $\star\beta$.

From Fig. 4.7 and the right panel of Fig. 4.8, it should not go without notice that the hairy BHs that have a zero horizon radius limit terminate along the trench $\star\beta$ of the perturbative soliton family. That is, *when* the hairy BHs have zero entropy, they have the same charge $\mathcal{Q}$ and mass $\mathcal{M}$ as the perturbative soliton. In a nutshell, hairy BHs with $e_c \leqslant e < e_{\rm s}$ have a behaviour that is qualitatively similar to those of $e_\gamma \leqslant e < e_c$ (section 4.3.2). However, the zero entropy BHs now terminate on top of the perturbative soliton in the $\mathcal{Q}$-$\mathcal{M}$ phase diagram instead of ending on the non-perturbative soliton (which is now an excited solution $\cdots CBbc \cdots$ in the bottom-left panel of Fig. 4.2). We also find that the critical charge $\mathcal{Q}_\star(e)$ decreases and approaches $\mathcal{Q}_P$ as e grows from e_c to $e_{\rm s}$. Moreover, we find that $\mathcal{Q}_\star \to \mathcal{Q}_P \to 0$ as $e \to e_{\rm s}$.

Fig. 4.9, displays the phase diagram of the microcanonical ensemble for $e = 2$: the entropy S/L^2 as a function of $\mathcal{Q}$ and $\Delta\mathcal{M}$. The colour code of this diagram is the same as Fig. 4.6. Because e is bigger than the cases considered before, we see that the region between the onset yellow curve and the extremal RN dark red curve where RN BHs are unstable is now quite visible. Again we find that the hairy BHs (blue circles) that bifurcate from the yellow onset curve always have

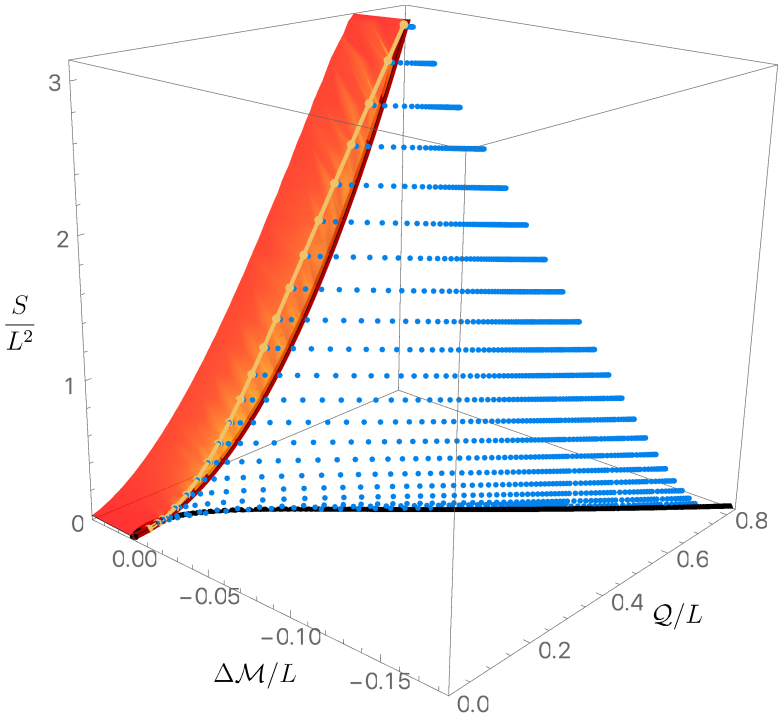

Fig. 4.9: Entropy as a function of the quasilocal charge and mass difference for Einstein theory with a scalar field charge $e = 2$ ($e_c \leqslant e < e_{\rm S}$) in a Minkowski box. When they coexist with RN BHs, for a given $(\mathcal{Q}, \mathcal{M})/L$, hairy BHs always have more entropy than RN, *i.e.* they dominate the microcanonical ensemble. For $e_c \leqslant e < e_{\rm S}$, when $\mathcal{Q} > \mathcal{Q}_\star(e)$, hairy BHs have a zero entropy limit where they coincide with the soliton (black disk) curve in the sense that they have the same $(\mathcal{Q}, \mathcal{M})/L$ as the soliton (the temperature and horizon curvature diverges). However, when $0 < \mathcal{Q} < \mathcal{Q}_\star(e)$, hairy BHs terminate at an extremal BH (*i.e.* with zero temperature) and finite entropy (and divergent horizon curvature) along a line that does not coincide with the black disk one for the soliton.

higher entropy that the RN BHs with the same $(\mathcal{Q}/L, \mathcal{M}/L)$ when they coexist. It follows that also for $e_c \leqslant e < e_{\rm S}$, hairy BHs are the preferred thermodynamic phase in the microcanonical ensemble. As expected from Fig. 4.7, for $\mathcal{Q} \geqslant \mathcal{Q}_\star \simeq 0.466$, the hairy BHs terminate with zero entropy on top of the perturbative boson star (black curve).

It is natural to expect that the hairy BHs we find should be the endpoint of the RN instability if we perturb an RN BH in the unstable region (where they always coexist with hairy BHs) and do a time evolution at constant charge and mass. The system would evolve to a final configuration that is stable against the original perturbation while respecting the second law of thermodynamics. Finally note that the hairy BHs with $e_c \leqslant e < e_{\rm S}$ described in this section were not studied in the perturbative analysis of [246] because the latter can only capture solutions that have a zero mass and charge limit.

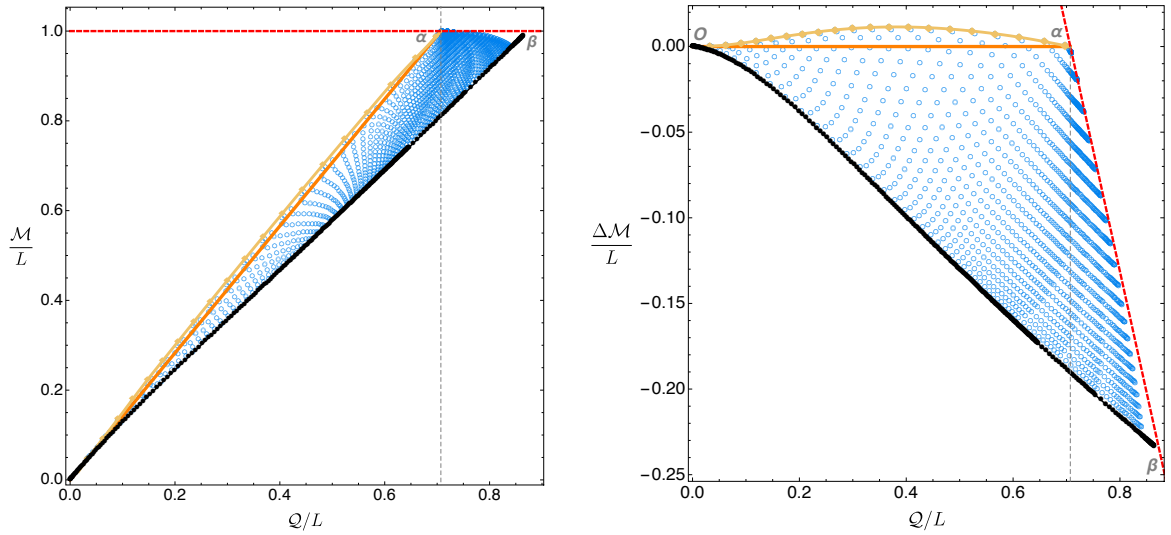

Fig. 4.10: Phase diagram for Einstein theory with a scalar field charge $e = 2.3$ ($e > e_{\rm S}$) in a Minkowski box. In the left panel we have the $\mathcal{Q}$-$\mathcal{M}$ phase diagram: we see that the solutions pile up and this is why we have instead been plotting the phase diagram $\mathcal{Q}$-$\Delta\mathcal{M}$ (right panel). The blue circles describe hairy black holes, the black disk curve is the perturbative soliton family and the orange line is the extremal RN BH (RN black holes exist above it). The yellow curve is the superradiant onset curve of RN. As it could not be otherwise, it agrees with the hairy solutions in the limit where these have $\epsilon = 0$ and thus merge with RN family. The gray and red dashed curves have the same interpretation as in Fig. 4.4. For $e > e_{\rm S}$, the zero entropy limit of the hairy BH is the soliton (black disk curve) in the sense that they have the same $(\mathcal{Q}, \mathcal{M})/L$ as the soliton.

4.3.4 Phase diagram for $e \geqslant e_{\rm s}$

The critical charge $e = e_{\rm S} = \frac{\pi}{\sqrt{2}} \sim 2.221$ is special for two main (related) reasons. First, it is the minimal charge above which scalar fields can drive *arbitrarily small* extremal RN BHs unstable via superradiance, as observed in the instability onset charge plot of the left panel of Fig. 4.1. Indeed, the extremal onset curve $e_{\rm onset}(R_+)$ reaches $e = e_{\rm S}$ as $R_+ \to 0$. The value of $e_{\rm S}$ can be predicted analytically as done in Section III.A of [246]. For $e > e_{\rm S}$, we can also have near-extremal BHs unstable for arbitrarily small R_+ or, equivalently, for arbitrarily small mass and charge.

This scalar charge $e_{\rm S}$ is also special because at $e = e_{\rm S}$ the slope of the perturbative soliton at the origin vanishes, *i.e.* $\frac{\delta\Delta\mathcal{M}}{\delta\mathcal{Q}}\big|_{\mathcal{Q}=0} = 0$. For $e < e_{\rm S}$, this slope is positive and we always have (some) perturbative solitons with higher quasilocal mass than the extremal RN (for sufficiently small $\mathcal{Q}$). On the other hand, for $e > e_{\rm S}$ the slope is always negative, $\frac{\delta\Delta\mathcal{M}}{\delta\mathcal{Q}}\big|_{\mathcal{Q}=0} < 0$, and thus perturbative solitons never coexist with RN BHs.

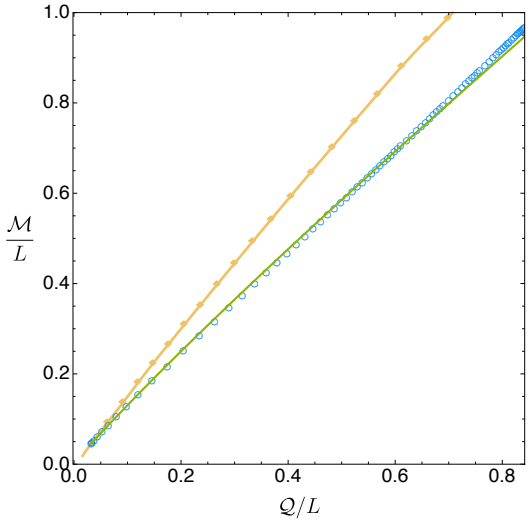

Fig. 4.11: Comparing the exact numerical results (blue circles) with the perturbative analytical predictions (4.20)-(4.21) (green curve) for a family of black holes with constant $R_+ = 0.05$ and $e = 2.3$. As expected, the perturbative analysis matches the exact results only for small R_+ and small ϵ (*i.e.* close to the origin and in the neighbourhood of the merger, yellow diamond, line which has $\epsilon = 0$). That is to say, for the $R_+ = 0.05$ family shown, good agreement occurs for small $\mathcal{Q}$, say $\mathcal{Q} \lesssim 0.2$.

Ultimately as a consequence of these two properties, two important changes occur in the phase diagram of Fig. 4.7 as we follow its evolution across $e_{\rm S}$ and land on Fig. 4.10. First, the minimal charge for instability − that we have been denoting as $\mathcal{Q}_P$ − approaches zero as $e \to e_{\rm S}^-$ and $\mathcal{Q}_P = 0$ for $e \geqslant e_{\rm S}$. This is illustrated in Fig. 4.10 for the case $e = 2.3$. Second, we find that the hairy BHs (blue circles inside $O\alpha\beta$) now *always* terminate on top of the perturbative boson star (black line $O\beta$) as we move down, *e.g.* at constant $\mathcal{Q}$, from the onset curve $O\alpha$. That is to say, one also has $\mathcal{Q}_\star = 0$ for $e \geqslant e_{\rm S}$. As hairy BHs approach this perturbative soliton curve, the Kretschmann curvature at the horizon, the entropy and temperature have the same behaviour as the one observed in Fig. 4.4 for BHs terminating along $\star\beta$: $K|_{\mathcal{H}} \to \infty$, $S \to 0$ and $T \to \infty$.

Since for $e \geqslant e_{\rm S}$ the hairy BHs exist all the way down to $(\mathcal{Q}, \mathcal{M}) \to (0, 0)$ one might expect that their properties can be captured by a perturbative analysis (to higher orders) around Minkowski space with gauge field in a box. This is indeed the case and such analysis was performed in [246]. This is a double expansion perturbation theory with the expansion parameters being the horizon radius R_+ and the scalar amplitude ϵ. Of course, here one assumes that $R_+ \ll 1$ and $\epsilon \ll 1$ which translates into $\mathcal{Q} \ll 1$ and $\mathcal{M} \ll 1$. The analysis of [246] culminates with explicit expansions for the thermodynamic quantities of the hairy BHs, which are listed in (5.27) of

[246]. In particular, the expansion for the quasilocal mass and charge are:

$$\begin{aligned}\mathcal{M}/L =&\left[\frac{R_+}{4}\left(\frac{\pi^2}{e^2}+2\right)+\frac{R_+^2}{32e^4}\left(\pi^4\Big(8[\mathrm{Ci}(2\pi)-\gamma-\ln(2\pi)]+5\Big)+4\left(e^2+\pi^2\right)e^2\right)+\mathcal{O}(R_+^3)\right]\\&+\epsilon^2\left[\frac{1}{2}+\frac{R_+}{12\pi e^2}\left(9\pi^3\Big[\gamma-\mathrm{Ci}(2\pi)-2+\ln(2\pi)\Big]+\left(8\pi^2-3e^2\right)\Big[2\mathrm{Si}(2\pi)-\mathrm{Si}(4\pi)\Big]\right)\right.\\&\left.+\mathcal{O}(R_+^2)\right]+\epsilon^4\left[\frac{15\pi^2-6e^2+16\pi\big[\mathrm{Si}(4\pi)-2\mathrm{Si}(2\pi)\big]}{24\pi^2}+\mathcal{O}(R_+)\right]+\mathcal{O}(\epsilon^6),\end{aligned} \tag{4.20}$$

$$\begin{aligned}\mathcal{Q}/L =&\left[\frac{\pi R_+}{2e}+\frac{R_+^2}{8e^3}\left(\pi^3\Big(2[\mathrm{Ci}(2\pi)-\gamma-\ln(2\pi)]+1\Big)+2\pi e^2\right)+\mathcal{O}(R_+^3)\right]+\epsilon^2\left[\frac{e}{2\pi}\right.\\&\left.+\frac{R_+}{12\pi^2 e}\left(12\pi^3\Big(\gamma-\mathrm{Ci}(2\pi)+\ln(2\pi)-\frac{7}{4}\Big)+\left(8\pi^2-3e^2\right)\left[2\mathrm{Si}(2\pi)-\mathrm{Si}(4\pi)\right]\right)+\mathcal{O}(R_+^2)\right]\\&-\epsilon^4\left[\frac{e\left(\left(8\pi^2-e^2\right)\left(2\mathrm{Si}(2\pi)-\mathrm{Si}(4\pi)\right)+4\pi e^2-8\pi^3\right)}{8\pi^4}+\mathcal{O}(R_+)\right]+\mathcal{O}(\epsilon^6),\end{aligned} \tag{4.21}$$

where $\mathrm{Ci}(x)=-\int_x^\infty \frac{\cos z}{z}\mathrm{d}z$ and $\mathrm{Si}(x)=\int_0^x \frac{\sin z}{z}\mathrm{d}z$ are the cosine and sine integral functions, respectively, and $\gamma\sim 0.577216$ is Euler's constant. This perturbation scheme assumes that R_+ and ϵ do not have a hierarchy of scales. When $R_+=0$, (4.20)-(4.21) reduces to the soliton thermodynamics and, when $\epsilon=0$, (4.20)-(4.21) yields the expansion of the caged RN BH thermodynamics. In [246] it was argued that (4.20)-(4.21) should provide a good approximation (as monitored by the first law) for $\epsilon\lesssim 0.1, R_+\lesssim 0.1$. Now that we have the exact (numerical) results for the hairy BHs in all their domain of existence we can use (4.20)-(4.21) to further check our numerics while, simultaneously, testing the regime of validity of (4.20)-(4.21) . As an example of this exercise, in Fig. 4.11 we compare the perturbative prediction (4.20)-(4.21) − the green curve− to our exact numerical results (blue circles) for the 1-parameter family of hairy BHs with $R_+=0.05$ parametrised by ϵ (with $\epsilon=0$ at the merger with RN; the yellow curve). As expected, we observe good agreement for $\mathcal{Q}\lesssim 0.2$, say. Of course, the fact that the perturbative analysis does not differ much from the exact results for higher values of $\mathcal{Q}$ is to be seen as accidental; the perturbative is certainly not valid for such high charges.

As in the previous cases, we end our discussion of the $e\geqslant e_{\rm s}$ case with the plot of Fig. 4.12 of the entropy as a function of the charge and mass. The colour coding is the same as in previous cases so it suffices to emphasize that again the hairy BHs (blue circles) are the preferred phase in the microcanonical ensemble. Indeed, in the region between the onset yellow curve and the extremal RN dark red curve

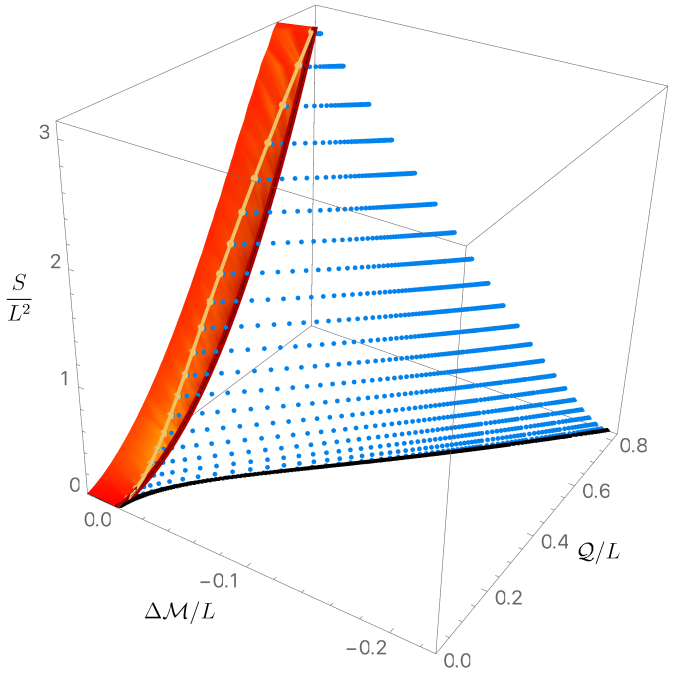

Fig. 4.12: Entropy as a function of the quasilocal charge and mass difference for Einstein theory with a scalar field charge $e = 2.3$ ($e > e_{\rm S}$) in a Minkowski box. When they coexist with RN BHs, for a given $(\mathcal{Q}, \mathcal{M})/L$, hairy BHs always have more entropy than RN, *i.e.* they dominate the microcanonical ensemble. For $e > e_{\rm S}$, the zero entropy limit of the hairy BH is the soliton (black disk curve) in the sense that they have the same $(\mathcal{Q}, \mathcal{M})/L$ as the soliton (the temperature and horizon curvature diverges).

with $\Delta\mathcal{M} = 0$ where they coexist with (unstable) RN BHs, hairy BHs always have higher dimensionless entropy for a given charge $\mathcal{Q}/L$ and mass $\mathcal{M}/L$. It further follows from the second law, that the unstable RN BHs should evolve in time towards the hairy BH we find with the same $\mathcal{Q}/L$ and $\mathcal{M}/L$.

4.4 Discussion and junction conditions

Recapping what we did so far, we integrated the equations of motion in the domain $R \in [R_+, 1]$ subject to regular boundary conditions at horizon and vanishing scalar field at the box. This is all we need to get the quasilocal phase diagrams of the previous section. But the description of the solution is only complete once we give the full solution all the way up to the asymptotically flat boundary.

Studies of scalar fields confined in a Minkowski cavity are already available in the literature: 1) at the linear level [269–279], 2) within a higher order perturbative analysis of the elliptic problem [245, 246], 3) as a nonlinear elliptic problem (without

having asymptotically flat boundary conditions [280–282] or without matching with the exterior solution [283]), and 4) as an initial-value problem [265–267]. However, with the exception of the perturbative analysis of [246], the properties of the "internal structure" of the cavity required to confine the scalar field and its contribution to the ADM mass and charge that ultimately describe, by Birkhoff's theorem, the exterior RN solution are not discussed.

However, having the interior solution, we can compute the Lanczos-Darmois-Israel surface stress tensor (4.15) that describes the energy-momentum of the box Σ. We impose the three Israel junction conditions (4.14a)-(4.14c) on the gravito-electric fields on the surface layer Σ. The fields f, A_t, ϕ are then continuous across Σ and the component of the electric field orthogonal to Σ is also C^0 across Σ. The latter means that we can confine the charged scalar condensate without needing to have a surface electric charge density on Σ. The three conditions (4.14a)-(4.14c) permit us to match the interior and exterior solutions, *i.e.* they fix the parameters M_0, c_A, ρ in (4.5) as a function of the reparametrisation freedom parameter N introduced in (4.13):

$$M_0 = \frac{1}{N^2}\left(1 - \frac{A_t'(1)^2}{2}\right) - 1, \qquad c_A = \frac{A_t'(1) + A_1(1)}{N}\,, \qquad \rho = -\frac{A_t'(1)}{N}\,. \tag{4.22}$$

Effectively, these conditions fix the exterior RN solution as a function of the interior solution and of the box's energy-momentum. Not surprisingly, we have a 1-parameter freedom (N) to choose the box content that is able to confine the scalar condensate. Several cavities can do the job.

Ideally, we would fix N requiring that the gravitational field is not only C^0 but also differentiable across the box. That is, the fourth junction condition (4.14d) would also be obeyed and thus the extrinsic curvature

$$K^t{}_t = -\frac{f'(R)}{2f(R)\sqrt{g(R)}}\,, \qquad K^i{}_j = \frac{1}{R\sqrt{g}}\,\delta^i{}_j\,, \quad (i,j) = (\theta,\varphi), \tag{4.23}$$

would also be continuous across the box. But, except when $\phi(R) = 0$, no choice of N allows us to simultaneously set $[K^t_t] = 0$ and $[K^i_i] = 0$. All we can do is to fix N requiring that $[K^t_t] = 0$ (at the expense of having $[K^i_i] \neq 0$) or vice-versa, or any other combination.

A choice of N fixes the energy density and pressure of the box since its stress tensor can be written in the perfect fluid form, $\mathcal{S}_{(a)(b)} = \mathcal{E} u_{(a)} u_{(b)} + \mathcal{P}(h_{(a)(b)} + u_{(a)} u_{(b)})$,

with $u = f^{-1/2}\partial_t$ and local energy density $\mathcal{E}$ and pressure $\mathcal{P}$ given by

$$\mathcal{E} = -S^t{}_t\,, \qquad \mathcal{P} = S^x{}_x = S^\phi{}_\phi\,. \tag{4.24}$$

We are further constrained to make a choice such that relevant energy conditions are obeyed. Ultimately, failing these would mean that we cannot build the necessary box with the available materials. Different versions of these energy conditions read $(i = \theta, \varphi)$ [241]:

$$\text{Weak energy condition:} \qquad \mathcal{E} \geqslant 0 \quad \wedge \quad \mathcal{E} + \mathcal{P}_i \geqslant 0\,; \tag{4.25}$$

$$\text{Strong energy condition:} \qquad \mathcal{E} + \mathcal{P}_i \geqslant 0 \quad \wedge \quad \mathcal{E} + \sum_{i=1}^{2} \mathcal{P}_i \geqslant 0\,; \tag{4.26}$$

$$\text{Null energy condition:} \qquad \mathcal{E} + \mathcal{P}_i \geqslant 0\,; \tag{4.27}$$

$$\text{Dominant energy condition:} \qquad \mathcal{E} + |\mathcal{P}_i| \geqslant 0\,. \tag{4.28}$$

We have experimented with different choices of N and found that are many selections that indeed satisfy (4.25) (and equally many others that don't). An example of this exercise is given in [248] for the boson star case. Given that there seems to be no preferred choice, we do not do a further aleatory illustration here. Instead, we approach the problem from an experimental perspective. That is to say, in practice, we are given a cavity (that obeys the energy conditions or else it could not have been built with available materials). In principle, we can identify its stress tensor and hence compute N. We then insert this into the Israel matching conditions (4.22) to find the exact RN exterior solution and, in particular, the asymptotic ADM charges. We end up with an asymptotically flat static black hole solution (or boson star [248]) that is regular everywhere except across the box (where the extrinsic curvature has a discontinuity) and that describes confined scalar radiation floating above the horizon and in thermodynamic equilibrium with it.

Chapter 5

Conclusion and outlook

In Reissner-Nordström, it is well known that there are two families of quasinormal mode — photon sphere (PS) and near-horizon (NH) modes. They can be unambiguously distinguished by following the eigenvalues to the near-extremal limit where they agree with either a WKB expansion or a matched asymptotic expansion. In Chapter 2 we found the full scalar field QNM spectra of Kerr-Newman black holes, focusing on perturbations with angular quantum numbers $m = \ell = 2$. We found that, surprisingly, it is no longer possible to uniquely classify the PS and NH modes away from the RN limit, as they strongly interact via eigenvalue repulsions. This phenomenon is very sensitive to the black hole parameters, meaning that the QNM spectra of Kerr-Newman is much more complicated than RN or Kerr, despite being composed of the same mode families.

By the time we have marched all the way to the Kerr limit, it is better to think of the modes as entangled PS-NH modes, since they are well-described by both approximations. However, if we trace the modes in Kerr back to the RN limit, we see that the original RN PS mode is nestled in between the NH modes. It remains an open question as to whether this mode has vanishing imaginary part in the extremal limit (like the other NH modes) or tends to a non-zero limit. Ultimately, this will likely only be resolved by an explicit computation of the QNM spectra of extremal Kerr(-Newman).

In Chapter 3, we studied the scalar QNM spectra of asymptotically de Sitter black holes in higher dimensions. In the simplest example, Schwarzschild-de Sitter, we observe that the de Sitter modes have highly non-trivial behaviour in higher dimensions, especially in $d = 5$. Beyond that, we find the QNM spectrum of cohomogeneity-one Myers-Perry de Sitter. Much like Kerr (and Kerr-dS), the PS

modes are merged with the NH modes (except for one PS mode overtone that is subdominant near extremality). The PS modes with large $m = \ell$ dominate the spectrum, enforcing strong cosmic censorship (SCC) in $d = 5, 7, 9, 11$, and likely all odd dimensions.

One of the broad conclusions of Chapter 3 is that the SCC behaviours of Kerr-dS and RNdS are not unique to those spacetimes, but are more likely general features of charged and rotating black holes in any dimension. Astrophysical black holes are expected to have negligible charge [19–21], and thus one could argue that weakly-charged Kerr-Newman-de Sitter (KNdS) is a more realistic form of initial data than RNdS. There is evidence to suggest that initial data close to KNdS does violate SCC, at least for some parts of the parameter space [284]. One would expect a type of phase transition in the (a, Q) parameter space between the two regimes, and this may yield insights about what kind of fields and initial data we should consider to rescue SCC. In future work, we try to find this transition boundary explicitly [46].

Nevertheless, any violation of SCC with well-behaved initial data such as RNdS or slowly-rotating KNdS is cause for concern. This prompts the question of whether the Christodoulou formulation is in fact the most appropriate formulation of strong cosmic censorship. In all of our SCC discussions we assumed smooth initial data. But given that we allow non-smooth solutions of the Einstein equations, it seems reasonable to also allow non-smooth initial data. This "rough formulation" of strong cosmic censorship is respected in RNdS (and BTZ), since the solution at the Cauchy horizon is, generically, rougher than the initial data [47, 285] (also see the discussion in [89]).

General Relativity is an effective field theory, so perhaps it is too much to require predictability beyond the Cauchy horizons — it's still unclear how much of the black hole interior we should take seriously. However, the theory of quantum gravity that replaces it *must* be predictable. As a stepping stone, we can consider semi-classical corrections. These indeed appear to rescue SCC in RNdS, since the semi-classical stress tensor diverges at the Cauchy horizon [89, 286–288].

The BTZ black hole severely violates SCC [47], and this is expected to be a rather special result, as discussed in Section 1.3. Further corroborating this is the fact that the semi-classical result above does not save SCC in the case of BTZ [286]. However, a braneworld construction of a BTZ black hole that incorporates the exact quantum backreaction was found in [289, 290]. Since the classical bulk of this

construction is similar to Kerr-AdS$_4$, it is argued that the next-to-leading order backreaction will enforce SCC in BTZ.

The classical violation of SCC in BTZ only occurs for sufficiently extremal BTZ black holes, so one would expect to see some parameter-dependent signature of the change in regularity of the bulk field to be reflected in the boundary theory, for example in the two-point function. There are a number of studies in this direction which try to probe the Cauchy horizon holographically [291, 292]. The two-point function used for the rotating BTZ black hole has been computed in Euclidean signature, and does not appear to have any pathological behaviour. However, it seems likely one would instead need to use the real-time formalism [293, 294] to probe the Lorentzian bulk behind the event horizon. This formalism has so far only been applied to static BTZ black holes.

In Chapter 4 we found the phase diagram of static solutions of the Einstein-Maxwell-Scalar system, confined to a cavity that forces the scalar field to vanish at and outside a shell of fixed radius. In addition to RN black holes, we also found hairy black holes, with scalar hair floating above the horizon. Furthermore, we found that the stress energy tensor of the shell that is required by the Israel junction conditions can be made to obey appropriate energy conditions.

In other words, we have established that the configuration originally envisioned (in the rotating case) by Zel'dovich [138], Press-Teukolsky [137] and [250–255] using linear considerations indeed exists as a non-linear equilibrium solution of the Einstein-Maxwell-Scalar equations. We further established that this is the thermal phase that dominates the microcanonical ensemble. It should be possible to extend the current analysis to the rotating BH bomb system.

The hairy BHs we find are stable to the RN instabilities (since they merge with RN precisely at the onset of the original instability; see also [280, 281]) and have higher entropy than the RN BHs. It follows from this and the second law of thermodynamics that the charged black hole bomb does not need to break apart: in a time evolution at fixed energy and charge, the unstable RN BH should simply evolve towards the hairy BH we find. It would be interesting to confirm this, performing a time evolution along the lines of those performed in [265–267], in the precise setup we described.

No less interestingly, Minkowski space in a box (*i.e.* no horizon) with a scalar perturbation is itself non-linearly unstable to the formation of a BH for arbitrarily small amplitudes [295], very much alike pure global AdS [296–302, 232]. The

weakly turbulent phenomenon is responsible for this instability [296–300, 303–305]. It would be interesting to study this non-linear instability when the scalar field is charged. Unlike the neutral case, for certain windows of charge and energy, there are now two possible families of BHs and not just the RN one. Therefore a time evolution of the non-linear instability along the lines of [298, 301, 302, 295, 306–309, 232] should lead in some cases to gravitational collapse into an RN BH and into a hairy BH in other cases. There will also be a wide range of cases in which no black hole forms at all.

Appendix A

Near-horizon geometry of Kerr-Newman

In Chapter 2 we studied the scalar QNM spectra of the $\ell = m = 2$ and $\ell = m = 0$ modes of Kerr-Newman. These are representative elements of the two distinct classes or sectors of QNM that KN can have. As discussed in [57–59], these two classes of QNM can be (within a very good approximation) identified analysing the sign of the quantity δ^2 − defined in (2.39) − that appears naturally in the near-horizon analysis of modes. Concretely, for the QNM sector with $\delta^2 < 0$ (e.g. the $\ell = m = 0$ modes), the QNM spectra has two independent and clearly distinct families of modes − PS and NH modes − in the entire parameter space of KN. On the other hand, the QNM sector with $\delta^2 > 0$ (e.g. the $\ell = m = 2$ modes) is such that sufficiently close to extremality and for high Θ one can state that there is a single PS-NH family of QNMs and its overtones (although for small Θ one might still say that the PS and NH families are present and clearly distinguishable). Thus, the condition $\delta^2(m, \ell, \Theta) = 0$, which depends on $\{m, \ell, \Theta\}$, provides a good approximation for the boundary that separates the two QNM sectors. In certain points of Chapter 2, we used the equivalent notion of a critical value $\Theta_c(m, \ell)$ at which $\delta^2 = 0$. Furthermore, in the literature other critical quantities such as μ_c, $\mathcal{F}_0$ and $\mathcal{J}$ (all defined later) are used to describe this boundary [57, 58, 310, 311, 59]. In this appendix, we attempt to clarify the relationship between the plethora of critical quantities, and provide a complementary first-principles identification of this boundary in terms of the effective AdS_2 Breitenlöhner-Freedman (BF) bound [197, 198] on the near-horizon extremal Kerr-Newman (NHEKN) geometry. The analysis presented here is quite similar to that of Myers-Perry-de Sitter in

Chapter 3. This section is self-contained, but see Section 3.2.3 for further details and motivation of the near-horizon geometry.

To find the near-horizon geometry, we take the Kerr-Newman metric (2.1) at extremality, and zoom into the horizon by first making the coordinate and gauge transformations

$$\begin{aligned} &r \to r_+ + (r_+^2 + a^2)\epsilon\,\rho, \qquad t \to \frac{\tau}{\epsilon}, \qquad \phi \to \psi + \Omega_H^{\text{ext}}\frac{\tau}{\epsilon}, \\ &A \to \mathcal{A} + \frac{r_+ Q}{r_+^2 + a^2}\frac{d\tau}{\epsilon}, \end{aligned} \tag{A.1}$$

where $\Omega_H^{\text{ext}} = \frac{a}{r_+^2+a^2}\Big|_{\text{ext}}$. The near-horizon limit is then given by the limit $\epsilon \to 0$. The ϕ-transformation ensures that the coordinates $(\tau, \rho, \theta, \psi)$ co-rotate with the horizon, and the gauge transformation of A is required for the near-horizon limit to yield a finite gauge field. Using the fact that at extremality Δ has a double root, $\Delta|_{r_+} \sim (r - r_+)^2$, the resulting near-horizon (NHEKN) geometry is

$$\begin{aligned} ds^2 &= \Sigma(r_+,\theta)\left(-\rho^2 d\tau^2 + \frac{d\rho^2}{\rho^2}\right) + \frac{(r_+^2+a^2)^2\sin(\theta)^2}{\Sigma(r_+,\theta)}\left(d\psi + 2r_+\Omega_H\rho d\tau\right)^2 + \Sigma(r_+,\theta)d\theta^2, \\ \mathcal{A} &= Q\left[\rho d\tau - \frac{r_+}{\Sigma(r_+,\theta)}\left(2r_+\rho d\tau + a\sin^2\theta d\psi\right)\right], \end{aligned} \tag{A.2}$$

where $\Sigma(r_+,\theta) \equiv r_+^2 + a^2\cos^2\theta$. This is still a solution of 4-dimensional Einstein-Maxwell theory (with zero cosmological constant). The $\tau - \rho$ part of this metric describes the 2-dimensional anti-de Sitter (AdS_2) spacetime, a solution of the vacuum Einstein equations with a negative cosmological constant, with Ricci scalar $R_{(2)} = -2/\Sigma(r_+,\theta)$, and hence AdS_2 radius $L^2_{\text{AdS}} = \Sigma(r_+,\theta)$. The geometry is much like $\text{AdS}_2 \times S^2$, being exactly $\text{AdS}_2 \times S^2$ in the RN limit $a = 0$, or e.g. when $\theta = 0$ or $\theta = \pi$. The isometry group $SL(2,R) \times U(1)$ of this near-horizon or *throat* geometry was first described in [312], and has been studied extensively in the context of the *Kerr/CFT correspondence* [313], which has since been extended to include Kerr-Newman. See [314] for a review of NHEKN and its CFT interpretation.

We now want to find the Klein-Gordon equation on NHEKN. This can be done in two equivalent ways, either by directly computing the Klein-Gordon equation on the near-horizon geometry (A.2), or by taking the near-horizon limits (A.1) of the Klein-Gordon equation (2.8a)-(2.8b) on the full KN geometry. We take the latter approach. First, note that in order to preserve the form of the Fourier ansatz $e^{-i\omega t + im\phi}$, all finite frequencies must approach the superradiant frequency in the near-horizon limit, $\omega \to m\Omega_H + \epsilon\,\hat{\omega}$. Applying this, and the near-horizon

transformations (A.1) to (2.8a)-(2.8b), we get the radial and angular ODEs for the Klein-Gordon equation on NHEKN,

$$\frac{d}{d\rho}\left(\rho^2\frac{dR}{d\rho}\right)+\left[(2r_+^2+a^2)m^2\Omega_H^2+\frac{1}{\rho^2}\left(\hat{\omega}+2mr_+\rho\,\Omega_H\right)^2-\lambda\right]R(\rho)=0, \quad \text{(A.3a)}$$

$$\frac{d}{dx}\left((1-x^2)\frac{dS}{dx}\right)+\left[\frac{m^2}{x^2-1}+\left(a\,m\,\Omega_H\,x\right)^2+\lambda\right]S(x)=0, \quad \text{(A.3b)}$$

where recall that $x=\cos\theta$ and λ is the separation constant of the problem. Note that the angular equation (A.3b) is still the oblate spheroidal harmonic equation, but it does not contain the eigenfrequency $\hat{\omega}$ since in the near-horizon limit (and at leading order) the original frequency ω has been replaced by the superradiant frequency $\omega\to m\Omega_H$. In the limits $m=0$ or $a=0$ the angular component of the Klein-Gordon equation can be solved exactly, since the eigenvalues are simply those of the spherical harmonics $\lambda=\ell(\ell+1)$, but otherwise we can solve the NHEKN angular equation (A.3b) numerically, using the same redefinition (2.11) as the angular equation (2.8b) on the full KN geometry.

What is the interpretation of the radial part (A.3a) of the NHEKN Klein-Gordon equation? Using the standard Fourier decomposition $\Phi=e^{-i\hat{\omega}\tau+im\psi}R(\rho)$, we can rewrite the near-horizon radial equation (A.3a) as a Klein-Gordon equation for a massive charged scalar field on AdS_2,

$$\left(\hat{\nabla}-iq_{\text{eff}}A_{\text{eff}}\right)^2\Phi=L_{\text{AdS}}^{-2}\left[\lambda-m^2(a^2+2r_+^2)\Omega_H^2\right]\Phi, \qquad q_{\text{eff}}\equiv-2mr_+\Omega_H \quad \text{(A.4)}$$

where $\hat{\nabla}-iq_{\text{eff}}A_{\text{eff}}$ is the gauge covariant derivative of pure AdS_2 with a homogeneous electric field:

$$ds^2_{\text{AdS}_2}=L^2_{\text{AdS}}\left(-\rho^2d\tau^2+\frac{d\rho^2}{\rho^2}\right), \qquad A_{\text{eff}}=-\rho\,d\tau. \quad \text{(A.5)}$$

In other words, starting with a massless and uncharged scalar field and taking the near-horizon limit (A.1), the scalar field acquires an effective mass and charge from the perspective of the near-horizon geometry, where the charge arises as a consequence of the horizon rotation Ω_H.

In pure AdS_2, it is well known that massive scalar field perturbations are normalisable even if their squared mass ξ^2 is negative, provided it is above the Breitenlöhner-Freedman (BF) bound: $\xi^2L^2_{\text{AdS}}\geqslant-\frac{1}{4}$ [197, 198]. On the other hand, if the mass is below the BF bound, the scalar field perturbation is not stable. A similar argument applies to the NHEKN geometry. The asymptotic behaviour of a

solution of the near-horizon radial equation (A.3a) is $R|_{\rho\to\infty} \sim \rho^{\Delta_\pm}$, where $\Delta_\pm$ are the 2-dimensional conformal scaling dimensions

$$\Delta_\pm = \frac{1}{2}\left(-1 \pm \sqrt{1+4\xi_{\text{eff}}^2 L_{\text{AdS}}^2}\right), \qquad \xi_{\text{eff}}^2 L_{\text{AdS}}^2 \equiv \lambda - (6r_+^2 + a^2)m^2\Omega_H^2 \tag{A.6}$$

$$= \lambda - m^2 \frac{\sin^2\Theta\left(6+\sin^2\Theta\right)}{\left(1+\sin^2\Theta\right)^2}. \tag{A.7}$$

These solutions do not oscillate at large ρ (i.e. they are normalisable, with finite energy) provided that

$$\xi_{\text{eff}}^2 L_{\text{AdS}}^2 \geqslant -\frac{1}{4}. \tag{A.8}$$

This defines the effective BF bound for NHEKN[1]. Note that while the effective AdS_2 length scale L_{AdS} is a function of θ (and consequently so is the mass ξ_{eff}), the physically relevant quantity is the dimensionless mass $\xi_{\text{eff}} L_{\text{AdS}}$ which is independent of θ.

The quantity $\delta^2 = (6r_+^2 + a^2)m^2\Omega_H^2 - \frac{1}{4} - \lambda$ was defined in (2.39) in the context of the matched asymptotic expansion of the NH modes $\tilde{\omega}_{\text{MAE}}$ of (2.54). As discussed at the end of section 2.2.2, the sign of δ^2 indicates two distinct types of behaviour of the matched asymptotic expansion of the NH modes, since it determines whether δ gives a real or imaginary contribution to $\tilde{\omega}_{\text{MAE}}$. By studying the numerical QNM spectrum, it has also been observed that the sign of δ^2 approximately corresponds to the phase boundary of the families of QNMs (*i.e.* whether there are one or two distinct families): see [57–59] and the discussion in section 2.4.1.

Complementing the analysis of [57–59] we add that from the perspective of the NHEKN geometry, we see that δ^2 is related to the effective near-horizon mass by

$$1 + 4\xi_{\text{eff}}^2 L_{\text{AdS}}^2 = -4\delta^2. \tag{A.9}$$

Therefore, we conclude that the sign of δ^2 effectively indicates whether the effective AdS_2 BF bound of the near-horizon geometry is violated or not. Namely, one has $\delta^2 \leqslant 0$ when the BF bound (A.8) is respected and $\delta^2 > 0$ when the BF bound is violated. In the RN limit ($\Theta = 0$), the BF bound is always respected. However, as we move to the Kerr limit ($\Theta = \pi/2$), perturbations with certain combinations of the angular quantum numbers $\{m, \ell\}$ violate the BF bound. Concretely, in

[1]Note that an instability of the near-horizon geometry does not *necessarily* imply an instability of the full extremal KN geometry, see Section 3.2.3 and [144, 225] for a detailed discussion about this point regarding Kerr.

	azimuthal number m								
ℓ	2	3	4	5	6	7	8	9	10
2	0.88								
3	-	0.71							
4	-	-	0.66						
5	-	-	-	0.62					
6	-	-	-	1.00	0.60				
7	-	-	-	-	0.88	0.59			
8	-	-	-	-	-	0.80	0.59		
9	-	-	-	-	-	-	0.75	0.58	
10	-	-	-	-	-	-	1.10	0.71	0.57

TABLE A.1: The critical value $\Theta_\star$ of $\Theta = \arctan(a/Q)$ above which the effective AdS_2 BF bound (A.8) in KN is violated, for a range of values of the angular quantum numbers $\{m, \ell\}$. Dashed entries indicate that the BF bound is respected for all Θ. Perturbations with $\ell < 2$ respect the BF bound for all Θ and so are not displayed.

Table A.1 we display the critical value $\Theta_\star$ of $\Theta = \arctan(a/Q)$ above which the BF bound (A.8) is violated (and thus $\delta^2 > 0$), while the values of $\{m, \ell\}$ which always respect the BF bound, for all Θ, are indicated by a dash. In the former case, there are two families of QNMs (the NH and PS modes) for $0 \leqslant \Theta < \Theta_\star$ and a single 'NH-PS' family for $\Theta_\star < \Theta \leqslant \pi/2$, while in the latter case there are two clearly distinct families of PS and NH modes for any Θ. For example, the $m = \ell = 2$ entry is $\Theta_\star \sim 0.881$ as discussed in section 2.2.2: for $0 \leqslant \Theta < 0.881$ there are two distinct families (PS and NH) of QNMs but for $0.881 < \Theta \leqslant \pi/2$ there is a single 'NH-PS' family (and its overtones). Our results are consistent with previous discussions in the Kerr limit; e.g. compare our Table A.1 with Fig. 1 in [57], which computed the phase boundary in Kerr numerically, by searching the QNM spectrum for each pair of quantum numbers $\{m, \ell\}$.

In Kerr, at extremality, one can transform the radial part of the Klein-Gordon equation to a Schrödinger-type equation with a real potential (under the assumption that the frequencies approach the superradiant bound $\omega \to m\Omega_H$), and determine the location of the peak of the effective potential [57]. A critical quantity $\mathcal{F}_0$ was defined such that the effective potential has a peak outside the horizon when $\mathcal{F}_0^2 > 0$. $\mathcal{F}_0^2$ differs from the Kerr limit of δ^2 by 1/4. In [59] it was argued that the generalisation of $\mathcal{F}_0$ to Kerr-Newman is a quantity $\mathcal{J}^2$, which again differs from δ^2 by a quarter

$$\mathcal{J}^2 = \delta^2 + 1/4. \tag{A.10}$$

By comparison with (A.9) we see that $\mathcal{J}$ is essentially the near-horizon effective mass, $\mathcal{J}^2 = -\xi^2_{\text{eff}} L^2_{\text{AdS}}$. Hence the criteria $\mathcal{J}^2 = 0$ is the point at which the near-horizon mass ξ_{eff} vanishes, while the condition $\delta^2 = 0$ is when the effective mass ξ^2_{eff} decreases even further and violates the BF bound. Thus our BF bound analysis explains the physical relevance of the two quantities δ^2 and $\mathcal{J}^2$ introduced in [57–59] and why they differ by 1/4.

In the eikonal limit, we can parameterize the phase boundary or separatrix curve between the two QNM behaviours by just two parameters $\{\mu, \Theta\}$, where $\mu \equiv \frac{m}{\ell+1/2}$ is called the *inclination parameter* [57–59]. By considering the location of the peak of the WKB potential[2] in the eikonal limit $(\ell + \frac{1}{2}) \gg 1$, a criterion for a peak to exist outside the event horizon was given in [59] (see also [310, 311]):

$$\mu^2 \leqslant \mu_c^2, \qquad \mu_c^2 \equiv \frac{1}{2}\left(3 + \frac{12 - \sqrt{136 + 56(a/M)^2 + (a/M)^4}}{(a/M)^2}\right), \tag{A.11}$$

and it was also shown that the exact numerical phase boundary is well-described by $\mu = \mu_c$. The inclination parameter μ is bounded by $0 \leqslant \mu^2 \leqslant 1$. Setting $\mu_c = 1$, corresponding to equatorial modes $|m| = \ell$, in the eikonal prediction (A.11) yields the criteria that $a/M = 1/2$, or $\Theta = \pi/6$. As expected, this is the eikonal $(m = \ell)$ critical value $\Theta^{\text{eik}}_\star = \pi/6$ at which the PS modes have vanishing imaginary part in the extremal limit, as discussed in section 2.3.1. The criteria $\mu^2 \leqslant \mu_c^2$ that one gets from considering the location of the peak of the WKB potential can also be found by taking the eikonal limit of the BF bound criteria (A.8) in the eikonal limit, as we now show. In [59, 69], in addition to the eikonal approximation $(\ell + \frac{1}{2}) \gg 1$, a further approximation was made for the angular eigenvalues of (A.3b):

$$\lambda \sim \left(\ell + \frac{1}{2}\right)^2 + \frac{1}{2}\left[-1 + \frac{m^2}{(\ell + 1/2)^2}\right] m^2 a^2 \Omega_H^2. \tag{A.12}$$

Inserting this into the BF bound criteria (A.8), and solving for μ, we find that the leading-order eikonal condition for the BF bound to be respected is equivalent to the eikonal condition (A.11) above. The criteria for the vanishing of the near-horizon mass $\xi^2_{\text{eff}} L^2_{\text{AdS}}$ (or equivalently the vanishing of $\mathcal{J}^2$) also yields the same μ_c (A.11) in the eikonal limit, since the factor of $\frac{1}{4}$ is sub-leading.

Strictly speaking, the eikonal condition $\mu^2 \leqslant \mu_c^2$ in (A.11) is only valid in the eikonal limit $(\ell + \frac{1}{2}) \gg 1$, whereas the BF bound criteria (A.8) has no such restriction (both

[2] Note that this is different to the WKB expansion derived in section 2.2.1.2, as we allow the possibility that $m \neq \ell$ here.

are derived in the near-extremal limit). However, in practice the two criteria are in very close agreement even for small ℓ. For example, even as low as $m = \ell = 2$, the eikonal prediction is $\Theta|_{\mu=\mu_c} = 0.876$ for the $m = l = 2$ modes, versus $\Theta_\star = 0.881$ for the BF bound criteria — see Table A.1. Given that these are both only considered to be approximate criteria we use them interchangeably in Chapter 2.

The computation of the near-horizon geometry in this appendix generalises naturally to other spacetimes, even those which are not asymptotically flat. For example, in Chapter 3, a violation of the near-horizon BF bound was found to a necessary (but not sufficient) condition for strong cosmic censorship to be respected in Myers-Perry de Sitter, and this is intimately related to the fact that for sufficiently large $|m| = \ell$ there is only a single family of modes (just like in Kerr and KN).

Appendix B

Near-horizon QNMs of MPdS: explicit expressions

In Section 3.2.3.3 we employed a matched asymptotic expansion procedure to find an analytic expression for the frequencies $\omega_{\rm NH}$ of the near-horizon (NH) modes which very well approximate the associated numerical frequencies of the system near-extremality. This $\omega_{\rm NH}$ is given by (3.54)-(3.55) and in this appendix we provide the explicit expression for the quantities $\Omega_{(1)}$ and $\kappa_{(1)}$ that appear in (3.55). Note that, for all N, we can express the black hole parameters (a, M, L) in terms of the dimensionless horizon radii $(y_+,\, y_-)$ by

$$\begin{aligned}
\frac{a^2}{r_c^2} &= \frac{y_-^2 y_+^2}{(1-y_-^2)(1-y_+^2)(1-y_-^{2N+2})(1-y_+^{2N+2})(y_+^2-y_-^2)(y_+^{2N+2}-y_-^{2N+2})} \\
&\quad\times\Big\{(1-y_+^2)((y_-^{4N+4}+1)y_+^{2N}(y_+^2-y_-^2)-(1-y_-^2)(y_-^{4N+4}+y_+^{4N+4})) \\
&\qquad + y_-^{2N}(-y_-^4(y_+^{2N+2}+1)^2+2y_-^4(y_+^4+1)y_+^{2N}+(1-y_+^{2N+2})^2(y_-^2-(1-y_-^2)y_+^2))\Big\}, \\
\frac{M}{r_c^{2N}} &= \frac{(1-y_-^2)(1-y_+^2)(y_+^2-y_-^2)(1-y_-^{2N+2})(1-y_+^{2N+2})(y_+^{2N+2}-y_-^{2N+2})}{2(y_+^2-y_-^2-(1-y_-^2)y_+^{2N+4}+(1-y_+^2)y_-^{2N+4})^2}, \\
\frac{L^2}{r_c^2} &= \frac{y_-^2-y_+^2+(1-y_-^2)y_+^{2N+4}-(1-y_+^2)y_-^{2N+4}}{y_-^2-y_+^2+(1-y_-^2)y_+^{2N+2}-(1-y_+^2)y_-^{2N+2}}.
\end{aligned} \tag{B.1}$$

The near-horizon modes, as previously derived in Section 3.2.3.3 and written in (3.54), can be written for all N as

$$\omega_{\rm NH} = m\,\Omega(r_+)|_{\rm ext} + \left\{m\Omega_{(1)} - \frac{i}{2}\left(1+2n+2iq_{\rm AdS}+\sqrt{1+4{\mu_{\rm eff}}^2{L_{\rm AdS}}^2}\right)\kappa_{(1)}\right\}\sigma, \tag{B.2}$$

where $q_{\rm AdS}$, $\mu_{\rm eff}$ and $L_{\rm AdS}$ are given by (3.40)-(3.42). The terms $\Omega_{(1)}$ and $\kappa_{(1)}$ are the first-order coefficients of the Taylor expansions of $\Omega(r_+)$ and κ_+ in the near-extremal parameter $\sigma = 1 - y_-/y_+$, as previously defined in (3.43). Explicitly, these are given by

$$\kappa_{(1)} \equiv \left.\frac{d\kappa_+}{d\sigma}\right|_{\sigma=0} = \frac{1}{r_c y_+} \frac{\sqrt{1+N}(2y_+^2(-1+y_+^{2N}) - N(-1+y_+^2)(1+y_+^{2+2N}))}{\sqrt{(1-y_+^2)(1-y_+^{2+2N})}\sqrt{1+y_+^{2+2N}(-2+y_+^2+N(-1+y_+^2))}}, \tag{B.3}$$

$$\begin{aligned}\Omega_{(1)} \equiv \left.\frac{d\Omega(r_+)}{d\sigma}\right|_{\sigma=0} &= \frac{1}{r_c}\frac{2y_+^2(1-y_+^{2N}) - N(1-y_+^2)(1+y_+^{2+2N})}{2y_+(1-y_+^2)(1-y_+^{2+2N})} \\ &\times \frac{1+y_+^{4+4N}(3+2N-2(1+N)y_+^2) - y_+^{2+2N}(3-(N-(1+N)y_+^2)^2)}{(1-y_+^{2+2N}(2+N-(1+N)y_+^2))^{3/2}\sqrt{(1+N)(N(1-y_+^2)-y_+^2(1-y_+^{2N}))}},\end{aligned} \tag{B.4}$$

and $\Omega(r_+)$ at extremality is given by

$$\Omega(r_+)|_{\rm ext} = \frac{1}{r_c y_+}\sqrt{\frac{N(1-y_+^2)-y_+^2(1-y_+^{2N})}{(1+N)(1+y_+^{2+2N}(-2+y_+^2+N(-1+y_+^2)))}}. \tag{B.5}$$

Appendix C

Numerical convergence tests for MPdS

We use pseudospectral collocation methods to generate our numerical data, and thus our numerical results should (and do) have exponential convergence as the number of points used to discretise the numerical grid increases (see e.g [166]). All of our numerical results have converged with an error that is not higher than 10^{-8}. To illustrate our numerical error analysis, a convergence test is given in Fig. C.1 for $d = 5$ MPdS at $r_- = 0.9995\, r_+$, with $m = l = 10$. To test convergence, we recompute these modes with increasing grid resolution and precision (increasing the precision proportionally to the resolution), up to (resolution, precision) =

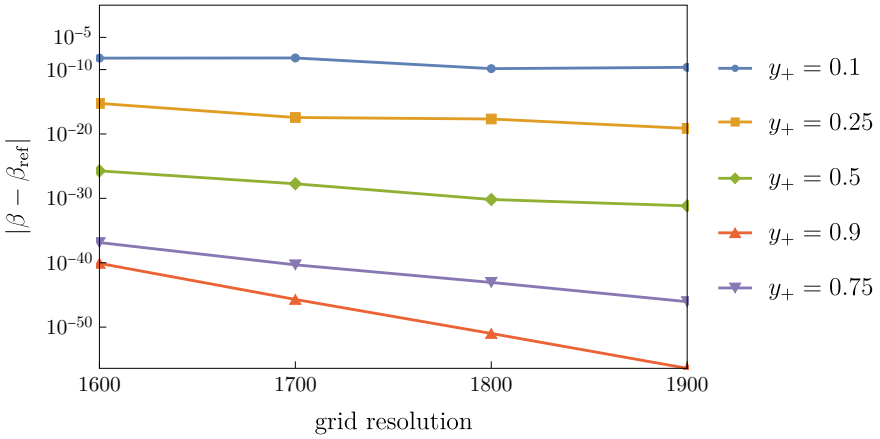

Fig. C.1: Convergence of β for $d = 5$ MPdS with $m = l = 10$ and $r_- = 0.9995\, r_+$, as displayed in Fig. 3.10. These modes were computed at (resolution, precision) = $(1600, 500)$. The precision is scaled linearly with the grid resolution, *i.e.* a maximum (resolution, precision) = $(2000, 625)$ which is used to compute the reference value β_{ref}.

$(2000, 625)$. This maximum value is used to compute β_{ref}. The maximum error $|\beta - \beta_{\text{ref}}|$ is $\sim 10^{-8.2}$, as expected.

References

[1] A. Davey, O. J. C. Dias and P. Rodgers, *Phase diagram of the charged black hole bomb system*, *Journal of High Energy Physics* **2021** (May, 2021) 189, [2103.12752].

[2] A. Davey, O. J. C. Dias, P. Rodgers and J. E. Santos, *Strong Cosmic Censorship and Eigenvalue Repulsions for rotating de Sitter black holes in higher-dimensions*, *Journal of High Energy Physics* **2022** (July, 2022) 86, [2203.13830].

[3] A. Davey, O. J. C. Dias and J. E. Santos, *Scalar QNM spectra of Kerr and Reissner-Nordström revealed by eigenvalue repulsions in Kerr-Newman*, *(submitted to JHEP)* (May, 2023) , [2305.11216].

[4] T. Adamo and E. Newman, *The Kerr-Newman metric: A Review*, 1410.6626.

[5] E. T. Newman, R. Couch, K. Chinnapared, A. Exton, A. Prakash et al., *Metric of a Rotating, Charged Mass*, *J.Math.Phys.* **6** (1965) 918–919.

[6] D. Robinson, *Four decades of black holes uniqueness theorems*, *in "The Kerr Spacetime: Rotating Black Holes in General Relativity."* (Editors: D. L. Wiltshire, M. Visser, S. M. Scott (Cambridge University Press, 2009).) .

[7] P. T. Chrusciel, J. L. Costa and M. Heusler, *Stationary Black Holes: Uniqueness and Beyond*, *Living Rev.Rel.* **15** (2012) 7, [1205.6112].

[8] P. T. Chruściel, *Remarks on stationary vacuum black holes*, 2305.07329.

[9] S. W. Hawking and G. F. R. Ellis, *The Large Scale Structure of Space-Time: 50th Anniversary Edition*. Cambridge University Press, Feb., 2023.

[10] S. W. Hawking, *Black holes in general relativity*, *Communications in Mathematical Physics* **25** (June, 1972) 152–166.

[11] LIGO Scientific Collaboration and Virgo Collaboration, B. P. Abbott, R. Abbott, T. D. Abbott, M. R. Abernathy, F. Acernese et al., *Observation of Gravitational Waves from a Binary Black Hole Merger*, *Physical Review Letters* **116** (Feb., 2016) 061102.

[12] T. L. S. Collaboration, *Advanced LIGO*, *Classical and Quantum Gravity* **32** (Apr., 2015) 074001, [1411.4547].

[13] F. Acernese, M. Agathos, K. Agatsuma, D. Aisa, N. Allemandou, A. Allocca et al., *Advanced Virgo: A 2nd generation interferometric gravitational wave detector*, *Classical and Quantum Gravity* **32** (Jan., 2015) 024001, [1408.3978].

[14] R. P. Kerr, *Gravitational Field of a Spinning Mass as an Example of Algebraically Special Metrics*, *Physical Review Letters* **11** (Sept., 1963) 237–238.

[15] T. Clifton, P. G. Ferreira, A. Padilla and C. Skordis, *Modified Gravity and Cosmology*, *Physics Reports* **513** (Mar., 2012) 1–189, [1106.2476].

[16] O. J. C. Dias, M. Godazgar, J. E. Santos, G. Carullo, W. Del Pozzo and D. Laghi, *Eigenvalue repulsions in the quasinormal spectra of the Kerr-Newman black hole*, *Phys. Rev. D* **105** (2022) 084044, [2109.13949].

[17] G. Carullo, D. Laghi, N. K. Johnson-McDaniel, W. Del Pozzo, O. J. C. Dias, M. Godazgar et al., *Constraints on Kerr-Newman black holes from merger-ringdown gravitational-wave observations*, *Phys. Rev. D* **105** (2022) 062009, [2109.13961].

[18] O. J. C. Dias, M. Godazgar and J. E. Santos, *Eigenvalue repulsions and quasinormal mode spectra of Kerr-Newman: an extended study*, *JHEP* **07** (2022) 076, [2205.13072].

[19] G. W. Gibbons, *Vacuum polarization and the spontaneous loss of charge by black holes*, *Communications in Mathematical Physics* **44** (Oct., 1975) 245–264.

[20] R. D. Blandford and R. L. Znajek, *Electromagnetic extraction of energy from Kerr black holes*, *Monthly Notices of the Royal Astronomical Society* **179** (July, 1977) 433–456.

[21] C. Palenzuela, C. Bona, L. Lehner and O. Reula, *Robustness of the Blandford-Znajek mechanism*, *Classical and Quantum Gravity* **28** (July, 2011) 134007, [1102.3663].

[22] P. Auclair, D. Bacon, T. Baker, T. Barreiro, N. Bartolo, E. Belgacem et al., *Cosmology with the Laser Interferometer Space Antenna*, Apr., 2022. 10.48550/arXiv.2204.05434.

[23] P. Amaro-Seoane, H. Audley, S. Babak, J. Baker, E. Barausse, P. Bender et al., *Laser Interferometer Space Antenna*, Feb., 2017. 10.48550/arXiv.1702.00786.

[24] A. G. Riess, A. V. Filippenko, P. Challis, A. Clocchiattia, A. Diercks, P. M. Garnavich et al., *Observational Evidence from Supernovae for an Accelerating Universe and a Cosmological Constant*, *The Astronomical Journal* **116** (Sept., 1998) 1009–1038, [astro-ph/9805201].

[25] S. Perlmutter, G. Aldering, G. Goldhaber, R. A. Knop, P. Nugent, P. G. Castro et al., *Measurements of Omega and Lambda from 42 High-Redshift Supernovae*, *The Astrophysical Journal* **517** (June, 1999) 565–586, [astro-ph/9812133].

[26] P. Collaboration, P. A. R. Ade, N. Aghanim, C. Armitage-Caplan, M. Arnaud, M. Ashdown et al., *Planck 2013 results. XVI. Cosmological parameters*, *Astronomy & Astrophysics* **571** (Nov., 2014) A16, [1303.5076].

[27] R. H. Price, *Nonspherical Perturbations of Relativistic Gravitational Collapse. I. Scalar and Gravitational Perturbations*, *Physical Review D* **5** (May, 1972) 2419–2438.

[28] R. H. Price, *Nonspherical Perturbations of Relativistic Gravitational Collapse. II. Integer-Spin, Zero-Rest-Mass Fields*, *Physical Review D* **5** (May, 1972) 2439–2454.

[29] P. R. Brady, C. M. Chambers, W. Krivan and P. Laguna, *Telling tails in the presence of a cosmological constant*, *Physical Review D* **55** (June, 1997) 7538–7545.

[30] P. R. Brady, C. M. Chambers, W. G. Laarakkers and E. Poisson, *Radiative falloff in Schwarzschild–de Sitter spacetime*, *Physical Review D* **60** (Aug., 1999) 064003.

[31] E. Witten, *Anti De Sitter Space And Holography*, Apr., 1998. 10.48550/arXiv.hep-th/9802150.

[32] J. M. Maldacena, *The Large N Limit of Superconformal Field Theories and Supergravity*, *International Journal of Theoretical Physics* **38** (1999) 1113–1133, [hep-th/9711200].

[33] O. Aharony, S. S. Gubser, J. Maldacena, H. Ooguri and Y. Oz, *Large N Field Theories, String Theory and Gravity*, *Physics Reports* **323** (Jan., 2000) 183–386, [hep-th/9905111].

[34] P. K. Kovtun and A. O. Starinets, *Quasinormal modes and holography*, *Physical Review D* **72** (Oct., 2005) 086009, [hep-th/0506184].

[35] D. T. Son and A. O. Starinets, *Viscosity, Black Holes, and Quantum Field Theory*, *Annual Review of Nuclear and Particle Science* **57** (Nov., 2007) 95–118, [0704.0240].

[36] S. S. Gubser, *Breaking an Abelian gauge symmetry near a black hole horizon*, *Physical Review D* **78** (Sept., 2008) 065034, [0801.2977].

[37] S. A. Hartnoll, C. P. Herzog and G. T. Horowitz, *Building an AdS/CFT superconductor*, *Physical Review Letters* **101** (July, 2008) 031601, [0803.3295].

[38] S. A. Hartnoll, C. P. Herzog and G. T. Horowitz, *Holographic Superconductors*, *Journal of High Energy Physics* **2008** (Dec., 2008) 015–015, [0810.1563].

[39] K. Schwarzschild, *On the gravitational field of a mass point according to Einstein's theory*, *Sitzungsber. Preuss. Akad. Wiss. Berlin (Math. Phys.)* **1916** (1916) 189–196.

[40] H. Reissner, *über die Eigengravitation des elektrischen Feldes nach der Einsteinschen Theorie*, *Annalen der Physik* **355** (1916) 106–120.

[41] G. Nordström, *On the Energy of the Gravitation field in Einstein's Theory*, *Koninklijke Nederlandse Akademie van Wetenschappen Proceedings Series B Physical Sciences* **20** (Jan., 1918) 1238–1245.

[42] E. Berti, V. Cardoso and A. O. Starinets, *Quasinormal modes of black holes and black branes*, *Classical and Quantum Gravity* **26** (Aug., 2009) 163001, [0905.2975].

[43] R. A. Konoplya and A. Zhidenko, *Quasinormal modes of black holes: From astrophysics to string theory*, *Reviews of Modern Physics* **83** (July, 2011) 793–836, [1102.4014].

[44] K. D. Kokkotas and B. G. Schmidt, *Quasi-Normal Modes of Stars and Black Holes*, *Living Reviews in Relativity* **2** (Dec., 1999) 2, [gr-qc/9909058].

[45] H.-P. Nollert, *Quasinormal modes: The characteristic 'sound' of black holes and neutron stars*, *Classical and Quantum Gravity* **16** (Dec., 1999) R159.

[46] A. Davey, O. J. C. Dias and D. Sola-Gil, "Strong Cosmic Censorship in Kerr-Newman-de Sitter (to appear)."

[47] O. J. C. Dias, H. S. Reall and J. E. Santos, *The BTZ black hole violates strong cosmic censorship*, *JHEP* **12** (2019) 097, [1906.08265].

[48] E. W. Leaver, *An Analytic representation for the quasi normal modes of Kerr black holes*, *Proc. Roy. Soc. Lond. A* **402** (1985) 285–298.

[49] E. Berti, V. Cardoso and M. Casals, *Eigenvalues and eigenfunctions of spin-weighted spheroidal harmonics in four and higher dimensions*, *Physical Review D* **73** (May, 2006) 109902, [gr-qc/0511111].

[50] E. S. C. Ching, P. T. Leung, A. Maassen van den Brink, W. M. Suen, S. S. Tong and K. Young, *Quasinormal-mode expansion for waves in open systems*, *Reviews of Modern Physics* **70** (Oct., 1998) 1545–1554.

[51] E. W. Leaver, *Spectral decomposition of the perturbation response of the Schwarzschild geometry*, *Physical Review D* **34** (July, 1986) 384–408.

[52] N. Andersson, *Excitation of Schwarzschild black-hole quasinormal modes*, *Physical Review D* **51** (Jan., 1995) 353–363.

[53] E. Berti and V. Cardoso, *Quasinormal ringing of Kerr black holes: The excitation factors*, *Physical Review D* **74** (Nov., 2006) 104020, [gr-qc/0605118].

[54] C. Gundlach, R. Price and J. Pullin, *Late-Time Behavior of Stellar Collapse and Explosions: I. Linearized Perturbations*, *Physical Review D* **49** (Jan., 1994) 883–889, [gr-qc/9307009].

[55] R. A. Konoplya and A. Zhidenko, *A massive charged scalar field in the Kerr-Newman background I: Quasinormal modes, late-time tails and stability*, *Physical Review D* **88** (July, 2013) 024054, [1307.1812].

[56] M. Dafermos and I. Rodnianski, *A proof of Price's law for the collapse of a self-gravitating scalar field*, *Inventiones mathematicae* **162** (Nov., 2005) 381–457, [gr-qc/0309115].

[57] H. Yang, F. Zhang, A. Zimmerman, D. A. Nichols, E. Berti et al., *Branching of quasinormal modes for nearly extremal Kerr black holes*, *Phys.Rev.* **D87** (2013) 041502, [1212.3271].

[58] H. Yang, A. Zimmerman, A. Zenginoğlu, F. Zhang, E. Berti and Y. Chen, *Quasinormal modes of nearly extremal Kerr spacetimes: spectrum bifurcation and power-law ringdown*, *Phys. Rev.* **D88** (2013) 044047, [1307.8086].

[59] A. Zimmerman and Z. Mark, *Damped and zero-damped quasinormal modes of charged, nearly extremal black holes*, *Phys. Rev. D* **93** (2016) 044033, [1512.02247].

[60] C. J. Goebel, *Comments on the "vibrations" of a Black Hole.*, *Astrophys. J.* **172** (Mar., 1972) L95.

[61] V. Ferrari and B. Mashhoon, *New approach to the quasinormal modes of a black hole*, *Phys. Rev.* **D30** (1984) 295–304.

[62] V. Ferrari and B. Mashhoon, *Oscillations of a Black Hole*, *Phys. Rev. Lett.* **52** (1984) 1361.

[63] B. Mashhoon, *Stability of charged rotating black holes in the eikonal approximation*, *Phys. Rev.* **D31** (1985) 290–293.

[64] B. F. Schutz and C. M. Will, *Black hole normal modes: A semianalytic approach*, *Astrophys. J. Lett.* **291** (1985) L33–L36.

[65] L. Bombelli and E. Calzetta, *Chaos around a black hole*, *Class. Quant. Grav.* **9** (1992) 2573–2599.

[66] N. J. Cornish and J. J. Levin, *Lyapunov timescales and black hole binaries*, *Class. Quant. Grav.* **20** (2003) 1649–1660, [gr-qc/0304056].

[67] V. Cardoso, A. S. Miranda, E. Berti, H. Witek and V. T. Zanchin, *Geodesic stability, Lyapunov exponents and quasinormal modes*, *Phys. Rev.* **D79** (2009) 064016, [0812.1806].

[68] S. R. Dolan, *The Quasinormal Mode Spectrum of a Kerr Black Hole in the Eikonal Limit*, *Phys. Rev.* **D82** (2010) 104003, [1007.5097].

[69] H. Yang, D. A. Nichols, F. Zhang, A. Zimmerman, Z. Zhang and Y. Chen, *Quasinormal-mode spectrum of Kerr black holes and its geometric interpretation*, *Phys. Rev.* **D86** (2012) 104006, [1207.4253].

[70] S. Iyer and C. M. Will, *Black Hole Normal Modes: A Semianalytic Approach. 1. Foundations*, .

[71] S. Iyer, *Black Hole Normal Modes: A WKB Approach. 2. Schwarzschild Black Holes*, *Phys. Rev. D* **35** (1987) 3632.

[72] K. D. Kokkotas and B. F. Schutz, *Black Hole Normal Modes: A WKB Approach. 3. The Reissner-Nordstrom Black Hole*, *Phys. Rev. D* **37** (1988) 3378–3387.

[73] E. Seidel and S. Iyer, *Black Hole Normal Modes: A WKB Approach. 4. Kerr Black Holes*, *Phys. Rev. D* **41** (1990) 374–382.

[74] V. Cardoso, A. S. Miranda, E. Berti, H. Witek and V. T. Zanchin, *Geodesic stability, Lyapunov exponents and quasinormal modes*, *Physical Review D* **79** (Mar., 2009) 064016, [0812.1806].

[75] S. R. Dolan, *Quasinormal mode spectrum of a Kerr black hole in the eikonal limit*, *Physical Review D* **82** (Nov., 2010) 104003.

[76] H. Yang, D. A. Nichols, F. Zhang, A. Zimmerman, Z. Zhang and Y. Chen, *Quasinormal-mode spectrum of Kerr black holes and its geometric interpretation*, *Physical Review D* **86** (Nov., 2012) 104006, [1207.4253].

[77] S. Teukolsky and W. Press, *Perturbations of a rotating black hole. III - Interaction of the hole with gravitational and electromagnetic radiation*, *Astrophys.J.* **193** (1974) 443–461.

[78] S. L. Detweiler, *Black holes and gravitational waves. III. The resonant frequencies of rotating holes.*, *Astrophys.J.* **239** (1980) 292–295.

[79] M. Sasaki and T. Nakamura, *Gravitational Radiation from Extreme Kerr Black Hole*, *Gen. Rel. Grav.* **22** (1990) 1351–1366.

[80] N. Andersson and K. Glampedakis, *A Superradiance resonance cavity outside rapidly rotating black holes*, *Phys. Rev. Lett.* **84** (2000) 4537–4540, [gr-qc/9909050].

[81] K. Glampedakis and N. Andersson, *Late time dynamics of rapidly rotating black holes*, *Phys.Rev.* **D64** (2001) 104021, [gr-qc/0103054].

[82] S. Hod, *Slow relaxation of rapidly rotating black holes*, *Phys. Rev. D* **78** (2008) 084035, [0811.3806].

[83] S. Hod, *Universality of the quasinormal spectrum of near-extremal Kerr–Newman black holes*, *Eur. Phys. J. C* **75** (2015) 272, [1410.2252].

[84] S. Hod, *Numerical evidence for universality in the relaxation dynamics of near-extremal Kerr–Newman black holes*, *Eur. Phys. J. C* **75** (2015) 611, [1511.05696].

[85] K. D. Kokkotas, R. A. Konoplya and A. Zhidenko, *Quasinormal modes, scattering, and Hawking radiation of Kerr-Newman black holes in a magnetic field*, *Physical Review D* **83** (Jan., 2011) 024031.

[86] V. Cardoso, J. L. Costa, K. Destounis, P. Hintz and A. Jansen, *Quasinormal modes and Strong Cosmic Censorship*, *Physical Review Letters* **120** (Jan., 2018) 031103, [1711.10502].

[87] H. Yang, F. Zhang, A. Zimmerman, D. A. Nichols, E. Berti and Y. Chen, *Branching of quasinormal modes for nearly extremal Kerr black holes*, *Physical Review D* **87** (Feb., 2013) 041502, [1212.3271].

[88] A. Zimmerman and Z. Mark, *Damped and zero-damped quasinormal modes of charged, nearly extremal black holes*, *Physical Review D* **93** (Apr., 2016) 089905, [1512.02247].

[89] O. J. C. Dias, H. S. Reall and J. E. Santos, *Strong cosmic censorship: Taking the rough with the smooth*, *Journal of High Energy Physics* **2018** (Oct., 2018) 1, [1808.02895].

[90] J. B. Griffiths and J. Podolsky, *A new look at the Plebanski-Demianski family of solutions*, *International Journal of Modern Physics D* **15** (Mar., 2006) 335–369, [gr-qc/0511091].

[91] J. F. Plebanski and M. Demianski, *Rotating, charged, and uniformly accelerating mass in general relativity*, *Annals of Physics* **98** (May, 1976) 98–127.

[92] W. Kinnersley and M. Walker, *Uniformly Accelerating Charged Mass in General Relativity*, *Physical Review D* **2** (Oct., 1970) 1359–1370.

[93] K. Destounis, R. D. B. Fontana and F. C. Mena, *Counterexamples to strong cosmic censorship in asymptotically flat black hole spacetimes*, *arXiv:2006.01152 [gr-qc, physics:hep-th]* (June, 2020) , [2006.01152].

[94] O. J. C. Dias, F. C. Eperon, H. S. Reall and J. E. Santos, *Strong cosmic censorship in de Sitter space*, *Physical Review D* **97** (May, 2018) 104060, [1801.09694].

[95] Y. Fourès-Bruhat, *Théorème d'existence pour certains systèmes d'équations aux dérivées partielles non linéaires*, *Acta Mathematica* **88** (1952) 141 – 225.

[96] Y. Choquet-Bruhat and R. P. Geroch, *Global aspects of the Cauchy problem in general relativity*, *Commun. Math. Phys.* **14** (1969) 329–335.

[97] R. H. Boyer and R. W. Lindquist, *Maximal Analytic Extension of the Kerr Metric*, *Journal of Mathematical Physics* **8** (Dec., 2004) 265–281.

[98] C. DeWitt-Morette and J. A. Wheeler, *Battelle Rencontres: 1967 Lectures in Mathematics and Physics*. Benjamin, 1968.

[99] J. Sbierski, *Instability of the Kerr Cauchy Horizon Under Linearised Gravitational Perturbations*, *Annals of PDE* **9** (Mar., 2023) 7.

[100] D. Christodoulou, *On the global initial value problem and the issue of singularities*, *Classical and Quantum Gravity* **16** (Dec., 1999) A23.

[101] R. Penrose, *Singularities of spacetime.*, in *Theoretical Principles in Astrophysics and Relativity*, pp. 217–243. University of Chicago Press, Jan., 1978.

[102] M. Dafermos and J. Luk, *The interior of dynamical vacuum black holes I: The $C\hat{0}$-stability of the Kerr Cauchy horizon*, *arXiv:1710.01722 [gr-qc, physics:math-ph]* (Oct., 2017) , [1710.01722].

[103] J. Sbierski, *The $C\hat{0}$-inextendibility of the Schwarzschild spacetime and the spacelike diameter in Lorentzian Geometry*, Apr., 2016. 10.48550/arXiv.1507.00601.

[104] S. Klainerman and J. Szeftel, *Kerr stability for small angular momentum*, Apr., 2021. 10.48550/arXiv.2104.11857.

[105] M. Dafermos, *The interior of charged black holes and the problem of uniqueness in general relativity*, *arXiv:gr-qc/0307013* (Nov., 2004) , [gr-qc/0307013].

[106] J. Luk and S.-J. Oh, *Strong cosmic censorship in spherical symmetry for two-ended asymptotically flat initial data II. The exterior of the black hole*

region, *arXiv:1702.05716 [gr-qc, physics:math-ph]* (Feb., 2019) , [1702.05716].

[107] A. Ori, *Inner structure of a charged black hole: An exact mass-inflation solution*, *Physical Review Letters* **67** (Aug., 1991) 789–792.

[108] D. Christodoulou, *The Formation of Black Holes in General Relativity*, 0805.3880.

[109] D. A. d. W. zu Berlin, *Histoire de l'Académie royale des sciences et des belles-lettres de Berlin: avec les mémoires pour la même année, tirez des registres de cette Academie*. Ambroise Haude, 1749.

[110] P. J. Olver, *Introduction to Partial Differential Equations*. Undergraduate Texts in Mathematics. Springer International Publishing, Cham, 2014, 10.1007/978-3-319-02099-0.

[111] P. Hintz and A. Vasy, *Analysis of linear waves near the cauchy horizon of cosmological black holes*, *Journal of Mathematical Physics* **58** (Aug, 2017) 081509.

[112] J. L. Costa and A. T. Franzen, *Bounded energy waves on the black hole interior of Reissner-Nordström-de Sitter*, *Annales Henri Poincare* **18** (2017) 3371–3398, [1607.01018].

[113] E. Poisson and W. Israel, *Internal structure of black holes*, *Phys. Rev. D* **41** (1990) 1796–1809.

[114] M. Dafermos, *The Interior of charged black holes and the problem of uniqueness in general relativity*, *Commun. Pure Appl. Math.* **58** (2005) 0445–0504, [gr-qc/0307013].

[115] J. Luk and S.-J. Oh, *Proof of linear instability of the Reissner-Nordström Cauchy horizon under scalar perturbations*, *Duke Mathematical Journal* **166** (Feb., 2017) , [1501.04598].

[116] J. Luk and S.-J. Oh, *Strong cosmic censorship in spherical symmetry for two-ended asymptotically flat initial data I. The interior of the black hole region*, 1702.05715.

[117] M. Dafermos and Y. Shlapentokh-Rothman, *Time-Translation Invariance of Scattering Maps and Blue-Shift Instabilities on Kerr Black Hole Spacetimes*, *Communications in Mathematical Physics* **350** (Mar., 2017) 985–1016, [1512.08260].

[118] M. Dafermos and J. Luk, *The interior of dynamical vacuum black holes I: The C^0-stability of the Kerr Cauchy horizon*, 1710.01722.

[119] M. Simpson and R. Penrose, *Internal instability in a Reissner-Nordström black hole*, *International Journal of Theoretical Physics* **7** (Apr., 1973) 183–197.

[120] P. R. Brady, I. G. Moss and R. C. Myers, *Cosmic Censorship: As Strong As Ever*, *Physical Review Letters* **80** (Apr., 1998) 3432–3435.

[121] P. Hintz and A. Vasy, *Analysis of linear waves near the Cauchy horizon of cosmological black holes*, *Journal of Mathematical Physics* **58** (Aug., 2017) 081509, [1512.08004].

[122] O. J. C. Dias, H. S. Reall and J. E. Santos, *Strong cosmic censorship for charged de Sitter black holes with a charged scalar field*, *Classical and Quantum Gravity* **36** (Feb., 2019) 045005, [1808.04832].

[123] Y. Mo, Y. Tian, B. Wang, H. Zhang and Z. Zhong, *Strong cosmic censorship for the massless charged scalar field in the reissner-nordstrom–de sitter spacetime*, *Phys. Rev. D* **98** (Dec, 2018) 124025.

[124] V. Cardoso, J. a. L. Costa, K. Destounis, P. Hintz and A. Jansen, *Strong cosmic censorship in charged black-hole spacetimes: Still subtle*, *Phys. Rev. D* **98** (Nov, 2018) 104007.

[125] R. Luna, M. Zilhão, V. Cardoso, J. a. L. Costa and J. Natário, *Strong cosmic censorship: The nonlinear story*, *Phys. Rev. D* **99** (2019) 064014, [1810.00886].

[126] R. Luna, M. Zilhão, V. Cardoso, J. L. Costa and J. Natário, *Addendum to "Strong cosmic censorship: The nonlinear story"*, *Physical Review D* **103** (May, 2021) 104043, [2012.08413].

[127] G. Holzegel and J. Smulevici, *Decay properties of Klein-Gordon fields on Kerr-AdS spacetimes*, *arXiv:1110.6794 [gr-qc, physics:hep-th]* (Mar., 2013) , [1110.6794].

[128] F. S. Miguel, *Interior quasinormal modes and strong cosmic censorship*, *Physical Review D* **103** (Mar., 2021) 064077.

[129] A. Pandya and F. Pretorius, *The rotating black hole interior: Insights from gravitational collapse in AdS_3 spacetime*, *Phys. Rev. D* **101** (2020) 104026, [2002.07130].

[130] R. Penrose, *Gravitational collapse: The role of general relativity*, *Riv. Nuovo Cim.* **1** (1969) 252–276.

[131] D. Christodoulou, *Reversible and irreversible transformations in black-hole physics*, *Phys. Rev. Lett.* **25** (Nov, 1970) 1596–1597.

[132] J. D. Bekenstein, *Extraction of energy and charge from a black hole*, *Phys. Rev.* **D7** (1973) 949–953.

[133] S. W. Hawking, *Particle creation by black holes*, *Communications in Mathematical Physics* **43** (Aug., 1975) 199–220.

[134] R. Brito, V. Cardoso and P. Pani, *Superradiance: New Frontiers in Black Hole Physics*, vol. 971 of *Lecture Notes in Physics*. Springer International Publishing, Cham, 2020, 10.1007/978-3-030-46622-0.

[135] D. Sudarsky and R. M. Wald, *Extrema of mass, stationarity, and staticity, and solutions to the Einstein-Yang-Mills equations*, *Physical Review D* **46** (Aug., 1992) 1453–1474.

[136] J. M. Bardeen, B. Carter and S. W. Hawking, *The four laws of black hole mechanics*, *Communications in Mathematical Physics* **31** (June, 1973) 161–170.

[137] W. H. Press and S. A. Teukolsky, *Floating Orbits, Superradiant Scattering and the Black-hole Bomb*, *Nature* **238** (1972) 211–212.

[138] Y. B. Zel'dovich, *Generation of Waves by a Rotating Body*, *JETP Lett.* **14** (1971) 180.

[139] G. Denardo and R. Ruffini, *On the energetics of Reissner Nordström geometries*, *Phys. Lett.* **B45** (1973) 259–262.

[140] S. W. Hawking and H. S. Reall, *Charged and rotating AdS black holes and their CFT duals*, *Physical Review D* **61** (Dec., 1999) 024014, [hep-th/9908109].

[141] V. Cardoso and O. J. C. Dias, *Small Kerr-anti-de Sitter black holes are unstable*, *Physical Review D* **70** (Oct., 2004) 084011, [hep-th/0405006].

[142] T. J. M. Zouros and D. M. Eardley, *Instabilities of massive scalar perturbations of a rotating black hole*, *Annals of Physics* **118** (Mar., 1979) 139–155.

[143] S. Detweiler, *Klein-Gordon equation and rotating black holes*, *Physical Review D* **22** (Nov., 1980) 2323–2326.

[144] M. Durkee and H. S. Reall, *Perturbations of near-horizon geometries and instabilities of Myers-Perry black holes*, *Physical Review D* **83** (May, 2011) 104044, [1012.4805].

[145] O. J. C. Dias and J. E. Santos, *Origin of the Reissner-Nordström–de Sitter instability*, *Phys. Rev. D* **102** (2020) 124039, [2005.03673].

[146] O. J. C. Dias and J. E. Santos, *The origin of the Reissner-Nordström de Sitter instability*, 2005.03673.

[147] P. Breitenlohner and D. Z. Freedman, *Stability in gauged extended supergravity*, *Annals of Physics* **144** (1982) 249–281.

[148] L. Mezincescu and P. K. Townsend, *Stability at a local maximum in higher dimensional anti-deSitter space and applications to supergravity*, *Annals of Physics* **160** (Apr., 1985) 406–419.

[149] S. Hollands and A. Ishibashi, *Instabilities of extremal rotating black holes in higher dimensions*, *Communications in Mathematical Physics* **339** (Nov., 2015) 949–1002, [1408.0801].

[150] R. Gregory and R. Laflamme, *Black strings and p-branes are unstable*, *Physical Review Letters* **70** (May, 1993) 2837–2840.

[151] P. Figueras, K. Murata and H. S. Reall, *Stable non-uniform black strings below the critical dimension*, *Journal of High Energy Physics* **2012** (Nov., 2012) 71, [1209.1981].

[152] L. Lehner and F. Pretorius, *Black Strings, Low Viscosity Fluids, and Violation of Cosmic Censorship*, *Physical Review Letters* **105** (Sept., 2010) 101102, [1006.5960].

[153] J. D. Bekenstein, *Black Holes and Entropy*, *Physical Review D* **7** (Apr., 1973) 2333–2346.

[154] J. D. Bekenstein, *Generalized second law of thermodynamics in black-hole physics*, *Physical Review D* **9** (June, 1974) 3292–3300.

[155] L. N. Trefethen and Society for Industrial and Applied Mathematics, *Spectral Methods in MATLAB*. Society for Industrial and Applied

Mathematics (SIAM, 3600 Market Street, Floor 6, Philadelphia, PA 19104), Philadelphia, Pa., 2000.

[156] O. J. C. Dias, J. E. Santos and B. Way, *Numerical Methods for Finding Stationary Gravitational Solutions*, *Class. Quant. Grav.* **33** (2016) 133001, [1510.02804].

[157] O. J. Dias, P. Figueras, R. Monteiro and J. E. Santos, *Ultraspinning instability of anti-de Sitter black holes*, *JHEP* **1012** (2010) 067, [1011.0996].

[158] O. J. C. Dias, G. S. Hartnett and J. E. Santos, *Quasinormal modes of asymptotically flat rotating black holes*, *Class. Quant. Grav.* **31** (2014) 245011, [1402.7047].

[159] O. J. Dias, R. Monteiro and J. E. Santos, *Ultraspinning instability: the missing link*, *JHEP* **1108** (2011) 139, [1106.4554].

[160] O. J. Dias, P. Figueras, R. Monteiro, J. E. Santos and R. Emparan, *Instability and new phases of higher-dimensional rotating black holes*, *Phys.Rev.* **D80** (2009) 111701, [0907.2248].

[161] O. J. Dias, P. Figueras, R. Monteiro, H. S. Reall and J. E. Santos, *An instability of higher-dimensional rotating black holes*, *JHEP* **1005** (2010) 076, [1001.4527].

[162] O. J. C. Dias, R. Monteiro, H. S. Reall and J. E. Santos, *A Scalar field condensation instability of rotating anti-de Sitter black holes*, *JHEP* **11** (2010) 036, [1007.3745].

[163] O. J. C. Dias, P. Figueras, S. Minwalla, P. Mitra, R. Monteiro and J. E. Santos, *Hairy black holes and solitons in global AdS_5*, *JHEP* **08** (2012) 117, [1112.4447].

[164] V. Cardoso, O. J. C. Dias, G. S. Hartnett, L. Lehner and J. E. Santos, *Holographic thermalization, quasinormal modes and superradiance in Kerr-AdS*, *JHEP* **04** (2014) 183, [1312.5323].

[165] O. J. C. Dias, H. S. Reall and J. E. Santos, *Strong cosmic censorship: taking the rough with the smooth*, 1808.02895.

[166] O. J. C. Dias, J. E. Santos and B. Way, *Numerical Methods for Finding Stationary Gravitational Solutions*, *Classical and Quantum Gravity* **33** (July, 2016) 133001, [1510.02804].

[167] T. Regge and J. A. Wheeler, *Stability of a Schwarzschild singularity*, *Phys.Rev.* **108** (1957) 1063–1069.

[168] F. Zerilli, *Perturbation analysis for gravitational and electromagnetic radiation in a Reissner-Nordstrom geometry*, *Phys.Rev.* **D9** (1974) 860–868.

[169] V. Moncrief, *Gravitational perturbations of spherically symmetric systems. I. The exterior problem.*, *Annals Phys.* **88** (1974) 323–342.

[170] S. Chandrasekhar and S. L. Detweiler, *The quasi-normal modes of the Schwarzschild black hole*, *Proc.Roy.Soc.Lond.* **A344** (1975) 441–452.

[171] V. Moncrief, *Odd-parity stability of a Reissner-Nordstrom black hole*, *Phys.Rev.* **D9** (1974) 2707–2709.

[172] V. Moncrief, *Stability of Reissner-Nordstrom black holes*, *Phys.Rev.* **D10** (1974) 1057–1059.

[173] E. Newman and R. Penrose, *An Approach to gravitational radiation by a method of spin coefficients*, *J.Math.Phys.* **3** (1962) 566–578.

[174] R. P. Geroch, A. Held and R. Penrose, *A space-time calculus based on pairs of null directions*, *J.Math.Phys.* **14** (1973) 874–881.

[175] S. Teukolsky, *Rotating black holes - separable wave equations for gravitational and electromagnetic perturbations*, *Phys.Rev.Lett.* **29** (1972) 1114–1118.

[176] S. Chandrasekhar, *The Mathematical Theory of Black Holes*. Oxford Press (1983), 1983.

[177] B. F. Whiting, *Mode Stability of the Kerr Black Hole*, *J.Math.Phys.* **30** (1989) 1301.

[178] H. Onozawa, *A Detailed study of quasinormal frequencies of the Kerr black hole*, *Phys.Rev.* **D55** (1997) 3593–3602, [gr-qc/9610048].

[179] K. Glampedakis and N. Andersson, *Quick and dirty methods for studying black hole resonances*, *Class. Quant. Grav.* **20** (2003) 3441–3464, [gr-qc/0304030].

[180] E. Berti, V. Cardoso, K. D. Kokkotas and H. Onozawa, *Highly damped quasinormal modes of Kerr black holes*, *Phys.Rev.* **D68** (2003) 124018, [hep-th/0307013].

[181] E. Berti and K. D. Kokkotas, *Quasinormal modes of Kerr-Newman black holes: Coupling of electromagnetic and gravitational perturbations*, *Phys.Rev.* **D71** (2005) 124008, [gr-qc/0502065].

[182] O. J. C. Dias, M. Godazgar and J. E. Santos, *Linear Mode Stability of the Kerr-Newman Black Hole and Its Quasinormal Modes*, *Phys. Rev. Lett.* **114** (2015) 151101, [1501.04625].

[183] E. Giorgi, *Electromagnetic-gravitational perturbations of Kerr–Newman spacetime: The Teukolsky and Regge–Wheeler equations*, *J. Hyperbol. Diff. Equat.* **19** (2022) 1–139, [2002.07228].

[184] L. D. Landau and L. M. Lifshitz, *Quantum Mechanics Non-Relativistic Theory, Third Edition: Volume 3*. Butterworth-Heinemann, 3 ed., Jan., 1981.

[185] C. Cohen-Tannoudji, B. Diu and F. Laloë, *Quantum mechanics; 1st ed.* Wiley, New York, NY, 1977.

[186] W. Xiong and P.-C. Li, *Quasinormal modes of rotating accelerating black holes*, *arXiv e-prints* (May, 2023) , [2305.04040].

[187] C. M. Will and J. W. Guinn, *Tunneling near the peaks of potential barriers - Consequences of higher-order Wentzel-Kramers-Brillouin corrections*, *Phys. Rev. A* **37** (1988) 3674–3679.

[188] V. Cardoso, J. L. Costa, K. Destounis, P. Hintz and A. Jansen, *Quasinormal modes and Strong Cosmic Censorship*, *Phys. Rev. Lett.* **120** (2018) 031103, [1711.10502].

[189] O. J. C. Dias, H. S. Reall and J. E. Santos, *Strong cosmic censorship for charged de Sitter black holes with a charged scalar field*, *Class. Quant. Grav.* **36** (2019) 045005, [1808.04832].

[190] M. Abramowitz and I. A. Stegun, *Handbook of Mathematical Functions with Formulas, Graphs, and Mathematical Tables*. Dover Publications, New York, 1964.

[191] C. Kittel, *Introduction to solid state physics*. John Wiley & Sons (8th ed.), 2004.

[192] E. W. Leaver, *Quasinormal modes of Reissner-Nordstrom black holes*, *Phys. Rev. D* **41** (1990) 2986–2997.

[193] N. Andersson, *Normal-mode frequencies of Reissner-Nordstrom black holes*, *R. Soc. Lond. A* **442** (1993) 427–436.

[194] H. Onozawa, T. Mishima, T. Okamura and H. Ishihara, *Quasinormal modes of maximally charged black holes*, *Phys. Rev. D* **53** (1996) 7033–7040, [gr-qc/9603021].

[195] N. Andersson and H. Onozawa, *Quasinormal modes of nearly extreme Reissner-Nordstrom black holes*, *Phys. Rev. D* **54** (1996) 7470–7475, [gr-qc/9607054].

[196] R. A. Konoplya and A. Zhidenko, *Massive charged scalar field in the Kerr-Newman background: Quasinormal modes, late-time tails and stability*, *Physical Review D* **88** (July, 2013) 024054.

[197] P. Breitenlohner and D. Z. Freedman, *Stability in Gauged Extended Supergravity*, *Annals Phys.* **144** (1982) 249.

[198] L. Mezincescu and P. K. Townsend, *Stability at a local maximum in higher dimensional anti-deSitter space and applications to supergravity*, *Annals of Physics* **160** (Apr., 1985) 406–419.

[199] S. Hod, *Quasinormal modes and strong cosmic censorship in near-extremal Kerr–Newman–de Sitter black-hole spacetimes*, *Phys. Lett. B* **780** (2018) 221–226, [1803.05443].

[200] M. Casals and C. I. S. Marinho, *Glimpses of Violation of Strong Cosmic Censorship in Rotating Black Holes*, 2006.06483.

[201] H. Liu, Z. Tang, K. Destounis, B. Wang, E. Papantonopoulos and H. Zhang, *Strong Cosmic Censorship in higher-dimensional Reissner-Nordström-de Sitter spacetime*, *Journal of High Energy Physics* **2019** (Mar., 2019) 187, [1902.01865].

[202] R. A. Konoplya and A. Zhidenko, *Instability of higher dimensional charged black holes in the de-Sitter world*, *Phys. Rev. Lett.* **103** (2009) 161101, [0809.2822].

[203] V. Cardoso, M. Lemos and M. Marques, *On the instability of Reissner-Nordstrom black holes in de Sitter backgrounds*, *Phys. Rev. D* **80** (2009) 127502, [1001.0019].

[204] R. A. Konoplya and A. Zhidenko, *Instability of D-dimensional extremally charged Reissner-Nordstrom(-de Sitter) black holes: Extrapolation to arbitrary D*, *Phys. Rev. D* **89** (2014) 024011, [1309.7667].

[205] M. Rahman, S. Chakraborty, S. SenGupta and A. A. Sen, *Fate of Strong Cosmic Censorship Conjecture in Presence of Higher Spacetime Dimensions*, *Journal of High Energy Physics* **2019** (Mar., 2019) 178, [1811.08538].

[206] S. Barreto and M. Zworski, *Distribution of resonances for spherical black holes*, *Math. Res. Lett.* **4** (1997) 103.

[207] J.-F. Bony and M. Hafner, *Decay and non-decay of the local energy for the wave equation on the de sitter–schwarzschild metric*, *Communications in Mathematical Physics* **282** (2008) 697.

[208] S. Dyatlov, *Asymptotic distribution of quasi-normal modes for kerr–de sitter black holes*, *Annales Henri Poincaré* **13** (Jan, 2012) 1101–1166.

[209] S. Dyatlov, *Asymptotics of linear waves and resonances with applications to black holes*, *Communications in Mathematical Physics* **335** (Jan, 2015) 1445–1485.

[210] P. Hintz and A. Vasy, *The global non-linear stability of the kerr–de sitter family of black holes*, *Acta Mathematica* **220** (2018) 1–206.

[211] P. Hintz, *Non-linear stability of the kerr–newman–de sitter family of charged black holes*, *Annals of PDE* **4** (Apr, 2018) .

[212] O. J. C. Dias, M. Godazgar, J. E. Santos, G. Carullo, W. Del Pozzo and D. Laghi, *Eigenvalue repulsions in the quasinormal spectra of the Kerr-Newman black hole*, *Physical Review D* **105** (Apr., 2022) 084044, [2109.13949].

[213] R. C. Myers and M. J. Perry, *Black holes in higher dimensional space-times*, *Annals of Physics* **172** (Dec., 1986) 304–347.

[214] S. W. Hawking, C. J. Hunter and M. M. Taylor-Robinson, *Rotation and the AdS/CFT correspondence*, *Physical Review D* **59** (Feb., 1999) 064005, [hep-th/9811056].

[215] G. W. Gibbons, H. Lu, D. N. Page and C. N. Pope, *The General Kerr-de Sitter Metrics in All Dimensions*, *Journal of Geometry and Physics* **53** (Jan., 2005) 49–73, [hep-th/0404008].

[216] G. W. Gibbons, H. Lu, D. N. Page and C. N. Pope, *Rotating Black Holes in Higher Dimensions with a Cosmological Constant*, *Physical Review Letters* **93** (Oct., 2004) 171102, [hep-th/0409155].

[217] O. J. C. Dias, R. Monteiro, H. S. Reall and J. E. Santos, *A scalar field condensation instability of rotating anti-de Sitter black holes*, 1007.3745.

[218] O. J. C. Dias, P. Figueras, R. Monteiro, H. S. Reall and J. E. Santos, *An instability of higher-dimensional rotating black holes*, *Journal of High Energy Physics* **2010** (May, 2010) 76, [1001.4527].

[219] P. Hoxha, R. R. Martinez-Acosta and C. N. Pope, *Kaluza-Klein Consistency, Killing Vectors, and Kahler Spaces*, *Classical and Quantum Gravity* **17** (Oct., 2000) 4207–4240, [hep-th/0005172].

[220] A. López-Ortega, *Quasinormal modes of D-dimensional de Sitter spacetime*, *General Relativity and Gravitation* **38** (Oct., 2006) 1565–1591, [gr-qc/0605027].

[221] B. Mashhoon, *Stability of charged rotating black holes in the eikonal approximation*, *Physical Review D* **31** (Jan., 1985) 290–293.

[222] V. Ferrari and B. Mashhoon, *New approach to the quasinormal modes of a black hole*, *Physical Review D* **30** (July, 1984) 295–304.

[223] S. Hod, *Black-hole quasinormal resonances: Wave analysis versus a geometric-optics approximation*, *Physical Review D* **80** (Sept., 2009) 064004, [0909.0314].

[224] S. R. Dolan, *The Quasinormal Mode Spectrum of a Kerr Black Hole in the Eikonal Limit*, *Physical Review D* **82** (Nov., 2010) 104003, [1007.5097].

[225] S. Hollands and R. M. Wald, *Stability of Black Holes and Black Branes*, *Commun. Math. Phys.* **321** (2013) 629–680, [1201.0463].

[226] O. J. C. Dias, R. Masachs, O. Papadoulaki and P. Rodgers, *Hunting for fermionic instabilities in charged AdS black holes*, *Journal of High Energy Physics* **2020** (Apr., 2020) 196, [1910.04181].

[227] H. Yang, A. Zimmerman, A. Zenginoğlu, F. Zhang, E. Berti and Y. Chen, *Quasinormal modes of nearly extremal Kerr spacetimes: Spectrum bifurcation and power-law ringdown*, *Physical Review D* **88** (Aug., 2013) 044047, [1307.8086].

[228] F. W. J. Olver, A. B. Olde Daalhuis, D. W. Lozier, B. I. Schneider, R. F. Boisvert, C. W. Clark, B. R. Miller, B. V. Saunders, H. S. Cohl, and M. A. McClain, eds., "NIST digital library of mathematical functions." http://dlmf.nist.gov/.

[229] V. Cardoso, O. J. C. Dias, J. P. S. Lemos and S. Yoshida, *The Black hole bomb and superradiant instabilities*, *Phys. Rev.* **D70** (2004) 044039, [hep-th/0404096].

[230] O. J. C. Dias, G. T. Horowitz and J. E. Santos, *Black holes with only one Killing field*, *JHEP* **07** (2011) 115, [1105.4167].

[231] O. J. C. Dias, J. E. Santos and B. Way, *Black holes with a single Killing vector field: black resonators*, *JHEP* **12** (2015) 171, [1505.04793].

[232] M. W. Choptuik, O. J. C. Dias, J. E. Santos and B. Way, *Collapse and Nonlinear Instability of AdS Space with Angular Momentum*, *Phys. Rev. Lett.* **119** (2017) 191104, [1706.06101].

[233] T. Ishii and K. Murata, *Black resonators and geons in AdS5*, *Class. Quant. Grav.* **36** (2019) 125011, [1810.11089].

[234] T. Ishii, K. Murata, J. E. Santos and B. Way, *Superradiant instability of black resonators and geons*, *JHEP* **07** (2020) 206, [2005.01201].

[235] T. Ishii, K. Murata, J. E. Santos and B. Way, *Multioscillating black holes*, 2101.06325.

[236] C. A. R. Herdeiro and E. Radu, *Kerr black holes with scalar hair*, *Phys. Rev. Lett.* **112** (2014) 221101, [1403.2757].

[237] W. Israel, *Singular hypersurfaces and thin shells in general relativity*, *Nuovo Cim.* **B44S10** (1966) 1.

[238] W. Israel, *Discontinuities in spherically symmetric gravitational fields and shells of radiation*, *Proceedings of the Royal Society of London A: Mathematical, Physical and Engineering Sciences* **248** (1958) 404–414, [http://rspa.royalsocietypublishing.org/content/royprsa/248/1254/404.full.pdf].

[239] K. Kuchar, *Charged shells in general relativity and their gravitational collapse*, *Czech. J. Phys. B* **B18** (1968) 435.

[240] C. Barrabes and W. Israel, *Thin shells in general relativity and cosmology: The Lightlike limit*, *Phys. Rev.* **D43** (1991) 1129–1142.

[241] R. M. Wald, *General relativity*. Chicago Univ. Press, Chicago, IL, 1984.

[242] D. Wiltshire, *Spherically symmetric solutions of einstein-maxwell theory with a gauss-bonnet term*, *Physics Letters B* **169** (1986) 36 – 40.

[243] R. D'Inverno, *Introducing Einstein's Relativity*. Clarendon Press, 1992.

[244] S. S. Gubser, *Breaking an Abelian gauge symmetry near a black hole horizon*, *Phys. Rev.* **D78** (2008) 065034, [0801.2977].

[245] O. J. Dias and R. Masachs, *Charged black hole bombs in a Minkowski cavity*, *Class. Quant. Grav.* **35** (2018) 184001, [1801.10176].

[246] O. J. Dias and R. Masachs, *Evading no-hair theorems: hairy black holes in a Minkowski box*, *Phys. Rev. D* **97** (2018) 124030, [1802.01603].

[247] S. L. Liebling and C. Palenzuela, *Dynamical Boson Stars*, *Living Rev. Rel.* **20** (2017) 5, [1202.5809].

[248] O. J. C. Dias, R. Masachs and P. Rodgers, *Boson stars and solitons confined in a Minkowski box*, 2101.01203.

[249] J. D. Brown and J. W. York, Jr., *Quasilocal energy and conserved charges derived from the gravitational action*, *Phys. Rev.* **D47** (1993) 1407–1419, [gr-qc/9209012].

[250] S. W. Hawking, *Black Holes and Thermodynamics*, *Phys. Rev. D* **13** (1976) 191–197.

[251] G. W. Gibbons and M. J. Perry, *Black Holes and Thermal Green's Functions*, *Proc. Roy. Soc. Lond.* **A358** (1978) 467–494.

[252] S. W. Hawking and W. Israel, *Penrose, R. (Chapter 12) at General Relativity: An Einstein Centenary Survey*. Univ. Pr., Cambridge, UK, 1979.

[253] D. Page, *Black hole formation in a box*, *Gen Relat Gravit.* **13** (1981) 1117–1126.

[254] S. W. Hawking and D. N. Page, *Thermodynamics of Black Holes in anti-De Sitter Space*, *Commun. Math. Phys.* **87** (1983) 577.

[255] H. W. Braden, J. D. Brown, B. F. Whiting and J. W. York, Jr., *Charged black hole in a grand canonical ensemble*, *Phys. Rev.* **D42** (1990) 3376–3385.

[256] T. Andrade, W. R. Kelly, D. Marolf and J. E. Santos, *On the stability of gravity with Dirichlet walls*, *Class. Quant. Grav.* **32** (2015) 235006, [1504.07580].

[257] P. Basu, J. Bhattacharya, S. Bhattacharyya, R. Loganayagam, S. Minwalla and V. Umesh, *Small Hairy Black Holes in Global AdS Spacetime*, *JHEP* **10** (2010) 045, [1003.3232].

[258] S. Bhattacharyya, S. Minwalla and K. Papadodimas, *Small Hairy Black Holes in $AdS_5 x S^5$*, *JHEP* **11** (2011) 035, [1005.1287].

[259] S. A. Gentle, M. Rangamani and B. Withers, *A Soliton Menagerie in AdS*, *JHEP* **05** (2012) 106, [1112.3979].

[260] R. Arias, J. Mas and A. Serantes, *Stability of charged global AdS_4 spacetimes*, *JHEP* **09** (2016) 024, [1606.00830].

[261] J. Markeviciute and J. E. Santos, *Hairy black holes in $AdS_5 \times S^5$*, *JHEP* **06** (2016) 096, [1602.03893].

[262] J. Markeviciute, *Rotating Hairy Black Holes in $AdS_5 \times S^5$*, *JHEP* **03** (2019) 110, [1809.04084].

[263] O. J. Dias and R. Masachs, *Hairy black holes and the endpoint of AdS_4 charged superradiance*, *JHEP* **02** (2017) 128, [1610.03496].

[264] R. L. Arnowitt, S. Deser and C. W. Misner, *The Dynamics of general relativity*, *Gen. Rel. Grav.* **40** (2008) 1997–2027, [gr-qc/0405109].

[265] N. Sanchis-Gual, J. C. Degollado, P. J. Montero, J. A. Font and C. Herdeiro, *Explosion and Final State of an Unstable Reissner-Nordström Black Hole*, *Phys. Rev. Lett.* **116** (2016) 141101, [1512.05358].

[266] N. Sanchis-Gual, J. C. Degollado, C. Herdeiro, J. A. Font and P. J. Montero, *Dynamical formation of a Reissner-Nordström black hole with scalar hair in a cavity*, *Phys. Rev.* **D94** (2016) 044061, [1607.06304].

[267] N. Sanchis-Gual, J. C. Degollado, J. A. Font, C. Herdeiro and E. Radu, *Dynamical formation of a hairy black hole in a cavity from the decay of unstable solitons*, *Class. Quant. Grav.* **34** (2017) 165001, [1611.02441].

[268] C. W. Misner, K. S. Thorne and J. A. Wheeler, *Gravitation*. W.H. Freeman and Co., San Francisco, 1973.

[269] C. A. R. Herdeiro, J. C. Degollado and H. F. Rúnarsson, *Rapid growth of superradiant instabilities for charged black holes in a cavity*, *Phys. Rev.* **D88** (2013) 063003, [1305.5513].

[270] S. Hod, *Analytic treatment of the charged black-hole-mirror bomb in the highly explosive regime*, *Phys. Rev.* **D88** (2013) 064055, [1310.6101].

[271] J. C. Degollado and C. A. R. Herdeiro, *Time evolution of superradiant instabilities for charged black holes in a cavity*, *Phys. Rev.* **D89** (2014) 063005, [1312.4579].

[272] S. Hod, *Resonance spectra of caged black holes*, *Eur. Phys. J.* **C74** (2014) 3137, [1410.4567].

[273] R. Li, J.-K. Zhao and Y.-M. Zhang, *Superradiant Instability of D-Dimensional Reissner-Nordstrm̈ Black Hole Mirror System*, *Commun. Theor. Phys.* **63** (2015) 569–574, [1404.6309].

[274] S. Hod, *The charged black-hole bomb: A lower bound on the charge-to-mass ratio of the explosive scalar field*, *Phys. Lett.* **B755** (2016) 177–182, [1606.00444].

[275] O. Fierro, N. Grandi and J. Oliva, *Superradiance of charged black holes in Einstein-Gauss-Bonnet Gravity*, 1708.06037.

[276] R. Li and J. Zhao, *Superradiant instability of charged scalar field in stringy black hole mirror system*, *Eur. Phys. J.* **C74** (2014) 3051, [1403.7279].

[277] R. Li and J. Zhao, *Numerical study of superradiant instability for charged stringy black hole mirror system*, *Phys. Lett.* **B740** (2015) 317–321, [1412.1527].

[278] R. Li, Y. Tian, H.-b. Zhang and J. Zhao, *Time domain analysis of superradiant instability for the charged stringy black hole mirror system*, *Phys. Lett.* **B750** (2015) 520–527, [1506.04267].

[279] R. Li, J. Zhao, X. Wu and Y. Zhang, *Scalar clouds in charged stringy black hole-mirror system*, *Eur. Phys. J.* **C75** (2015) 142, [1501.07358].

[280] S. R. Dolan, S. Ponglertsakul and E. Winstanley, *Stability of black holes in Einstein-charged scalar field theory in a cavity*, *Phys. Rev.* **D92** (2015) 124047, [1507.02156].

[281] S. Ponglertsakul, E. Winstanley and S. R. Dolan, *Stability of gravitating charged-scalar solitons in a cavity*, *Phys. Rev.* **D94** (2016) 024031, [1604.01132].

[282] S. Ponglertsakul and E. Winstanley, *Effect of scalar field mass on gravitating charged scalar solitons and black holes in a cavity*, *Phys. Lett.* **B764** (2017) 87–93, [1610.00135].

[283] P. Basu, C. Krishnan and P. N. B. Subramanian, *Hairy Black Holes in a Box*, *JHEP* **11** (2016) 041, [1609.01208].

[284] M. Casals and C. I. S. Marinho, *Glimpses of Violation of Strong Cosmic Censorship in Rotating Black Holes*, *Physical Review D* **106** (Aug., 2022) 044060, [2006.06483].

[285] M. Dafermos and Y. Shlapentokh-Rothman, *Rough initial data and the strength of the blue-shift instability on cosmological black holes with* $\Lambda > 0$, *Class. Quant. Grav.* **35** (2018) 195010, [1805.08764].

[286] S. Hollands, R. M. Wald and J. Zahn, *Quantum Instability of the Cauchy Horizon in Reissner-Nordström-deSitter Spacetime*, *Classical and Quantum Gravity* **37** (June, 2020) 115009, [1912.06047].

[287] S. Hollands, C. Klein and J. Zahn, *Quantum stress tensor at the cauchy horizon of the reissner–nordström–de sitter spacetime*, *Phys. Rev. D* **102** (Oct, 2020) 085004.

[288] C. Klein and J. Zahn, *Renormalized charged scalar current in the reissner–nordström–de sitter spacetime*, *Phys. Rev. D* **104** (Jul, 2021) 025009.

[289] R. Emparan, A. M. Frassino and B. Way, *Quantum BTZ black hole*, *JHEP* **11** (2020) 137, [2007.15999].

[290] R. Emparan and M. Tomašević, *Strong cosmic censorship in the BTZ black hole*, *Journal of High Energy Physics* **2020** (June, 2020) 38, [2002.02083].

[291] K. Papadodimas, S. Raju and P. Shrivastava, *A simple quantum test for smooth horizons*, *Journal of High Energy Physics* **2020** (Dec., 2020) 3, [1910.02992].

[292] V. Balasubramanian, A. Kar and G. Sárosi, *Holographic Probes of Inner Horizons*, *Journal of High Energy Physics* **2020** (June, 2020) 54, [1911.12413].

[293] K. Skenderis and B. C. van Rees, *Real-time gauge/gravity duality: Prescription, Renormalization and Examples*, *Journal of High Energy Physics* **2009** (May, 2009) 085–085, [0812.2909].

[294] K. Skenderis and B. C. van Rees, *Real-time gauge/gravity duality*, *Physical Review Letters* **101** (Aug., 2008) 081601, [0805.0150].

[295] M. Maliborski and A. Rostworowski, *Time-Periodic Solutions in an Einstein AdS-Massless-Scalar-Field System*, *Phys. Rev. Lett.* **111** (2013) 051102, [1303.3186].

[296] M. Dafermos, *The black hole stability problem*, in *Talk at the Newton Institute*, Available at: http://www-old.newton.ac.uk/webseminars/pg+ws/2006/gmx/1010/dafermos/, University of Cambridge, 2006.

[297] M. Dafermos and G. Holzegel, *Dynamic instability of solitons in 4+1 dimensional gravity with negative cosmological constant*, in *Seminar at DAMTP*, Available at: https://www.dpmms.cam.ac.uk/∼md384/ADSinstability.pdf, University of Cambridge, 2006.

[298] P. Bizon and A. Rostworowski, *On weakly turbulent instability of anti-de Sitter space*, *Phys. Rev. Lett.* **107** (2011) 031102, [1104.3702].

[299] O. J. C. Dias, G. T. Horowitz and J. E. Santos, *Gravitational Turbulent Instability of Anti-de Sitter Space*, *Class. Quant. Grav.* **29** (2012) 194002, [1109.1825].

[300] O. J. C. Dias, G. T. Horowitz, D. Marolf and J. E. Santos, *On the Nonlinear Stability of Asymptotically Anti-de Sitter Solutions*, *Class. Quant. Grav.* **29** (2012) 235019, [1208.5772].

[301] A. Buchel, L. Lehner and S. L. Liebling, *Scalar Collapse in AdS*, *Phys. Rev.* **D86** (2012) 123011, [1210.0890].

[302] A. Buchel, S. L. Liebling and L. Lehner, *Boson stars in AdS spacetime*, *Phys. Rev.* **D87** (2013) 123006, [1304.4166].

[303] O. J. C. Dias and J. E. Santos, *AdS nonlinear instability: moving beyond spherical symmetry*, 1602.03890.

[304] A. Rostworowski, *Comment on "AdS nonlinear instability: moving beyond spherical symmetry" [Class. Quantum Grav. 33 23LT01 (2016)]*, 1612.00042.

[305] O. J. C. Dias and J. E. Santos, *AdS nonlinear instability: breaking spherical and axial symmetries*, *Class. Quant. Grav.* **35** (2018) 185006, [1705.03065].

[306] V. Balasubramanian, A. Buchel, S. R. Green, L. Lehner and S. L. Liebling, *Holographic Thermalization, Stability of Anti-de Sitter Space, and the Fermi-Pasta-Ulam Paradox*, *Phys. Rev. Lett.* **113** (2014) 071601, [1403.6471].

[307] P. Bizon and A. Rostworowski, *Comment on Holographic Thermalization, Stability of Anti-de Sitter Space, and the Fermi-Pasta-Ulam Paradox?*, *Phys. Rev. Lett.* **115** (2015) 049101, [1410.2631].

[308] E. da Silva, E. Lopez, J. Mas and A. Serantes, *Collapse and Revival in Holographic Quenches*, *JHEP* **04** (2015) 038, [1412.6002].

[309] V. Balasubramanian, A. Buchel, S. R. Green, L. Lehner and S. L. Liebling, *Reply to Comment on Holographic Thermalization, Stability of Anti-de Sitter Space, and the Fermi-Pasta-Ulam Paradox?*, *Phys. Rev. Lett.* **115** (2015) 049102, [1506.07907].

[310] S. Hod, *Resonance spectrum of near-extremal kerr black holes in the eikonal limit*, *Physics Letters B* **715** (sep, 2012) 348–351.

[311] P. Zhao, Y. Tian, X. Wu and Z.-Y. Sun, *The quasi-normal modes of charged scalar fields in kerr-newman black hole and its geometric interpretation*, *Journal of High Energy Physics* **2015** (nov, 2015) .

[312] J. M. Bardeen and G. T. Horowitz, *The Extreme Kerr throat geometry: A Vacuum analog of AdS(2) x S**2*, *Phys. Rev.* **D60** (1999) 104030, [hep-th/9905099].

[313] M. Guica, T. Hartman, W. Song and A. Strominger, *The kerr/cft correspondence*, *Phys. Rev. D* **80** (Dec, 2009) 124008.

[314] G. Compère, *The kerr/CFT correspondence and its extensions*, *Living Reviews in Relativity* **15** (Oct., 2012) .